Quasi-real photo-production of hyperons

and their impact on Λ^0 polarization measurements

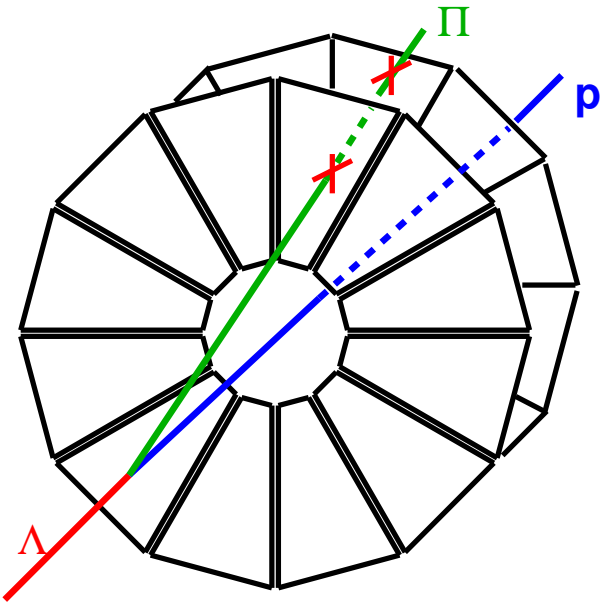

A.J. Reischl

March 5, 2007

Cover photo by jsteel [75]

Printed by Ponsen & Looijen b.v., Wageningen.

Quasi-real photo-production of hyperons

and their impact on Λ^0 polarization measurements

ACADEMISCH PROEFSCHRIFT

ter verkrijging van de graad van doctor

aan de Universiteit van Amsterdam

op gezag van de Rector Magnificus

prof. dr. J.W. Zwemmer

ten overstaan van een door het college voor promoties ingestelde

commissie, in het openbaar te verdedigen in de Aula der Universiteit

op dinsdag 3 april 2007, te 12:00 uur

door **Andreas Johannes Reischl**

geboren te Pforzheim, Duitsland

Promotiecommissie

Promotor:	prof. dr. G. van der Steenhoven
Co-promotor:	dr. J.J.M. Steijger
Overige Leden:	dr. E-C. Aschenauer
	prof. dr. S.C.M. Bentvelsen
	dr. D. Hasch
	prof. dr. J.H. Koch
	prof. dr. P.M. Kooijman
	prof. dr. F.L. Linde

Faculteit der Natuurwetenschappen, Wiskunde en Informatica

The work described in this thesis is part of the research program of the *Nationaal Instituut voor Kernfysica en Hoge-Energiefysica* (NIKHEF) in Amsterdam, the Netherlands. The work was financially supported by the *Stichting voor Fundamenteel Onderzoek der Materie* (FOM), which is financially supported by the Nederlandse organisatie voor Wetenschappelijk Onderzoek (NWO).

für **Mechthild**

Contents

Chapter 1

Introduction

Fundamental research in subatomic physics is probing the structure of matter. After discovering that matter is made up of atomic nuclei with a core which is built from protons and neutrons, even smaller constituents were identified, the quarks and gluons. So far, these particles are assumed to be the smallest constituents of matter. All composite particles consisting of quarks and gluons are referred to as hadrons. Many hadrons have been been discovered and are grouped according to their properties such as mass, charge and spin.

Deep-inelastic electron scattering experiments showed that the quarks (gluons) are spin-$\frac{1}{2}$ (spin-1) particles. The gluons act like the carrier of the strong force which is described by the theory of Quantum Chromo Dynamics (QCD). While QCD is very successful in describing the physics at small distances, it cannot be used in a straight forward manner at large distance, like in nucleons, because of the increase of the value of the strong coupling constant α_s. Still, it is possible to calculate lepton nucleon scattering in the framework of QCD by introducing so-called structure functions which describe the internal structure of nucleons. In order to account for the spin of the particles as well spin-dependent structure functions were introduced.

Initially, the composite spin of the nucleon was assumed to be due to the spins of the valence quarks alone. In this model the spin of two quarks are oriented in opposite directions and therefore the third quark is responsible for the nucleon spin which is $\frac{1}{2}$. The first polarized Deep Inelastic Scattering (DIS) experiment at CERN, European Muon Collaboration ([17, EMC]), surprisingly found that the spin of the quarks are responsible for at most $20 - 30$ % of the nucleon spin. Subsequent experiments at CERN, SLAC and DESY confirmed this relatively small quark contribution to the nucleon spin.

The origin of the nucleon spin developed into one of the major open issues in quark-gluon physics. Now it is believed that the nucleon spin has several components as expressed by:

$$\frac{1}{2} = \frac{1}{2}\Delta\Sigma + \Delta G + L_q + L_g, \tag{1.1}$$

with $\Delta\Sigma$ the quark spin component, ΔG the gluon spin component and L_q respectively

L_g the orbital angular momentum component of the quarks and the gluons, respectively. The contribution to the nucleon spin originating from quarks can be expressed as:

$$\Delta\Sigma = \Delta u + \Delta\bar{u} + \Delta d + \Delta\bar{d} + \Delta s + \Delta\bar{s}. \tag{1.2}$$

To study the origin of nucleon spin many approaches have been proposed over the years. Among them the most prominent one is spin-dependent lepton-nucleon DIS. It should be noted, however, that each approach has its own limitations and model dependencies. One alternative method measures the origin of the nucleon spin via Λ^0 hyperon production. This method is particular interesting, as advertised by Jaffe [54] and Ellis [53]. As explained in these papers Λ^0 production can also be used to get information on the spin structure of other hadrons than the proton and neutron, such as the spin structure of the Λ^0 hyperon itself. In a naive model the spin of the Λ^0 is due to the s-quark, while the u and d-quark spin cancel. Measurements of the Λ^0 polarization can be used to verify this idea or instead determine if the u and d quark contribute to the nucleon spin as well.

The quoted model of Ellis distinguishes two kinematical regimes, that are the current and target fragmentation region. In this model the polarization measurements in the target fragmentation region give information on the relative orientation of s and u-quarks in the nucleon. Moreover, Lambda production in the current fragmentation domain gives access to the spin structure of the Λ^0 hyperon. With a transversely polarized target transversity, the only unmeasured Leading Order (LO) structure function of the nucleon, can be studied.

In order to apply these ideas, we need to understand the Λ^0 hyperon production mechanism. A key problem there is the role of heavier hyperons decaying to a Λ^0. Since these heavier hyperons can also be polarized, a substantial heavy hyperon contribution to the Λ^0 signal may modify, or if unpolarized dilute, the Λ^0 polarization signal.

The goal of this thesis is to study the influence of heavier hyperons on Λ^0 production in a novel approach. This analysis is carried out using data taken at HERMES (HERA Measurement of Spin) experiment which is located at the HERA (Hadron-Elektron-Ring-Anlage) storage ring at (Deutsches Elektronen SYnchrotron) DESY Hamburg, Germany. As many hyperons as possible are reconstructed from the HERMES data in a consistent way. Form the measured particle yields the production cross sections are calculated. With the help of Monte Carlo generators these cross sections are corrected for inefficiencies and extrapolated to the 4π acceptance. With these results in hand, the question on how many Λ^0 hyperons are produced directly in the scattering and fragmentation processes and how many are coming from decays of heavier hyperons is addressed. Previously, only MC predictions for this so-called feeding process existed. In this work the measured yields are corrected for acceptance differences between the various hyperons using a simple MC model to derive conclusions on the feeding of heavier hyperons to the Λ^0 signal.

This thesis is thus devoted to two main subjects. Firstly, the development of a new instrument, the Lambda Wheels (LW), that will make it possible to observe more Λ^0 hyperons in DIS experiments at HERMES. This instrument, which is an addition to the HERMES spectrometer, is co-developed and commissioned in the framework of the

present research project. The LW has a larger acceptance as the spectrometer and therefore allows to increase the statistics of reconstructed hyperons. Furthermore, it increases the range covered by the kinematic observable Feynman x_f into the target fragmentation region. The second main subject of this thesis is an experimental study of the feeding from heavier hyperons. The latter issue has never been studied before using experimental data. This is crucial as MC simulations of hyperon production are notoriously difficult and are therefore not considered to be reliable.

The outline of the thesis

The thesis is organized as follows. An overview of the relevant physics issues is presented in chapter 2. This chapter introduces the concept of nucleon spin, followed by an introduction of the physics of DIS. The same chapter describes the concepts of *semi-inclusive* physics and, finally, the production and spin transfer model for hyperon production is presented.

Chapter 3 describes the experiment. First, the facility and the accelerator at DESY are briefly described. Then, the HERMES experiment itself with all its components are discussed as detailed as necessary for the analysis presented in this thesis.

The next two chapters describe the two hardware components which were co-developed in the framework of this thesis. The first one is the LW project presented in chapter 4 which was the main focus of this work. Secondly, the Beam Loss Monitor (BLM) is described in chapter 5. The BLM protects the sensitive detector components of the LW's and other sub-detectors of the HERMES experiment. In the end of this chapter the analysis of the first data which have been taken with both components are presented.

The second main focus of this thesis is the analysis of hyperon production data collected with the HERMES experiment. This analysis is presented in chapter 6. After discussing the data quality aspects, the reconstruction of Λ^0 hyperons is described as it is the basis of all other hyperon analyses. Then, the analysis of the heavier hyperons is discussed. The last section deals with the Monte Carlo studies carried out for this analysis. Two generators have been used, the PYTHIA and the DCAY generator, to determine efficiencies and subprocess fractions.

In the last chapter the main conclusions of this thesis are summarized.

Chapter 2

Physics

> "I think it is safe to say that no one understands quantum mechanics." Richard Feynman

In this chapter the basic physics issues addressed in this thesis are presented. As the subject of this thesis is quasi-real photo-production of hyperons, both the physics of hyperon production and the physical process in which photo-production occurs, that is deep-inelastic lepton scattering, need to be addressed. Polarization plays an important role in the discussion, as on the one hand hyperon polarization is poorly understood, while on the other hand spin-dependent deep-inelastic scattering allows to probe polarization phenomena.

Section 2.1 discusses the physics of hyperon production. The section focuses on hyperon polarization, the purities of the production process and the yields. It also presents the model of hyperon production implemented in the Monte Carlo generator PYTHIA which is the code used throughout this thesis for simulations. The next section 2.2 describes deep inelastic lepton scattering, including a discussion of its spin dependence and an introduction of the necessary kinematical variables used in the analysis. In the last section 2.3 recent results obtained in the field of hyperon production from various experiments are presented.

2.1 Hyperon production

Baryon production in high energy lepton- or photo-production experiments can be used to study the process of fragmentation of quarks and gluons into observable hadrons. At present no theoretical description of this process exists that makes it possible to carry out calculations from first principles. It is assumed that all baryons are produced by a similar mechanism during the fragmentation process. There exists a hierarchy of production rates from spin 1/2 particles with strangeness one (Λ^0) via the double strange particles ($\Xi^{0/-}$) down to the spin 3/2 excited single strange states ($\Sigma^{*0/\pm}$) and finally the triple strange Ω^-.

In figure 2.1 the SU(3) baryon octet and decuplet are depicted. This hierarchy depends first of all on the mass of the produced hyperon. Additionally, mechanisms are required to suppress or enhance the production of hyperons depending on their strangeness and or spin configuration. Hence, measurements of the production rates of many different hyperons in one experiment provides a testing ground for various baryon production mechanisms. The studies presented in this work can also be used to compare the observed production rates of hyperons to other baryon production rates measured at HERMES, in particular those of the orbitally excited $\Lambda(1520)$ and the alleged penta-quark state $\Theta(1530)$[10].

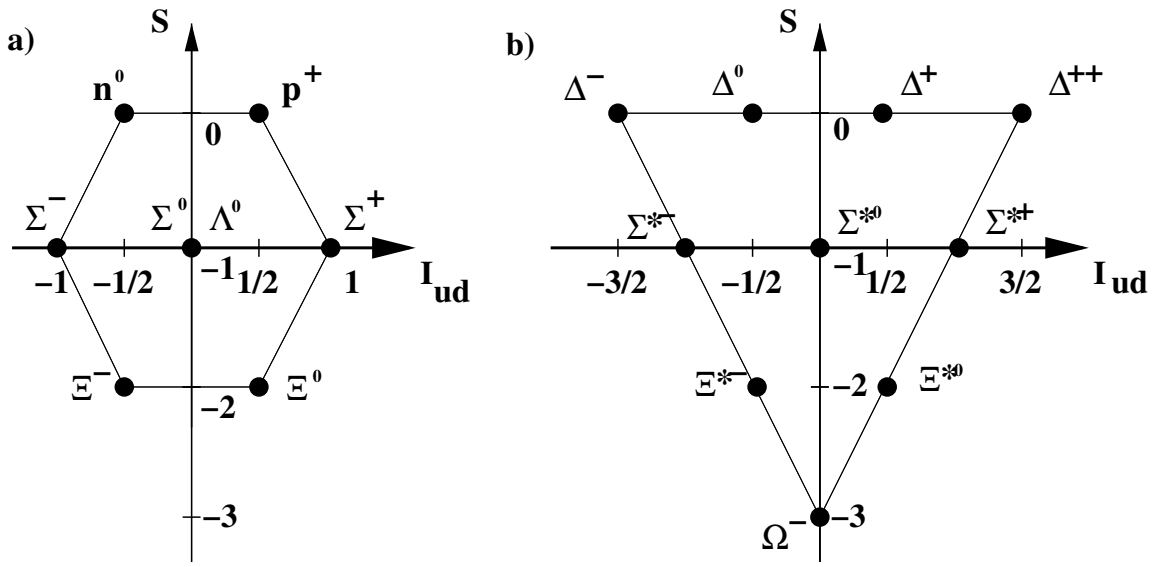

Figure 2.1: Shown are the baryon octet a) and decuplet b). The y-axis corresponds to the strangeness content and the x-axis to the sum of the quark spins where $I_u = +1/2$ and $I_d = -1/2$.

Hyperons are especially interesting as they contain a strange valence quark which is not present in the target protons. As a result models of hadron structure developed for non-strange hadrons, can be tested on a separate class of hadrons. Furthermore, many hyperons decay weakly and therefore enable a measurement of their polarization. Their displaced vertices are a good means to separate them from the background. Furthermore, weak decays make it possible to measure the polarization through the angular dependence of the decay products. This allows a study of the spin structure of hyperons, which is a subject of considerable interest in view of the non-trivial nucleon spin structure.

For each of the subjects mentioned above, a pure sample of well identified hyperons is needed. However, as many heavy hyperons decay via lighter hyperons, in particular the sample of light hyperons is possibly seriously contaminated. The Λ^0 hyperon is a special case as its self analyzing decay into a proton and a pion can be used to study various aspects of hadron spin physics. For the interpretation of results obtained with a Λ^0 polarization measurement it is crucial to know the fraction of Λ^0 hyperons which are produced directly in the fragmentation process and the fraction originating from decays of heavier hyperons. It is the purpose of the present thesis to investigate both

through simulations and measurements the purity of Λ^0 hyperons that are produced at the HERMES experiment. Once such purity factors are established, similar data can be used to study the spin structure of hyperons (the Λ^0 in particular), their production mechanism and other subjects in hadron spin physics such as transversity and the relative orientation of s-quarks and u-quarks in the nucleon.

2.1.1 Feeding and subprocess fractions

In this thesis two methods are used to determine the relative amounts of Λ^0 hyperons which are due to heavier hyperon decays. This process is also denoted as *feeding*, that is the contribution to hyperon production coming from decays of heavier hyperons. For example, the decay of $\Sigma^0 \to \Lambda^0 + \gamma$ is feeding Λ^0 hyperon production.

The first method to determine the amount of feeding is mainly based on data. The starting point is the experimental yield of heavy hyperons N^Y. This factor is multiplied by a relative acceptance factor evaluated by means of the DCAY Monte Carlo simulation. To evaluate this factor the number of Λ^0s originating from hyperon Y that are reconstructed in HERMES for every hyperon Y that was fully reconstructed in HERMES needs to be evaluated. This gives an estimate of how many Λ^0 are coming from those hyperons. The total feeding fraction is determined by adding all subprocess contributions considered. This method only includes feedings from hyperons that are reconstructed in the experiment. The formula to determine the feeding of hyperon L from hyperon Y in the HERMES acceptance is given by

$$F_L^Y = N^Y \cdot C_L^Y, \tag{2.1}$$

where N^Y is the observed yield of hyperon of type Y in the HERMES acceptance and C_L^Y the relative acceptance factor determined from the DCAY MC. The acceptance factor is evaluated by taking the ratio of the number of hyperons of type Y of which only the Λ^0 track was observed in the acceptance to the total number of reconstructed hyperons of type Y in the HERMES acceptance, that is

$$C_L^Y = \frac{N_{MC}^{Y\to\Lambda}}{N_{MC}^{Y\to\Lambda\pi}}. \tag{2.2}$$

In order to calculate the percentage of Λ^0 hyperons which were produced directly the following formula can thus be used:

$$P^\Lambda = 1 - \sum_Y N^Y \cdot C_L^Y. \tag{2.3}$$

It is crucial to realize the advantage of Eq. 2.3, as the yield factors are determined experimentally while the acceptance correction factors only weakly depend on the details of the MC simulations since they represent relative numbers (see Eq. 2.2). Therefore the pure Λ^0 yield P^Λ is almost entirely driven by measured quantities.

In the second method the so-called *subprocess fractions* are determined from Monte Carlo studies only. The fractions f_L^Y are a simple result of counting the parents of type Y resulting in a hyperon of type L in a given bin i and normalizing it to the total yield of hyperons of type L, like

$$\sum_i f_{Li}^Y = \frac{N_L^Y}{N_L}. \tag{2.4}$$

The result depends on the model encoded in the MC and will vary with the settings and parameters used. The subprocess fractions determined in this way have the advantage that all channels implemented in the MC model are included. With the MC implementation in PYTHIA (see following section) the determination of the subprocess fractions is straight forward. In special MC tables of the UDST-files produced by the MC the actual parent of each reconstructed particle can be identified. The parent is either a quark or a diquark or it is a heavier hyperon. Next the subprocess fraction is evaluated by calculating the ratio of the number of events originating from hyperon Y to the total amount of hyperons L produced in the acceptance. The purity of the yield of Λ^0 hyperons is thus calculated by

$$P^\Lambda = 1 - \sum_Y f_L^Y. \tag{2.5}$$

This can also be done separately for different kinematical bins as discussed in section 6.5.4.

2.1.2 PYTHIA

Generally, Monte Carlo generators are used to fill the gap between the measurable parts of a given distribution and the parts which lie outside the measurable area. For the extraction of cross sections, for example, the acceptance function of the spectrometer has to be known, which essentially represents the relative acceptance in a given kinematic bin with respect to the overall acceptance. This acceptance function can be determined utilizing Monte Carlo methods.

In this analysis the main MC tool is the PYTHIA 6.2 [71] generator. It is one of the main generators used in DIS experiments such as HERMES, because the PYTHIA generator models many high energy physics events quite well including, for instance, scattering of leptons from nucleons. The generator describes the physics of deep inelastic scattering involving hard interactions with virtual photons and soft processes including real photons. In fact, the generator includes all leading order QCD processes.

It should be noted, however, that PYTHIA contains a number of parameters. These parameters are mostly related to the fragmentation process, which needs to be tuned using experimental input as the fragmentation functions cannot be calculated from first principles. The tuned parameters may even be energy dependent.

Originally, the PYTHIA generator has been tuned to high energy e^+e^- experiments like the ones at LEP. At HERMES great efforts have been spent to tune the generator settings for the corresponding kinematical regime (see [52, 61]). Further tuning [58] for hyperon

production has led to very good agreements for many kinematical distributions involved in Λ^0 production. An overview of the tuned parameters is given in table 2.1, in the column labeled 2004C.

PARJ	default	2004C	explanation
1	0.10	0.029	diquark suppression P(qq)/P(q)
2	0.30	0.283	s quark suppression P(s)/P(u)
3	0.40	0.4	extra suppression of strange diquarks
4	0.05	0.05	suppression of spin-1 diquarks over spin-0
11	0.50	0.5	Vector-Meson to pseudo-scalar suppression
12	0.60	0.6	VM to pseudo-scalar supp. for strangeness
21	0.36	0.40	width (σ) for p_x, p_y transverse momentum distributions for primary hadrons
23	0.01	0.01	fraction of non Gaussian tails to the p_t distribution times a factor to increase PARJ 21
24	2.0	2.0	
41	0.30	1.94	parameter a for symmetric Lund fragmentation function
42	0.58	0.54	parameter b for symmetric Lund fragmentation function
45	0.50	1.05	parameter a for the symmetric Lund fragmentation function for diquarks

Table 2.1: Shown are the default and tuned parameters used when employing the PYTHIA event generator.

Three stages can be identified in the MC event generation process. First, the hard scattering of a lepton from a nucleon calculated which involves the exchange of a virtual photon is calculated. Second, the fragmentation of partons into photons, leptons, mesons and baryons is evaluated. Third, the decay of any unstable particles produced into observable hadrons in the detector is taken into account.

The first stage simulates the perturbatively calculable (in QCD) partonic processes contributing to the scattering. PYTHIA simulates the total virtual photon-nucleon cross section, and weights it with the virtual photon flux obtaining the lepton nucleon cross section.

The second stage of the fragmentation process is modeled by the LUND string fragmentation model [15]. This model is based on color confinement at large distances. Two colored objects, for example a quark and an anti-quark, are bound together by a string. The energy of the string grows linearly with its length. If the energy stored is large enough to create new colored objects the string can break. This process continues until the energy of the remaining string falls below a threshold for the production of a particle.

In the LUND string fragmentation model, for a given initial quark the creation of a quark/anti-quark pair which breaks the string is implemented as well. The initial quark and the new anti-quark may form a meson while the new quark propagates further. The flavor of the quark/anti-quark pair is determined by the production probabilities where, for example, the production of a $s\bar{s}$ pair is suppressed. This suppression can

be adjusted with a parameter. The production of baryons is implemented using the so-called *Diquark picture*. Here, the initial parton is allowed to be either a quark or a colored triplet involving an anti-diquark for instance. Similar to meson production new quarks or diquarks can be produced. This process has three main parameters. The first one is the relative probability to pick a diquark rather than a quark. The second one is the extra suppression for strange diquarks and the third one is a suppression of spin-1 diquarks over spin-0 diquarks. There are two baryon multiplets implemented in PYTHIA, namely the SU(3) octet with $S = J = 1/2$ and the decuplet with $S = J = 3/2$ covering all hyperons which are analyzed in this thesis. In figure 2.1 the SU(3) baryon octet and decuplet are depicted.

There are three main event classes which are used in the MC model. The first one is the so-called *anomalous* process where the photon splits into two quarks and interacts via a gluon with a parton from the nucleon. The second process is the so-called *Vector Meson Dominance (VMD)* process where the photon turns into a vector meson before it interacts with the nucleon. This process covers all diffractive hadron interactions from elastic and diffractive scattering to non-diffractive scattering. In these first two cases a hadronic structure of the photon is taken into account. The second class also includes hard non-diffractive processes and the soft so-called *low-pt* events. The later process turns out to dominate at HERMES energies [63]. The third class is the so-called *direct* process where the photon interacts directly with a parton of the nucleon. The main contribution here is the leading order DIS process but it also includes QCD Compton and photon-gluon fusion (PGF). Uncertainties in the PYTHIA model cannot be truly quantified as there are no alternative models of similar quality available.

2.2 Deep-Inelastic-Scattering

The spin structure of the nucleon is under investigation since many years. The first results in this field [17, EMC] revealed the fact that the nucleon spin is not only carried by its constituent quarks and thus that there must be other carriers of angular momentum in the proton. This result has been subsequently confirmed by many other experiments [4, SMC], [1] and also by HERMES [3]. The anomalous spin structure of the nucleon, raises the question whether the spin structure of the hyperon is anomalous as well. The Λ^0 hyperon is particularly interesting because the angular momentum is preserved in the decay and its polarization can be measured by the angular distribution of the decay products. In fact, the question can be asked whether the Λ^0 hyperon spin is exclusively carried by its constituent strange quark or not. In order to address this issue the following section briefly summarizes the available knowledge of the nucleon spin. In section 2.2.2 deep-inelastic lepton scattering is introduced as this is the process used to study nucleon spin and it serves as a framework for the present work. In section 2.3 the most recent results on hyperon polarization are summarized, and it is explained how hyperon polarization experiments can be used to study several issues in hadron spin physics.

2.2.1 Nucleon spin

The total spin of the nucleon can be split in three parts

$$\frac{1}{2} = \frac{1}{2}\Delta\Sigma + \Delta G + L_z. \tag{2.6}$$

We know that the total, which is the intrinsic spin of the nucleon, is equal to $\frac{1}{2}$. The quantity $\Delta\Sigma$ is the fraction of the nucleon spin carried by the quarks, Δg is the contribution from the gluons and L_z is the contribution from the orbital angular momentum of the partons. The polarized DIS experiments mentioned above measured $\Delta\Sigma$ by evaluating asymmetries of the cross section with respect to the relative spin orientation of beam and target in inclusive DIS. The contributions of the different quark flavors have also been measured by determining the cross section asymmetry separately for data with a pion or kaon in the final state [7, 9].

2.2.2 DIS kinematics

The DIS process can be denoted by the following general form

$$l + N \rightarrow l' + X, \tag{2.7}$$

where l and l' are the initial and final states of the scattered lepton and N is the target nucleon which is broken up yielding the final state hadron system denoted by X. The incident lepton energy at HERMES is 27.6 GeV, which corresponds to a center of mass energy of $\sqrt{s} = \sqrt{(k+P)^2} = \sqrt{2ME + M^2} = 7.26$ GeV. In this energy domain the exchange bosons are almost exclusively photons. The process is depicted in figure 2.2.

An incoming lepton with four-momentum $\mathbf{k} = (E, \vec{p})$ scatters off a nucleon with four-momentum $\mathbf{P} = (M, \vec{0})$ by exchanging a photon with four-momentum $\mathbf{q} = (\nu, \vec{q})$. In a fixed-target experiment such as HERMES the initial nucleon has a negligible momentum. The scattering process is denoted as deep inelastic scattering if the energy transfered to the nucleon is so high that the reaction is dominated by the interaction with a point like quark. In the experiment each track is identified by the measured value of its absolute momentum, its position and scattering angles (θ, ϕ).

There are a couple of observables which characterize the scattering event. The first to mention is Q^2 which is defined as:

$$Q^2 \equiv -\mathbf{q^2} = -(\mathbf{k} - \mathbf{k}')^2 \overset{\text{Lab}}{=} EE' \sin^2\left(\frac{\theta}{2}\right), \tag{2.8}$$

where Q^2 is the negative four momentum transfered by the photon from the lepton to the target nucleon. Here, the quantity θ represents the angle between the scattered and incident lepton. The second observable is the corresponding energy ν transfered from the lepton to the nucleon

$$\nu \equiv \frac{\mathbf{P}\cdot\mathbf{q}}{M} \overset{\text{Lab}}{=} E - E' \tag{2.9}$$

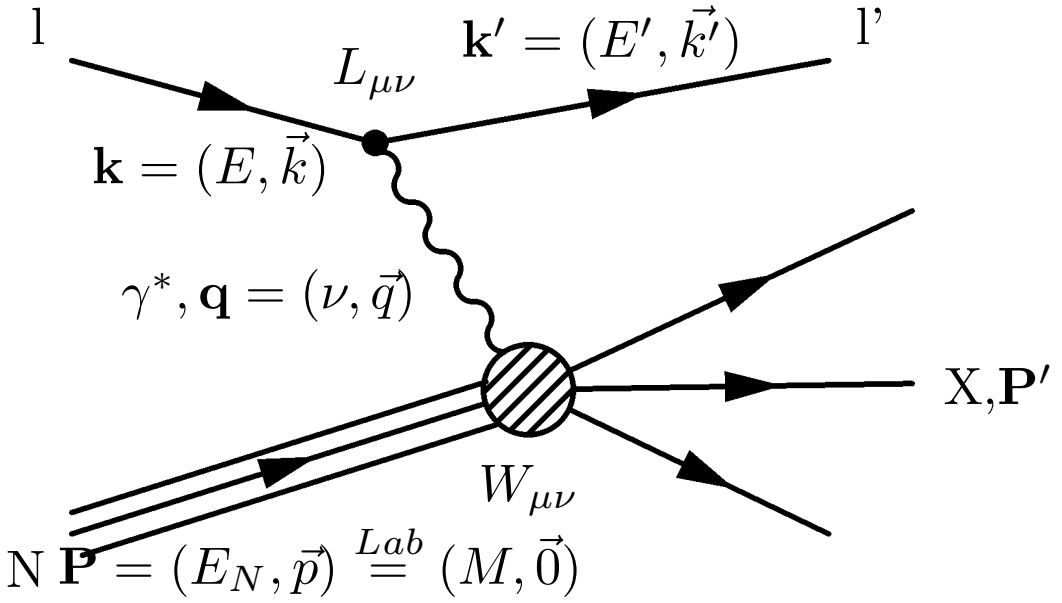

Figure 2.2: Deep-inelastic lepton scattering on a proton target. All relevant kinematic variables shown are described in the text.

with E the initial and E' the final state lepton energy. The squared invariant mass of the final hadronic system can be calculated using:

$$W^2 = (\mathbf{P} + \mathbf{q})^2 \overset{\text{Lab}}{=} M^2 + 2M\nu - Q^2, \tag{2.10}$$

here M is the mass of the target nucleon. The deep-inelastic scattering region is usually defined by requiring $Q^2 > 1$ GeV^2 and $W > 2$ GeV.

The DIS events can also be characterized using dimensionless variables like the Bjorken scaling variable x which is a measure of the inelasticity of the process

$$x = \frac{Q^2}{2\mathbf{P} \cdot \mathbf{q}} \overset{\text{Lab}}{=} \frac{Q^2}{2M\nu} \tag{2.11}$$

and the fractional energy transfer y from the virtual photon to the target

$$y = \frac{\mathbf{P} \cdot \mathbf{q}}{\mathbf{P} \cdot \mathbf{k}} \overset{\text{Lab}}{=} \frac{\nu}{E}. \tag{2.12}$$

The kinematically allowed region for x ranges from 0 to 1, with the upper limit corresponding to elastic scattering where the invariant mass of the final hadronic system W is equal to the target mass (M).

The most important kinematic variables characterizing any hadron produced in DIS are the fractional energy z of the hadron and its energy E_h

$$z = \frac{\mathbf{P_h} \cdot \mathbf{P}}{\mathbf{P} \cdot \mathbf{q}} = \frac{E_h}{\nu}, \tag{2.13}$$

and the Feynman scaling variable x_f

$$x_f = \frac{\vec{q}_{cm} \cdot \vec{h}_{cm}}{\vec{q}_{cm}^2} \tag{2.14}$$

where $\vec{q}_{cm}$ stands for the momentum of the exchanged photon in the center of mass frame of the Lambda particle and $\vec{h}_{cm}$ for the hadron momentum.

2.3 Recent results

In the past many hyperon hadro-production experiments have been carried out, which gave a first indication that the induced hyperon polarization cannot be easily understood [50]. In this section a short overview of hyperon electro- and photo-production experiments in high energy physics is given as these results are more directly related to those presented in this thesis. Two types of experiments are distinguished: hyperon production in DIS experiments and in e^+e^- experiments. In presenting the recently obtained data a different distinction is made, that is between hyperon yields (discussed in section 2.3.1) and hyperon polarization measurements (discussed in section 2.3.2).

2.3.1 Hyperon yields

An example of hyperon yields obtained from e^+e^- experiments [19, 13] is shown in figure 2.3, where the mean production rate per event of hyperons is shown versus their mass. The presented rates are normalized by the total particle spin (2J+1) and include both the particle and antiparticle states. A clear dependence on the available e^+e^- center of mass energy $\sqrt{s}$ is visible. These experimental results cannot be directly compared to DIS measurements but are suitable as a starting point for comparison. As the fragmentation process in e^+e^- and DIS are quite similar, a similar decrease of hyperon yields with mass is expected for DIS. However, deviations in the description of hadronization processes between e^+e^- and DIS experiments are known.

Before being able to interpret the measured yields it is necessary to discuss the influence of feeding. With the knowledge of the particle yields and their branching ratios the production cross sections of lighter hyperons can be corrected for the feeding. This correction is particular important for polarization measurements as neighboring hyperons may have opposite spin.

2.3.2 Polarization measurements

The Λ^0 polarization is determined by measuring the asymmetry in the angular distribution of protons in the parity violating decay process $\Lambda \to p\pi$. In the Lambda rest frame the

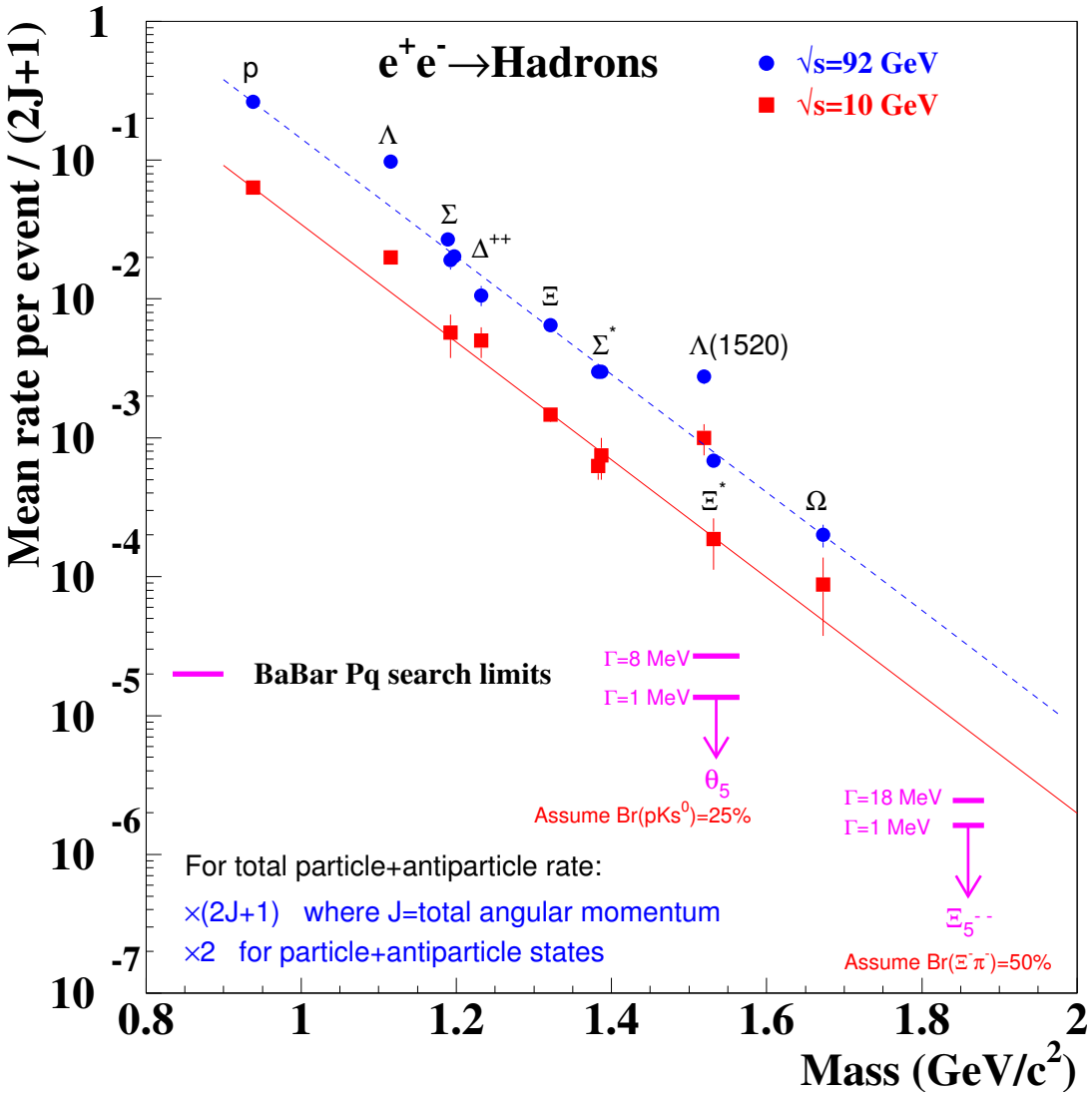

Figure 2.3: Baryon production rates in e^+e^- annihilation from experiments at the mass of the Z^0 (solid circle) and $\sqrt{s} = 10$ GeV (solid squares) as a function of baryon mass. The vertical scale accounts for the number of spin and particle + antiparticle states, and the lines are chosen to guide the eye. The plot is taken from from [19]

.

decay protons are distributed as:

$$\frac{dN}{Nd\Omega} = \frac{1}{4\pi}(1 + \alpha\vec{P}\cdot\vec{k}), \tag{2.15}$$

where $\vec{P}$ is the Lambda polarization vector, $\alpha = 0.642 \pm 0.013$ is the decay asymmetry parameter and $\vec{k}$ is the unit vector along the decay proton direction.

The polarization of the Λ^0 is measured by evaluating the $\cos\theta$ distribution of the decaying proton with respect to a given coordinate system, where θ is for example the angle of the proton in the rest frame of the Λ^0. There is some freedom in choosing the coordinate system used for evaluating the Λ^0 polarization. In the case of the HERMES experiment usually the normal to the scattering plane is chosen as the reference direction. The obtained experimental $\cos\theta$ distribution has to be corrected for acceptance effects. After corrections a fit of the $\cos\theta$ distribution using Eq. 2.15 provides a measure of the Λ^0 polarization.

In the HERMES experiment the spin transfered from a polarized beam to a Λ^0 hyperon can be measured. In practice the Λ^0 polarization P^Λ is measured, which is given by

$$P^\Lambda = P_b \cdot D(y) \cdot D^\Lambda_{LL'}, \tag{2.16}$$

where P_b is the beam polarization, $D(y)$ the depolarization factor of the virtual photon and $D^\Lambda_{LL'}$ the spin transfer coefficient. The polarization data for P^Λ can thus be used to determine the quantity $D^\Lambda_{LL'}$. In theoretical models the spin transfer coefficient $D^\Lambda_{LL'}$ is defined as

$$D^\Lambda_{LL'} = \frac{G^\Lambda_{1,f}(z)}{D^\Lambda_{1,f}(z)}, \tag{2.17}$$

where $G^\Lambda_{1,f}(z)$ ($D^\Lambda_{1,f}(z)$) is the spin (in)dependent fragmentation function for Λ^0s produced in DIS. Assuming u quark dominance and iso-spin symmetry between u and d quarks the spin transfer coefficient can be approximated as

$$D^\Lambda_{LL'} \approx \frac{\Delta q^\Lambda_u}{q^\Lambda_u}. \tag{2.18}$$

This approximation can be understood by considering the probability to form a polarized Λ^0 starting from a u quark, which is the dominant process. The probability for this process is proportional to the extend by which the u quarks in the Λ^0 are polarized, that is the spin-dependent distribution function for u-quarks, which in Eq. 2.18 is given by Δq^Λ_u. Similarly, the probability to form a Λ^0 hyperon from a u-quark is proportional to the distribution of u quarks in the Λ^0, q^Λ_u. Thus, a relation between the measured Λ^0 polarization and the u-quark polarization in the Λ^0 hyperon is established. In other words, polarization transfer measurements to the Λ^0 can be used to study the spin structure of the lightest hyperon.

The Λ^0 polarization has firstly been measured in ν_μ charged current interactions by the NOMAD experiment [18]. A non-zero polarization along the W-boson direction has been

observed in both the target fragmentation region: $D^{\Lambda}_{LL'}(x_f < 0) = 0.21 \pm 0.04(\text{stat}) \pm 0.02(\text{sys})$, and in the current fragmentation region: $D^{\Lambda}_{LL'}(x_f > 0) = +0.09 \pm 0.06(\text{stat}) \pm 0.03(\text{sys})$. These data are shown in figure 2.4. The $x_f > 0$ data seem to suggest that the u-quarks are possibly slightly polarized in the Λ^0 hyperon. However, apart from the statistical uncertainty these data sets suffer from a crucial systematic uncertainty as the purity of the Λ^0 signal is likely less than 100 %. This leads to serious uncertainties as long as no experimental information on the feeding from heavier hyperons is available. It is the purpose of the present thesis to provide such information for the first time.

Initial measurements at HERMES [6] yielded a longitudinal spin transfer coefficient $D^{\Lambda}_{LL'} = 0.11 \pm 0.10$ (stat) ± 0.03 (syst) at an average fractional energy carried by the Λ^0 hyperon $\langle z \rangle = 0.45$. The dependence of $D^{\Lambda}_{LL'}$ on both the fractional energy z and the fractional longitudinal momentum x_f is also shown in figure 2.4. The HERMES data are seen to be consistent with the NOMAD data. Moreover, the E665 experiment has measured the Λ^0 polarization as well with rather large error bars. The result is shown in figure 2.4 and was published in Ref. [5].

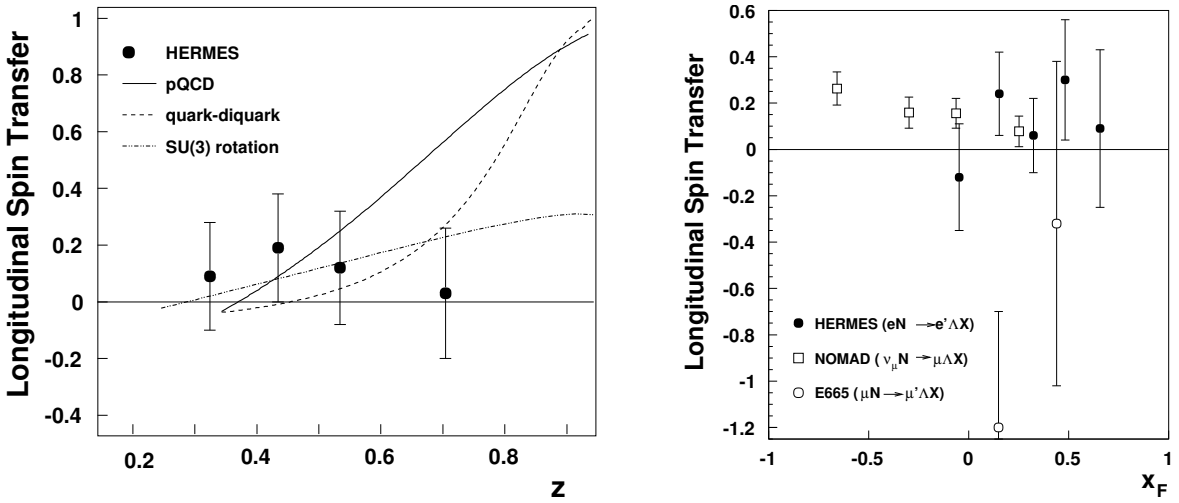

Figure 2.4: On the left side the z-dependence of the longitudinal spin-transfer coefficient $D^{\Lambda}_{LL'}$ for $x_F > 0$ is shown. The curves represent phenomenological model calculations [6]. On the right side the dependence of the longitudinal spin-transfer coefficient $D^{\Lambda}_{LL'}$ on x_F can be seen. The HERMES measurements are represented by the solid circles, while the open symbols represent data from NOMAD [18] (squares) and E665 [5] (circles).

The $x_f < 0$ data in figure 2.4 can be interpreted as a measurement of the relative orientation of u and s quarks in the target nucleon according to [53]. However, the interpretation of these data suffers from the same problem regarding the unknown feeding from heavier hyperons as was mentioned above for the $x_f > 0$ case. Additionally, a transverse polarization in the direction orthogonal to the production plane of $P_x(x_f < 0) = -0.22 \pm 0.03(\text{stat}) \pm 0.01(\text{sys})$ has been measured by NOMAD. Similar data will soon be published by the HERMES experiment, as well.

All these measurements have in common that the interpretation of the obtained results depend on the model used to describe the polarization transfer and on the number of Λ^0

hyperons which are produced directly. It thus needs to be investigated whether the Λ^0s have inherited their spin from a direct spin transfer of the target, or whether the Λ^0 spin is coming from decays of heavier hyperons where the polarization might be different.

"I am still confused, but on a higher level." Enrico Fermi

Chapter 3

The HERMES Experiment

The main design goal of the HERMES experiment [51] is the study of the spin structure of the nucleon. For this purpose deep-inelastic scattering experiments of polarized leptons on polarized internal gas targets are carried out using the HERA accelerator complex. It is crucial that both beam and target are highly polarized to obtain a high sensitivity to the various carriers of angular momentum in the nucleon. The HERMES experiment was installed and commissioned in the year 1995. The first Deep Inelastic Scattering (DIS) data were accumulated utilizing a polarized ^{3}He gas target. In the following years (1996-1998) mainly polarized hydrogen gas was used while in 1999 and 2000 polarized deuterium has been used as a target gas. In addition, a large amount of data on unpolarized gases like Neon, Nitrogen and Krypton has been taken. Since then the experiment is mostly devoted to measurements with a transversely polarized target.

In this chapter, the HERMES experiment is described. First, the HERA electron-proton collider at DESY is discussed in Sec. 3.1. The following section 3.2 presents the HERMES gas target. Then, the HERMES Spectrometer is discussed in Sec. 3.3. To conclude there is a brief description of the luminosity monitor of the HERMES experiment in Sec. 3.4.

3.1 DESY and HERA

The HERMES experiment is located at the HERA electron-proton collider at DESY in Hamburg, Germany. The collider consists of two rings, one for leptons and the other one for protons each with a circumference of 6.3 km. The HERMES experiment uses only the lepton ring. The maximum energy of the proton machine is 920 GeV while the lepton machine has a maximum energy of 27.6 GeV. There are 180 lepton bunches available which can store 60 mA beam current. The time between two bunches is 96 ns. One bunch completes one revolution in about 21.13 μs. The injection and acceleration of leptons takes about half an hour. Thereafter, the experiments can then take data for up to 12 hours.

There are four experiments located around the ring (see Fig. 3.1). The two collider

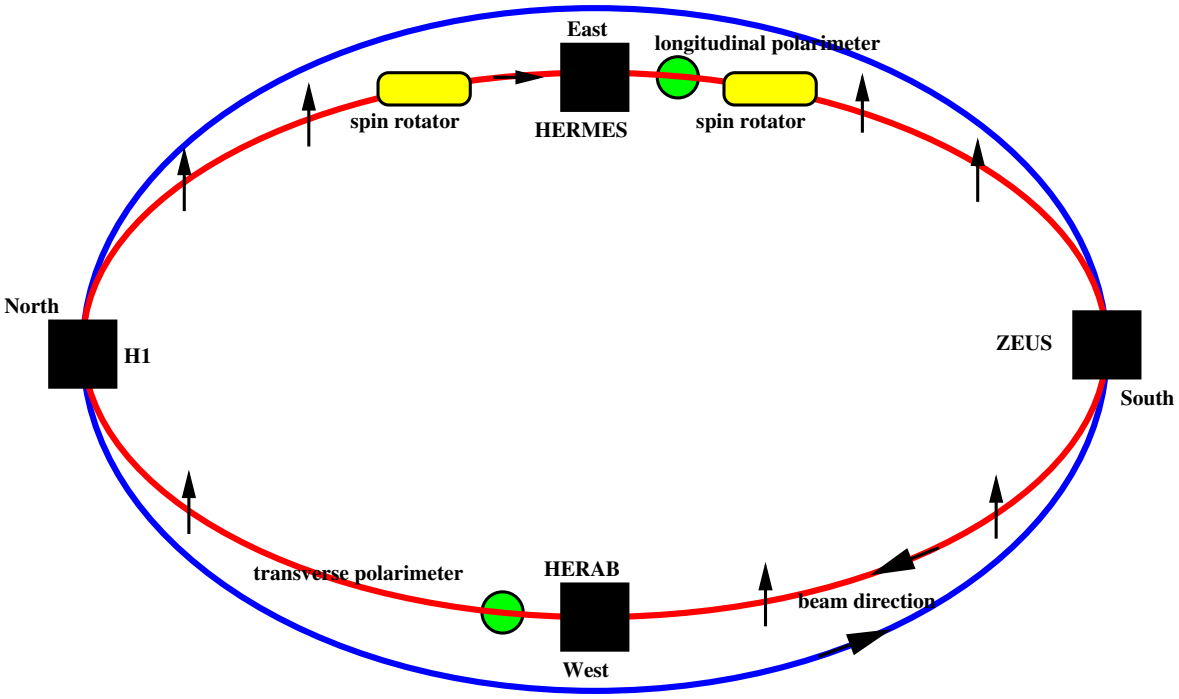

Figure 3.1: The HERA electron-proton collider and storage ring at the German institute for particle physics DESY, Hamburg.

experiments H1 and ZEUS use both the lepton and the proton beam. Both the H1 [40] detector and the ZEUS [87] detector are complex instruments designed to detect particles which are created when high energy leptons and protons collide. The main interest of research of the H1 and ZEUS collaborations is to measure the unpolarized structure of the proton, to study the fundamental interactions between particles, and to search for physics beyond the Standard Model of elementary particles and fields. In addition, the ZEUS and H1 experiments also carry out and compare measurements of neutral and charged current processes, observe high energy photo-production processes and search for new interactions and new particles.

The third experiment is the HERA-B [41] experiment which makes use of the proton beam only. HERA-B is a large-aperture high-rate spectrometer built for studies of collisions of 920 GeV protons with the atomic nuclei of target wires positioned in the halo of the HERA proton beam. The detector provides a good B decay vertex resolution, lepton and kaon identification, and multiple event reconstruction per bunch crossing. In 2003 the experiment has been stopped and was disassembled.

The fourth experiment, HERMES, is located at the east side of the HERA ring. As mentioned before, the HERMES experiment uses the lepton beam only, which scatters off a gas target. HERMES employs targets of nuclear-polarized atomic hydrogen or deuterium gas and various unpolarized gases. Several polarization asymmetries are measured for inclusive and semi-inclusive deep inelastic lepton scattering, as well as exclusive processes such as Deeply Virtual Compton Scattering (DVCS). The angles and energies of scattered and produced particles are determined using a spectrometer with complete

hadron identification. Measurements with longitudinally polarized targets were carried out in 1995-2000. Since 2002 the program has been continued with transversely polarized targets. A target recoil detector surrounding an unpolarized hydrogen target for further exclusive DVCS measurements has been installed for the last two years (2006-2007) of HERMES data taking.

3.1.1 Lepton beam polarization

From 1995 to 2000 (with the exception of 1998) and from 2002 to the end of 2004 the lepton ring was filled with positrons. In 1998 and since December 2004 again electrons are injected into the HERA accelerator. The lepton beam is naturally polarized through the Sokolov-Ternov effect [74]. This polarization arises due to a small asymmetric spin-flip amplitude in the emission of the synchrotron radiation with respect to the orientation of the magnetic bending field, which thus enhances transverse polarization of the beam leptons. The polarization would rise for an idealized ring with time t as

$$P(t) = P_{\infty} \cdot (1 - \exp^{-t/\tau}) \tag{3.1}$$

with P_{∞} the asymptotic polarization and τ the rise time constant. A typical polarization rise-time curve is shown in Fig. 3.2. Various depolarizing effects, mostly related to imperfect tunes of the HERA beam, dilute the polarization of the beam. The result is that values of P_{∞} are considerably lower then 100 %. For the HERA storage ring with a most commonly used lepton energy of 27.6 GeV a typical polarization of 55 % has been reached in the period 1995-2000 with a time constant of about 22 minutes. The achievement of 50 % beam polarization in 1993 (see Ref. [22, 23]) was an important step towards the approval of the HERMES experiment.

The study of the spin structure of the nucleon requires the availability of a longitudinally polarized lepton beam. Hence, the polarization direction of the lepton beam has to be rotated into the longitudinal direction before entering the experiment. This is done with so-called spin rotators, located in front of and behind the experiment. The configuration of the rotators can be changed to carry out measurements with opposite beam helicity in order to reduce systematic uncertainties and measure single beam asymmetries.

A precise measurement of the beam polarization is essential for an experiment which investigates the spin structure of the proton. This is achieved with two different polarimeters. The transverse polarimeter [62] was set up in the West hall of the HERA collider in 1993. It is a laser backscattering Compton polarimeter which uses an Argon-ion laser with a power of 10 Watt. A Pockels cell switches the photon polarization with a frequency of $\sim$ 84 Hz. The energy and the vertical position of the back-scattered photons are measured with a sandwich Tungsten calorimeter. The polarization of the beam is determined from the top-bottom asymmetry of the back scattered photons. The total uncertainty of a polarization measurement with the transverse polarimeter has been determined to be $\Delta P/P \approx 3$ % and includes both the statistical (after 10 min.) and systematical error.

The second polarimeter measures the longitudinal polarization of the lepton beam. It was installed in 1996 in the East-Hall of HERA and is located 50 meters downstream of the

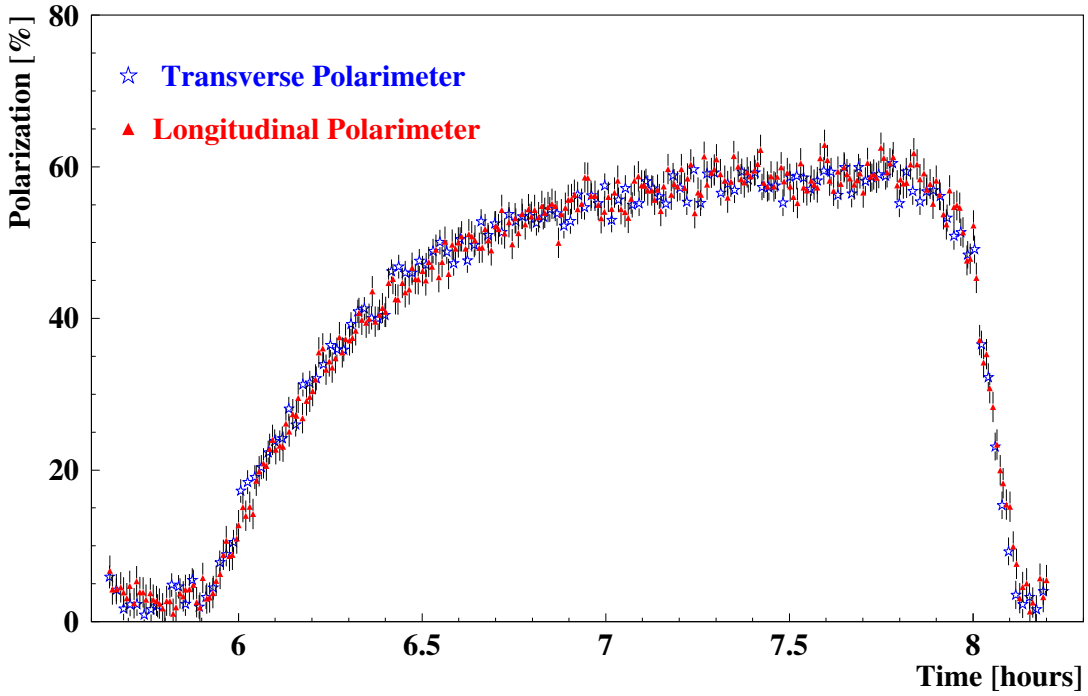

Figure 3.2: Comparison of the rise of the measured polarization for the longitudinal and transverse polarimeter.

HERMES experiment. The polarimeter uses a pulsed Nd:YAG laser with a wavelength of 532 nm. The polarization measurement uses the spin dependent cross section for Compton scattering of photons on leptons. Scattering on longitudinally polarized leptons gives a spin dependent energy spectrum of the back scattered photons. In contrast to the transverse polarimeter, where each back-scattered photon is measured separately the longitudinal polarimeter measures the total energy deposited per bunch (see [27]). The device is able to measure the polarization with a total uncertainty of $\Delta P/P = 1.6$ % in a time interval of one minute.

3.2 Internal Gas Target

The HERMES polarized ^{1,2}H gas target [8] is in use since 1996. It consists of an atomic beam source (ABS), a target vacuum chamber containing a target cell and a magnet. A target gas analyzer (TGA) and a Breit-Rabi polarimeter (BRP) are also present for diagnostic purposes. A schematic picture of the set up for a longitudinal polarized hydrogen target is shown in Fig. 3.3. The various components are described in the following paragraphs.

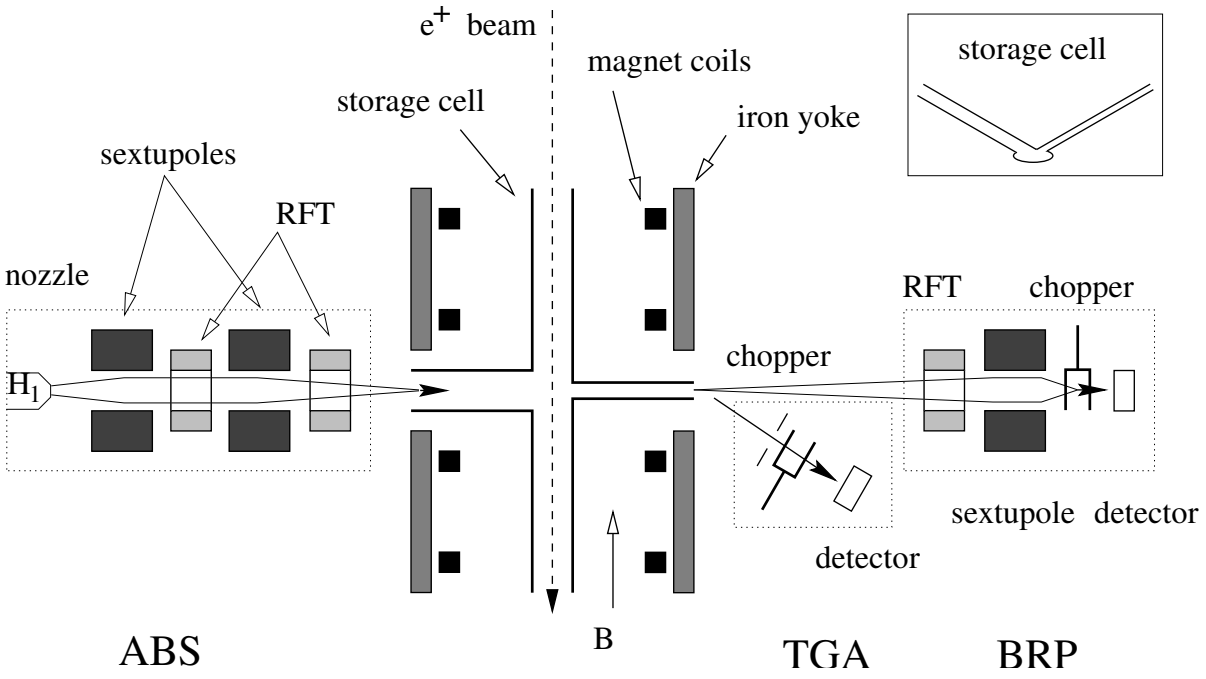

Figure 3.3: A schematic layout of the HERMES hydrogen target. From left to right: the atomic beam source (ABS), target chamber with cell and magnetic holding field, sample tube taking gas to the target gas analyzer (TGA) and the Breit-Rabi polarimeter (BRP). The inserted picture shows a cross sectional view of the storage cell perpendicular to the direction of motion of the lepton beam.

Atomic Beam Source (ABS) The ABS [66] provides polarized hydrogen (H) and deuterium (D) gas for the HERMES experiment. Its working principle is based on Stern-Gerlach separation of atomic hydrogen or deuterium. The molecules are split into atoms by a dissociator and the desired hyperfine states are populated with a system of radio frequency transmitters (RFT). By switching between the various RF units the relative occupation of the various atomic states can be changed. A degree of dissociation of 92.8 % for H (and 94.5 % for D) has been achieved with a nuclear polarization of 0.92 (0.97). The polarized atomic beam is brought to the storage cell via an injection tube.

Target cell The target cell [26] is built from 75 μm thick Aluminum, has a length of 40 cm and an elliptical cross section of 2.1×0.89 cm^2. The cell confines the atoms to the vicinity of the lepton beam in the radial direction while both ends are open. In this way the gas can be pumped away by means of a high-performing pumping system to ensure that the high vacuum of the HERA electron beam pipe is maintained at a level of 10^{-9} mbar. To increase the target density the cell is cooled to 100 K for hydrogen and 90 K for deuterium. With this setup, a polarized target density of $\sim 10^{14}$ nucleons/cm^2 has been achieved. This corresponds to a luminosity of $\sim 10^{32}$ cm^{-2} s^{-1}. Such a target thickness has only a minor influence on the lepton beam life time. Unpolarized targets with higher densities, which are used at the end of a fill, can reduce the life time to one hour. For a longitudinal target polarization a superconducting holding magnet with a field strength of 350 mT provides the quantization axis for the spin of the polarized nucleons.

Target Gas Analyzer and Breit Rabi Polarimeter A small amount of target gas is directed towards an analyzing system via a sampling tube. The target gas analyzer (TGA) [25] determines the relative atomic and molecular content of the gas. The TGA consists of a beam forming unit which directs the gas towards an ionizing volume. The particle flux is then measured by a quadrupole mass spectrometer which selects gas atoms or molecules depending on the magnet setting. The signal is read out with continuous dynode electron multipliers. A typical average value for the measured atomic fraction $\alpha^{TGA} = 96.8 \pm 0.9$ % has been found for the year 2000.

The target polarization is measured by the Breit-Rabi Polarimeter (BRP) [24]. It measures the relative population of the hyperfine states. Similar to the ABS, states are selected with RF transition units and sextuple magnets. The detection part of the BRP is similar to that of the TGA.

During the shutdown period in 2001, the longitudinally polarized target set-up has been replaced by a transversely polarized target. Since 2002 this system has provided the experiment with a transversely polarized hydrogen target.

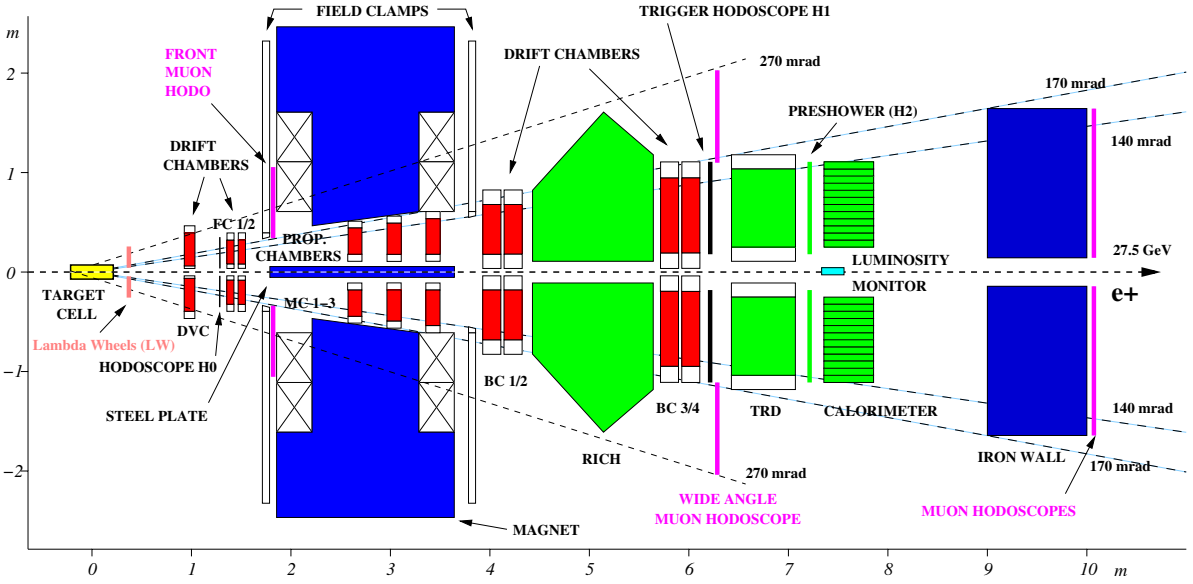

Figure 3.4: A schematic drawing of the HERMES experiment. The individual components are described in the text.

3.3 HERMES Spectrometer

The HERMES spectrometer is designed to detect semi-inclusive DIS events at forward angles. In Fig. 3.4 a schematic drawing of the HERMES experiment [2] is shown. The spectrometer consists of two identical halves, one above and one below the lepton beam pipe. The detectors in both halves are identical and can be treated as independent detectors. In doing this it is possible to suppress systematic uncertainties. Furthermore, the spectrometer is divided into a front and a back part by the dipole spectrometer magnet. The magnet has an integrated field strength of $\int B \cdot dl = 1.3$ Tm. Particle tracks are reconstructed in the front and back part separately, and are matched with the help of tracking stations located inside the magnet.

The HERMES coordinate system is right handed where the z-axis is chosen to be along the beam, the y-axis is pointing upwards and the x-axis is pointing to the left, towards the outside of the ring. The acceptance of the detector in the x-direction is limited to the angular range $|\theta_x| < 170$ mrad. Due to the gap between top and bottom part of the detector, the acceptance in the y-direction is limited to the angular range $40 < |\theta_y| < 140$ mrad. The resulting accessible kinematical range can be expressed in the DIS kinematic variables x and Q^2, which are defined in section 2.2.2, as $0.02 < x < 0.8$ and $0.2 < Q^2 < 20$ GeV^2.

In the following sections the different parts of the spectrometer (shown in Fig. 3.4) are discussed in more detail. The tracking devices are discussed in section 3.3.1. The first devices of this type are the Lambda Wheels (LW), a double sided silicon strip detector. In the front region behind the LW the Drift Vertex Chambers (DVC) and the Front Chambers (FC) are located. They are both multi-wire drift chambers. Inside the magnet three proportional chambers, the so-called Magnet Chambers (MC), connect the front and

back tracks. Two sets of Back Chambers (BC) each consisting of two modules, are located in the back part of the spectrometer. They are large drift chambers which are placed just before and behind the RICH. There are various particle identification detectors which are also shown in Fig. 3.4. These detectors are detailed in section 3.3.2, where also the hadron-lepton separation technique is discussed. The Hodoscopes are used for triggering and for the time-of-flight measurements. The threshold Čerenkov detector, which was replaced in 1998 by the Ring Imaging Čerenkov (RICH) detector, the Pre-shower and Calorimeter are used in combination to determine the particle type. In addition, the trigger and Data Acquisition (DAQ) system are discussed in section 3.3.3.

3.3.1 Tracking detectors

The tracking system can be split in three regions: the parts in the front of the magnet, inside and behind the spectrometer magnet. The aim is to determine the scattering angles (θ and ϕ) and a position of the tracks. The position can be given either as the interaction vertex (as done for the front tracks) or as a position in a plane in the middle of the magnet (as done for the back tracks). The angular resolution of the tracking system is better then 0.6 mrad, and the momentum, which is determined by the bending of the tracks in the magnet has a resolution dp/p of $1 - 3$ %.

The Lambda Wheels (LW) As this system is discussed in greater detail in chapter 4, here only a brief overview of the LW system is given for completeness. The LW system is a silicon strip detector, which is located in the pump cross behind the target in the lepton beam vacuum. It consists of two layers of double sided silicon wafers, which are 5 cm apart. Each layer consists of twelve trapezoidal shaped modules arranged in a circular fashion around the beam pipe. Each silicon wafer is 300 μm thick and has 499 channels on each side. The strips on the front and back have a stereo angle of 30°. Combining strips from both sides allows to reconstruct a point in the plane of the wafer. The front-end electronics is mounted inside the beam vacuum at the top end of the silicon modules. The front-end electronics uses the HELIX chip to read out the analog signals from the strips.

Drift Vertex Chambers (DVC) At 1.1 m behind the target center the Drift Vertex Chambers (see [65]) are located. The DVCs were added to the initial design to improve the spatial resolution and increase the redundancy of the front tracking. They consist of 2×3 layers with wires along the y-direction, which are tilted by $+30$ and $-30°$, respectively. The second layer of wires, for the same direction, is staggered by half a cell width to be able to resolve left-right ambiguities. All tracking drift chambers of the HERMES spectrometer have this double layer feature. The DVCs have an increased vertical acceptance ($\times 2$) compared to the standard HERMES acceptance. The spatial resolution is about 250 μm and it has a good efficiency for track reconstruction.

The Front tracking Chambers (FC) The main tracking detectors in the front region are the FCs [35]. They are located at 1.52 m and 1.66 m downstream of the target center and consist of two times six planes. The FCs are of a standard horizontal drift chamber design with alternating anode and cathode wires. The pitch between the wires is 7 mm and the distance between the cathode foils is 8 mm. They have an efficiency of 97–99 % and a resolution ranging from 150–230 μm depending on the distance between the track and one of the wires.

Magnet Chambers (MC) Inside the magnet three multi-wire proportional chambers (MWPC) are installed. Each chamber contains a series of anode and cathode wire planes with the wires running along -30, 0 and $+30$ degrees with respect to the y-axis. A spatial resolution of $\sim$ 600 μm has been reported for the MCs in Ref. [16]. The chambers are used to bridge the gap between tracks derived from the front and back chambers. In addition, the MCs can be used to reconstruct low momentum tracks which do not extend through the whole spectrometer. These tracks, which are known as *short-tracks*, do not enter the RICH and hence have no PID information. For these tracks the reconstruction program provides a coarse momentum determination based on curvature of the tracks.

Back Chambers (BC) The tracking in the region behind the magnet is performed by the Back Chambers [30]. They are made of two pairs of large drift chambers with six planes each. The chambers are located at 4.05/4.25 m, respectively 5.80/6.00 m, downstream of the target. Each drift cell has a surface area of 15×16 mm^2. The single plane efficiency is $\sim$ 99 % and the resolution determined from the residual width is $\sim$ 250 μm for the first and $\sim$ 275 μm for the second larger, pair of wire chambers. To stabilize the gain of these chambers the pressure inside the gas volume is monitored and controlled.

3.3.2 Particle Identification Detectors

Particle identification at HERMES is performed with the help of four different components of the spectrometer. These are the hodoscopes, the threshold Čerenkov detector, the TRD and the calorimeter. The following paragraphs describe some aspects of each of these detectors. Besides the first hodoscope they are all located in the back region of the spectrometer. The hodoscopes were initially only used for triggering purposes but can also be used for Time-Of-Flight (TOF) measurements. While the main focus of the PID detectors is the discrimination between hadrons and leptons, the installation of the RICH (in 1998 to replace the Čerenkov detector) also enables differentiating between pions, protons and kaons. The response of all PID detectors is combined in a log-likelihood method to separate hadrons from leptons. This method is described in the last paragraph of his section.

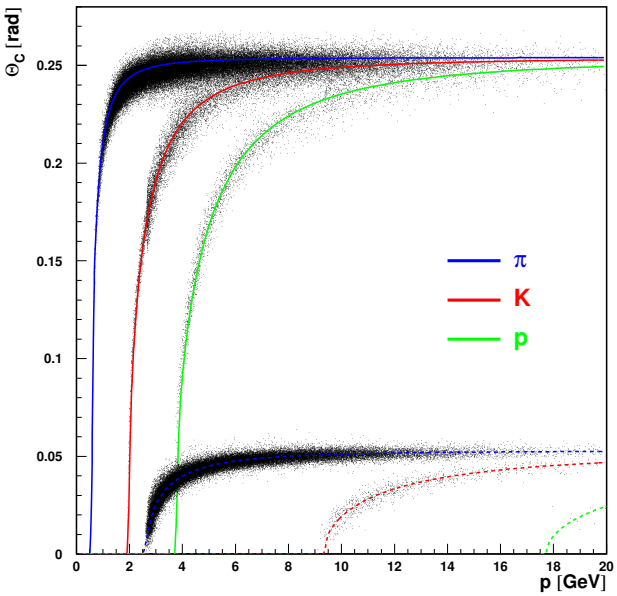

Figure 3.5: Čerenkov angles versus momentum for different particles passing through the two different media in the RICH. The upper distributions correspond to the aerogel and the lower to the C_4F_{10} gas. Also shown are curves representing the anticipated behavior of the čerenkov angles.

Čerenkov detector Initially, a threshold Čerenkov detector was used in HERMES to discriminate between hadrons and leptons (see Ref. [70]). It was operational from 1995 to 1997 and was replaced in 1998 by a RICH. Both components utilize the principle of Čerenkov radiation.

Particles traversing a medium with refractive index n emit Čerenkov radiation if their velocity v_p is greater than the velocity $v_m = c/n$ of light in the medium. The opening angle of the wave front of the Čerenkov radiation can be calculated as,

$$\cos\Theta = \frac{v_m}{v_p} = \frac{c}{nv_p} = \frac{1}{n\beta}, \tag{3.2}$$

with $\beta = v_p/c$ the relative velocity (with respect to the velocity of light c) of the particle. Čerenkov radiation is emitted when $v_p > v_m$, which corresponds to a threshold momentum $p > \gamma mc/n$. As the threshold momentum depends on the mass of the particle, different particles can be separated by observing whether or not they emit Čerenkov radiation in the medium.

The double radiator Ring-Imaging Čerenkov **(RICH)** [12] also uses the angular information of the emitted photons. It provides particle identification over a wider range in momentum (2–15 GeV). In addition to the large gas radiator (C_4F_{10}) a silica aerogel with a thickness of 5 cm is used. Two times four mirrors reflect the photons on to a matrix of 1934 photo multiplier tubes (PMT) which yield an angular resolution of about 7 mrad. The photomultiplier signals only provide a pulse if there was a hit above threshold, but do not provide pulse-height information. Two different methods exist to analyze the response of the RICH. The first method is called the *Inverse Ray Tracing* (IRT), in which all possible Čerenkov angles and all possible particle hypotheses are calculated for each track. This algorithm therefore needs high computational resources during the reconstruction of an event. The second method is the *Direct Ray Tracing* (DRT) method. In this method, additional information from the tracking is used. Taking the emission point

from the momentum reconstruction a most probable particle hypothesis is calculated. For this procedure a Monte Carlo based simulation of the RICH is needed as input.

RICH PID Both methods, IRT and DRT, determine a probability matrix for each track to be one of the possible hadrons types. The two highest probabilities are combined into a quality factor. Based on conditions that were developed independently (see Ref. [12]) one of the methods is chosen to identify the track.

The PID scheme for the RICH is based on an algorithm which calculates a likelihood for a given particle hypothesis (see Ref. [55]). The aim is to differentiate between pions, kaons and protons, while lepton-hadron separation is realized by the other PID detectors. The likelihood algorithm takes the momentum and the average Čerenkov angle into account. Additionally, the threshold behavior is accounted for. A probability value $P(\langle\theta\rangle, t)$ for a particle to be of type t, when an average angle $\langle\theta\rangle$ is measured, can be calculated knowing the conditional probability $P(t, \langle\theta\rangle)$ that if a particle is of type t, it is observed under an angle $\langle\theta\rangle$, like

$$P(\langle\theta\rangle, t) = \frac{P(t, \langle\theta\rangle) \cdot \phi_t}{\sum_j P(j, \langle\theta\rangle) \cdot \phi_j}, \tag{3.3}$$

with the flux factor ϕ_j. For this conditional probability a likelihood distribution taken

$$P(t, \langle\theta\rangle) \sim L(\langle\theta\rangle) = \exp \frac{-(\theta^{th} - \langle\theta\rangle)^2}{2\sigma^2_{\langle\theta\rangle}}. \tag{3.4}$$

with the resolution of the average angle $\sigma_{\langle\theta\rangle}$ and the angle θ^{th} from a fit to distribution based on theoretical calculations.

The most probable particle type is obtained from these likelihoods and specified as an integer value. In addition, a quality parameter is given as $QP = \log_{10}(L_1/L_2)$ with the likelihoods of the two most probable particles. If the two highest probability values ($L_1 = L_2$) are equal the particle is labeled as 'not identified'.

Transition Radiation Detector (TRD) The Transition Radiation Detector is used for lepton/hadron separation. The detector comprises 6 modules each consisting of 6.35 cm of poly-propylene/ethylene fiber radiators and a 2.54 cm thick MWPC. The transition radiation is produced by charged particles traversing the boundary of the di-electric radiators. It is detected in a heavy gas mixture of Xenon (90 %) and CH_4 in the MWPC. As the yield of the transition radiation photons, which is in the keV range, is proportional to the Lorenz factor γ of the particle, the energy deposit of leptons is on average two times larger than that of hadrons. The signals from all modules but the one with the highest signal are combined. With this so-called truncated mean method it is possible to suppress the large tail of the energy spectrum produced by hadrons.

Hodoscope There are three hodoscopes installed in the HERMES experiment. The first one, the so-called H0 hodoscope is located in front of the spectrometer magnet, and

has been installed in 1996. The H0 hodoscope is built of 3.2 mm thick plastic scintillator material. The second and third hodoscopes (H1 and H2) are installed in the back part of the spectrometer before and after the TRD. They consist of 1.0 cm thick, 9.3 cm wide and 91.0 cm long paddles. These paddles have been installed vertically and are staggered with an overlap of 2–3 mm. When matched with the back hodoscopes the trigger signal of H0 can also be used as a veto trigger for backward going particles originating from the proton beam. The second hodoscope is also used as a pre-shower detector in combination with the calorimeter. For this reason a 1.1 cm thick lead wall is installed in front of H2 which initiates electro-magnetic showers for leptons. Hadrons, in contrast to leptons induce only a minimum ionizing signal.

Initially, the hodoscopes were only used for the trigger but it was soon realized that they can also be used for particle identification. The time information of the detector can be used when synchronized to the beam bunches as a Time-of-Flight (TOF) PID detector for particles of less then 3 GeV (see Ref. [57, 11]). The detector is calibrated using leptons under the assumption that they travel with the speed of light. By measuring the deviation of the particle velocity compared to c, their mass can be extracted using

$$m^2 \cdot c^2 = p^2(1/\beta^2 - 1), \tag{3.5}$$

with $\beta = v/c$. Applying this technique it is possible to extend the hadron identification towards lower momenta.

The calorimeter The Calorimeter [20] is made of two arrays of lead glass blocks: one above and one below the beam pipe. It is mounted on a movable support to ensure that the radiation sensitive detectors can be moved away from the beam during injections. Once the beam has reached stable conditions, it is moved in again. One calorimeter array (see Fig. 3.6) consists of 42×10 blocks of lead-glass. The front face of each calorimeter block is 9×9 cm^2, and each block has a length of 50 cm which corresponds to ~ 18 radiation lengths for leptons at 27.6 GeV.

The electromagnetic calorimeter is one of the four detectors of the HERMES PID system and measures the particle energy. It provides a first-level trigger for scattered positrons, based on the energy deposition in a localized spatial region. This energy measurement is less precise than that derived from the curvature of the charged tracks in the magnetic field. However, it is the only available measurement for neutral particles like photons coming for example from radiative processes or from π^0 or η decays.

The calorimeter has a rejection factor for pions of more than 10 at the first-level trigger, and an additional factor of more than 100 in the offline analysis. Moreover, the calorimeter array gives a coarse position measurement of scattered electrons and photons.

The performance of the calorimeter can be summarized as follows. The response to positrons and electrons of all counters is uniform within 1 % over the energy range $1 - 30$ GeV. The energy resolution for the calorimeter (see [20]) is:

$$\frac{\sigma(E)}{E}[\%] = \frac{(5.1 \pm 1.1)}{\sqrt{E}(GeV)} + (2.0 \pm 0.5) + \frac{10.0 \pm 2.0}{E(GeV)}. \tag{3.6}$$

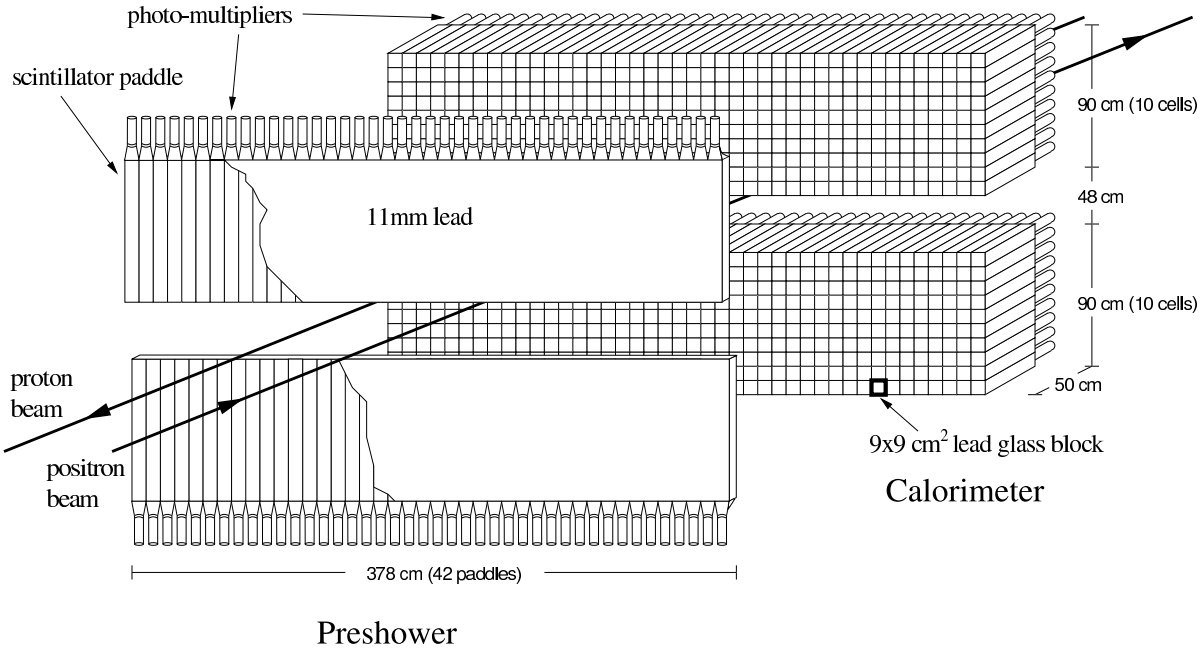

Figure 3.6: A schematic drawing of the electromagnetic calorimeter of the HERMES experiment. Some size measures are indicated.

The calorimeter has a position reconstruction resolution of about 0.7 cm. There is no observed degradation of performance due to radiation damage, within the accuracy of the measurements. Over the operational period of HERMES the measured masses of the π^0 and η particles, which can be reconstructed from two photons detected in the calorimeter, are in agreement with the PDG [67] values (see also 6.4.1).

Hadron / Lepton separation

A probabilistic algorithm is used at HERMES to convert the detector response to a logarithmic likelihood ratio [86, 56]. By combining all four PID detectors, which have distinct responses to the various particle types, the efficiency for identifying a lepton track is optimized. The tuning of a single detector is done on the basis of data. While one detector is being investigated, the other detectors are used to determine the particle ID using very strict requirements. This procedure assumes that the responses of the different detectors are uncorrelated. This method has the advantage that it accounts for the present status of the detectors.

The probability $P(A_i|X)$ that a measured detector response X was caused by particle A_i can be written according to Bayes' Theorem as:

$$P(X|A_i) = \frac{P(A_i|X) \cdot \Phi(A_i)}{\sum_j P(A_j) \cdot \Phi(A_j)}, \tag{3.7}$$

with $\Phi(A_i)$ the particle flux. To use the detector responses in a probability analysis they

have to be converted in conditional probabilities $\mathcal{L}^i$. The probability is then given by

$$\mathcal{P}^i = \frac{\phi^i \cdot \mathcal{L}^i}{\sum_j \phi^j \cdot \mathcal{L}^j}. \tag{3.8}$$

For the case of only two particles, the lepton probability is given as

$$\mathcal{P}^l = \frac{\mathcal{L}^l}{\Phi\mathcal{L}^h + \mathcal{L}^l} \quad \text{and} \quad \mathcal{P}^h = \frac{\mathcal{L}^h}{\Phi\mathcal{L}^l + \mathcal{L}^h}, \tag{3.9}$$

where in this case $\Phi = \phi^h/\phi^l$ is the ratio of the hadron and lepton fluxes. The PID parameter is calculated by taking the logarithm of the ratio

$$PID \equiv \log_{10}\left(\frac{\mathcal{P}^l}{\mathcal{P}^h}\right) = log_{10}\left(\frac{\mathcal{L}^l}{\Phi\mathcal{L}^h}\right) = log_{10}\left(\frac{\mathcal{L}^l}{\mathcal{L}^h}\right) - log_{10}\Phi. \tag{3.10}$$

There are three PID quantities defined which are evaluated in the analysis. By combining the calorimeter and the pre-shower, the first PID measure is obtained, known as $PID2$

$$PID2 \equiv PID_{cal} + PID_{pre}. \tag{3.11}$$

By combining PID2 with the Čerenkov response, $PID3$ is defined,

$$PID3 \equiv PID_{cal} + PID_{pre} + PID_{cer}. \tag{3.12}$$

If also the TRD output is used the definition of $PID5$ is obtained

$$PID5 \equiv PID_{trd} = \sum_{i=1,6} PID_{trd,i} \tag{3.13}$$

where the summation is over the individual TRD modules.

In practice $PID3$ and $PID5$ are added to a single value, on which a requirement is imposed to separate hadrons and leptons. For data collected since the year 1998 the $PID3$ value is obtained by using the RICH as a threshold counter similar to the Čerenkov. Using the criterion $(PID3 + PID5) > 2$, the efficiency for leptons is above 97 % with a hadron contamination below 0.01 %. For hadrons the value $(PID3 + PID5) < 0$ is chosen, yielding a hadron efficiency of 99 % with a contamination below 1 %.

3.3.3 Trigger and Data Acquisition

The main physics trigger (T21) at HERMES is constructed from the output of four detector components. These are the three hodoscopes H0, H1, H2 and the calorimeter. Additional triggers include, for example, the magnet chambers or the Muon hodoscopes. As the whole spectrometer is divided in an upper and a lower half, separate triggers exist for each half. For a T21 trigger either the top or bottom hodoscopes must have given a signal. Furthermore, the calorimeter response for two adjacent columns should be above

a certain adjustable threshold. For DIS physics and quasi-real photo-production this threshold is normally set to 1.4 GeV, while for unpolarized target running the threshold has to be increased to 3.5 GeV. The generation of a trigger signal takes only 465 ns. Upon a trigger the digitization and readout of the detector is initialized. During this time no further trigger is accepted and a dead-time is introduced. This dead-time normally adds up to only a few percent. For unpolarized high-density running it can become considerably higher. If the dead time is larger than 10 % one or more triggers have to be rescaled to prevent large dead-time corrections. The typical data taking rate for polarized running is on the order of 50 Hz and can go up to 500 Hz for unpolarized running. In addition, so-called slow-control data are read out every 10 s. This time interval of 10 s is called a *burst*. These slow-controlled data include scaler and status information from the triggers and all detector components. The next division in which the HERMES data is split up is in runs. A run has a data volume of about 450 MB. The data are also separated according to the fills of the lepton accelerator they belong to and finally in the different years of data taking.

The Data AcQuisition (DAQ) at HERMES is realized with a backbone of FASTBUS crates for the digitization of the detector signals. CERN Host Interfaces (CHI) are used to read and check the equipment and build the event. The data are written to disks and stored on tape in EPIO [37] format.

Part of the data is analyzed online to provide checks of single detector components and obtain information on the overall data taking status. Offline, the raw data are treated similarly. First the EPIO files are decoded by the HERMES DeCoder (HDC) and stored in ADAMO [38] database files. Subsequently, the HERMES ReConstruction (HRC) program evaluates the partial tracks in the front and back region, and joins the partial tracks in the center of the magnet. The momentum for each track is then determined from the curvature of the total track and the efficiencies of the tracking devices are evaluated. The PID values are calculated and eventually all relevant information is collected in so-called Micro Data Summary Tables (μDST's). The offline data analysis (tracking and PID) is repeated once or twice to account for improved knowledge of the various calibration constants and alignment information of the detectors.

3.4 Luminosity monitor

An important observable that is needed to be able to compare different data sets is the accumulated luminosity. The luminosity of the experiment is measured by the so-called luminosity monitor (see Ref. [29, 28, 45]). This equipment consists of two calorimeter arrays left and right of the beam pipe. Each array comprises 12 radiation hard $NaBi(WO_2)_4$ crystals. The luminosity monitor is located at the same z-position as the calorimeter and is also movable.

This device measures the coincidence rate R of two particles. In the case of a positron beam, Bhabha scattering is used while for an electron beam elastic Møller scattering is used. In both cases the reference cross section σ_{ref} is calculable, which makes it possible

to evaluate the actual value of the luminosity $\mathcal{L}$ via

$$\mathcal{L} = R/\sigma_{ref}. \tag{3.14}$$

The acceptance as well as the efficiency of the device has to be taken into account. In practice the rate R of the luminosity monitor is determined per burst. The coincidence rate is fitted to the data and multiplied with a trigger dead-time correction and the actual burst length δ_{burst}. To convert this rate into a real luminosity it then has to be scaled with a calibration constant C_{year},

$$\mathcal{L} = C_{year} \cdot R \cdot \delta_{burst} \tag{3.15}$$

where the calibration constant accounts for all detector effects during a specific year of data taking.

The calibration constants have been evaluated in Ref. [44] for various HERMES running periods and are shown in table 3.1.

	1998	1999	2000
$C_{year}[mb^{-1}]$	250 ± 18	417 ± 30	417 ± 30
DIS [million]	1.116	1.256	7.035
Luminosity $[pb^{-1}]$	24.8	29.2	155.2

Table 3.1: Luminosity Constants as taken from Ref. [44]. The accumulated number of DIS events and the actual integrated luminosities are taken from the DQ web pages [48].

Chapter 4

The Lambda Wheels Project

This chapter describes the Lambda Wheels (LW) project. It is a silicon detector system for the HERMES front region. The project is a combined effort of four Institutes: Universität Erlangen-Nürnberg, PNPI St. Petersburg, Vrije Universiteit Amsterdam and NIKHEF Amsterdam. It has been proposed in the year 1997, together with a second silicon array called the Recoil Detector (RD). The LW are supposed to cover the front region, while the RD should be placed parallel to the target (see Ref. [82]). The system is described in full detail in the technical design report which is also available as an HERMES internal note (see Ref.[81]).

As a first step a small silicon test detector, the so-called Silicon Test Counter (STC) (see [84, 85]), was installed inside the beam vacuum below the target in the HERMES front region. Following the successful operation of the STC it was decided to build the Lambda Wheels. A prototype module was installed in the year 1999 and was operated successfully until the HERA shutdown in summer 2000 (see Ref.[49]).

The aim of the present work is to complete the project based on the achievements of the prototype [80]. The full LW *detector* consists of twelve single *modules*. First data have been collected with the complete detector in the year 2003. These data were used to finalize the software, to properly align the LW with respect to the HERMES experiment and to determine the resolution of the device.

The chapter is organized as follows: In section 4.1 the physics motivation of the detector project is summarized. Then a general introduction to semiconductor detectors is given in section 4.2. The detector and the additional hardware is described in section 4.3. The last section, section 4.4, discusses the analysis of the data which were collected during the commissioning of the detector. At the end of the chapter a summary and an outlook is given.

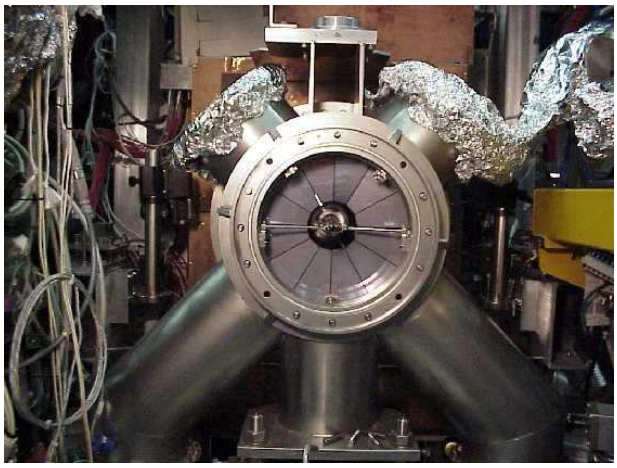

Figure 4.1: Photograph of the LW as they were installed in the vacuum system in between the target and the detector (known as the pumping cross) in the year 2002. The picture is taken looking along the direction of the beam. The first layer of the 12 silicon wafers is visible.

4.1 Physics motivation

The main goal of the Lambda Wheels is the increase of the geometrical acceptance in the front region. The gain in acceptance increases the yield of reconstructed particles (mainly pions) produced at large angles. These pions play a key role in the reconstruction of decaying particles like the Λ^0 hyperon. In addition, many heavier hyperons have decay channels including a Λ^0 hyperon and a pion like Σ, Σ^* and Ξ particles. Similarly, charmed baryons like the Λ_c decay into a Λ^0 hyperon and a pion and can therefore also benefit from the LW installation. From this main objective of increasing the Λ^0 yield for various reaction channels the name of the project was derived: the Lambda Wheels (LW) project.

Several physics cases profit from the existence of the Lambda Wheels. As mentioned before the increase in acceptance yields a higher number of reconstructed Λ^0 hyperons. The larger sample of reconstructed Λ^0 hyperons results in a better precision of the longitudinal and transverse Λ^0 polarization measurements. A detailed discussion of the importance of Λ^0 polarization measurements is given in section 2.1. One of the key issues is the measurement of the spin transfer from a u-quark in the target nucleon to a Λ^0 hyperon, which gives information on the spin structure of the Λ^0 hyperon. This illustrates how the LW will shed light on the spin structure of other hadrons than the proton.

The LW also increase the kinematic acceptance for the reconstruction of Λ^0 hyperons in the negative x-Feynman region which is the so-called target fragmentation region. As Ellis has shown in Ref. [53], from such a measurement of the Λ^0 polarization in this domain, one can derive the probability that the struck u-quark is parallel or anti-parallel to the s-quark. Therefore, information on the polarization of the strange sea can be obtained.

Due to the increased number of reconstructed particles the charmed baryons and mesons profit from the LW twofold. On the one hand, more of them are reconstructed, and on the other hand the background for such processes can be determined with a higher precision. At HERMES the photo-production of the Λ_c baryon and other charmed particles like the D^* and the J/Ψ meson, can be studied in the threshold regime where widely differing cross section predictions exist. As it is believed that the Λ_c is preferably produced in photon-gluon-fusion, it is possible to derive a value for the gluon polarization $\Delta G/G$

from polarized Λ_c production data as was demonstrated in Ref. [49].

4.2 Semiconductor general

Semiconductor (SC) detectors are commonly used for particle detection in High-Energy-Physics (HEP) experiments Ref. [59, 46]. They are produced from crystalline silicon (Si) or germanium (Ge). The working principle is the liberation of charge by particles traversing the sensitive area of the detector. SC detectors have several advantages. The energy needed to create an electron-hole pair is low. Therefore, a good energy resolution can be achieved. The high density of solid state detectors allows to produce small and compact devices. The fast response time makes these detectors usable in high luminosity experiments and, furthermore, SC have a high efficiency and can be used in vacuum. These advantages are the main reasons why they were chosen for the LW.

The most fundamental property of SC is the energy band structure of the electrons in the solid state lattice. For SCs three different regions can be distinguished (see also right side of Fig.4.2). At low energies there is the so-called *valence*-band. It is separated by an *energy gap* E_g from the *conduction*-band. At zero temperature all states of the valence-band are filled and the conduction band is empty. As there are no free charge carriers the system is an insulator. At finite temperatures some electrons can be excited to the conduction-band. The intrinsic charge concentration in a SC due to thermal energy in equilibrium can be calculated as

$$n_i = C \cdot T^{3/2} \cdot \exp \frac{-E_g}{2k_B T} \quad , \tag{4.1}$$

where E_g is the energy gap, k_B the Boltzmann-constant and T the temperature. A typical value for the charge concentration in intrinsic silicon at 300 K is $1.5 \cdot 10^{10}\text{cm}^{-3}$. In a SC the energy gap is much larger than the thermal energy of the electrons $E_g \gg k_b T$. Typical values of E_g are in the order of 1 eV. The size of the energy gap is determined by the structure of the lattice, and depends on the temperature and pressure of the crystal.

The thermally excited electrons and holes are mobile and can carry a current. The drift velocity of the charge carriers can be expressed as

$$v_{\text{drift}} = \mu \cdot E \tag{4.2}$$

where the mobility μ depends on the temperature and the applied external electric field E. For lower values of the electric field the mobility does only depend on the temperature. The mobility decreases with increasing temperature as the mean free path of the electron reduces due to collisions with atoms. For higher values of the electric field the mobility decreases with $1/\sqrt{E}$. For electric fields above 10^4 V/cm the mobility saturates like $\sim 1/E$ and the drift velocity approaches a constant value.

Once created electron-hole pairs can recombine in the crystal. In an ideal crystal of a SC the only possibility for this process is the so-called direct recombination. With only

direct recombination processes the lifetime of electron-hole pairs would be in the order of seconds. Unavoidable impurities in the crystal provide so-called *recombination centers* which can catch electrons which then recombine with a hole. Another cause for charge loss in a SC is the *trapping* of one charge in intermediate energy levels. From these traps the charge carriers are released after a certain time.

In contrast to these detrimental effects some materials can enhance the characteristic of the SC. They contain shallow energy levels very close to the conduction and valence band which can be easier exited and do not trap the charge (see also Fig. 4.2). As silicon is tetravalent it can be *doped* with penta- or trivalent atoms which will integrate in the lattice. These other atoms will leave one charge in those energy levels close to the bands. If silicon is, for example, doped with a pentavalent atom (arsenic, phosphorus or antimony) one additional electron is present in the crystal which is not bound and can be exited into the conduction band. Furthermore, it can fill up a hole which causes holes to become a minority charge carrier in such doped crystals. This kind of SC is then called *n-type* and has electrons as majority charge carriers and holes as minority charge carriers.

Doping with trivalent atoms (like gallium, boron or indium) works similarly. In this case, holes become majority charge carriers and the SC is of *p-type*. Typically, SCs with a density of 10^{22} atoms/cm^3 are doped with a density of about 10^{13} atoms/cm^3. For metal contacts heavily doped SCs are used that can have doping densities up to 10^{20} atoms/cm^3 and are then called either n+ or p+ type. Note that the crystal is still electrically neutral.

The most basic doping scheme is that a crystal is doped on one side with donors (n-type) and on the other with acceptors (p-type) like a diode. Because of the different charge concentrations a diffusion of the electrons to the p-side and of the holes to the n-side will happen. These charges will then recombine and an immobile space charge is built up. The effect of the charge distribution establishes an electric field which will stop the diffusion of charge carriers and is called the *contact potential*. Because of this the energy band structure will deform at the so-called *junction* of the pn-SC. The region in which the free charge carriers have recombined is called the *depletion zone*, see Fig. 4.2. If there are electron-hole pairs created they will be separated and swept out of the region by the electric field. The depth of the depletion zone depends among other things on the resistance (ρ) and the contact potential (V_0) of the SC. If the two sides are not equally doped the depletion zone will extend further into the lighter doped region. This electrical configuration and the depletion zone exhibit a capacitance which most generally depends on the depth of the depletion and the area of the junction zone. The intrinsic field is not strong enough for a good and fast charge collection. Furthermore, the depletion depth is small (only a couple of μm) which leads to a big capacitance where charge could be produced. Therefore, applying a *reverse bias* voltage with the negative to the p-side (will attract holes) and the positive to the n-side (will attract electrons) will increase the depletion zone and the sensitive area becomes larger. The voltage will also increase the charge collection efficiency due to the higher mobility of the charges.

There are two points that deteriorate the performance of a silicon detector. These are the leakage current and radiation damage. The *leakage current* is an important characteristic of SC detectors. This is a current which arises when a voltage is applied across the

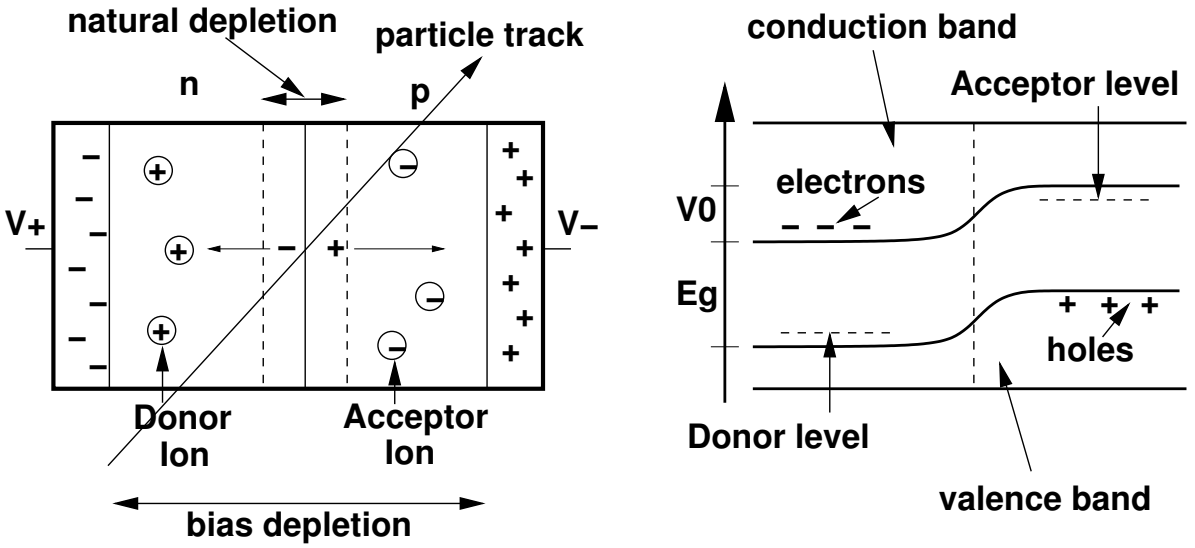

Figure 4.2: Schematic drawing of a SC. On the left side the configuration of the charges in a np-SC is depicted. On the right side the energy levels of an SC are given.

SC. One component is due to the movement of minority carriers and thermal production of electron-hole pairs at defects of the crystal. The highest contribution to the leakage current occurs in surface channels. If the leakage current becomes too high a so-called *break-through* occurs and the detector is not operable anymore. During normal operation the leakage current causes noise in the electronic system. First, because the input of the preamplifier is disturbed by the apparent current on its input and second, the leakage current enhances the fluctuations of the noise. Another important characteristic of SC detectors is that their performance changes due to radiation damage. This can be understood as the crystalline structure gets damaged due to the radiation. It creates trapping centers for charges which disturb the signal. Consequently, the detector performance gets worse over time.

Semiconductors have some characteristics which make them especially suitable as tracking detectors. The average energy needed to produce an electron-hole pair is low. For example, 3.62 eV is needed in a silicon detector at room temperature (300 K) to create such a pair. This energy does not depend on the particle type or energy. Compared to gas chambers the energy needed for the creation of a pair is one order of magnitude smaller. However, if the particles are not completely absorbed in the depletion zone the measured energy loss ΔE is a non-linear function of the energy of the particle.

The intrinsic detection efficiency of SC detectors is close to 100 %. It is only limited by the noise which can be larger than the produced charge. Semiconductor detectors are fast. The rise-time of the signal induced due to the movement of the charge is of the order of several nanoseconds. Different from gas detectors there is no secondary charge amplification in SC. Therefore, the signal is low and has to be amplified. This amplification is important and requires low noise electronics and a preamplifier. As the capacitance of the detector is temperature dependent one normally chooses charge sensitive amplifiers which have a much larger capacitance than the detector. But it also

has to be kept as low as possible to avoid noise from the preamplifier. The coupling of the signal from the detector to the preamplifier is done via a capacitor to avoid grounding problems. This coupling is referred to as *ac-coupling*.

4.3 The Lambda Wheels

This section gives an overview of the hardware of the complete LW project. This includes the mechanical system which is described in the following section. The details about the chosen silicon sensors are presented in Sec. 4.3.2. The electronics control and read-out are described in Sec. 4.3.3. Details about the power consumption are given in Sec. 4.3.4 and finally the cooling of the detector is described in the last section. Further descriptions of the design of the LW can be found in Ref [76, 77].

4.3.1 LW Mechanical System

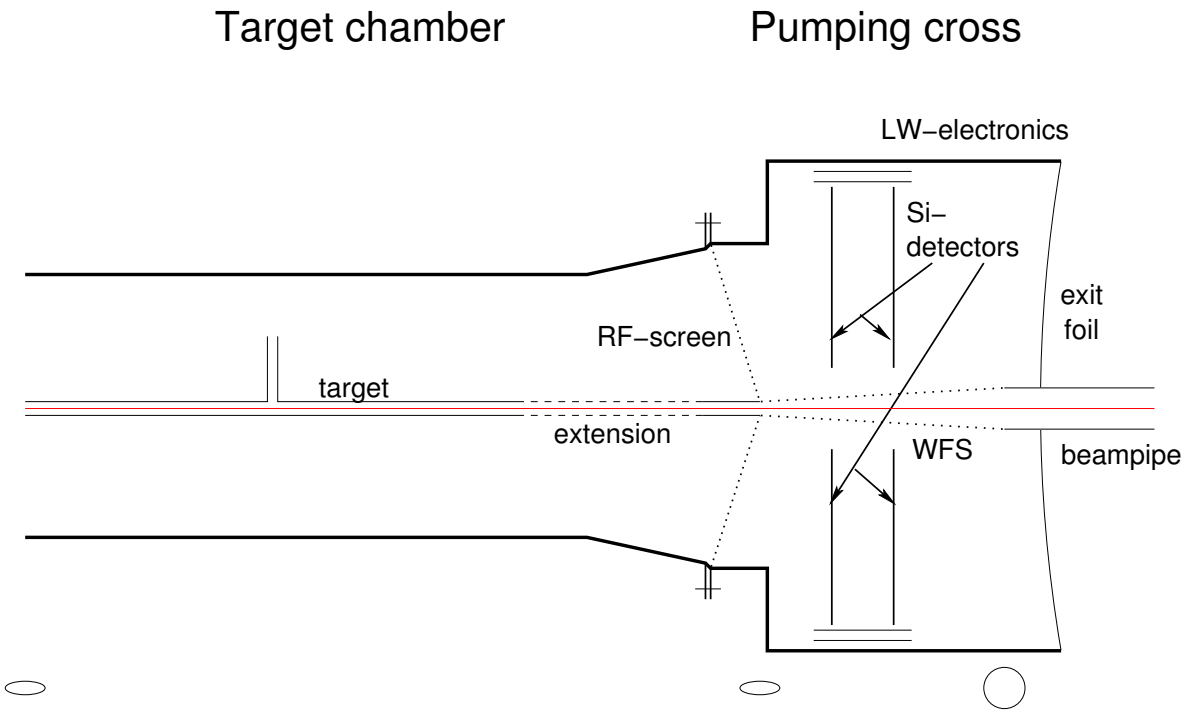

Figure 4.3: Schematic diagram of the HERMES front region with the equipment close to the LW detector (from [78]).

The center of the detector is located at $z = 47.5$ cm downstream of the center of the target. The detector is positioned in a large diameter vacuum vessel, the so-called pumping cross, on which the target chamber is mounted. A sketch of the set-up is shown in Fig. 4.3. The vacuum vessel is closed on the back side towards the spectrometer by a 300 μm thick stainless steel foil. The requirements on the hardware for the detector are very stringent

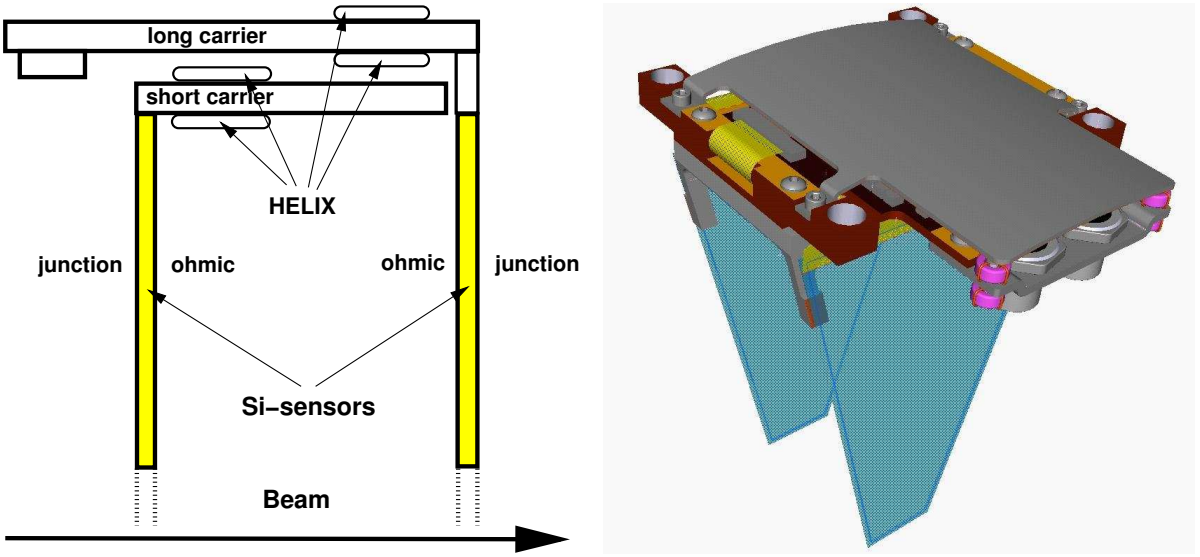

Figure 4.4: On the left a schematic side view of a LW module is shown. Indicated are the locations of the HELIX chips and the sensors. On the right a 3d CAD drawing of the LW module is displayed (from [49]).

as the detector is located inside the ultra-high vacuum ($< 10^{-7}$ mbar) of the beam. This implies that the detector material must have low out-gassing properties.

As the lepton beam is passing nearby the electronics of the system has to be protected against radio frequency (RF) interference. The RF of the beam disturbs not only the front-end electronics but deteriorates also the signals from the sensors by inducing noise on the aluminum readout strips. To suppress these effects the wake field suppressor (WFS) is covered by a fine mesh. In addition, a light-weight mesh has been installed covering the whole front face of the pumping cross.

The detector frame consists of two stainless steel rings. This frame can be rotated, around the line of the beam, inside the pumping cross moving on small plastic wheels. In this way each of the modules can be accessed through one flange on the pumping cross. The frame also holds the pipes for the cooling liquid and, additionally, the cabling for the control and readout of the electronics. For the purpose of a consistent alignment after moving the frame, dowel pins are used to fix the position.

Each of the 12 modules consists of front-end electronics and two silicon *sensors*. A schematic view of a module is given in Fig. 4.4. The first sensor (so-called *short*) is positioned at $z = 45$ cm and has its junction side facing the beam. The second (*long*) is positioned at $z = 50$ cm and is rotated vertically by 180° so that the ohmic side is on the front facing the beam. The modules are fixed on the LW frame with the connectors and the dowel pins.

The electronics and the sensors are held together by a rigid metal structure. The sensors are glued on aluminum braces. The carrier boards are mounted on a copper structure for better heat conductance. The electronic connection between the sensor and the read-out

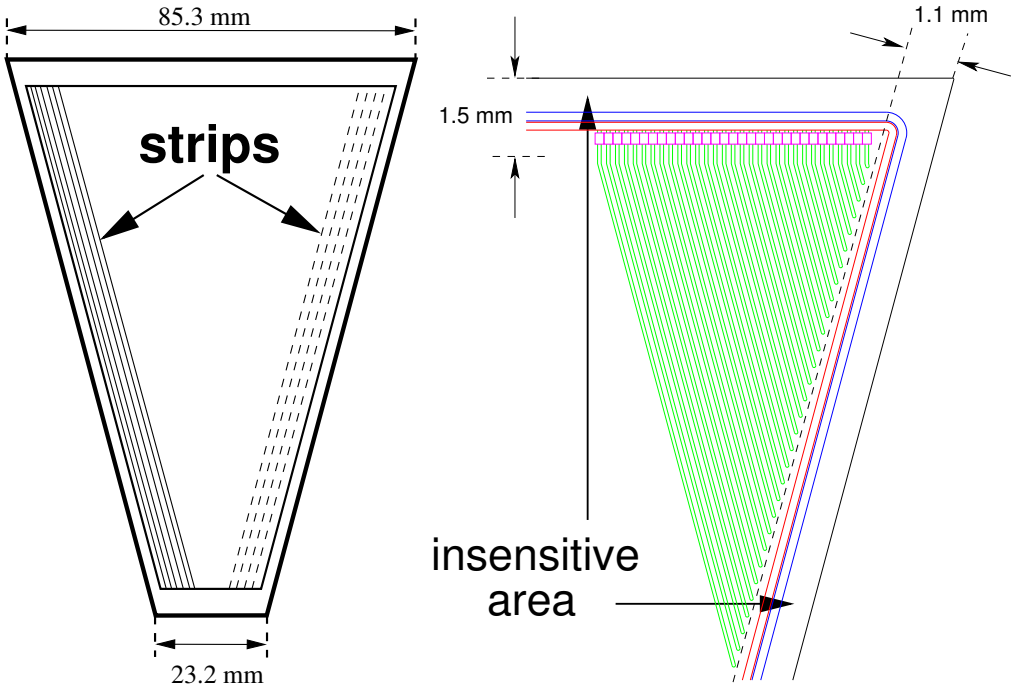

Figure 4.5: On the left, a schematic view of the trapezoidal shaped silicon sensor is given. Indicated are the directions of the strips on the front and back side. On the right figure, a detailed drawing of the strip pattern is shown. Indicated are the insensitive areas of the silicon.

electronics is realized with metalized Kapton foils. On both ends of the connection the strips as well as the chips are connected with 17 μm aluminum bond wires. On top of the module the electronics is protected by a stainless steal plate (see Fig. 4.4).

4.3.2 Lambda Wheels silicon sensors

Double sided silicon strip sensors are chosen for the LW. That means that each sensor has two *sides*. The sensors are cut out of a 6 inch n-type silicon wafer. They have a trapezoidal shape, with an apex of 30° degrees, a base of 85.3 mm, and a top of 23.2 mm (see Fig.4.5). The sensor has strips parallel to the oblique sides of the trapezoid. In total, each side has 516 strips which makes 24768 for the whole detector. The first 134 strips on the left have the same length. The last 17 strips are too short to be connected and they are left unbonded. In total 499 strips per side of a silicon are instrumented. The sensor has insensitive areas at the edges, shown in Fig. 4.5. Taking into account the unbonded strips and the insensitive areas 93 % of the surface is active. The partitioning of the sensor into strips produces the spatial resolution of the device.

Fig. 4.6 shows a schematic cut through a silicon sensor. It is an n-type silicon and has a thickness of 300 μm. On the junction side the strips are realized with p+ and on the ohmic with n+-implants. The pitch from strip to strip is 160 μm and the width of the implants is 60 μm. The n+-implants are isolated from each other by p+-stops. The sensor

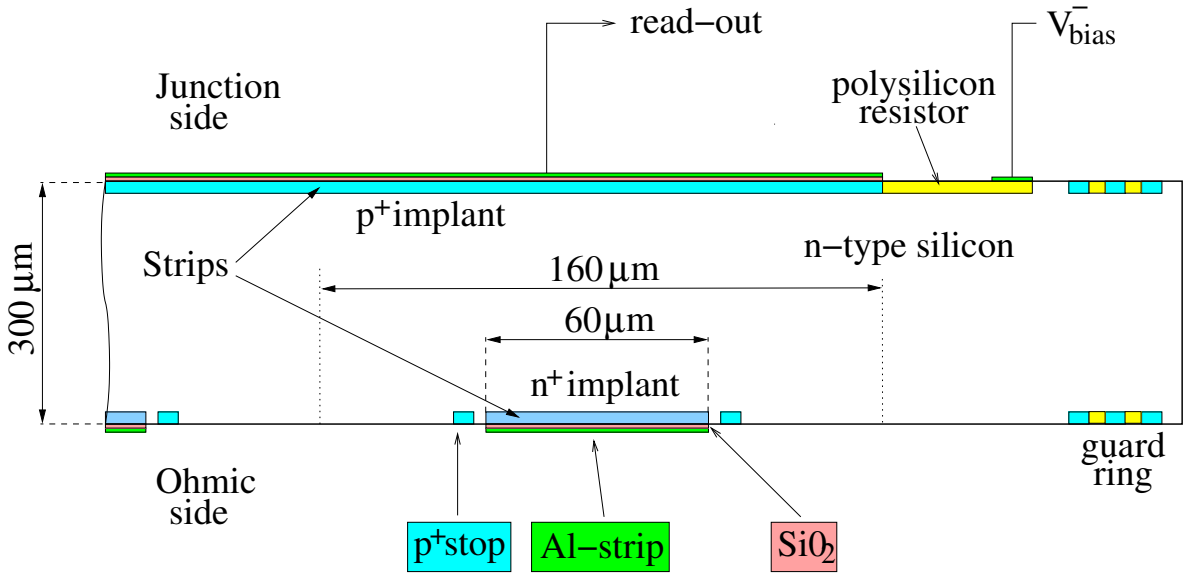

Figure 4.6: Schematic cut through the silicon sensor, further explanations are given in the text (from [49]).

is passivated with a 2 μm silicon oxide (SiO_2) layer. The metal connections are made of aluminum. They are placed on top of the implanted strip pattern and read out on the top end. The connection to the bias voltage is protected by a 2 MΩ resistor. Finally, the whole sensitive area is surrounded by three guard rings.

As the sensors are double sided, the signal created by a traversing particle is read out on both sides. Thus, the amplitudes of the signals from either side are correlated. This correlation is used in the tracking code (see Sec. 4.4.1) to identify strip combinations. Moreover, the metal strip read-out configuration of the sensors causes another effect. Because two neighboring strips are capacitively coupled, the moving charge will not only induce a signal on the strip that is actually hit but also on the neighboring strips. This effect is called *charge sharing* and can be used to improve the resolution, when the position of the track is calculated by a weighted mean of the strip position and the amplitude of the signal.

4.3.3 LW Electronic System

The following paragraphs describe the electronic system of the LW. It provides means to control and read out the detector. The system consists of the front-end electronics, including the HELIX chips, which are controlled via a control unit (HLCU) and the analog to digital converters (HADC), which are read out by the data acquisition (DAQ). As mentioned before, the front end electronics is placed on top of the modules whereas the rest of the electronic equipment is located beneath the detector platform in a VME crate.

Front-end electronics The HELIX (version 128-2.2 [47]) is an analog readout chip with 128 *channels*. Each channel is instrumented with a low noise charge sensitive preamplifier/shaper. The chips are produced in a 0.8 μm-AMS [14] process and have been specially designed for use at the HERA accelerator. The collected charge is sampled into an analog pipeline with a maximum latency of 128 sampling intervals. Their memory pipeline and the signal output are clocked with a frequency of 10.4 MHz which corresponds to the 96 ns bunch crossing time of HERA. When the chips receive the trigger signal they stop sampling and the data is sent out. The sending of the data is indicated on the output line as a DC offset. Four HELIX chips are used for the readout of each side of one silicon sensor.

HeLix Control Unit The HLCU is located in the VME crate below the platform. It supplies the front-end electronics with the necessary control signals. It has got a serial data communication to set the internal registers of the HELIX chips. There are 4 HELIX chips to read out one side of a sensor. In total there are 196 chips. Each HELIX chip has got its own address and can be programmed individually. Furthermore, the HLCU supplies the clock, trigger, reset and the test pulse for the HELIX chips.

HERMES Analog to Digital Converters The HADCs are located in the same VME crate as the HLCU. Thus, the analog signals have to travel only a couple of meters before they are converted to digital values. All analog lines from one LW module are connected to one HADC module. Each HADC module is divided into two parts for the two different signals from the ohmic and the junction side of the sensor. Each side has its own ADC input such that the data are processed in parallel with 48 ADCs for the whole LW. The offset in the analog signal mentioned before is registered by the HADC module with a discriminator and interpreted as a data-valid. From that time on, the analog signal is converted.

The conversion in each ADC proceeds in four steps (see Fig. 4.7). The analog signal is *converted* in a first step by a 10-bit ADC. The second step is the *pedestal-subtraction*. This is achieved by subtracting a pre-loaded value from the ADC value leaving a small positive offset. The third step is the determination and subtraction of the *common mode* noise. Common mode noise influences the height of all channels of one chip with approximately the same amount. The common mode subtraction algorithm, implemented in the HADC, calculates an average ADC value of 16 out of the first 32 channels. Very high ADC values are excluded by a high-threshold. The calculated mean offset is then subtracted from all channels. The fourth and last step is the so-called *zero suppression*. As it is expected that only very small numbers of channels actually have a real signal, a hit threshold is applied. Only values which lie above that value are stored in the internal memory to be read out by the DAQ. Additionally, some hot channels are disabled at this stage. The HADC memory can store up to four events. In addition to the data a header is stored together with the event. This header contains information about the length of the event, additional information to identify the equipment and scaler numbers for the accepted and rejected triggers.

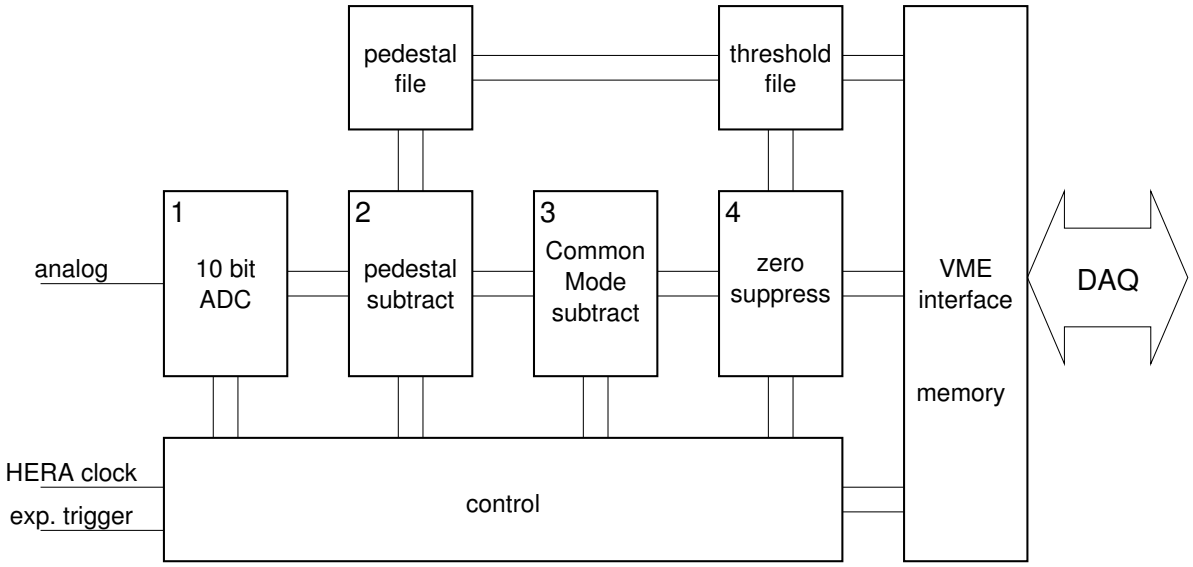

Figure 4.7: A block-diagram of the readout for the HADC modules. The conversion of the analog data is done in four steps. For an explanation of the diagram see text (from [78]).

4.3.4 Power supply

There are two different voltages needed to operate the LW. The first one is the bias voltage for the silicon sensors. This voltage is provided to the detector from a CAEN high voltage system (SY527). Two modules (of the type A516) with 16 channels (100 V, 200μA) each supply the voltages (further details can be found at [36]). The bias voltage is applied equally to the junction and the ohmic side of the detector. Therefore, only 24 of the channels are needed for the 12 silicon sensors. The voltages are supplied by twisted pair cables. The sensors are then connected via a filter located below the pumping cross. The second voltage is needed for the low voltage of the front-end electronics and to power the HELIX chips. There are again 24 channels providing the $\pm$2 V to the carrier board. Each channel draws about 1.45 A which results in a dissipation of 70 W for the complete detector. The power supplies and their controls are mounted on the platform below the detector. The equipment is controlled via a CAN[1]-node.

4.3.5 Cooling of the LW

The detector resides in a vacuum vessel. The absence of air makes it necessary to take special care about the cooling of the equipment. The cooling power is provided by Peltier elements. A schematic diagram of the cooling system is shown in Fig. 4.8. Two circuits with cooling liquid distribute the power. The first loop connects the detector equipment inside the vacuum. This internal loop has pure ethyl alcohol as a cooling liquid. The second outer loop is using the general HERMES cooling water which has a temperature of about 16° Celsius. The water is used to cool the warm side of the Peltier elements inside a

[1]Controller Area Network [83]

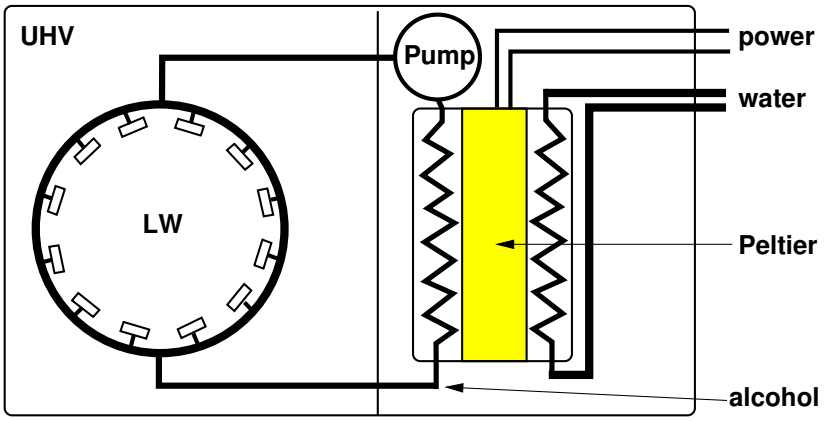

Figure 4.8: Schematic diagram of the LW cooling system. On the left side it is seen how the LW is cooled in the secondary circuit with alcohol. The alcohol is cooled in a separate secondary vacuum with Peltier elements which are on the hot side cooled with water, as can be seen in the right side of the figure.

secondary vacuum. The Peltier elements consist of two ceramic plates, in between which there are alternating n- and p-doped SC materials connected in series. A current flowing through the element cools one side while the other becomes warm. The temperature difference is proportional to the current. Due to the resistance of the elements the current produces also dissipative heat. This so-called Joule heat is proportional to the square of the current. Thus, at a certain point the cooling effect is over compensated by the heating. The system is capable of removing 100 W of heat from the detector.

4.4 Lambda Wheels Data Analysis

This section is dedicated to the analysis of the commissioning data taken in the year 2003 with the LW. In total 130 runs in two days have been collected and these data from the basis of the present analysis. First, the tracking procedure is explained in Sec. 4.4.1 starting from the raw hits and proceeding to the determination of tracks. Second, the alignment study of the LW is presented in Sec. 4.4.2. Finally, the efficiency and resolution of the detector is presented in Sec. 4.4.3. The section is concluded with a summary and outlook.

4.4.1 LW Tracking

The basic tracking algorithm has been developed and is described in detail in [49]. In this section the basic ideas are recapitulated. Improvements that are made besides the extension to the complete detector will be mentioned. The achieved results are compared to the results obtained with the prototype described in [49] where possible. Due to some read-out problems the DAQ had to be reset at regular intervals. During the reseting the

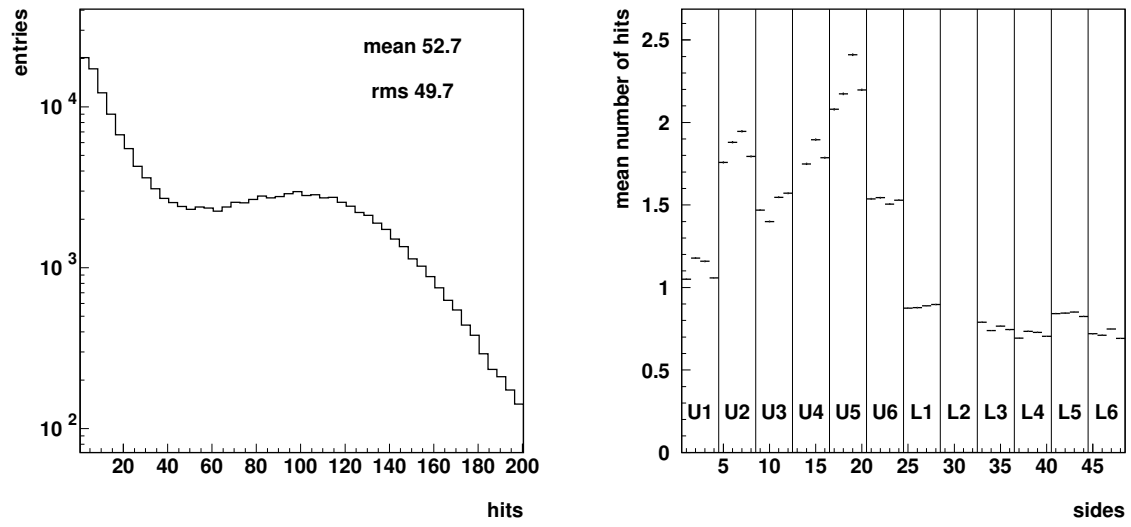

Figure 4.9: On the left, the number of hits per event is shown for the complete LW. On the right, the mean number of hits per event and side is plotted. The borders of the 12 modules are indicated by vertical lines.

data taking was interrupted. The result is that 10 % of the events are lost. Additionally, 13 % of the collected events are still unsynchronized[2]. The general steps of the tracking are discussed next.

Number of hits / wire-maps The multiplicity or the amount of channels with a signal above a threshold (*hits*) depends on the settings in the HADC. A lower ADC threshold results in a higher number of hits. Both the number of noise hits and the number of real hits increases. The ADC threshold has to be chosen such that most of the real hits are read out and the amount of noise hits is still reasonable.

A distribution of the number of hits per event in the entire equipment consisting of 43 working sides is shown in Fig. 4.9. As can be seen the mean number of hits is about 53 with a large spread. The same result is obtained from the plot on the right side of Fig. 4.9 where the mean number of hits is shown for each single sensor side. The vertical lines represent the borders of each module. The mean number varies for the top detectors (U1 − 6) between 1.0 and 2.5 hits per event with an average of 1.7. For the bottom (L1 − 6) the variation lies between 0.7 and 0.9 hits per event with an average of 0.8. Each of the sides contributes on average 1.3 hits per event which is in view of the tracking a low number. The up-down asymmetry can be explained by the upwards directed synchrotron halo which was present during this period and is also seen by the other detectors of the HERMES experiment.

The quality of the data recorded by the detector is also investigated by preparing the

[2]These problems were improved in 2004 when the LW were used in full data taking mode.

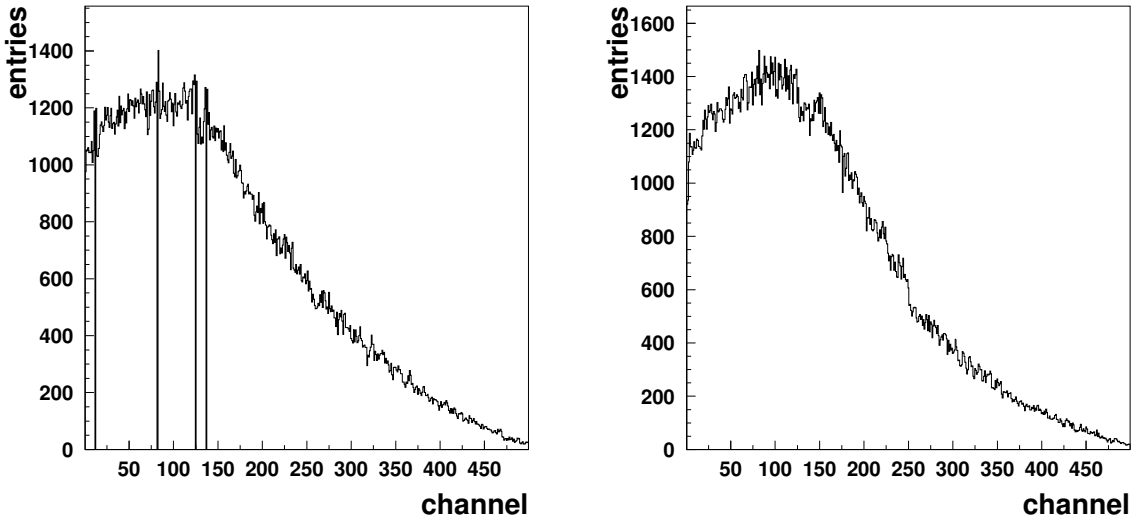

Figure 4.10: Wire-maps of one plane of the LW detector. The number of hits per channel is plotted versus the channel-number. On the left the data from the front (junction) side of the sensor is shown and on the right the data from the back (ohmic) side of the sensor.

distribution of events per channel, also know as the *wire-maps*. An example is shown in Fig. 4.10 for one sensor. The figure shows the total number of hits of a channel versus the channel number. There are two plots, one for the front and one for the back side of the same sensor. The number of times a channel has a hit depends on the length of the corresponding strip. This can be seen by the decrease towards higher channel numbers that correspond to the shorter strips on the end of the sensor. In addition dead channels are apparent as black lines and hot channels as spikes on top of the distribution.

Clustering of hits / ADC spectrum A track passing through a sensor will cross the sensitive volume of one or at most two channels. However, due to charge sharing a part of the signal will be induced on a neighboring channel. To increase the resolution, hits from adjacent channels are combined. This is done with a weighted mean calculation of the combined channel positions according to their ADC values. The result of the combined channels is called a *cluster* and gets assigned the summed ADC values. On average 1.25 channels on the junction and 1.30 channels on the ohmic side are combined. The average number of clusters per event for the complete detector is 42. This corresponds to a reduction of hits in going from the raw multiplicity shown in figure 4.9 to clusters of 20 %.

In Fig. 4.11 an ADC spectrum for clustered hits is shown. On the left side for the junction and on the right side for the ohmic side of one plane. The distribution has been fitted with a background function and a Landau curve. On average the mean position of the Landau distribution for the junction side is 36.8 with a spread of 1.7. For the ohmic side this mean is found to be 34.2 with a spread of 2.8.

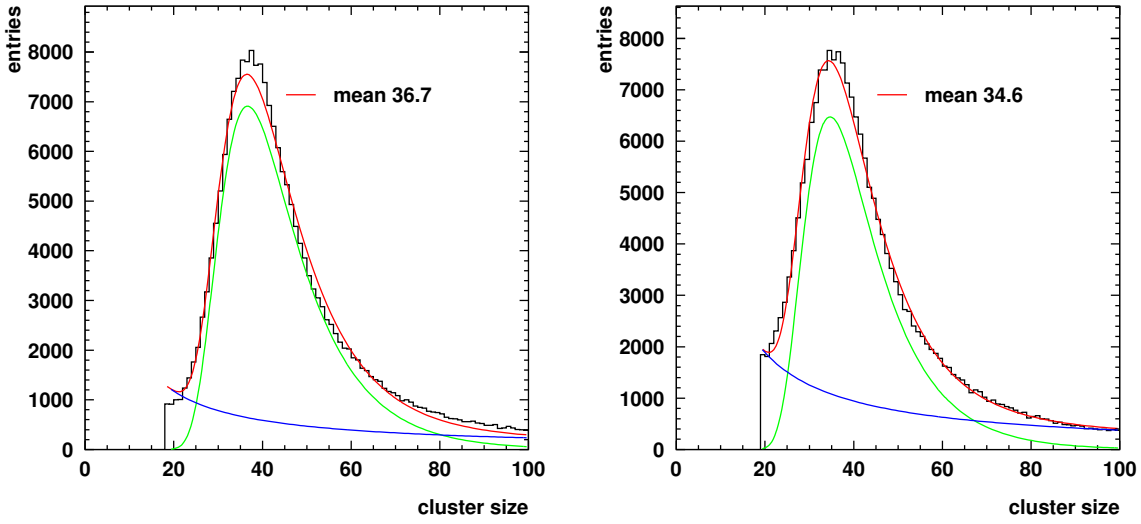

Figure 4.11: Clustered ADC spectrum of one silicon sensor. The left plot shows the distribution of clusters for the junction side and the right plot shows the distribution for the ohmic side. The mean position of the fitted Landau curve is given in the plot as well as the estimated background below the peak.

It is concluded that while the ohmic side has more hits in a cluster, it has a lower average signal. This is believed to be due to lower drift velocity of the majority charge carriers.

Combine front and back clusters to coordinates The next step in the tracking after clustering is to combine front and back clusters to construct coordinates. As the same signal is read out from the plane on either side a correlation requirement has been implemented. This so-called *Figure-of-Merit* (FOM) quantifies how well the two clusters correspond to each other with respect to their ADC values. The FOM is calculated with the front ADC value A_f and back ADC value A_b as:

$$\begin{aligned} \text{FOM} &= (A_f + A_b) \cdot \text{correlation} \cdot \text{high-cut} \\ \text{correlation} &= \begin{cases} \exp(-0.3\frac{A_f}{A_b}) & \text{if} \quad A_f > A_b \\ \exp(-0.3\frac{A_b}{A_f}) & \text{if} \quad A_b > A_f \end{cases} \\ \text{high-cut} &= \begin{cases} \exp(\frac{1025-A_f}{50}) & \text{if} \quad A_f > 1025 \\ \exp(\frac{1025-A_b}{50}) & \text{if} \quad A_b > 1025 \\ 1 & \text{else} \end{cases} \end{aligned} \tag{4.3}$$

In the first term both ADC values are summed. The second (*correlation*) term favors equal pulse heights from the front and back side. The third term (*high cut*) disfavors ADC values higher than a threshold starting at 1025 channels.

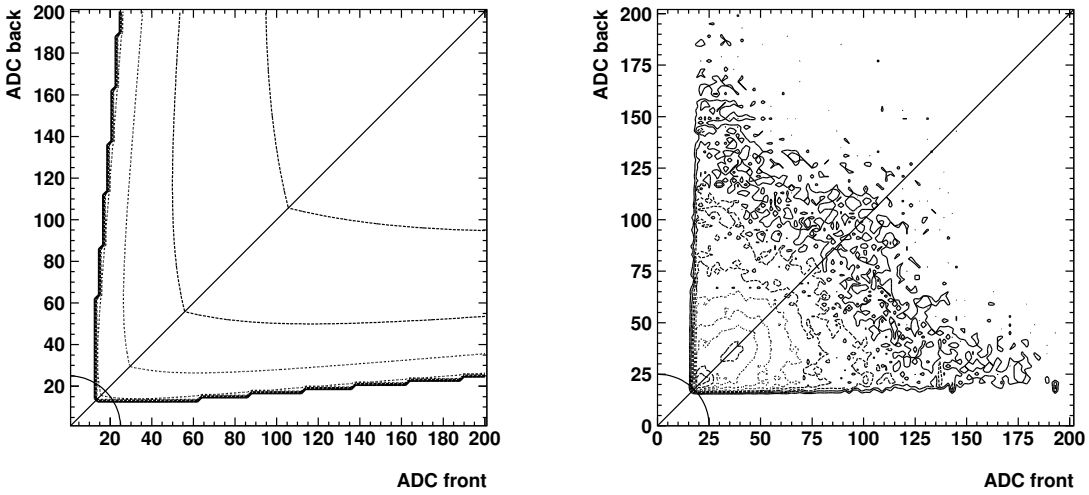

Figure 4.12: Both plots show ADC values of the front side versus ADC values of the back side. Left side: the levels of equal FOM are shown on the z-axis as indicated by the contours. The right side shows the number of entries.

In Fig. 4.12 an example for the calculated FOM is shown. In the left plot the levels of equal FOM values are shown by their contours. This plot defines the area in the 2d plot of ADC values which is selected by a requirement on the FOM. In the right plot in Fig. 4.12 an example from the data is plotted. In the lower left corner a highly populated area due to minimum ionizing particles is seen. The criterion for the FOM value used is that it has to be greater than 20 and the effect can be seen in the plot. First of all the FOM requirement acts like a threshold requirement on both ADC values. For unequal ADC values the correlation term starts to play a role. This can be seen in the right plot of Fig. 4.12 where for low values on one side and for high values on the other, data are removed. The high cut value disfavors equally higher ADC values on both sides.

After the coordinates have been calculated in the plane of the silicon sensor, they are transformed into the HERMES coordinate system. For this transformation an alignment of the detector is necessary which is discussed in section 4.4.2.

Combine coordinates to tracks / selection To construct the tracks all combinations of coordinates from the first and the second plane of a module are made. The two coordinates define the slope and the position of a LW track. At first all combinations are kept; only those which have an unreasonable high or low slope are rejected. To minimize the amount of tracks several checks are performed and a quality parameter is calculated. On the basis of this quality parameter one track is selected if several tracks have a common cluster in one plane. The checks which are performed are the following. Firstly, it is calculated if the tracks point back to the target region. If this is the case it means that they have a high chance to actually come from a beam interaction. Secondly, the track is extrapolated to the DVC planes. The DVC has a high efficiency and a passing

particle should have been reconstructed in some planes. After this it is counted how many planes of the DVC have a hit in the vicinity of the extrapolated LW track. Lastly, it is checked if the track passes the fiducial volume of the HERMES front region. If this is the case it is checked whether a track has been reconstructed by HRC with similar slope and position parameters. n

Multiplicities For the analyzed data set the average number of hits in one sensor side for the upper detector half is found to be 1.7 and for the lower half 0.8. The average number of clusters per sensor is found to be 1.3 and 0.6, respectively. The average number of channels which are combined to a cluster is 1.25 for the junction side and 1.30 for the ohmic side. A difference can also be seen in the mean position of a landau fit to the clustered ADC spectrum. Here, the junction side has a mean of 36.8 ADC channels and the ohmic side 34.2 ADC channels. After the de-selection procedure described above on average only 3.1 good tracks are produced per event for the complete detector. The resulting values of the multiplicity analysis from the commissioning data are shown in table 4.1.

part		upper (U)	lower (L)
	hits / event	1.7	0.8
side	cluster / event	1.3	0.6
		junction	ohmic
side	hits / cluster	1.25	1.30
	Landau mean	36.8	34.2
detector	tracks / event	3.1	

Table 4.1: Multiplicity numbers determined for the commissioning data of the LW collected in 2003. In the top part the difference between the upper and lower part of the detector and in the middle part the difference between junction and ohmic side is shown.

4.4.2 LW Alignment Study

The alignment of a detector is an important part of the commissioning. It is crucial for any analysis to know the positioning with respect to a chosen reference frame. In the case of the LW alignment the reference frame is given by the tracking information from the HERMES detector derived with the HRC program. Naturally, this reference frame has its own uncertainties. The HRC tracks have a better precision in the determination of angles, but the LW have a better position resolution. This section summarizes the alignment results obtained in Ref. [69].

As mentioned before, the LW consist of 12 modules. Each module has two double sided silicon wafers. These 24 wafers are the smallest unit which will be considered in the alignment procedure. Every one of these silicon sensors has six degrees of freedom. These are the position parameters x, y and z which determine a point in space, and three rotation

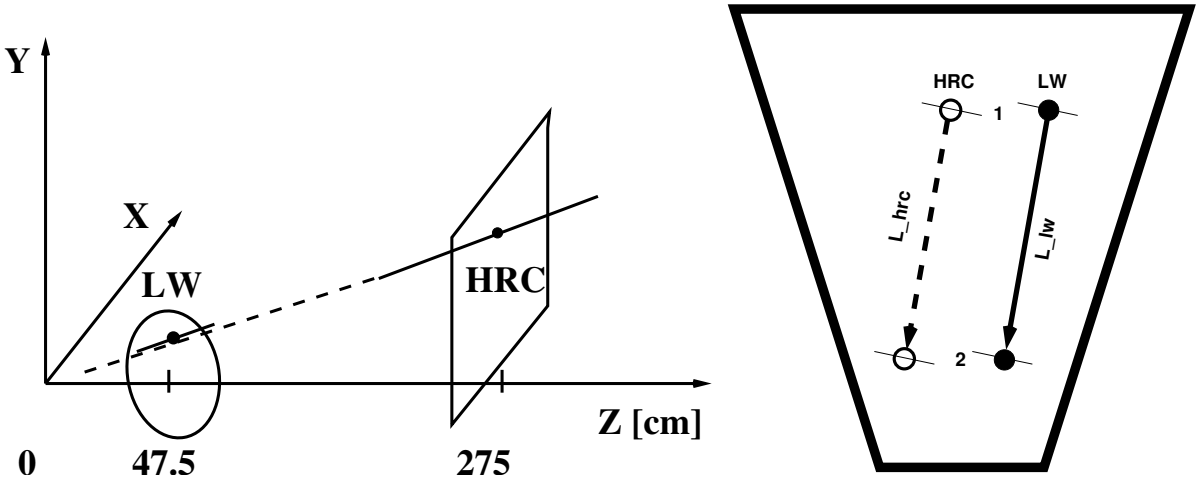

Figure 4.13: In the left plot the HERMES coordinate system is shown with the LW detector and the nominal position where the HRC track is given. The sketch includes a HERMES front track determined at the center of the magnet. The right plot shows a wafer with a HRC and a LW track. There are two points for each track. Open circles represent the HRC track position and closed circles the LW track.

angles around the Cartesian axes. These rotations are called *roll* for the rotation around the z-axis (corresponding to the angle Φ in polar coordinates), *pitch* for the rotation around x and *yaw* for the rotation around the y-axis. This means that the alignment makes it necessary to measure 144 parameters.

However, we have chosen a different approach. The alignment is first done for the complete detector. Here, all 6 degrees of freedom have been determined. Then, the modules are aligned and it is found that the only parameter necessary to modify is the radial distance from the beam. After that, the wafers have been corrected for three rotational angles. The reason for this choice is that the frame and the modules of the LW are a precisely machined structure which leaves very little freedom to move. It is found that 48 parameters are sufficient to resolve all differences with respect to the HRC coordinate system.

Positional offsets of the detector

The first correction which has been determined is the z-position of the detector. For the determination of this correction a method called the *vector-method* has been used. The basis of this method is to compare two HRC and LW tracks in the rigid plane of one wafer. In that way any internal misalignments cancel and the only unknown which contributes to the alignment arises from the extrapolation of the HRC track to the LW.

In Fig. 4.13 a schematic drawing of a wafer is shown. The vector-method works as follows: two pairs of points are shown which represent the location of where the HRC and LW tracks are found to pass the wafer. The solid circles represent the LW tracks and the open circles the HRC tracks. The idea is that in a perfectly well aligned detector the two pairs of points should be on top of each other. The HRC tracks are extrapolated to the

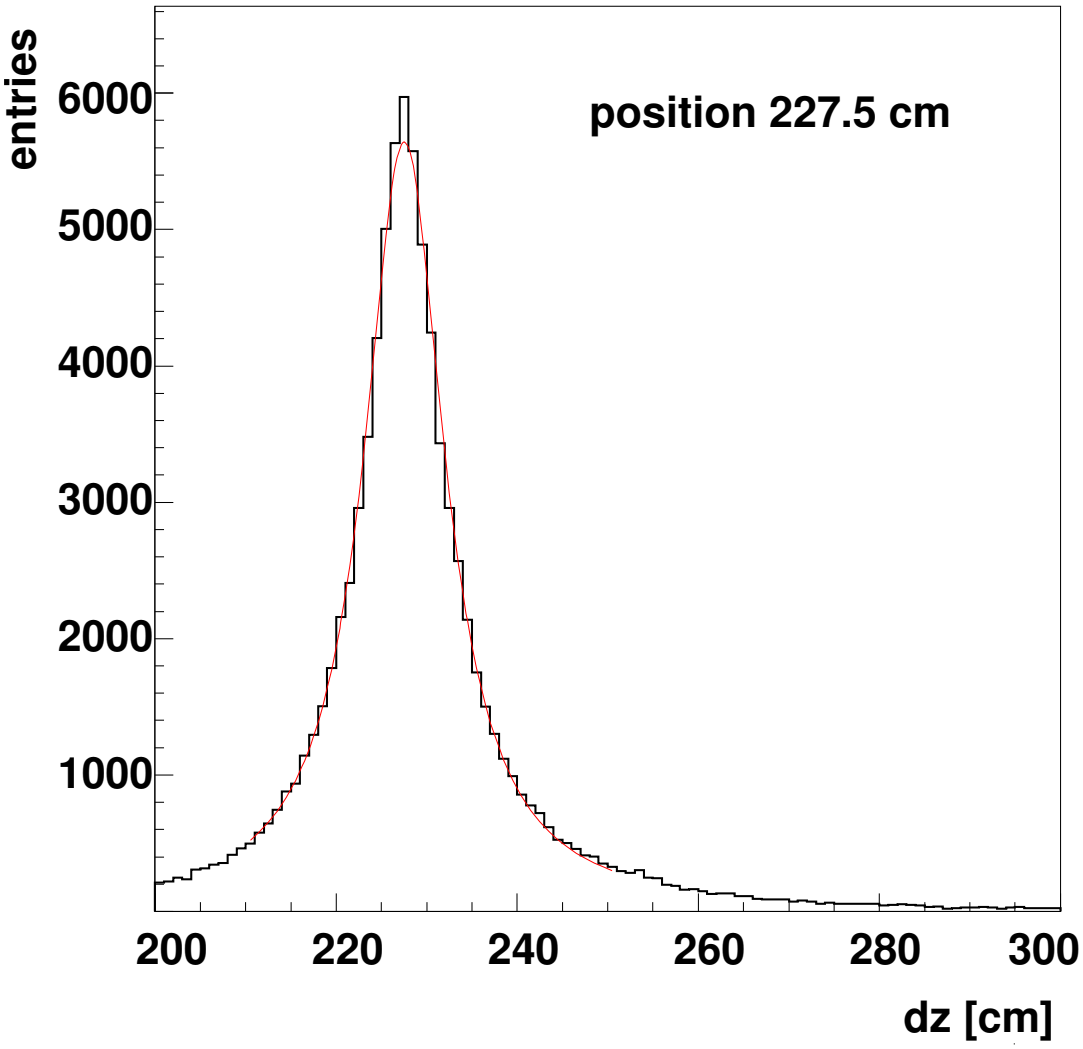

Figure 4.14: Alignment of the complete detector in the z-direction after several iterations. The corrected position is found to coincide with the nominal value of 227.5 cm, after applying an offset of $\Delta Z = 1.2$ cm.

position on the wafer using

$$HRC^{x,y}_{LW} = HRC^{x,y}_{position} + \Delta Z \cdot HRC^{x,y}_{slope}, \tag{4.4}$$

where ΔZ is the distance between the HRC track position and the LW position. As the length of the two vectors between point 1 to point 2 should be the same for the LW and the extrapolated HRC track, this equation can be solved for ΔZ. The resulting values of ΔZ are entered in a histogram. The result is shown in Fig. 4.14. The calculation has two solutions, only the solution which is closer to the expected value of 227.5 cm has been chosen for the determination of the position. The histogram has been fitted with a Lorenz shape curve to find the mean position. A correction of 1.2 cm had to be applied to the LW position with respect to its nominal position.

The x and y corrections of the complete detector cannot be determined with the vector method. Instead, the tracks have to be compared directly. In this case all uncertainties

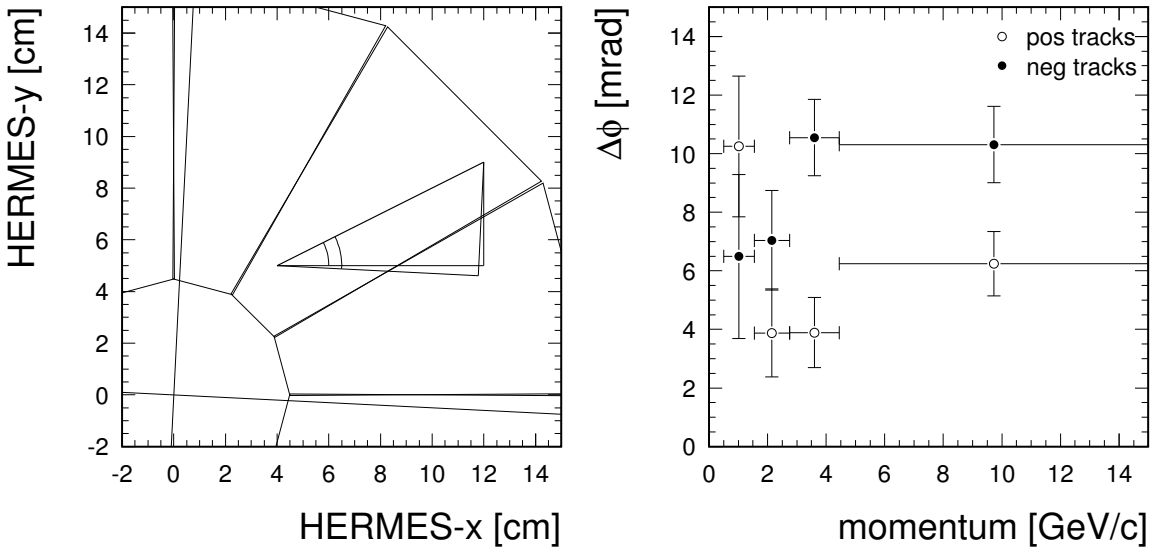

Figure 4.15: On the left plot the upper right quadrant of the LW is depicted. Additionally the HERMES coordinate system is shown with a tilt of 5.7 mrad. On the right side the results for the determined roll parameter are shown versus the track momentum.

from the misaligned detector are included. Furthermore, both parameters are correlated and therefore these parameters are the least accurate. The alignment in x and y has been done by comparing the mean difference in the x and y position of HRC and LW tracks in the LW. The results are summarized in table 4.2 on page 58. The offsets have been determined after all other alignments have been done.

Rotational offset of the detector

The roll alignment has been determined in the same way as the z alignment. Again two vectors in the plane of the wafer are used (see left side of Fig. 4.15). In the case of the roll alignment, however, not the length but the orientation has to be compared. The angle between the two points from a LW respectively a HRC track are compared like

$$\Phi_{LW/HRC} = \arctan\left(\frac{y_1 - y_2}{x_1 - x_2}\right), \tag{4.5}$$

where $\Phi_{LW/HRC}$ is the rotation angle. The result found for the roll as a function of the track momentum is shown in Fig. 4.15. Averaged over all track momenta and charges the relative roll $\Phi_{LW/HRC}$ is found to be 7.3 ± 2.6 mrad. The dependence on charge and momentum of this measurement carries a large margin of uncertainty. It is noted that the LW are leveled during installation to earth gravity while the HERMES experiment has a slight tilt of -5.73 mrad. This relative tilt is consistent with the average tilt found from the data.

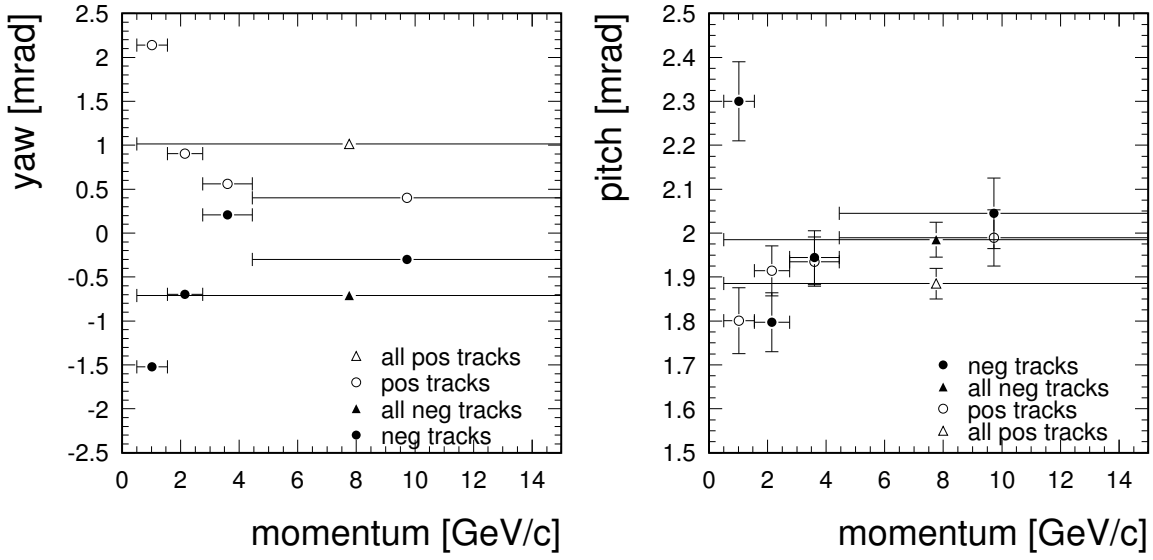

Figure 4.16: On the left side the yaw versus momentum for different charged tracks is plotted. On the right side the same is done for the pitch. Further explanations are given in the text.

Tilt parameters of the detector

Pitch and yaw can only be determined by directly comparing the slopes of the LW and HRC tracks. Before these numbers can be derived from the data a correction for another imperfection has to be applied. This correction is necessary as the silicon sensors are glued to the frame of each module near the rim of the wheel. Due to this, the sensors are slightly tilted towards each other at the tip. The difference between the nominal and the actual distance between the two wafers is 0.13 cm. This results in a slope offset of the LW tracks depending on the distance to the beam. After applying this correction the x-slopes for the yaw and the y-slopes for the pitch show no dependence on the distance from the track in the LW to the beam line anymore. The corrected slopes are then compared to the slopes derived by HRC (see Fig. 4.16). The result is a linear dependence between the two slopes. This dependence has been fitted with a straight line. An offset is interpreted as a real difference between the LW and HRC frame. The result for the pitch is 1.96 ± 0.13 mrad. Within the uncertainty it shows no dependency on the momentum and charge of the tracks. The yaw obtained with this method does show a dependence on the momenta. There are deviations especially for low momentum particles. The average for the different charged particles has a different sign. The average alignment correction for positive tracks is 1.0 ± 0.3 mrad while it is -0.7 ± 0.4 mrad for negative tracks.

Shifts in x-y plane of the modules

After aligning the overall detector position, shifts in the x-y plane of single LW modules have been determined. As the modules are mounted on the LW frame with good precision it is not expected that their origin varies freely. The only expected uncertainty is the radial distance with respect to the beam line. The shifts are determined by analyzing

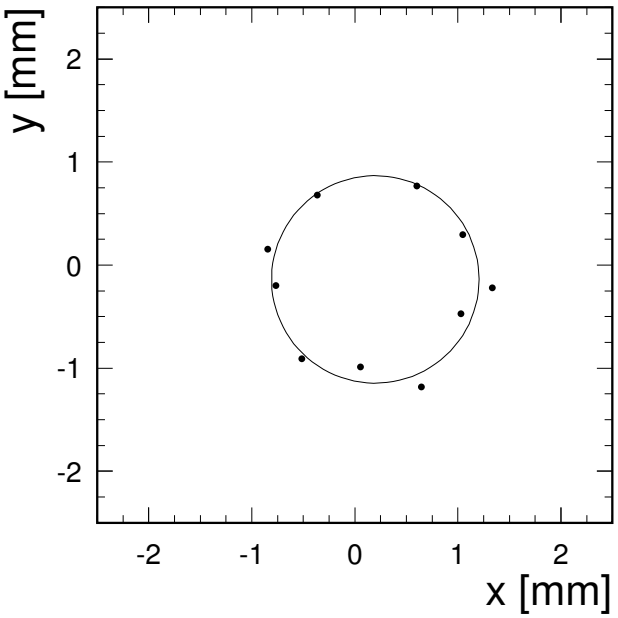

Figure 4.17: Shifts in the $x - y$ plane of the symmetry point of the modules. The symmetry point is the intersection of the first strips on either side of the silicon sensor. The shifts have been determined with an iterative method minimizing the distance of closest approach of two tracks.

events which include two tracks, assigned to two different LW modules. It is assumed that these two tracks come from the same scattering event and therefore have a common vertex. This procedure does not influence the previously discussed alignment factors as they are achieved by taking only tracks inside one module. For the radial alignment, the vertex calculation or determination of the point of closest approach has been done in an iterative way. While changing the radial position of the modules a least square algorithm determines a minimum of the distance of closest approach. It is found that radial shifts of typically 1 mm are needed to minimize the distance of closest approach. This can be seen in Fig. 4.4.2. These numbers agree within the margins of uncertainty to the position determined from drawings and measurements of the LW frame.

Internal corrections for wafers in a module

After the alignment of the complete detector and the individual modules the alignment of the individual silicon wafers has been studied. The corrections necessary for the wafers only apply to the slope of the LW tracks. These slope corrections are based on measurements which have been carried out at NIKHEF with a high precision optical alignment machine (Wenzel LH1210). With this instrument the positions of the silicon sensors relative to the frame of the modules have been measured with a precision of 5 μm. From these measurements three angles have been calculated that determine the displacement of the silicon sensors. The most important angular correction is the one for the γ-angle, see Fig. 4.18. This correction was already mentioned earlier in this section on page 55. It compensates for the fact that the sensors are tilted towards each other. Similarly, the β-angle influences the distance between the two wafers and therefore the calculation of the slopes. Because of the smaller lever arm this correction is less significant. The last angle, α, also influences the determination of the slopes. The effects of α on the x- and y-direction are different. The effect increases when going towards the tip of the silicon.

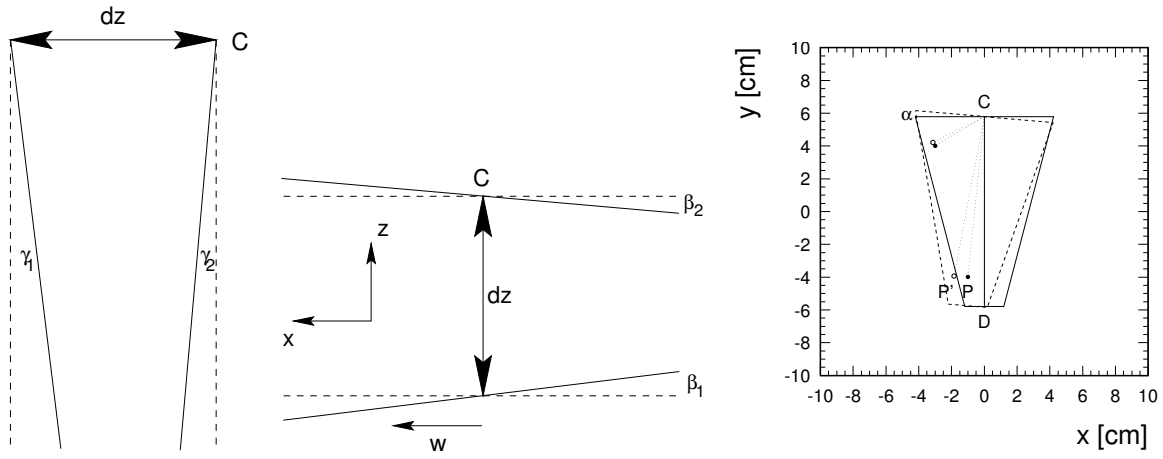

Figure 4.18: Three rotation angles of the silicon wafers in one module have been determined with the alignment machine. The misalignments have been expressed in three angles. The first angle γ expresses how much the two wafers are tilted towards each other. The second angle β is a measure for the angle in the $x-z$ plane. Finally, the angle α tells how much the wafers are rotated against each other in the x-y plane.

These corrections are implemented in the LW tracking code and are found to be sufficient to correct for the remaining differences in slopes of LW tracks compared to HRC tracks.

Left over ambiguities

After the final alignment the data have been split in four momentum bins and in positively and negatively charged tracks. The slopes of the tracks have been compared to those obtained with HRC in the x and y direction for those four momentum bins. The result is shown in Fig. 4.19. As can be seen in the left plot the difference in the mean value for the different charges depends on the momentum of the tracks in the x-direction. For the y-direction no such dependence is observed. The offset in the x-direction is a hint that the HRC tracking may not be perfect. This could be due to misalignments of the HERMES detector or due to an imperfection of the magnetic field map used for the reconstruction of HERMES tracks.

Applying all the corrections listed in table 4.2, there is a good agreement between tracks from the LW and from HRC. The determination of the alignment corrections is affected by the presence of the spectrometer and is limited by the resolution of the HERMES tracking. It is noted that these uncertainties exceed the intrinsic margins of uncertainty of the LW.

4.4.3 LW efficiency and resolution

Track Efficiencies The efficiency to find a HRC track in the LW has been studied. For the comparison HRC tracks passing the sensitive volume of the LW detector are selected.

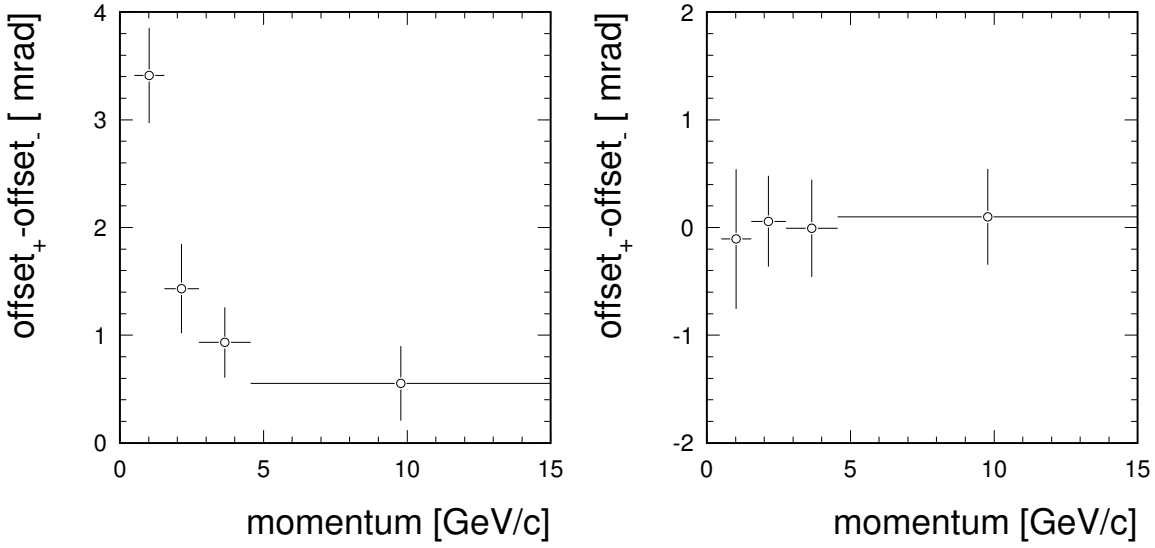

Figure 4.19: Charge dependent differences in the slopes between LW and HRC tracks after applying the final alignment parameters. On the left side these differences are shown for the x-direction and on the right side for the y-direction.

	parameter	nominal	value	error	unit
	x-position	0.0	-0.22	0.05	cm
detector	y-position	0.0	0.068	0.002	cm
	z-position	47.5	1.2	0.2	cm
	pitch	0.0	2.0	0.1	mrad
detector	yaw	0.0	0.2	0.9	mrad
	roll	5.73	7.0	2.6	mrad
modules	radial-shift	0.663	0.101	0.009	cm

Table 4.2: Table of the final LW alignment parameters for the complete detector and the modules. The values of the parameters α, β and γ for the alignment of the wafers are given in [69].

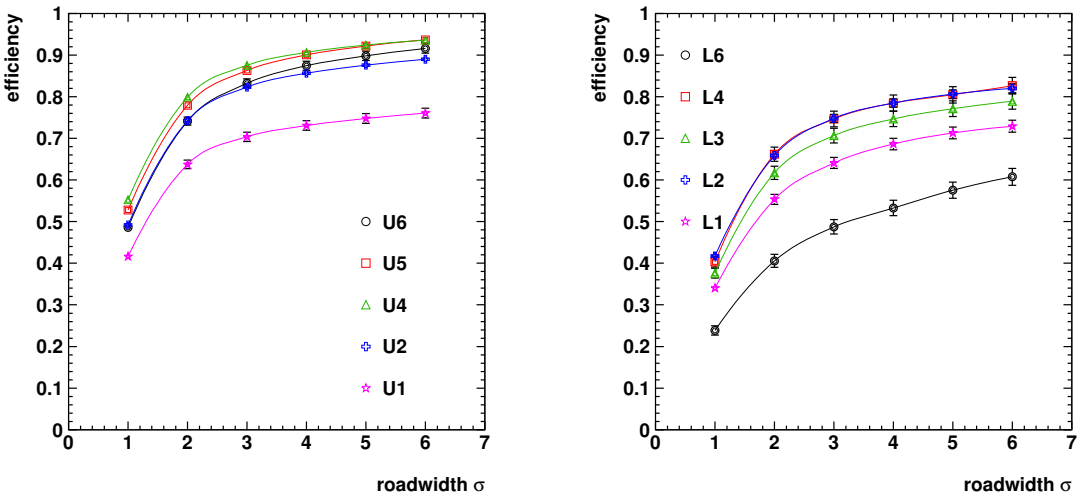

Figure 4.20: On the left side the efficiency for each module in the upper half is shown versus the road-width. On the right the same for the lower part is shown. The horizontal axis represents a measure of the road width in units of 0.2 cm.

This is done with a fiducial volume requirement on the sensors. The HRC track has to pass through a disk at the nominal z position of the planes with an inner radius of 5 cm and an outer radius of 16 cm. Furthermore, the gaps between the sensors are excluded. In Fig. 4.20 the efficiency is shown on the left side for the upper and on the right side for the lower modules. The efficiency to find a HRC track is plotted versus a road width σ. This σ corresponds to the combined distance in x and y between the LW and HRC track in units of 0.2 cm. As can be seen for most of the upper modules the efficiency reaches values of more than 90 % for road widths in excess of $5 \cdot 0.2$ cm $= 1.0$ cm. Taking the dependence on the road width out of the distribution and calculating the average efficiency for the upper modules a value of 92 % is derived. The lower modules have an average efficiency of 81 %. The reason for the differing efficiencies can be manifold. First, the relatively high threshold, used during the commissioning, causes an inefficiency. Note, that when a hit on one out of the four sides is not recorded the whole track is not reconstructed. Second, the synchronization problem of the readout affects the latter modules more.

Resolution studies With the aligned LW it is now possible to estimate the resolution of the LW by a comparison with HRC tracks. In Fig. 4.21 a comparison of the slopes determined by the LW and HRC is shown. As shown on the left plot the resolution of the LW in the $x - y$ direction depends on the angle with which the module is installed with respect to the HERMES frame. The so-called resolution elements defined by the strip configuration have a diamond shape. The results of Gaussian fits to the difference of LW and HRC slopes are shown in the right side plot of the figure. These widths vary between 2 and 4 mrad for the different configurations. For module 1 and 3 the x and y resolutions are different while for module 2 they are the same. The average over all modules is 3 mrad. This value compares well to the value calculated in [49] of 2.6 mrad.

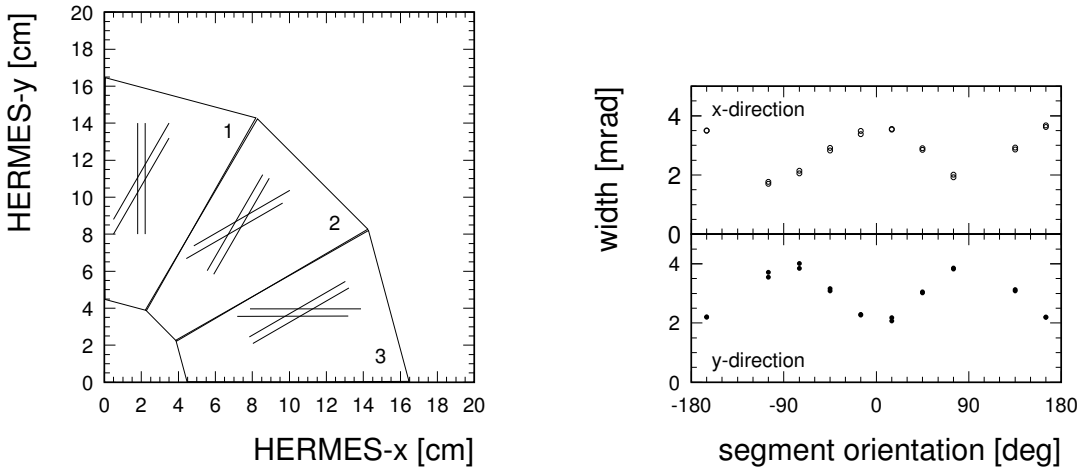

Figure 4.21: On the left side the upper right quadrant of the LW is depicted. Three segments with their strip configuration are shown. The intersections of the strips define a resolution element. On the right plot the angular resolution versus the segment orientation is shown. The width is determined by a fit to a residual distribution determined from HRC and LW tracks.

The reason for the slightly higher values obtained in this analysis might be due to the comparably high ADC thresholds.

In Fig. 4.22 the vertex resolution of the LW in x and y are compared to the HRC resolution. In addition results from a simulation are displayed. The width of the xy-vertex resolution is shown as a function of the z-vertex. As can be seen the x-vertex resolution is compatible with the spectrometer values for negative z values. The difference in the slopes of the resolution curves can be explained by the angular resolution. As the angular resolution of the LW is worse than that of the spectrometer, the dependence is steeper. The slightly worse x-resolution of the spectrometer can be explained by the larger distance of the front chambers to the vertex. In addition the results of simulations are shown in the plots. These simulations are in very good agreement with the observed data. Only for a negative z-vertex the y-resolution of the simulation does not compare so well to the spectrometer data. The vertex resolution of the LW at $z = 0$ cm is 0.10 cm in x and 0.11 cm in y.

4.5 Conclusion and outlook

The installation and commissioning of the Lambda Wheels in the year 2002/2003 has led to a successful - albeit brief - period of data taking. As shown the detector and its components fulfill the scheduled requirements and are since then included as a standard component of the HERMES spectrometer. As demonstrated the tracking performs well and the multiplicity of the device can be kept low. For the present data an average

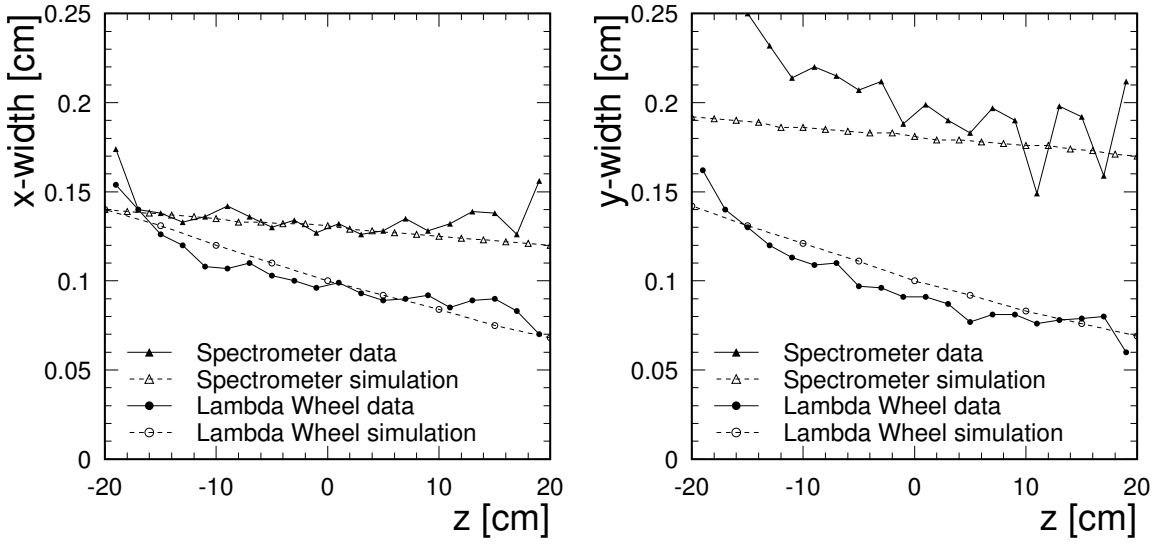

Figure 4.22: Vertex resolution in x (left) and y (right) for the LW and HRC tracks. For comparison, the results of a simulation are shown.

number of tracks of 3.1 per event for the entire LW system is found. Additionally, it is possible to align the detector with respect to the HERMES frame with high precision. Alignment parameters have been determined. It has been shown that the efficiency for a module can exceed 92 %. The angular resolution for the complete detector is 3 mrad on average. Finally a vertex resolution at $z = 0$ cm of 0.1 cm has been determined.

HERA had a shutdown from April until September 2003 in which the LW has been upgraded with a protection against the fringe fields of the target magnet. In addition a flash light has been installed which improves the start up time of the electronics. During the following period of data taking the LW has been operated successfully, which led to the collection of high statistics data. As can be seen in Fig. 4.5 a Λ^0 hyperon peak could be reconstructed on the basis of this data. In this measurement the pion is detected by the LW, while the proton is reconstructed with the spectrometer. The position of the Λ^0 peak corresponds to the PDG-value and has a width of 10 MeV.

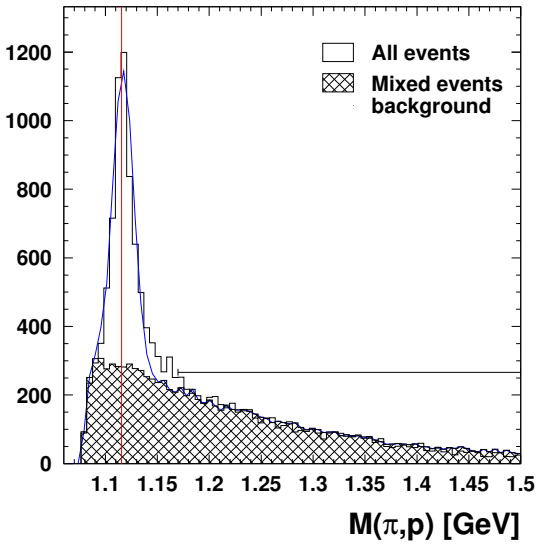

Figure 4.23: Invariant mass plot for a Λ^0 hyperon where the π has been reconstructed by the LW. These data are discussed and the plot is taken from Ref. [42].

Chapter 5

Beam Loss Monitor

In this chapter the Beam Loss Monitor (BLM) that was installed in 2002 in the HERMES experiment is described in detail. The purpose of the monitor is to protect radiation sensitive detector components such as the Lambda Wheels, the Recoil Detector and the target cell against accidental beam losses (see also Ref. [79]). The sensors of the monitor consist of ionization chambers (see Ref. [33]). It triggers the fast ($\approx$ 300 μs rise time) HERA kicker magnet installed in the west side of the accelerator in order to dump the lepton beam. The location of the BLM inside the HERMES experiment is illustrated in Fig. 5.1.

A sudden and large increase in the radiation level near the experiment is an useful indication of beam instabilities which may lead to a loss of the beam. The amount of damage caused by these accidents can be greatly reduced by removing the beam in a controlled manner out of the machine. The trigger system has to be fast and reliable to prevent accidental beam dumps. Ionization chambers are well known devices to measure radiation. They are robust and easy to maintain and hence have been selected for this project. In addition fast trigger electronics and signal transfer based on fiber optics has been chosen.

In the following sections the detector is described. The ionization chambers are described in section 5.1. The electronics of the system is explained in section 5.2. After that, the tests and the calibration of the detector are described in section 5.3. Then, the different kinds of events which have been observed are discussed in section 5.4. Finally, the chapter is concluded with an outlook in section 5.5.

5.1 Radiation detector

The radiation detection system consists of ionization chambers. There are two sets each consisting of three active and one dummy chamber(s). The sets are located left and right of the beam pipe. The first chamber is at a distance of about 6 cm from the beam pipe. The dummy chamber is on both sides the one farthest away from the beam. The detector is outside of the HERMES acceptance in the gap between the upper and lower half of the

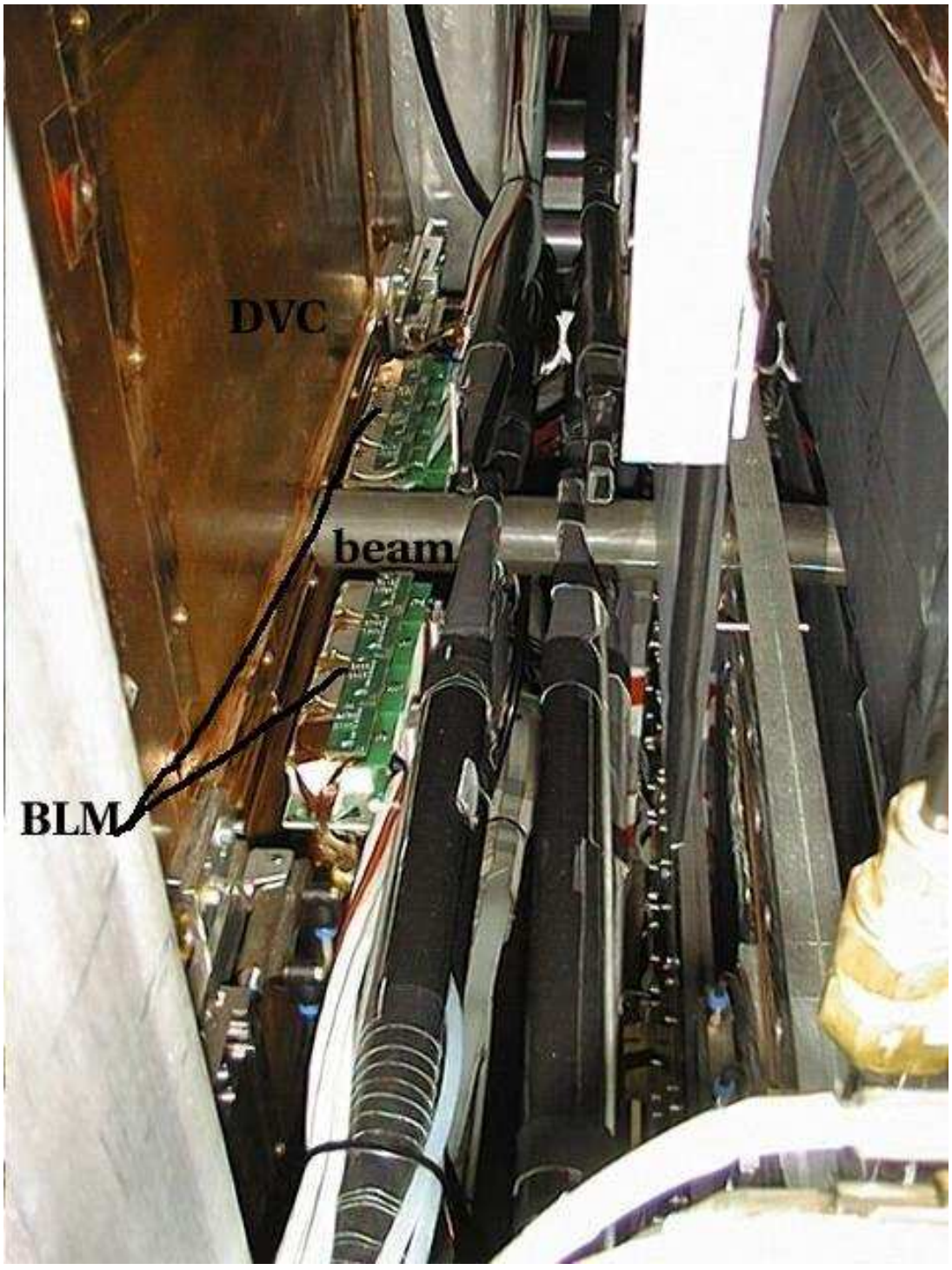

Figure 5.1: Photograph of the BLM taken inside the experiment. On the left side the exit foil of the DVC can be seen. In the middle of the picture from left to right a part of the beam pipe is visible. The BLM is located left and right of the beam pipe just before a scintillator. The front-end electronics of the BLM is mounted on top of the detectors.

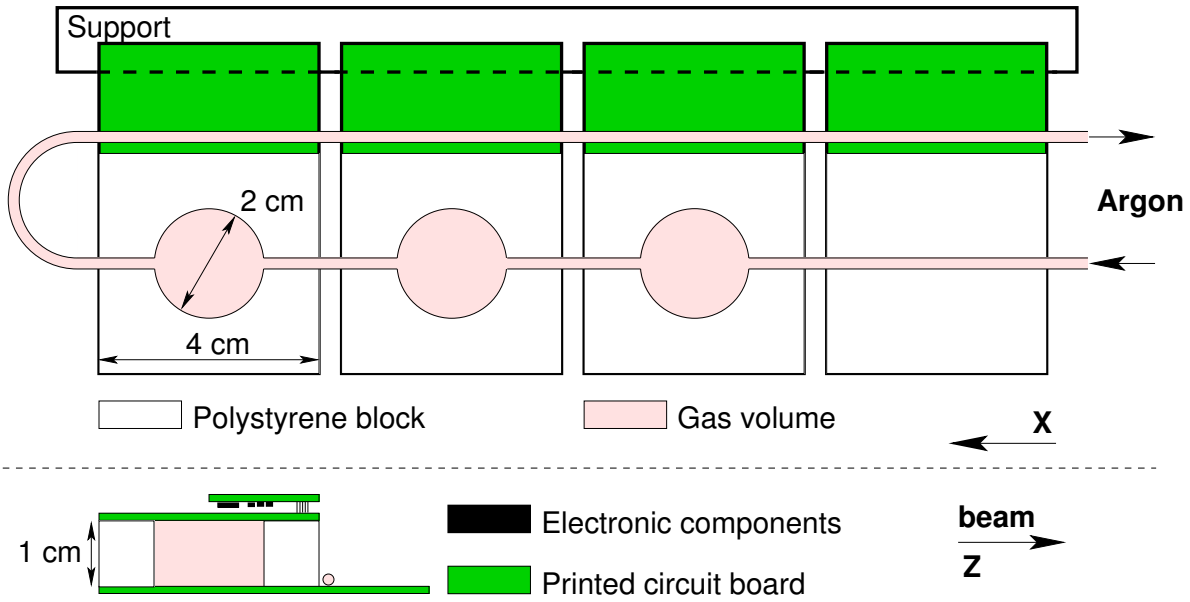

Figure 5.2: Schematic picture of one half of the BLM detector system. The upper picture is a top view of the three active and one dummy chamber(s). The bottom drawing shows a cross section of one chamber from the side.

spectrometer directly behind the DVCs (see Fig. 5.1). The BLM detectors are mounted on the support frame of nearby trigger scintillators.

A schematic drawing of one half of the system is presented in Fig. 5.2. The cylindrical gas volume is cut out of a $4 \times 4 \times 1.3$ cm^3 polystyrene block. The diameter of the cavity is 2 cm. All chambers share a common gas line. Argon gas is used in the BLM and flushed through the detector at a rate of 1.5 l/h. The chambers are closed on top and bottom with a printed circuit board which carries the electrodes. On one side of the detector the high voltage is supplied, which is again common to all chambers. On the other side the electrode is used as the read-out cathode. Every chamber has its own read-out line. The front-end electronics are placed on top of the chambers. These include a pre-amplifier and a line driver which feeds the signal to the receiving electronics in the electronic trailer. The front-end electronics is not radiation hard but can easily be replaced during a maintenance day of the accelerator.

5.2 Electronics and trigger

The BLM system comprises eight electronic channels, one for each chamber (see Fig. 5.3). The signals are read from the front-end electronics placed on top of the detectors. The front-end electronics consist of a pre-amplifier with a time constant of 5 μs and a line driver which sends the signals over a distance of 30 m to the electronic trailer (ET).

A two unit wide custom made NIM module houses the BLM trigger electronics. The signals are received and split up into two lines. One line is connected to an ADC which is

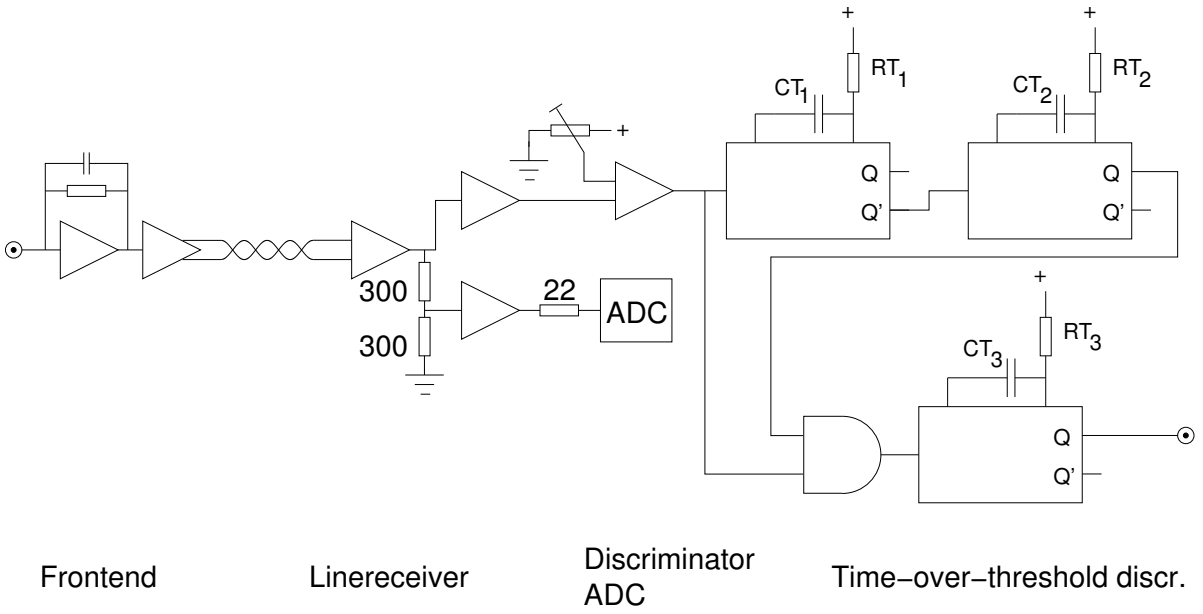

Figure 5.3: Block-diagram of the BLM electronics. The path of the signal goes from left to right. The front-end electronics on the far left, which are located on top of the chambers, amplifies the signal and sends it via a cable to the line receivers. After that, the signal is split. One line goes into the ADC and the other is fed into a discriminator. From the discriminator the signal goes to the time-over-threshold discriminator.

located on a PCI card in a LINUX computer. The ADC digitizes the input with 16 bits resolution and a frequency of 1.3 MHz. The values are stored in an internal buffer. Upon a trigger they can be written to a file. In this case data within a window of 47.5 ms before to 50 ms after a trigger are being stored in the file. The other signal line goes to the trigger electronics. First the signals are discriminated against an adjustable threshold. After that the signal is fed into a time-over-threshold discriminator realized by monostable multi-vibrators. If the duration of the signal is above an adjustable threshold a NIM-pulse is generated and used as a trigger signal. The time the signal has to be above the threshold can be adjusted between 1 and 10 μs.

A trigger signal can be generated from both halves of the BLM. In each half a majority of two out of three active chambers must be over threshold. The dummy chamber serves as a veto. As there are high radiation levels during injection and tuning of the lepton beam, the BLM trigger is vetoed during these phases. The radiation levels during injections are, however, analyzed and can thus be used to monitor the injections and the total dose received by the detector in a given period of time.

Upon a positive trigger decision the trigger is sent via two paths. The first one is realized with BNC copper cables. The logic in this path is realized with relays, this is the so-called slow path which serves as a backup and for administrative purposes. Additionally, the trigger is brought to the control room to indicate to the shift crew that a trigger has occurred. The second connection is realized with optical fibers. The electronic signal is converted to a light signal with so-called transceivers. These transceivers send a signal

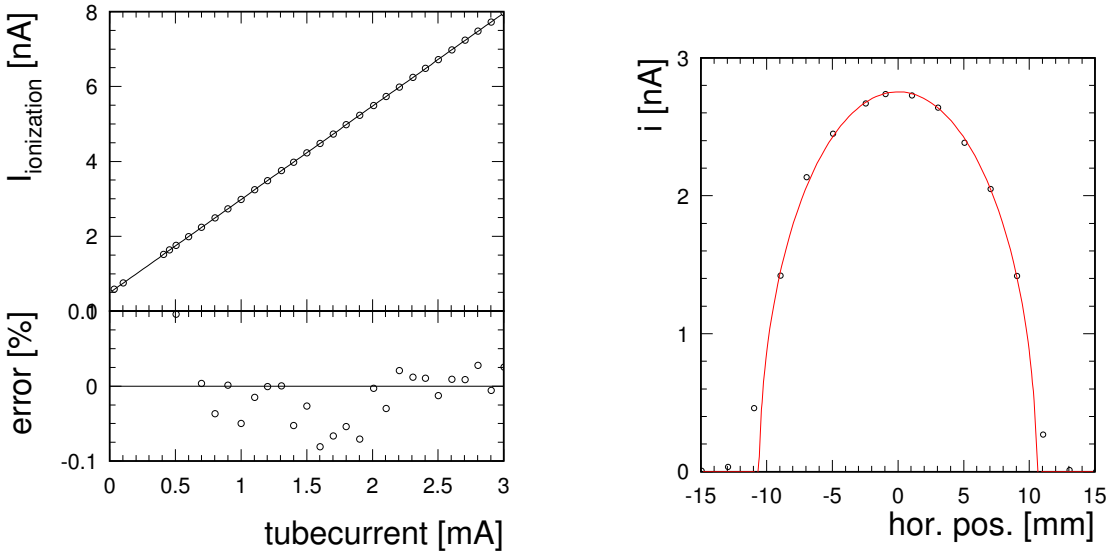

Figure 5.4: The left plot demonstrates the linearity of the BLM electronics by showing the measured ionization current as a function of the tube current of an X-ray source. The right plot shows a horizontal X-ray scan of the active detector volume. The measured data agree well with the line calculated using the geometrical shape of the chamber.

and receive the return signal from the device on the other end. This has been done to be able to check the integrity of the light path. The light has a wave length of 1.3 μm and is guided via 50/125 multi-mode light fibers. The signal has to go to the opposite side of the HERA ring to the West hall which is about 4 km away. The light is transmitted in the state where there is no trigger signal, upon a trigger the new state is represented by switching the light off. The delay between a trigger signal and the beam dump of the kicker magnet has been measured to be 374 μs dominated by the rise time of the kicker. Therefore, the BLM is the fastest beam dump trigger at HERA.

5.3 Test and calibration

The detector system has been tested and calibrated using an X-ray source. These tests have been carried out with a Philips PW2773/00 tube at the University of Mons-Hainaut, Belgium (see Ref. [34]). Here the results are summarized as it provides a characterization of the detector features.

At first the saturation voltage of the chambers has been determined. It was found that the current in the chambers saturates at an applied voltage in the range of $50-100$ Volt. The actual operational voltage in the experiment has been set well above the saturation level namely at 250 Volt.

The amount of ionizing radiation produced by the X-ray source depends on the applied tube current. The ionization current of the chambers has been measured as a function

of the tube current. The result is shown on the left side in Fig. 5.4. As can be seen the ionization current depends linearly on the amount of radiation produced by the source. Furthermore an absolute calibration constant for the chambers has been determined. With knowledge of the tube and the ionization current, and the mass of the Argon and the average energy required to produce an electron-ion pair, the dose rate dD/dt measured with the chamber has been determined to follow

$$\frac{dD}{dt} = C \cdot i \tag{5.1}$$

with the calibration constant $C = 4.27\ \frac{\mathrm{Gy}}{s\mu\mathrm{A}}$ and the ionization current i measured in μA. This result has been confirmed by measurements performed by irradiating dosimeters (TLDs).

Furthermore the sensitive volume of the chambers has been scanned with a focused X-ray beam in the horizontal and vertical direction with a constant tube current. The ionization current has then been measured with respect to the position. An example of such a horizontal scan is presented in the right panel of Fig. 5.4. The cylindrical shape of the active gas volume is well described as represented by the solid line.

Dose rate. Although the BLM was designed as a fast and reliable trigger device only, it was possible to calibrate the detector for measuring dose rates as well. As the detector is not permanently reading out the radiation levels but only upon a trigger, it cannot be used as a dosimeter. Still an integrated value of the dose deposited during the events which caused a trigger can be given. Since a data file is recorded during injection of the lepton accelerator it is possible to analyze those events. In Fig. 5.5 a typical plot of the dose collected in one week is shown. The six plots show the dose accumulated during electron beam injections for each ionization chamber. The left side of the panel shows one side of the BLM, the right side the other. The top plot is in both cases the chamber closest to the beam. As expected this chamber has observed the highest radiation level.

5.4 Various observed triggers

The BLM is recording high radiation events since the fall of 2001. Since the summer of 2002 the trigger signal is connected to the dump kicker. The intervening period was used to analyze the accumulated data to verify that the detector is operating reliably. During that time many different events were recorded and their cause and time dependence were analyzed.

The trigger conditions can be classified according to the radiation dose that was measured and the time duration of the event. There are three main classes of events which were observed by the BLM. The first class of events are the ones with very short duration. These events have a time span of the order of a couple beam revolutions (where one revolution lasts 21.13 μs). This is considerably shorter than the reaction time of the kicker magnet. The time dependence of such an event is illustrated in the left panel of

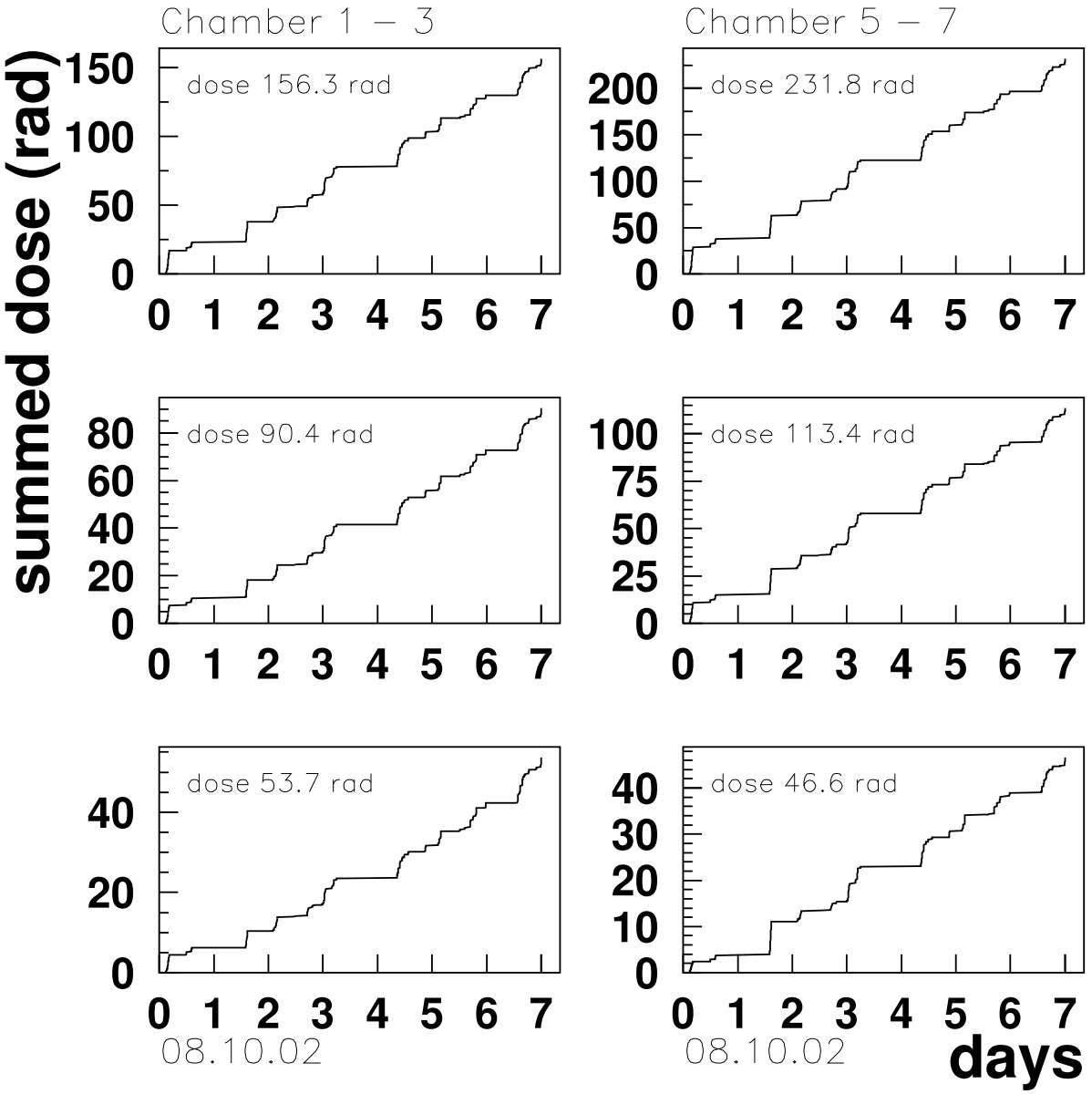

Figure 5.5: Plot of the does accumulated by the BLM during one week of HERA operations for each one of the six active chambers.

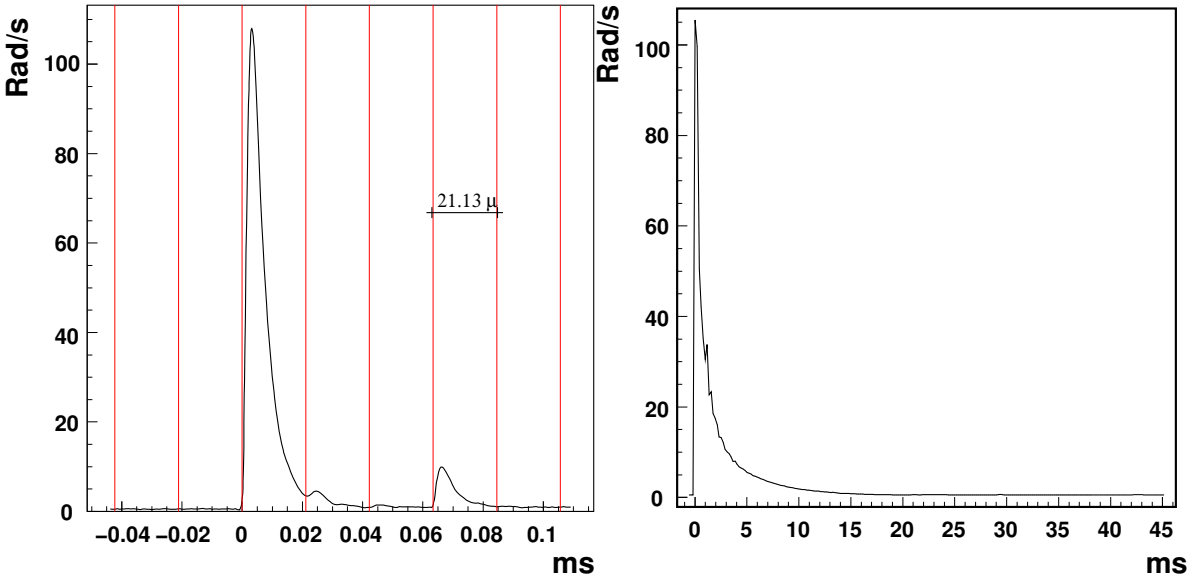

Figure 5.6: On the left panel a signal from the BLM is shown where most of the beam is lost in less than one revolution. The revolutions are indicated by the vertical lines. On the right hand side a typical injection signal is shown with high radiation levels lasting over a couple of milliseconds and a radiation tail with a time constant of 5 ms.

Fig. 5.6. The fast occurring events can be monitored but the system is not fast enough to react and can therefore not prevent radiation damage. These are, for example, equipment malfunctions that lead to a direct loss of the beam.

The second class of events has sufficiently high radiation doses and time durations long enough such that the BLM can react. In most cases a disturbance of the beam builds up slowly and is accompanied with increasing radiation levels until the beam cannot be controlled anymore and gets lost. Typical events in this class last a few milliseconds. They can be characterized by high radiation levels which, after a beam loss, decay with a time constant of about 3 ms. This class of events is of main interest for the BLM as the time is long enough to react and therefore a large amount of radiation can be avoided by dumping the beam in a controlled way.

The last class of events has a much longer duration but causes a low dose rate. These kind of events can last for a very long time. The cause can be equipment malfunctions which do not lead to a beam loss but to instabilities that cause radiation. Still, the low radiation rate integrated over a long time can result in a high integrated dose. An example of these kind of events is shown in Fig. 5.7. Here malfunctioning electronic equipment caused radiation measured by the BLM with a moderate dose rate. The event lasted for several minutes until the beam was lost. This example is from the time when the trigger was not yet connected to the dump kicker. It can be seen that the dose rate has a time dependence with a frequency of 50 Hz probably caused by equipment with one of three electrical phases missing. In addition the revolution time of the beam can be seen on the right plot. The integration time of the pre-amplifier is 5 μs and therefore not able to resolve single bunches. In this case, though, only the first five bunches were filled with

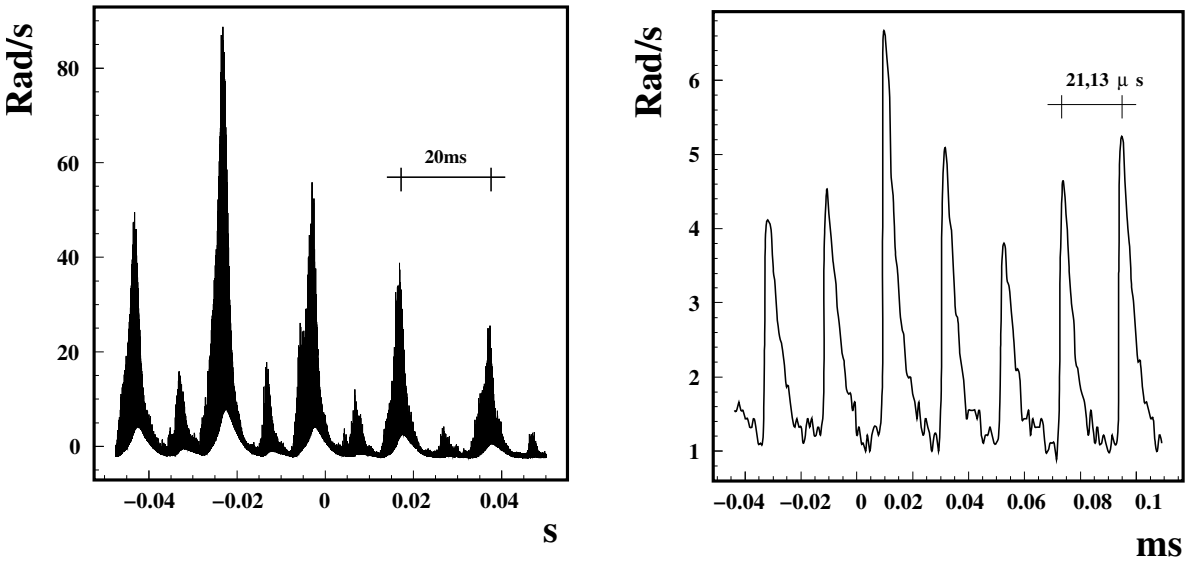

Figure 5.7: A so-called 50 Hz problem causing high radiation levels at the position of the BLM. Shown on the left panel is the dose rate versus time for a period of 100 ms. Indicated is the 20 ms time structure of these kind of events. On the right panel the same plot is shown, but now at a reduced time scale covering only 100 μs. The bunch structure of the beam is visible with a 21.13 μs beam revolution time.

positrons and the structure became visible.

Very low radiation levels cannot be detected by the BLM, since the current does not reach the threshold in that case. However, even for very low radiation levels the integrated dose can become high if it lasts long enough. To prevent high radiation doses from this class of events it was proposed to have an additional trigger with an integration time constant in the order of seconds.

Injections of the lepton beam have similar characteristics as class one events. These triggers are recorded but a veto signal prevents the BLM to dump the beam. Such an event is illustrated in Fig. 5.6 on the right panel. Injections of the proton beam can be monitored by the BLM as well. In addition, these events have a very short duration and a comparably low dose. The proton beam is in the same plane as the lepton beam and not too far away from the detection chambers. Using the time-over threshold trigger circuit it was possible to suppress signals of very short duration like proton injections as well.

5.5 Conclusion and outlook

The BLM was installed in 2001, and in June 2002 it was connected to the dump magnet. Since then it has been working reliably. It is the fastest beam dump currently installed at HERA. While beam dumps are occasionally triggered by the BLM, and hence it has protected the experiments, it has no detrimental effects on the operation of the accelerator.

The BLM system has been upgraded with an integrating circuit in 2004. The trigger has been designed and installed. It uses a second integrating circuit with a longer time constant of about 1 second. With that long integration time it is possible to trigger on events with very low intensity and long time duration periods.

Chapter 6

Hyperons production

This chapter describes an analysis of HERMES data. The focus of the present analysis is on production yields of hyperons. From these yields the hyperon production cross sections for HERMES kinematics are evaluated. The extrapolation of the yields in the HERMES acceptance to 4π is done utilizing Monte Carlo predictions. From these cross sections the dilution of the Λ^0 polarization measurements due to decays of heavier hyperons is estimated.

6.1 Introduction

In the following sections the analysis of various hyperons produced in quasi-real photoproduction at HERMES is discussed. The analysis includes only hyperons with a final state multiplicity of three tracks. This requirement enables one to reconstruct most hyperons except for the excited cascades. In the next section, the selection of the data is discussed. The starting point of the actual particle search is the reconstruction of the Λ^0 hyperon which is described in section 6.3. Since the Λ^0 is the lightest hyperon, it is included in most of the decay chains of heavier hyperons. The following section (6.4) focuses on these heavier hyperons. The first hyperons heavier than the Λ^0 are the Σ's. The neutral Σ^0 decays into a Λ^0 and a γ and is expected to contribute significantly to the Λ^0 hyperons detected in the HERMES experiment. The Σ^+ decays via a proton and a neutral pion (π^0). Since the production cross sections of the Σ's are expected to be very similar, the Σ^+ yields serve as a consistency check for the Σ^0. The Σ^- cannot be reconstructed as it has a neutron in the final state. The cascades (Ξ) and the excited sigmas (Σ^*) decay all via a Λ^0 and a pion. Hyperons with the same charge like the Ξ^- and the Σ^{*-} appear in the same invariant mass spectrum. The last and most heavy hyperon is the Ω^-. Its decay branch via Λ^0 and a negative kaon is discussed in Sec. 6.4.4, while the production cross sections of the observed hyperons are presented in Sec. 6.4.5. In section 6.5 the cross section predictions from the MC model are compared to the data. From this comparison information is derived on the purity of Λ^0 production at HERMES.

	spin	iso	mass [MeV/c^2]	quark	$c\tau$ [cm]	width [MeV]	decay	BR [%]
Λ^0	1/2	0	1115.683	uds	7.89		p π^-	63.9
Σ^+	1/2	1	1189.37	uus	2.404		p π^0	51.6
Σ^0	1/2	1	1192.642	uds	22.2E-7		Λ^0 γ	100
Σ^-	1/2	1	1197.449	dds	4.434		n + X	98.8
Ξ^0	1/2	1/2	1314.83	uss	8.71		Λ^0 π^0	98.5
Ξ^-	1/2	1/2	1321.31	dss	4.91		Λ^0 π^-	98.9
Σ^{*+}	3/2	1	1382.8	uus		35.8	Λ^0 π^+	88
Σ^{*0}	3/2	1	1383.7	uds		36	Λ^0 π^0	88
Σ^{*-}	3/2	1	1387.2	dds		39.4	Λ^0 π^-	88
Ξ^{*0}	3/2	1/2	1531.8	uss		9.1	Ξ π	100
Ξ^{*-}	3/2	1/2	1535.0	dss		9.9	Ξ π	100
Ω^-	3/2	0	1672.45	sss	2.461		Λ^0 K^-	67.8

Table 6.1: In this table a collection of baryons containing strange quarks are listed together with properties relevant for this analysis. The values are taken from Ref. [67].

Table 6.1 lists the hyperons of interest with their most important decay properties. The table displays the spin, iso-spin, mass, quark content, decay length or width, and the dominant decay channel with its branching ratio. Several hyperons with four particle final states are listed as well for completeness, but are not subject of this analysis.

6.2 Data selection

The data set presented in this thesis includes three years of data taking. These years are 1998, 1999 and 2000. As mentioned earlier, from 1998 on the RICH detector was used to distinguish between different hadrons. In 1999 and 2000 the accelerator was operated with positrons, while in 1998 the beam particles were electrons. There are two polarization modes for the longitudinal target. First, the vector polarization (VDPS) and secondly the tensor polarization (RDPS) mode. After the year 2000 the target polarization was changed from longitudinal to transverse polarization.

Only polarized deuterium data were used for this analysis. The reason for that is the lower calorimeter threshold used during this type of data taking which enhances the probability of observing more tracks in the one event. It has been shown that the data sample of unpolarized high density hydrogen, which has a higher calorimeter threshold, includes significantly fewer high multiplicity events.

6.2.1 Data quality

The data selection on burst level was done with the use of the polarized burst lists. These lists provide a bit pattern which can be used to differentiate data regarding the

data quality. The lists are provided by the Data Quality group which does a sophisticated analysis of the data quality of every burst. The analysis takes into account the actual states and settings of the detector components during each burst. (For the definition of the bits for each year see Ref. [48] and App. C.) The user can rely on this list for the selection of the bursts without studying in great detail the quality of each data sample.

Quality	bit(s)	explanation
Dead time	2, 30	select reasonable dead time of less than 50 %
Burst length	3	select burst length between $0 - 11$ s
Beam current	4	select beam current between $5 - 50$ mA
UDST	6	select good UDST records
	7	reject first burst in a run
PID	8	reject bursts with no PID information
Logbook	9	rejected on basis of logbook analysis
Experiment	10-15	select any experiment mode
Detectors	17-22,31	check for detector data quality and HV
Target	0,16,23-29	not considered

Table 6.2: Data Quality requirements for polarized burst lists. (A more detailed explanation is given in the text.)

The most important data quality requirements are summarized in table 6.2. The data are accepted on burst level when the following criteria are fulfilled. The first requirement selects bursts with a reasonable dead time of the DAQ system. That means that the percentage of rejected triggers remains below a limit of 50 %. The second requirement discards bursts with a length below 0 and above 11 s. The third makes sure that the beam current was in the range of 5 to 50 mA. Too low beam currents have a very low luminosity which leads to an increased error on the luminosity measurement. The next requirement ensures that there were no problems during the production of the data in UDST format. Furthermore, it rejects the first burst in a run. Additionally, the next requirement expressed by bit 7 discards bursts where the calculation of the PID values encountered problems. The analysis of the logbook also ends up in the data quality bit pattern (bit 9). In this particular analysis no conditions were imposed on the polarization mode. High density runs were discarded from the analysis. A check on all high voltage settings was performed to reject bursts where chambers tripped or were switched off. If the DAQ system indicates that there are problems during data taking this is flagged in the data flow and the bursts concerned can be discarded. Finally, all detector quality bits for detectors like the RICH, TRD and the calorimeter are checked. All values and bits are given in detail in Appendix C

The luminosity calculation is also done on the burst level (see Sec. 3.4). It takes into account the measured rate in the luminosity monitor, the burst length and the dead time correction. In the following sections the conditions imposed on the data at event and track level are discussed.

6.2.2 Track and multiplicity requirements

For every event from an accepted burst the reconstructed tracks are checked on different levels. First the complete collection of tracks is split in a hadron and a lepton set. This is done by a requirement on the PID value as defined in Sec. 3.3.2. A flux factor correction is not applied to the PID value as this analysis does not require a prefect hadron lepton separation. All tracks with a PID value > 0 are regarded as leptons. All tracks with a PID < 0 and tracks that have no PID value, like the short tracks (see Sec. 3.3.1), are considered to be hadrons. A minimum momentum of 0.5 GeV is required to reduce background. Furthermore, a so-called fiducial volume requirement is imposed. This requirement ensures that the tracks actually reach the sensitive volume of all detectors and do not hit any other material on their way through the spectrometer. This requirement is of importance as for example the field clamps of the magnet are close to the acceptance. Additionally, all short tracks are checked for so-called *ghost tracks*. These ghost tracks appear in the analysis as tracks which differ only slightly in their kinematics and are caused by the same physical particle. If both tracks would be used, artifacts can appear in the invariant mass spectrum.

A total sum of the momentum associated with each track in the event is calculated. To avoid multiple events in the same bunch it is required that this sum is below 32 GeV.

The DIS kinematical variables (see Sec. 2.2.2) are calculated if a lepton has been found in the event. After imposing the so-called DIS requirements on these variables, the number of DIS leptons is counted for reference. These DIS requirements are summarized below:

$$\begin{array}{ccccccc} 1 & < & Q^2 & < & 24 & & \text{(GeV)} \\ 4 & < & W^2 & & & & \text{(GeV)} \\ 0.02 & < & x & < & 0.95 & & \\ 0.07 & < & y & < & 0.85 & & \end{array}$$

For these leptons further requirements are imposed. A minimum energy deposited in the calorimeter of 3.5 GeV is required. Additionally, there are requirements on the vertex of the lepton. The vertex has to be inside the target, that is that the absolute value of the z-position needs to be smaller than 18 cm and the distance of closest approach to the beam needs to be less than 0.75 cm.

6.2.3 Statistics

The amount of data which was used in this analysis, with the requirements explained above, is summarized in table 6.3. For the analyzed data sets several numbers are displayed. The first column lists the year of data taking. Next to the year is the polarization mode of the target gas. The third column states the number of analyzed runs. The fourth column provides a count of the number of good bursts, also given as a percentage between brackets. In the fifth column the number of events analyzed is given in millions. Then, in the next column the corresponding number of DIS events is given. The last column specifies the accumulated luminosity in pb^{-1} together with the uncertainty on that number.

year	mode	runs	bursts [k] ([%])	events [M]	DIS [M]	luminosity [pb^{-1}]
1998	VDPS	6812	417 (93)	51.2	1.46	30.2 ± 1.1
1999	VDPS	11342	439 (93)	58.0	1.84	40.3 ± 1.4
2000	RDPS	6122	180 (95)	57.4	2.22	45.9 ± 1.7
2000	VDPS	19365	630 (95)	177.9	6.93	143.7 ± 5.2
total		43641	1666 (94)	344.6	12.45	260.1 ± 5.8

Table 6.3: The total statistics of the analyzed data set. The first column gives the year, the second the polarization mode, the third the number of runs, the fourth the number of burst, the sixth the number of events, the seventh the number of DIS events and the last the corresponding integrated luminosity. Further explanations are given in the text.

In the last row the total statistics of all four data sets is given.

Having presented the requirements on burst and track level the following sections deal with the analysis of the hyperons derived from these data. The analysis is separated into two parts. First the analysis of the Λ^0 hyperons is discussed, and second the analysis of all observed heavier hyperons is addressed.

6.3 Lambda analysis

The first hyperon which is analyzed is the Λ^0 hyperon. As mentioned before, it is the lightest hyperon and decays predominantly into two particles. The two most important decay channels of the Λ^0 are given in table 6.4. Only decay channel I is considered as a neutron cannot be detected by the HERMES experiment.

channel	decay chain	branching ration [%]
I	$\Lambda^0 \rightarrow p^+ + \pi^-$	63.9
II	$\Lambda^0 \rightarrow n^0 + \pi^0$	35.8

Table 6.4: The two most important decay channels of the Λ^0 hyperon.The first one (I) is the channel which was studied in this analysis. The second one cannot be observed at HERMES because a neutron can not be detected.

For the reconstruction of a Λ^0 hyperon all combinations of positive and negative hadrons are used. The proton has to be identified by the RICH detector. The pion can either be identified by the RICH, or it can be a short track.

6.3.1 Decay vertex reconstruction

For the study of resonances the reconstruction of a decay vertex is very important. The decay vertex is calculated from the track parameters of the two daughter particles. These two tracks are supposed to come from one point, that is the decay point of the mother

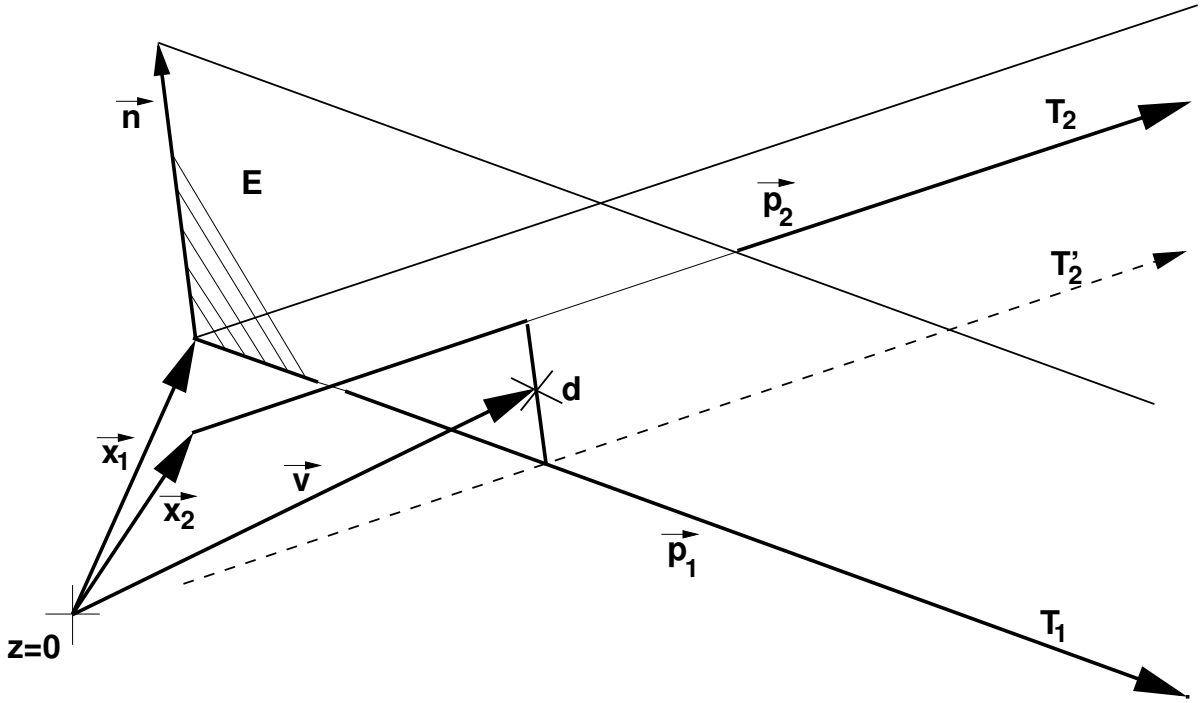

Figure 6.1: Schematic view of the method to calculate the DCA (d) of two straight tracks T_1 and T_2. Shown are the tracks defined by their parameters $\vec{x}$ and $\vec{p}$, the plane E, the normal $\vec{n}$ to the two tracks and the origin of the coordinate system denoted by $z = 0$. Additionally, the vertex vector $\vec{v}$, the vector from the origin to the mid point between the two line, is displayed.

particle. Because of the finite resolution this point is spread in space. The calculated distance between the two tracks at the point where they come closest, is the so-called *Distance of Closest Approach* (DCA). It is an important variable, on which requirements can be imposed to reduce the background of falsely combined tracks.

The method to calculate the vertex for two tracks is depicted in the schematic drawing shown in Fig. 6.1. The basic idea is as follows. The tracks T_n are defined as straight lines with $\vec{x_n}$ a point on the track and $\vec{p_n}$ the direction vector

$$T_n : \qquad \vec{x_n} + \alpha \cdot \vec{p_n}, \tag{6.1}$$

where α is a parameter. The normal vector $\vec{n}$ to the two tracks is defined by the vector product of the two direction vectors

$$\vec{n} = \frac{\vec{p_1} \times \vec{p_2}}{|\vec{p_1} \times \vec{p_2}|}. \tag{6.2}$$

The method starts with defining a plane which includes the first track T1 and the normal vector. The fixed point of the plane E is the position $\vec{x_1}$ of the first track. The distance between the two tracks is the difference of the two position vectors projected on the normal vector

$$d = \vec{n} \cdot (\vec{x_1} - \vec{x_2}). \tag{6.3}$$

Then the second track is shifted by this distance d into the plane E and the intersection of these two tracks is calculated by solving the following equations for α, β and d

$$T_1 : \quad \vec{y} = \vec{x_1} + \alpha \cdot \vec{p_1} \tag{6.4}$$

$$T_2' : \quad \vec{y} = \vec{x_2} - d \cdot \vec{n} + \beta \cdot \vec{p_2} \tag{6.5}$$

The result is a point on both tracks identified by the numerical values of α and β. The vertex is calculated as halfway between the two tracks at the point of closest approach

$$\vec{v} = \vec{x_1} + \alpha_0 \cdot \vec{p_1} + \frac{1}{2} d \cdot \vec{n}. \tag{6.6}$$

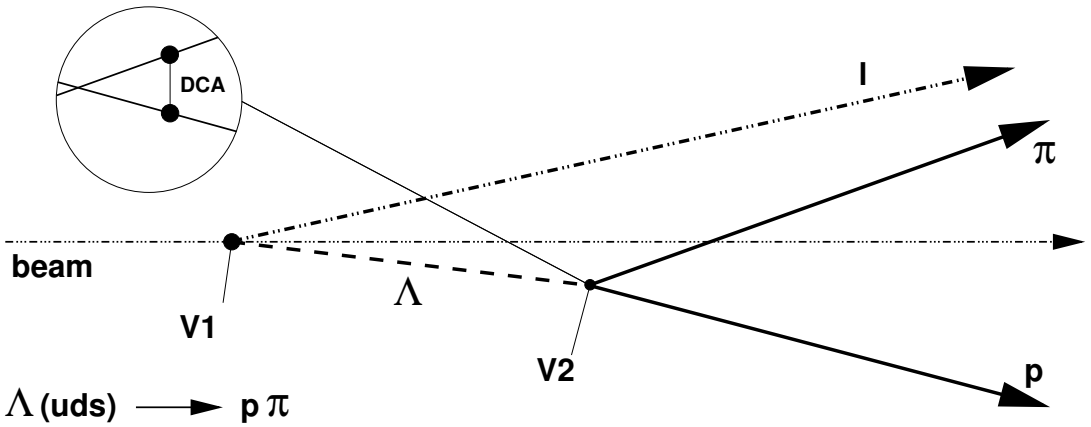

Figure 6.2: Schematic picture of the Λ^0 decay. Shown are the two relevant proton and pion tracks, the decay vertex V2 and the production vertex V1 on the beam line.

The general determination of a decay and production vertex is explained using the example of Λ^0 reconstruction. The Λ^0 production and decay is sketched in Fig. 6.2. The decay vertex is calculated from the track parameters of the proton and the pion. In this calculation the DCA of the two tracks is determined and required to be less than a given value. As can be seen from an analysis of MC events (see Fig 6.3 top), this requirement can be chosen between $1.6 - 2.0$ cm. In the upper left plot the histogram with all simulated Λ^0 candidates has been fitted with two exponentials. The first part and the second part have been fitted separately. For low values of DCA it can be expected that both signal and background are high. For the tail the opposite is true and the background is larger. The intersection point of these two exponentials is expected to indicate the best value for the signal to background ratio. From there on the background contribution is larger than the signal contribution. One can see from the top right plot that this does not completely apply and that there is an offset present. In the right plot the signal and background distributions have been fitted separately.

In the bottom panel of the same figure a similar analysis of the measured data is shown. The value for the crossing of the two exponentials is, with 2.2 cm, slightly higher than in the MC simulation. This is expected as the spatial resolution is overestimated in the MC. On the right side of this figure a plot of the significance is shown. For different

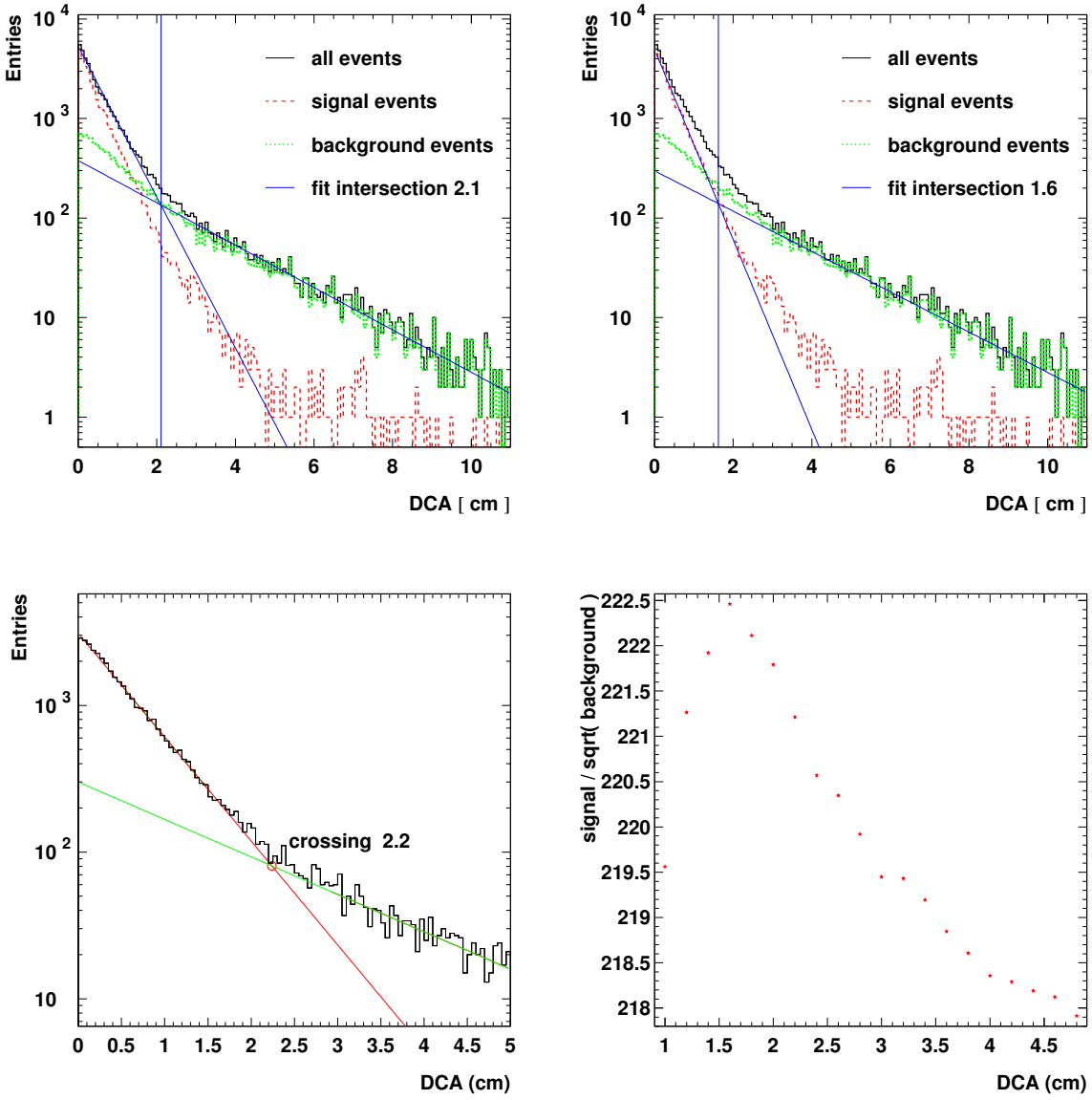

Figure 6.3: Results of MC simulations used to estimate the best value for the DCA requirement. In the top left plot the total MC distribution is fitted and in the top right plot the signal and background distribution have been fitted separately. The first exponential is fitted to the beginning of the distribution and the second one to the tail. Left plot: the same fit as in the top left plot applied to the data. In the right bottom plot the naive significance is shown versus the DCA value.

values of DCA the invariant mass spectra are fitted and the content of the peak and the background is calculated. From these values a significance has been estimated by:

$$\sigma = \text{signal}/\sqrt{\text{background}}. \tag{6.7}$$

The maximum value at 1.6 cm compares nicely to the MC results. As this requirement is the most important one to select Λ^0 hyperons it has been decided to use a rather strict requirement. A maximum value of 1.5 cm has been chosen in the final analysis.

The production vertex of the Λ^0 is also of interest for the analysis. With the knowledge of the production vertex two requirements can be imposed. The first one is a decay length requirement as the Λ^0 is a particle with a relatively long lifetime ($c\tau = 7.89$ cm). The second one is a so-called *c*ollinearity requirement where it is required that the derived Λ^0 momentum vector and the vector joining the production and decay vertex are in line with each other. Both of these requirements can be used to reduce the background of falsely reconstructed Λ^0 hyperons.

An alternative possibility to calculate the production vertex is based on the assumption that the Λ^0 is produced in the interaction of the scattered lepton with the target. If the scattered lepton is detected in additional to the Λ^0, one can assume that the production vertex is the vertex of the lepton with the beam. If, on the other hand, the lepton is not present in the event, the production vertex is estimated by evaluating a common vertex inside the target from all tracks available in the event. However, this could not be used as the track multiplicity is low, since the two tracks forming the Λ^0 have to be excluded and therefore very few tracks remain. Instead, a different approach is used which is similar to the first one which assumes that the Λ^0 is produced in the target on the beam line, even if the scattered lepton is not observed. Like the reconstruction of the decay vertex, the production vertex is calculated by intersecting two vectors, namely the Λ^0 vector and the beam line.

6.3.2 Decay length

The Λ^0 hyperon decays via a weak decay and has a life time on the order of $\tau = 10^{-10}$ s which corresponds to a decay length (DL) of 7.89 cm [67] in the rest frame of the Λ^0. In the laboratory frame the decay length is calculated like

$$DL = c\tau \cdot \beta \cdot \gamma = c\tau \cdot \frac{p_\Lambda^{\text{lab}}}{m_\Lambda}. \tag{6.8}$$

This implies that a Λ^0 has traveled a certain observable distance before it decays. By requiring that the vertices are separated, tracks from particles produced in the initial scattering are rejected from the Λ^0 search. In this analysis the distance between the z-components of the vertices is used for simplicity

$$\Delta z = \vec{v_2}_z - \vec{v_1}_z. \tag{6.9}$$

variable	minimum	maximum	unit	explanation
PID	-99.0	0.0	-	PID requirements for p and π
PA	0.0	—	-	relative energy requirement
DCA	—	1.5	cm	decay vertex distance of tracks
collinearity	-1.0	1.0	-	collinearity of lambda momentum and direction (not used)
ΔZ	-15.0	250	cm	decay length of the Λ
mass	1.08	1.18	GeV	mass range for the Λ

Table 6.5: Summary of the requirements imposed on the data to identify a Λ^0 hyperon. The variables and requirements are explained in more detail in the text.

This is a good approximation as the angle between the Λ^0 direction vector and the beam axis is small.

However, only loose limitations are imposed on Δz because of the following reasons. First, the RICH detector provides a good identification of hadrons. Thus, a wrong combination of oppositely charged hadrons is greatly suppressed. The signal of the Λ^0 hyperon in the invariant mass spectrum is clearly seen and the signal to noise ratio is very good without setting tight limits on the value of Δz. Second, the resolution of the vertices is on the order of the decay length. While the decay vertex of the Λ^0 hyperon can be reconstructed with a precision of about 1.5 cm the production vertex has greater uncertainties. Although it is not a priori known if the Λ^0 is directly coming from the beam it is traced back to the beam line. Given the already sizable uncertainty on the decay vertex the uncertainty of the production vertex is about 4.5 cm. A clear distinction between the two vertices would require the value of Δz to be a multiple of this uncertainty. On the other hand, the amount of real Λ^0 hyperons which are discarded by such a requirement increases exponentially. In addition, the requirement of long life times influences also a requirement on the momentum of the Λ^0 hyperon as higher momentum particles have a longer lifetime in the laboratory frame. Taking all the advantages and disadvantages into account it has been decided not to use the decay length requirement in favor of having higher statistics. The situation is different for the heavier hyperons like the Ξ^-, where the additional pion can be used to determine a relatively accurate production vertex of the Λ^0 hyperon, even in the absence of a scattered lepton in the event.

6.3.3 Kinematic selection criteria

As mentioned earlier the Λ^0 decays into a proton and a pion. The large difference in mass between the decay products can be exploited to define an additional requirement. It has been shown in Ref. [68], that in the decay of so-called V-events the relation between the momenta and angles of decay particles can be used to separate the signal from the background better than when only the initially measured values are used. These relations are based on applying energy and momentum conservation to the decay. Furthermore, it has been shown in Ref. [60] that there is an actual gap between the energy of the proton

and that of the pion if only Λ^0 momenta above a certain minimum value are observed in the experiment. This gap is used as a rather conservative requirement in the analysis, namely only Λ^0 hyperons are accepted where the energy of the proton is higher than the energy of the pion. This requirement is called PA in table 6.5 where in addition all other requirements are summarized.

6.3.4 Invariant mass spectrum, fits and yields

In this section the invariant mass spectra of the Λ^0 and $\bar{\Lambda}^0$ hyperons are presented. All requirements on the data have been discussed in previous sections. Here the determination of the yields is discussed in detail. The respective spectra have been fitted to determine the particle yield.

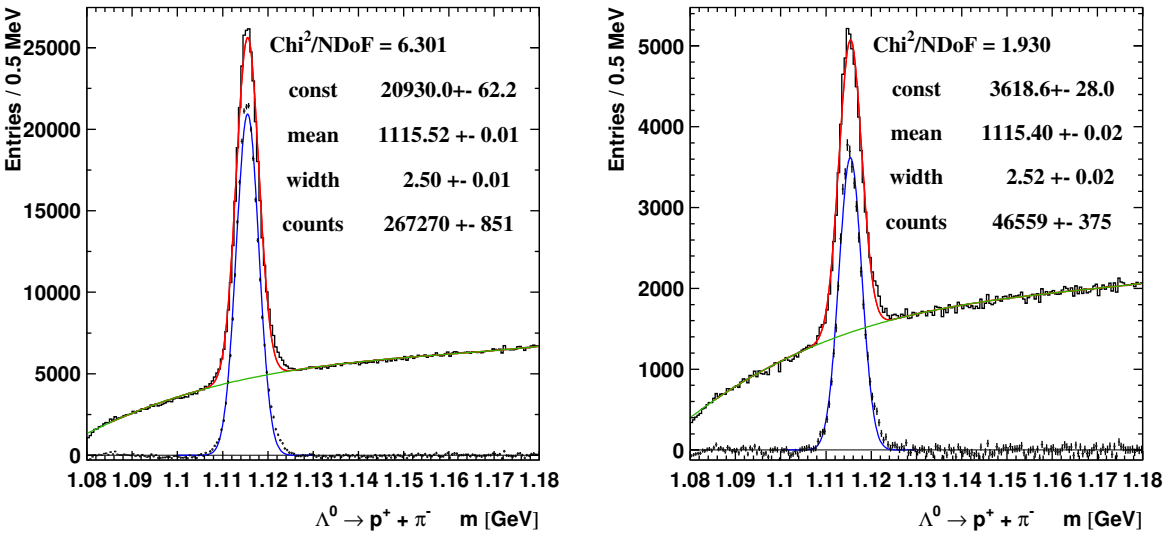

Figure 6.4: Proton-pion (Λ^0) invariant mass spectrum for all tracks. On the left side the particle and on the right side the anti-particle spectrum is shown. The peak has been fitted with a Gauss and the background with a Legendre polynomial of third degree. The fit parameters are displayed in each plot.

All combinations of tracks that fulfill the requirements are shown in figure 6.4. On the left side of the figure the Λ^0 hyperon invariant mass spectrum is shown, whereas on the right side the $\bar{\Lambda}^0$ hyperon spectrum can be seen. The lower threshold for the Λ^0 invariant mass spectrum is $m_p + m_\pi = 0.9383 + 0.1396 = 1.0779$ GeV and thus below the left boundary of 1.080 GeV of the histogram. Additionally, a fit to the whole spectrum is shown to describe the Λ^0 mass peak. For the fit the HMINUIT package, implemented in PAW, has been used to perform the fit in double precision and to determine the error matrix. The fitting function consists of two parts, one to describe the peak (Gaussian) and the other for the background. The background is described by a Legendre polynomial

of third order. They are expressed by the following formula:

$$P_n(x) = \frac{1}{2^n n!} \cdot \frac{d^n}{dx^n} \left[(x^2 - 1)^n\right] \qquad n \geq 0 \tag{6.10}$$

where n labels the order of the polynomial. The third order was found to be sufficient to describe the shape of the background. The Legendre polynomial was chosen because the different terms are orthogonal to each other in the range between $[-1, 1]$ with a weight of 1.

In order to satisfy this condition the mass x-axis has been transformed from the region of $[1.08, 1.18]$ GeV^2 to $[-1, 1]$. As the weights are not unity normality is not fulfilled. Still the fitting parameters of the polynomial are less correlated and are more controllable. Therefore, the fit is more stable and can be carried out without boundary conditions on the parameters. For the peak a Gaussian shape has been used. One can see that the Gaussian does not describe the shoulders of the peak very well. This discrepancy is also reflected in the χ^2 value. If the background is fitted alone the χ^2 value is closer to one. The reason for that is the limited acceptance of the HERMES spectrometer. The mass peak consists of different samples of protons and pions and their resolution is momentum dependent. A correction for those effects are beyond the scope of this analysis and are not needed, as the fit is only used to determine the background accurately. Other models for the shape of the peak would be two or more Gaussians to describe the distribution better. But then the width of the different Gaussians are hard to interpret.

The background function is deduced from the invariant mass spectrum, while the yield is determined by counting the entries of the resulting histogram. More details on the functions used for fitting the invariant mass spectrum are given in Appendix A.

The uncertainty on the yield contains two contributions. The first one is statistical and due to the number of entries. As this error is Poissonian it can be calculated as the square root of the number of the counts C like $\Delta C = \sqrt{C}$. The second contribution to the uncertainty comes from the background determination as determined by the fit. This error is calculated by integrating the error over the subtracted background region taking into account the error matrix from the fit. If $f(p_{1..n}; x)$ is the function with the variable x and the parameters p_n used to fit the distribution, then the error on the function is

$$\left(\Delta f(p_{1..n}; x_k)\right)^2 = \sum_{(i,j)=1}^{n} \frac{\partial f(x)}{\partial p_i}^T \sigma_{ij} \frac{\partial f(x)}{\partial p_j}. \tag{6.11}$$

Here σ_{ij} represents the error matrix of the parameters from the fit and $\partial f / \partial p_i$ the partial derivatives of the fitting function. The total error of the background fit is

$$F(p_{1..n}; x_1, x_2) = \int_{x_1}^{x_2} f(p_{1..n}; x) dx. \tag{6.12}$$

Here x_1 and x_2 are the lower respectively upper bin boundary of the first and last bin. This has the advantage that machine precisions and bin border effects do not play a big role. The yield P is then calculated by subtracting the integral over the background

B from the total histogram content C in the signal area like $P = C - B$. The final uncertainty on the yield is calculated from the two contributions. The first contribution is the error on the counting and the second is the error on the background

$$\Delta P = \sqrt{(\sqrt{C})^2 + (\delta f)^2}. \tag{6.13}$$

The results of the fit are summarized in table 6.6. The Λ^0 mass found in Ref. [67] is 1115.693 MeV. It compares well with the fitted values of 1115.5 GeV, as the systematic uncertainty on baryon mass measurements at HERMES is known to be $1 - 2$ MeV. The width of the Λ^0 reflects the detector resolution.

type	constant	mean [MeV]	σ [MeV]	counts
Λ^0	20930 ± 62	1115.52 ± 0.01	2.50 ± 0.01	267266 ± 851
$\bar{\Lambda}^0$	3618 ± 28	1115.40 ± 0.02	2.52 ± 0.02	46560 ± 375

Table 6.6: Table of peak parameters derived from a fit for the Λ^0 and $\bar{\Lambda}^0$ hyperons. The errors given on the constants are only from the fitting procedure. The fitting uncertainty of the mean and width is much less than the systematic uncertainty of $1 - 2$ MeV and 0.5 MeV, respectively. The determination of the uncertainty on the counting is described in the text.

6.4 Analysis of heavier Hyperons

In this section the analysis of the other hyperons from the SU(3) spin-$\frac{1}{2}$ octet and spin-$\frac{3}{2}$ decuplet is described. As the decay chain of some hyperons includes a neutral pion, the reconstruction of π^0 mesons is first discussed in sec. 6.4.1. Then, the results for spin-$\frac{1}{2}$ Σ hyperons are discussed in section 6.4.2. The analysis of the spin-$\frac{1}{2}$ Ξ and spin-$\frac{3}{2}$ Σ^* hyperons are presented together in section 6.4.3, since they have the same decay chains as they decay predominantly into a Λ^0 hyperon and a π meson. In the next section, an upper limit for the detection of a Ω^- hyperons decaying into a Λ^0 and a K^- is presented. In the final part of this section all hyperon yields are converted to cross sections and their mass spectra are presented.

6.4.1 Neutral Pion

Neutral heavier hyperons include a neutral pion in their decay chain. For that reason the present section is devoted to the reconstruction of neutral pions. A schematic picture of pion decay in the HERMES spectrometer is shown Fig. 6.5. The decay vertex of the π^0 cannot be reconstructed as there is no track information for the two decay photons. Neutral pions are reconstructed by using the information from the calorimeter. The calorimeter provides a measurement of the deposited energy and the position of the photons into which a π^0 decays. The energy and position resolution for photons measured by the calorimeter are worse than for charged tracks. As the calorimeter is calibrated for leptons a correction factor of 0.97 to the measured energy has to be applied [21]. The

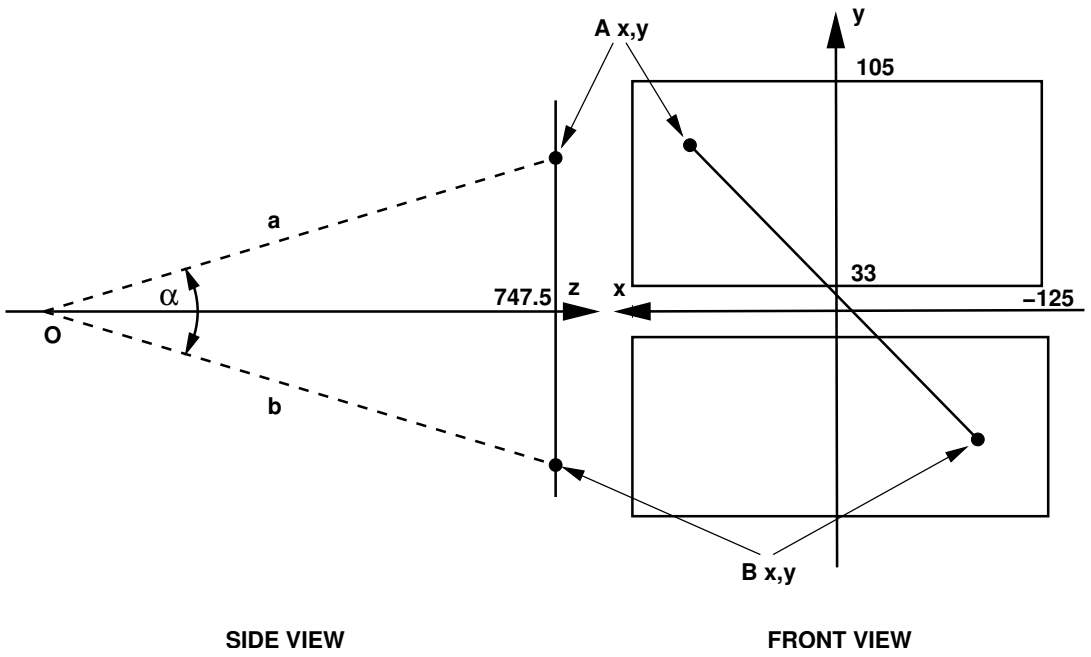

Figure 6.5: Schematic view of the reconstruction of the invariant mass of a π^0 meson from two photons detected in the calorimeter. Shown is a side view (left) of a depicted event and a front (right) view. Included are the two tracks which yield two measured positions A and B.

lower detection limit for photons in the calorimeter is about 0.8 GeV. Below that energy the signal is not distinguishable from the noise. The clusters of calorimeter blocks giving a signal are required to be inside a fiducial volume which is defined by a box with the following boundaries:

$$\begin{array}{ccccc} \text{-125} & < & x & < & 125 \quad \text{cm} \\ 33 & < & |y| & < & 105 \quad \text{cm} \end{array}$$

at the nominal z position of 747.5 cm. This fiducial volume is defined by the aperture for straight tracks passing through the spectrometer.

By assuming that the decay vertex is at $z = 0$ cm, the invariant mass is calculated from the measured energies of the two photons and their relative opening angle α

$$M^2 = 2E_aE_b - 2P_aP_b\cos(\alpha) = 2E_aE_b(1 - \cos(\alpha)). \tag{6.14}$$

The assumption on the decay vertex of the pion adds an uncertainty to the reconstructed invariant mass. Besides the uncertainty on the photon energy (of about 4 %), the determination of the angle α adds significantly to the uncertainty on the invariant mass. The uncertainty in the angle comes from the uncertainty in the position resolution in (x, y) of 1.4 cm and in z of ≈ 20 cm. The uncertainty in the position results in an uncertainty on the angle α of about 12 %. In total the uncertainty of the mass is expected to be 7 % which corresponds to 9.5 MeV.

The invariant mass spectrum for reconstructed π^0 mesons is shown in Fig. 6.4.1. A clear π^0 peak is reconstructed. The invariant mass of the pion is only slightly higher than in [67,

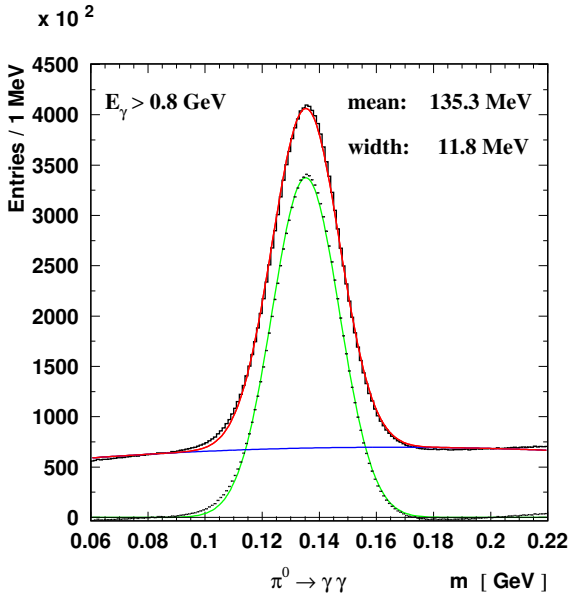

Figure 6.6: Invariant mass distribution of all $\gamma\gamma$ systems reconstructed in the whole data set. In addition a fit with a polynomial for the background and a Gaussian for the peak is shown. The derived mean position and width of the Gaussian are indicated in the plot.

PDG]. The width is about 12 MeV in rough agreement with the estimation based on the resolution of the calorimeter given above. Still the width is relatively high especially in view of the requirements imposed on the invariant mass spectrum when reconstructing heavier hyperons. The large width results in the inclusion of a large number of background events which will contribute to the background of heavier hyperons. Therefore, a rather strict requirement will be placed on the invariant mass of the pion of ± 15 MeV. This requirement includes about 8.2 million particles in the peak and 2.2 million particles in the background in the mass window $0.120 < m_{\pi^0} < 0.150$ GeV.

6.4.2 Sigma Hyperons

Three non excited spin-$\frac{1}{2}$ Σ hyperons exist. Namely, the Σ^- hyperon, which because of its decay into a neutron cannot be observed in HERMES, the Σ^0 and the Σ^+ hyperons. The latter two can -in principle- be observed in HERMES and their reconstruction is described in this section. The three sigma hyperons have the same angular momentum and iso-spin, only their quark content is different. Therefore, it is of interest to be able to compare the yield of those hyperons.

Neutral Sigma (Σ^0). The sigma zero decays into a Λ^0 and a photon. It is the only one of the three sigmas that contributes to the Λ^0 sample. The Σ^0 hyperon is the lightest, as it is only 77 MeV heavier than the Λ^0 hyperon itself. For the reconstruction of a Σ^0 all combinations of Λ^0 hyperons and photons are used. In addition to the standard requirements on the Λ^0 reconstruction, a mass window of ± 7.5 MeV, which corresponds to 3σ of the Λ^0 width, is set. This excludes the sidebands of the Λ^0 peak with a low signal to background ratio. The minimum photon energy is required to be 0.8 GeV and the photon is assumed to come from from $z = 0$ cm. As there is no further information

available on the photons, no further requirements can be imposed on these events. The requirements for the reconstruction of Σ^0 hyperons are listed in table 6.7.

	minimum	maximum	unit
DCA_Λ	—	1.5	cm
PA_Λ	0.0	—	GeV
$mass_\Lambda$	1.108	1.123	GeV
photon energy	0.8	—	GeV

Table 6.7: Summary of the requirements applied to the Σ^0 hyperon reconstruction. A further explanation of the chosen values is given in the text.

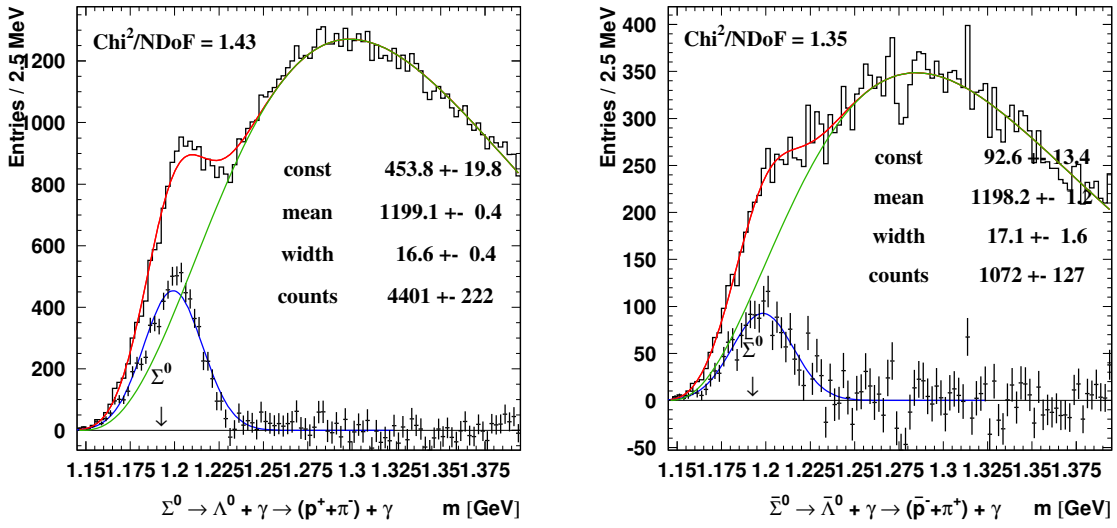

Figure 6.7: Invariant mass spectra of the p, π and γ system. The results for the (anti-) lambda are shown on the (left) right. Plotted are the data and a fit which described in the text. In addition the background subtracted data are shown.

	constant	position [MeV]	width [MeV]	counts
Σ^0	454±20	1199.1±0.4	16.6±0.4	$(4.40\pm0.22)10^3$
$\bar{\Sigma}^0$	93±13	1198.2±1.2	17.1±1.6	$(1.07\pm0.13)10^3$

Table 6.8: Peak parameters for the neutral sigma determined from a fit to the data. Additionally, the number of reconstructed Σ^0 respectively $\bar{\Sigma}^0$ are shown with their uncertainties.

The reconstructed invariant mass spectrum is shown in Figure 6.7 together with a fit. The fitting function consists of a Gaussian for the peak, and a background term. The background function is a combination of a power function with a threshold which describes the steep rise from a minimum invariant mass value. An exponential term is used to describe the drop for higher masses. More details on the fit function are given in Appendix A. As can be seen in Figure 6.7 the peak of the Σ^0 is clearly seen and the fits describe the spectra reasonably well. The χ^2 divided by the *Number of degrees of Freedom*

(NdF) of the fit is 1.43 for the Σ^0 and 1.35 for the $\bar{\Sigma}^0$, respectively. The reconstructed mean position of the Σ^0 is with 1.199 GeV about 6 MeV higher than the value listed in PDG[67] value. This offset can be due to two sources. Firstly, the calorimeter and its determination of the energy for low-energy photons is subject to systematic offsets, as discussed in section 3.3.2. These low-energy photons are the main contribution to this data sample. To study this problem, the same analysis has been performed for Monte Carlo events. Also in that case the mean position is found to be considerably higher (1.203 GeV) and has a comparable width (0.013 GeV). The MC study also revealed that the photons mainly have an energy below 2 GeV. Secondly, fitting a peak on a steep slope is particular sensitive, as it is not clear where the peak starts to rise over the background.

The same considerations are true for the anti-particle of the Σ^0, but for this particle the statistics are considerably less, due to the fact that the $\bar{\Lambda}^0$ is suppressed compared to the Λ^0 hyperon. Therefore, the significance of the peak is worse compared to the Σ^0, but still an enhancement over the background is clearly visible.

Finally, the number of counts found for the Σ^0 and $\bar{\Sigma}^0$ is derived from the background subtracted data. The error on the number of counts is the statistical one plus the error on the fitted background. Similarly, to the uncertainty in the Λ^0 reconstruction the uncertainty on the background function has been derived from the error matrix of the fit. The results are shown in table 6.8.

Positive Sigma (Σ^+) In the framework of this analysis it has been possible to reconstruct the Σ^+ hyperon for the first time using HERMES data. This second sigma adds confidence to the quality of the hyperon reconstruction techniques used in this thesis.

The Σ^+ has two main decay channels where only the first one (I) is accessible, as there is no neutron detection available in the HERMES spectrometer.

$$\begin{array}{llllll} \text{I} & \Sigma^+ & \rightarrow & p^+ + \pi^0 & \rightarrow & p^+ + \gamma\gamma \quad 51.57\ \% \\ \text{II} & \Sigma^+ & \rightarrow & n^0 + \pi^+ & & \quad\quad\quad\quad 48.31\ \% \end{array}$$

Several requirements are imposed on the proton and the neutral pion in the reconstruction procedure. The proton is required to be identified by the RICH detector with a quality factor $QP > 1.0$. Additionally, the proton is required to have a momentum larger than 4 GeV. These requirements ensure a clean proton sample with a low contamination of other hadrons like kaons and pions. The neutral pion is reconstructed from two photons with an energy > 0.8 GeV. Therefore, no production vertex of the Σ^+ can be evaluated and no requirement can be imposed on vertex differences. The only requirement which is imposed on the pion is a mass window of ± 15 MeV which corresponds to 1.25σ. This rather strict requirement ensures that the pion sample has a good signal to background ratio. All the requirements are summarized in table 6.9.

The results for the invariant mass spectra are shown in Figure 6.8. The number of events containing a proton and a neutral pion is high compared to the signal. As discussed before, there are no possibilities to further reduce the background for this channel. A MC study has shown that increasing the minimum energy of the π^0 would reduce the signal

	minimum	maximum	unit
PID_p	-99	0	—
RICH QP_p	1	—	—
$momentum_p$	4	15	GeV
energy photon	0.8	—	GeV
$mass_{\pi^0}$	0.120	0.150	GeV

Table 6.9: Summarized are the requirements for the identification of positive sigma hyperons. On both daughter particles, proton and π^0, requirements are imposed.

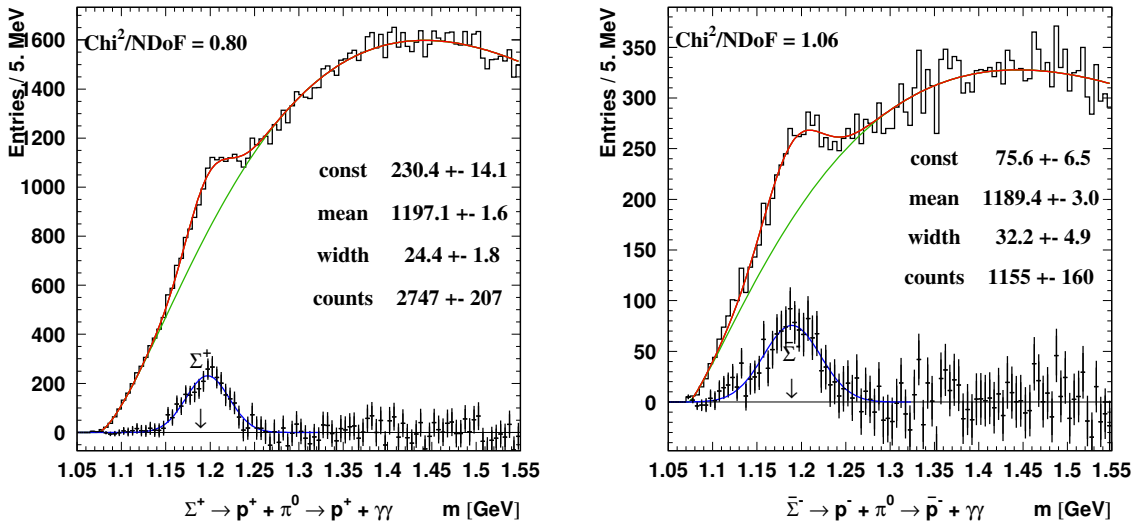

Figure 6.8: On the left the invariant mass spectrum for the (p,π^0)-system is shown. On the right side the same for the corresponding antiparticles ($\bar{p}, \pi^0$) is displayed. Shown is the number of counts versus the invariant mass. Additionally, a fit is included in the spectra. The background (thin curve), determined in the fit, is subtracted from the data and the resulting background subtracted spectrum is shown as well.

	constant	position [MeV]	width [MeV]	counts
Σ^+	230±14	1197.1±1.6	24.4±1.8	$(2.75\pm0.21)10^3$
$\bar{\Sigma}^-$	76± 7	1189.4±3.0	32.2±4.9	$(1.16\pm0.16)10^3$

Table 6.10: Shown are the fitted peak parameters values for the positive sigma. Additionally, the determined yields with their uncertainty are listed.

over background ratio. Additionally, this study revealed that the energy of the π^0 is low: 90 % of the events have a π^0 with an energy of less then 2 GeV.

The fit shown in Fig. 6.8 is performed in a very similar way as for the neutral sigma discussed above. The background function is composed of a power function including a threshold which describes the first rising part and an exponential that makes sure that for higher masses the function drops again. Even though the enhancement due to the Σ^+ peak is clearly visible, the fit is not well constrained. As a result, the determination of the position and the width is subject to large errors. For the Σ^+ a position of 1197.1 MeV has been derived. This value is about 8 MeV higher than the PDG value. The mass peak is expected to be wide due to the relatively poor energy resolution of the calorimeter for photon detection. Also for this particle a MC study has been performed which also showed a higher reconstructed mass. The fit derived from the MC had a Σ^+ peak at 1205 MeV and a width of 27 MeV. The two main sources of error are the fit of a peak on a steeply rising curve, and the reconstruction of the neutral pion.

The fitted values for the particle and antiparticle peaks are shown together with their uncertainties in table 6.10. In addition the yields are displayed. The error on the yield is, similar to the neutral sigma, combined from the statistical error and the error from the background fit.

6.4.3 Cascade and exited Sigma Hyperons

The reconstruction of cascades (Ξ) and excited sigmas (Σ^*) cannot be separated. Both particles decay via a Λ^0 hyperon and a π meson. Therefore, the analysis of these hyperons is presented in one section. The first part discusses the neutral hyperons of this type that decay via a neutral pion (π^0). The second part is about the decays which include charged pions ($\pi^\pm$). The cascades decay for > 99 % into a Λ^0 and a pion. The Σ^*'s have two main decay branches, one including a Λ^0 and a pion (88 %), and a second including a Σ and a pion. The latter channel is due to the high background contamination of the invariant mass spectra, as shown in the previous section, omitted from the present analysis.

Neutral Cascade (Ξ^0) and excited Sigma (Σ^{*0}) Both the neutral cascade and sigma decay via a Λ^0 hyperon and a π^0 meson. This decay chain involves at least two charged tracks and two untracked calorimeter clusters reconstructed in the HERMES acceptance. A requirement of a multiplicity of at least four in the acceptance reduces the data set substantially.

The invariant mass spectrum for a combined Λ^0 and π^0 analysis is shown in figure 6.9. In addition to the standard requirements on the Λ^0 hyperon and the neutral pions there are no further requirements used. This is due to the fact that there is no additional information available on the production vertex of the hyperons. The only possibility to impose more strict requirements would be offered by the Λ^0 peak. As can be seen in figure 6.9 the statistics of these channels are low. In addition the threshold for these particles including a π^0 with a minimum energy of 1.6 GeV is very close to the known

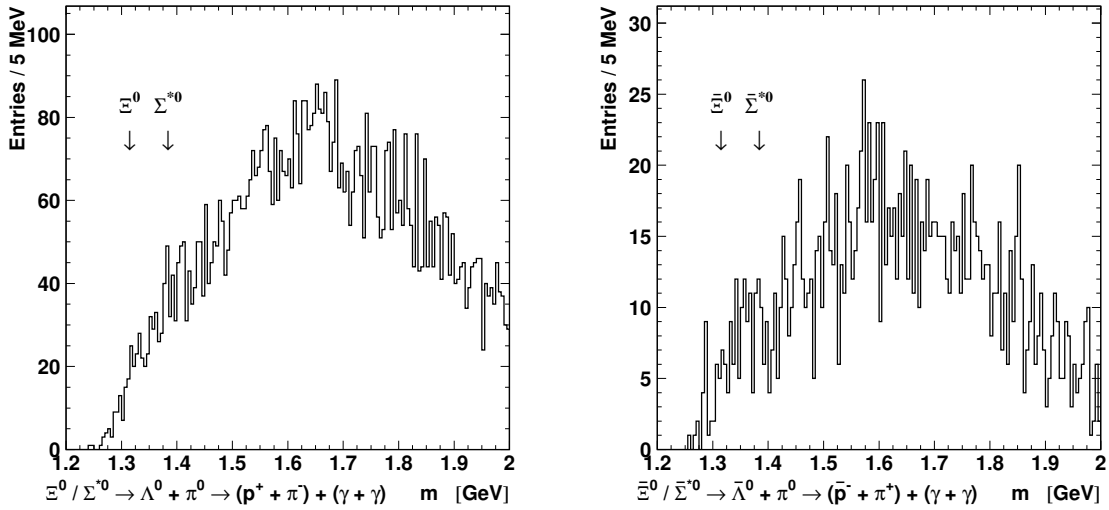

Figure 6.9: Invariant mass spectra for the (p,π,2γ) final state, on the left plot for the particles and on the right for the anti-particles. Additionally, the expected position of the various hyperon peaks is indicated.

masses of the Ξ^0 and Σ^{*0}. As a result of all these effects, it seems not to be possible to enhance the signal. As the position and the width of the peaks of the neutral cascade and the excited sigma are not easy to estimate, it has not been tried to estimate an upper limit for the cross section.

Charged Cascade (Ξ^-) and excited Sigma ($\Sigma^{*\pm}$) As mentioned in the introduction the Ξ^- and the excited $\Sigma^{*\pm}$ decay into a Λ^0 and a $\pi^\pm$. In figure 6.10 a schematic view of the decay is shown. The Ξ^- decay is taken as an example for all hyperons in this class of events. Here the reconstruction process is explained for this particle. The first step in this analysis is the reconstruction of a Λ^0 hyperon as explained in section 6.3. To select a Λ^0 sample, a mass window cut of $\pm$7.5 MeV corresponding to 3σ is used, in addition to the standard requirements. From the Λ^0 reconstruction the third vertex ($V3$) and the Λ^0 track parameters are calculated. Thereafter, all unused pions of the event are combined with the Λ^0 to calculate the other vertices. The Λ^0 and the pion are used to calculate the vertex $V2$ and a DCA for this vertex is determined. This second vertex is the decay vertex of the heavy hyperon and the production vertex of the Λ^0. The DCA is required to be less than 2 cm. If this requirement is fulfilled, then the hyperon is reconstructed including its mass and momentum vector. The difference in z between the third and second vertex is taken as the decay length of the Λ^0 and a requirement is imposed on its value. This was found to be necessary to avoid double counting of the various proton-pion- pion combinations as both pions can be combined to from a Λ^0 candidate. Finally, the last vertex $V1$ is reconstructed from the hyperon track combined with the beam line. Also in this case, a DCA to the beam line and a decay length is calculated. These two values are subject to large uncertainties and no strict requirements are therefore imposed

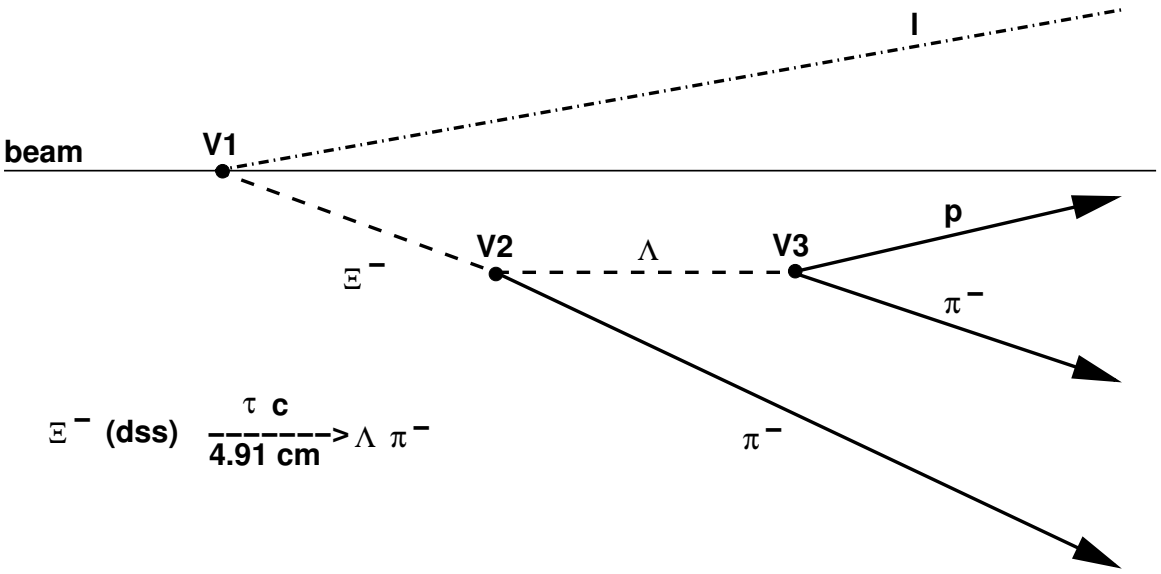

Figure 6.10: Schematic picture of a Ξ^- decay. This channel is taken as an example for all decays of this class. Shown in solid lines are the three tracks in the final state. Additionally, the three vertices are indicated. The dashed lines denote the hyperon tracks, the dashed-dotted line the track of the scattered lepton. The $\Sigma^{*\pm}$ have no measurable decay length, and therefore V1 and V2 coincide in this case.

on them.

All the requirements mentioned before are summarized in table 6.11. These requirements by themselves make it possible to distinguish the signal peaks from the background. More strict requirements would decrease the background as well as the signal. Instead of reducing the background it has been chosen to describe the background as well as possible.

The method used to determine the background is the so-called *event mixing*. The idea of event mixing is to use two independent samples of tracks and combine them in the same way as described above for the signal data. Here a Λ^0 track from one event and a pion from another event are taken. The result of these uncorrelated samples should give a smooth distribution without any peak structures and thus reflect the background of random (Λ^0,π)-combinations. To arrive at a good description of the background the mixed event data have to be treated in the same way as the normally reconstructed data. That means that the same requirements have to be imposed on the variables used. It was found that one combined background model fits the spectrum best. The result including the background is shown in figure 6.11. The background is normalized to fit the data best. The normalization has been obtained by scaling the mixed-event spectra to the right side of the peaks in an area indicated by the horizontal lines in the figures. As can be seen the background model fits the data well. Only in the case of the (Λ^0,π^-)-spectrum the higher mass region is not described satisfactorily.

The background subtracted spectra are shown in figure 6.12. These have been fitted with a Gaussian shape. This functional form is justified for the Ξ^- which has no physical

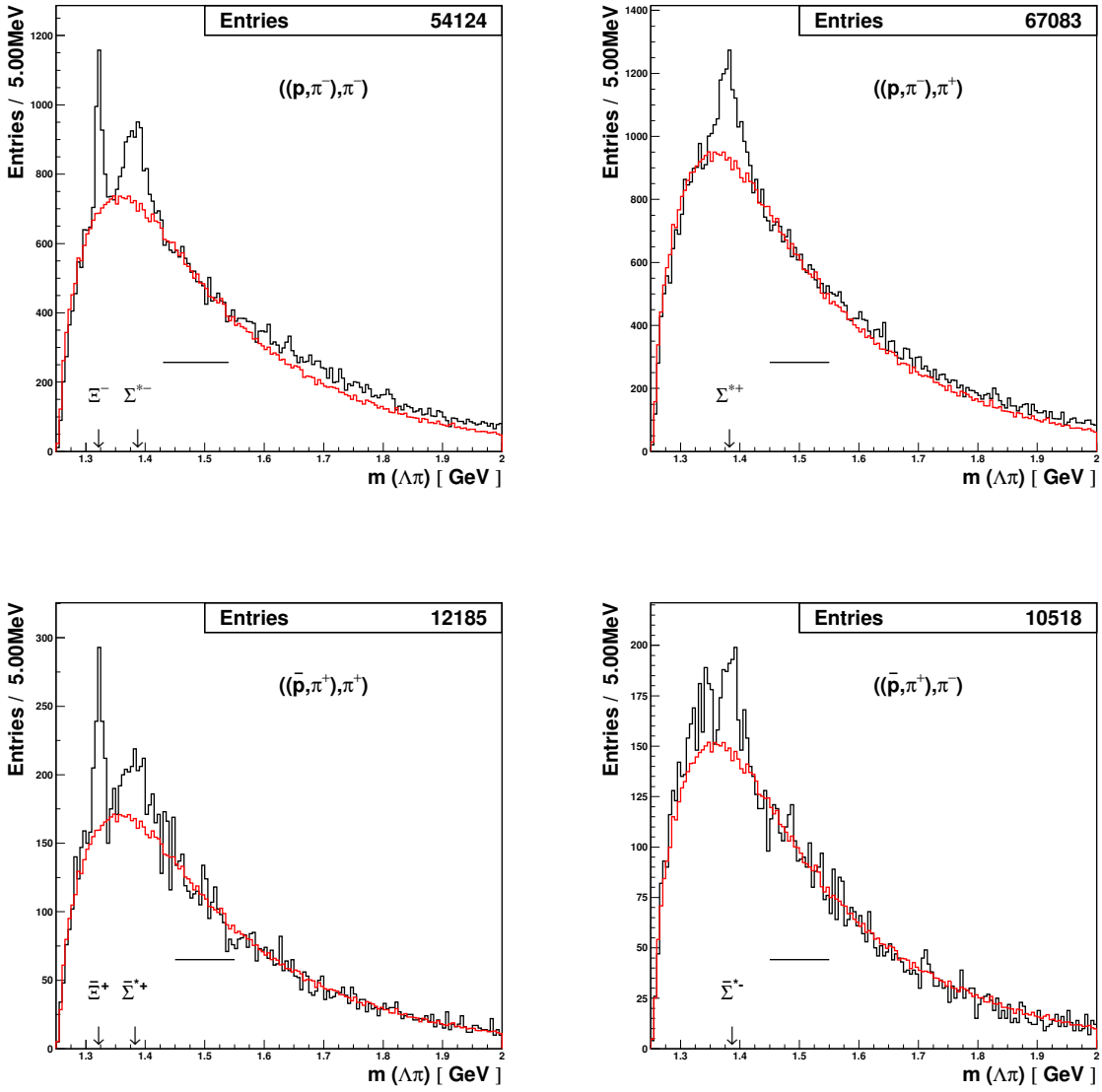

Figure 6.11: Invariant mass spectra for four combinations of $(p^+\pi^-)\pi^\pm$ and $(\bar{p}^-\pi^+)\pi^\pm$ events. The top left panel shows the (Λ^0,π^-)-combination together with the background derived by event mixing. The background is normalized in the region indicated by the horizontal line. On the right the same distribution is shown but now for a Λ^0 combined with a π^+. The lower two plots are again similar to the two plots above but now for the anti hyperon.

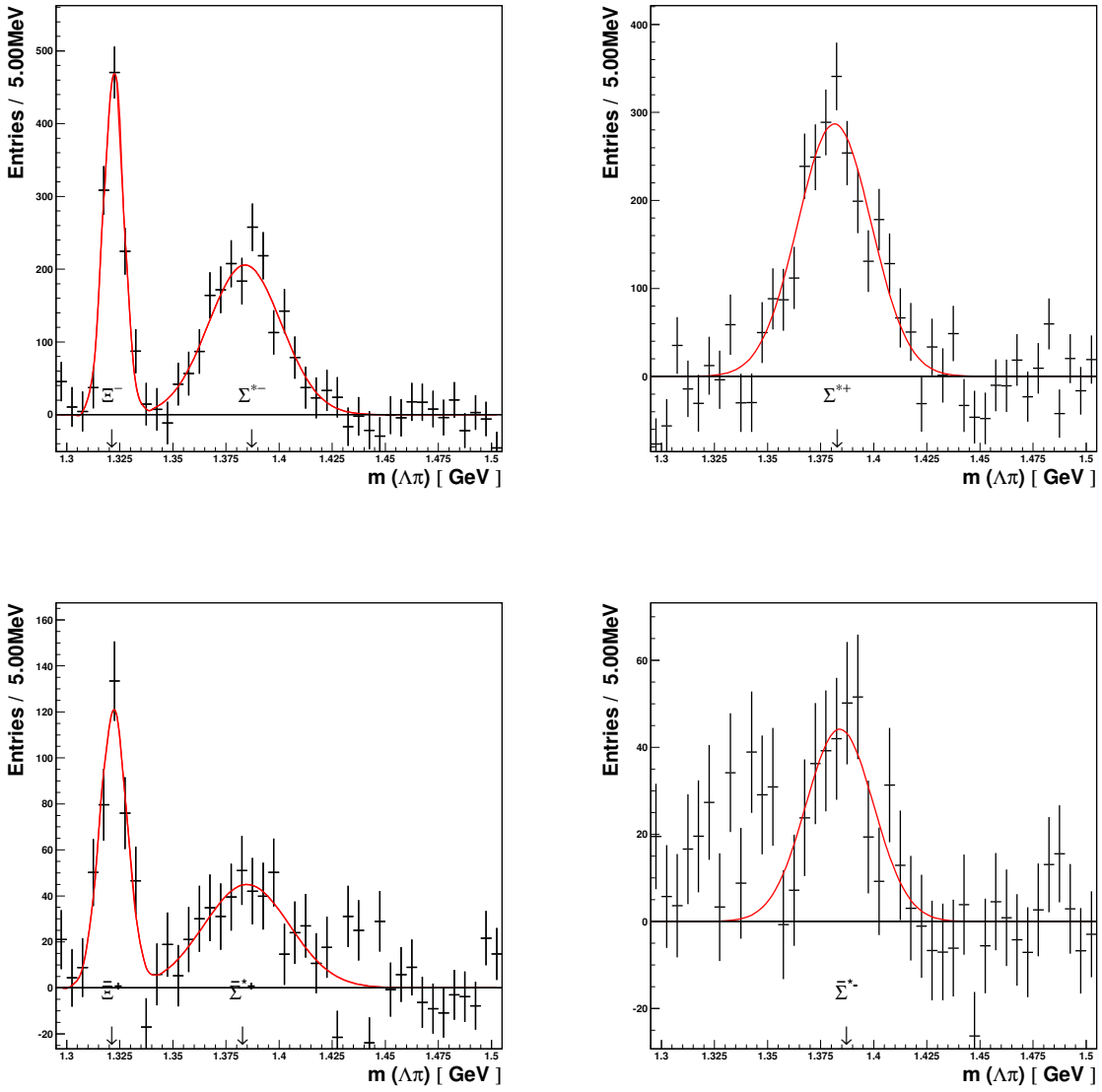

Figure 6.12: Here the same four spectra are shown as in figure 6.11 but the background model has been used to subtract the estimated background from the data. Additionally, the relevant mass region has been enlarged. Furthermore, a fit to the peaks with Gaussian shapes is shown.

	minimum	maximum	unit	explanation
Lambda:				
PID	-99.0	0.0	-	PID requirement hadrons
PA	0.0	-	-	relative proton pion energy
DCA	—	1.5	cm	DCA Λ^0 proton pion
ΔZ	0.0	250	cm	decay length of the Λ^0
mass	1.108	1.123	GeV	mass range for the Λ^0
Hyperon:				
DCA		2.0	cm	DCA Λ^0 pion
ΔZ	-15.0	200	cm	decay length of hyperon
DYB		2.0	cm	DCA hyperon and beam

Table 6.11: Cuts on hyperon variables as used in the reconstruction of (Λ^0,π, π) events. More explanation is given in the text.

width. For the $\Sigma^{*\pm}$ it was found that there is no difference between a fit with a Gaussian or a Breit-Wigner distribution. For the sake of simplicity a Gaussian was used in both cases.

The number of hyperons in the peaks has been calculated as follows. The entries in the bins have been added starting from the center bin to the left and right. Counting is continued as long as the value for the fitted Gauss was above 1 and the bin content itself is positive. The uncertainty for the number of hyperons has been evaluated from the statistical uncertainty of the counting and the background description. The results are listed in table 6.12.

	constant	mean [MeV]	width [MeV]	counts
Ξ^-	470 ± 33	1322.1 ± 0.4	4.7 ± 0.4	1147 ± 164
$\bar{\Xi}^+$	121 ± 13	1322.0 ± 0.8	6.3 ± 0.7	385 ± 85
Σ^{*+}	287 ± 19	1381.5 ± 1.2	40.7 ± 3.1	2462 ± 349
$\bar{\Sigma}^{*-}$	44 ± 8	1384.0 ± 3.0	37.5 ± 7.2	278 ± 129
Σ^{*-}	206 ± 7	1383.9 ± 1.4	40.4 ± 2.7	1759 ± 172
$\bar{\Sigma}^{*+}$	45 ± 7	1384.8 ± 3.3	47.5 ± 7.9	463 ± 143

Table 6.12: Fitting peak parameters of all hyperons reconstructed from a Λ^0 and a charged pion. The errors on the fit parameters are also shown. For the excited sigmas the Gaussian width has been converted to a FWHM value. Additionally the yields with their uncertainties are shown in the last column.

Only the $\bar{\Sigma}^{*-}$ is less clearly distinguished from the background. The fitted mass values of the other hyperons compare well to the PDG values. For the Ξ's the mean value is within 1 MeV of the book values. Additionally, the Gaussian width of $\approx$ 5 MeV lies in the expected range as this resolution is instrumentally defined and confirmed by MC studies. The same is true for the Σ^{*-} of which the width is also comparable to the PDG values.

	minimum	maximum	unit	explanation
Lambda:				
DCA	—	1.5	cm	secondary vertex track distance
ΔZ	0.0	250	cm	decay length of the Λ^0 hyperon
mass	1.108	1.123	GeV	mass range for the Λ^0 hyperon
Omega:				
DCA	—	2.0	cm	distance Λ^0 and K^- track
ΔZ	0.0	250	cm	decay length of the Ω^- hyperon

Table 6.13: Requirements for the Omega hyperon reconstruction.

6.4.4 Omega Hyperon

The Ω^- is the heaviest particle from the hyperon SU(6) decuplet. It contains three s-quarks and no valence quark remnants from the target. Hence, it is an all-sea object and thus of particular interest to study. The Ω^- has three main decay branches:

$$\begin{array}{lllll} \text{I} & \Omega^- \xrightarrow{0.678} & \Lambda^0\ K^- \xrightarrow{0.639} & p^+\ \pi^-\ K^- & 43.3\ \% \\ \text{II} & \Omega^- \xrightarrow{0.236} \Xi^0\ \pi^- \xrightarrow{0.985} & \Lambda^0\ \pi^0\ \pi^- \xrightarrow{0.639} & p^+\ \pi^-\ \gamma\ \gamma\ \pi^- & 14.9\ \% \\ \text{III} & \Omega^- \xrightarrow{0.086} \Xi^-\ \pi^0 \xrightarrow{0.989} & \Lambda^0\ \pi^-\ \gamma\ \gamma \xrightarrow{0.639} & p^+\ \pi^-\ \pi^-\ \gamma\ \gamma & 5.4\ \% \end{array}$$

Only the first decay chain has been investigated in this analysis. The other two decay chains include neutral pions and therefore have three tracks plus two photons in the final state. This relatively high multiplicity in an event plus the previously discussed disadvantages associated with the reconstruction of the π^0-meson strongly reduce the prospects of finding an Ω^- hyperon in such events. The total branching ratio for the first channel is 43.3 %.

The hadron separation of the RICH detector is not optimal for energies below 4 GeV (see Sec. 3.3.2) due to the different thresholds involved. A Monte Carlo study has shown that about 60 % of the K^- meson from a decay of an Ω^- have a momentum below the RICH K identification threshold. Therefore, in addition to the identified K also low momentum hadrons that are not identified as a pion have been included in the sample of tracks that are used to reconstruct the Ω^- invariant mass. The requirements used for the reconstruction are the standard requirements for the Λ^0 hyperon and additional requirements for the decay vertex of the Ω^-. First of all the K^- track is required to have a DCA to the lambda track of less then 2 cm. In addition, the Ω^- is required to decay before the Λ^0 hyperon. All requirements are summarized in table 6.13.

As can be seen in figure 6.13 the invariant mass distribution starts at the threshold of $M_\Lambda + M_K = 1.609$ GeV and rises quickly. For higher invariant masses, and therefore higher momentum of the decay particles, the distribution declines. In addition to the data points the wrong charge combination, which in the case of a Ω^- is a combination of Λ^0 and a K^+, is shown. For the Ω^- the normalized wrong charge distribution has essentially the same shape as the data. For the $\bar{\Omega}^+$ the wrong charge combination has very low statistics and fails to reproduce the shape of the data. Indicated in the figures

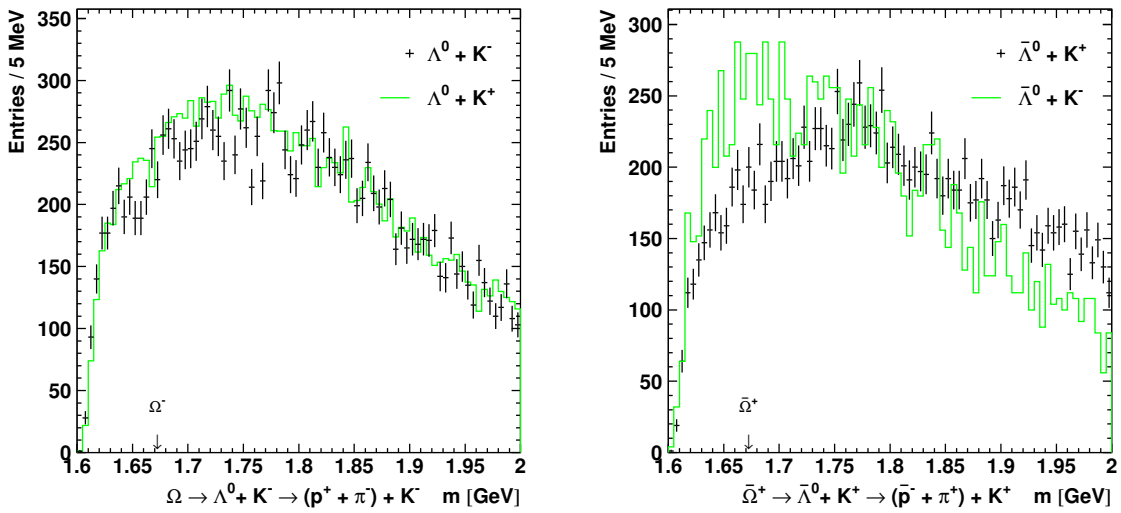

Figure 6.13: Invariant mass distribution of the sample of combined (Λ^0,K^-)-events. On the left side the Ω^- candidates together with the wrong charge combination are shown. On the right side the same distribution for the antiparticle $\bar{\Omega}^+$ is shown.

are also the positions where the Ω^- (or the $\bar{\Omega}^+$) is expected to be found. There is no sign of an enhancement at that location and further efforts to reduce the background did not result in any evidence indicating that an Ω^- has been observed.

Omega yield upper limit As mentioned in the previous paragraph no signal for the Ω^- hyperon could be found. In the remainder of this section an upper limit for the yield is derived. For that purpose a Monte Carlo simulation for Ω^- production has been carried out, which yields information on the mass resolution and the detection efficiency. Both MC generators, DCAY and PYTHIA have been used in this study (more details on the MC are given in sec. 6.5).

With the DCAY generator a high statistics sample of (Λ^0, K^-)-pairs have been generated. In total 617852 events are produced in 4π. From this sample 1687 Ω^- hyperons are reconstructed in the HERMES acceptance imposing all requirements previously used in the analysis. Because of the missing particle identification in the MC analysis only kaon tracks are used. The acceptance of HERMES for the Ω^- production derived from the DCAY generator studies is 0.27 % as a fraction of 4π. The simulated Ω^- peak has a width, derived from a Gaussian fit, of 4.1 MeV.

The same acceptance study has also been performed with the PYTHIA generator. There has not been a dedicated MC production for Ω^- events, but instead an existing production for Λ^0 hyperons has been used. The disadvantage of that choice is that there is only very limited number of Ω^- events available. Still, an estimate of the acceptance was possible and yielded the number of 0.27 % as a fraction of 4π. This is the same as was found with the DCAY generator and therefore gives confidence that this estimate is reasonable.

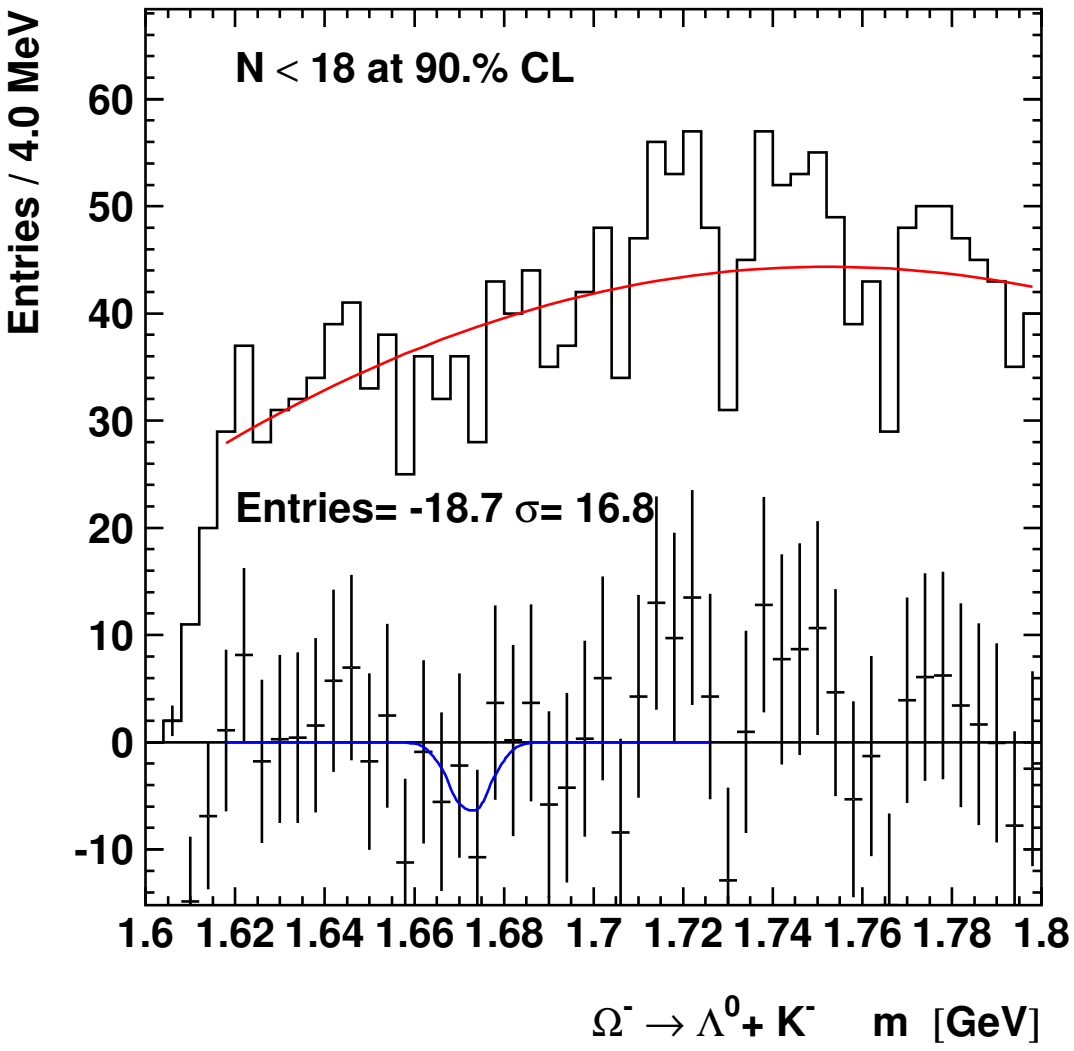

Figure 6.14: Invariant mass distribution of $\Lambda^0 + K^-$ candidates with all requirements imposed as described in the text (solid histogram). A second order Legendre polynomial is fitted to the histogram to describe the background. The background subtracted spectrum is shown below in the same plot. The curve is a fit to the subtracted data assuming a fixed signal shape. Only the number of entries was used as a free parameter in the fit.

In figure 6.14 the invariant mass spectrum for $\Omega^-(\Lambda^0, K^-)$ hyperon candidates is shown, now zoomed in on the relevant mass range. The solid histogram represents the data with all requirements imposed as discussed before. A second order Legendre polynomial is fitted to the spectrum to describe the shape. This shape is used as a background estimate and subtracted from the data. The subtracted spectrum is shown in the same plot as data points with error bars. A χ^2 fit of a Gaussian with fixed position (PDG value) and width (4.1 MeV) yielded a value of $\bar{N} = -14.8$ with an error dN of ± 24.1 entries.

To calculate an upper limit from this unphysical yield a Bayesian inference is used as follows. The likelihood distribution $p(d|N, I)$ for the data d is written as a Gaussian distribution with N events

$$p(d|N, I) = \frac{1}{\sqrt{2\pi}dN} \exp\left[-\frac{1}{2}\left(\frac{N - \bar{N}}{dN}\right)^2\right] \tag{6.15}$$

where $\bar{N}$ and dN are the mean value and the error from the fit and I stands for known parameters in the model like the assumed position and width. This leads to a posterior distribution

$$p(N|d, I) = \frac{C}{\sqrt{2\pi}dN} \exp\left[-\frac{1}{2}\left(\frac{N - \bar{N}}{dN}\right)^2\right] p(N|I) \tag{6.16}$$

where C is a normalization constant and $p(N|I)$ is the prior for the Ω^- yield N. The prior knowledge that $N \geq 0$ is used to calculate the constant C. The resulting Gaussian is renormalized to unity for $N \geq 0$ and the upper limit is calculated by integrating the distribution. The maximum number of Ω^- hyperons for a confidence level of $3\sigma = 99.7$ % is found to be 61.

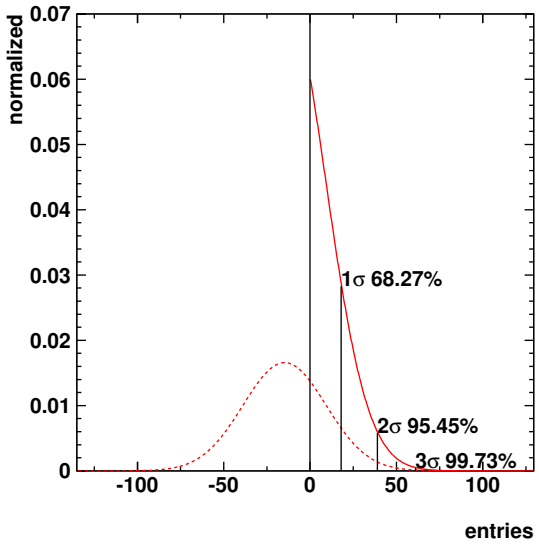

Figure 6.15: Normalized probability distributions for the number of fitted Ω^- hyperons. The dashed line shows a Gaussian with a mean of -14.8 and a width of $\sigma = 24.1$. This distribution is re-normalized for the area $N \geq 0$. In addition the confidence levels are indicated in the plot.

The quoted value of the upper limit is in agreement with the estimate of the amount of background events in a $\pm 3\sigma$ region around the expected position of the Ω^-. Integrating

type	cross section [pb]		ratios		
	particle	antiparticle	$Y/\bar{Y}$	Λ^0/Y	$\bar{\Lambda}^0/\bar{Y}$
Λ^0	2680 ± 327	467 ± 57	5.7 ± 1.0	1.0	1.0
Σ^+	34.6 ± 4.9	14.5 ± 2.7	2.4 ± 0.6	78 ± 15	32.1 ± 7.1
Σ^0	44.1 ± 5.8	10.8 ± 1.8	4.1 ± 0.9	61 ± 11	43.4 ± 9.1
Ξ^-	11.5 ± 2.2	3.9 ± 1.0	3.0 ± 0.9	233 ± 52	121 ± 34
Σ^{*+}	28.4 ± 5.3	3.2 ± 1.5	8.9 ± 4.6	94 ± 21	146 ± 72
Σ^{*-}	20.3 ± 3.2	5.3 ± 1.8	3.8 ± 1.4	132 ± 26	88 ± 31

Table 6.14: Hyperon cross sections in [*pb*] as determined from the yield normalized with the luminosity. All corrections as described in the text have been applied. The error is calculated as in formula 6.18. The left column is the particle type. The second column is for particles and the third one for anti-particles cross section. The last columns represent various ratios of particle to anti-particles and Λ^0 to hyperons.

the background and taking the square root yields a number of 25 entries which is consistent with the estimate mentioned before.

6.4.5 Hyperon production cross sections in HERMES

The particle yields can be expressed in cross sections utilizing a normalization constant. At HERMES two possible normalizations can be used for this purpose. The first one is a normalization to the accumulated number of DIS events (see Sec. 2.2.2). The second one is to normalize to the integrated luminosity (see Sec. 3.4). The result is a differential quasi-real photoproduction cross section for the HERMES experiment. This cross section includes the effect of the limited acceptance and limited kinematical range of the detector, that it is a production cross section *in the* HERMES *acceptance*. The reason for evaluating such a cross section is that it is not model dependent, as a true '4π cross section' is, and the acceptance effects can be included in the MC based model calculations (see Sec.6.5). Using the luminosity measurement, the cross section is calculated as

$$\sigma_{acc}(lp \to hX) = \frac{N}{\mathcal{L} \cdot B \cdot \epsilon_d \cdot \epsilon_t} \tag{6.17}$$

with N the number of detected particles, $\mathcal{L}$ the luminosity, B the branching ratio of the particle and $\epsilon_{d/t}$ the efficiency for dead time and trigger.

Two additional corrections are applied to the cross sections. Both of these corrections deal with the efficiency of the detector. The first one is the dead time correction of the DAQ system. Generally the detector has a low dead time of $2-3$ % during polarized data taking with normal density targets (see also section 3.3.3). The average dead time used for the data set is 5.0 % with a spread of 3.0 %. This gives a dead time correction factor of 95 ± 3 % which has been applied to the yields.

The second correction is for the trigger efficiency. There exists no MC simulation that includes the effect of the triggers used in the experiment and therefore the trigger efficiency

has to be estimated. The unknown trigger efficiencies are expected to have some influence on the presented results but their exact treatment is beyond the scope of this work. There are two main triggers that contribute to the sample. This is first of all the so-called DIS trigger T21 which requires a signal in the hodoscopes and the calorimeter. For events where the leading particle is a proton the efficiency of T21 is expected to be low. The second trigger (T28) is the so-called photo-production trigger which requires the hodoscopes and the back chambers in top and bottom to fire. This trigger evaluates if there are more than two tracks per detector half. Hyperon events have at least two tracks in the spectrometer and therefore the efficiency for this trigger is expected to be higher. In ref. [61] a detail study for hadron trigger efficiencies for multiple hadron photo-production at HERMES is presented. From that study a parameterization of the trigger efficiencies was taken. Averaging the momentum dependent trigger efficiency yielded a value of 63 ± 7 % is obtained. This factor has been applied to the data.

The uncertainty on the cross section calculation derives mainly from the efficiencies, the error on the number of counts δN and the error on the luminosity $\delta\mathcal{L}$. Taking these uncertainties as independent the error on the cross section is calculated as

$$(\Delta\sigma)^2 = \left(\frac{\delta N}{\mathcal{L}B\epsilon_d\epsilon_t}\right)^2 + \left(\frac{N\cdot\delta\mathcal{L}}{\mathcal{L}^2B\epsilon_d\epsilon_t}\right)^2 + \left(\frac{N\cdot\delta B}{\mathcal{L}B^2\epsilon_d\epsilon_t}\right)^2 + \left(\frac{N\cdot\delta\epsilon_d}{\mathcal{L}B\epsilon_d^2\epsilon_t}\right)^2 + \left(\frac{N\cdot\delta\epsilon_t}{\mathcal{L}B\epsilon_d\epsilon_t^2}\right)^2 \quad (6.18)$$

The resulting cross sections are shown in table 6.14 and in figure 6.16. Two observations can be made when considering the combined data. The first one is that the cross section decreases with increasing hyperon mass. The spin-$\frac{3}{2}$ sigmas represent an exception. Otherwise the dependence with mass is obvious. The spin dependence of the cross section might give a hint to a different production mechanism. The second observation is that the cross section for particles is higher then that of anti-particles. The ratio of particles to anti-particles varies between 2.4 and 8.9. This is further illustrated in fig. 6.17, where the number of (anti) hyperons produced per Λ^0 ($\bar{\Lambda}^0$) produced is plotted. Also in this case the exceptional behavior of the $\Sigma^{*\pm}$ hyperons is obvious. It is noted that if a renormalization by a factor (2J+1) is adopted, as suggested by Fig. 2.3, most of the difference is compensated for.

6.5 Monte Carlo Studies

In order to interpret the data described in the previous section and obtain information on the importance of heavy hyperon decays in Λ^0 production, Monte Carlo (MC) studies are needed. The MC studies discussed in this section are based on the PYTHIA 6.2 generator [71, 73, 72]. PYTHIA incorporates JETSET, which is used to simulate the hadronization process, and together they are used to generate physics events. PYTHIA is integrated into the General Monte Carlo (GMC) software package used by the HERMES collaboration. The generator itself creates physics events and calculates normalization constants to extrapolate the obtained results to 4π cross sections. Optionally, this information is

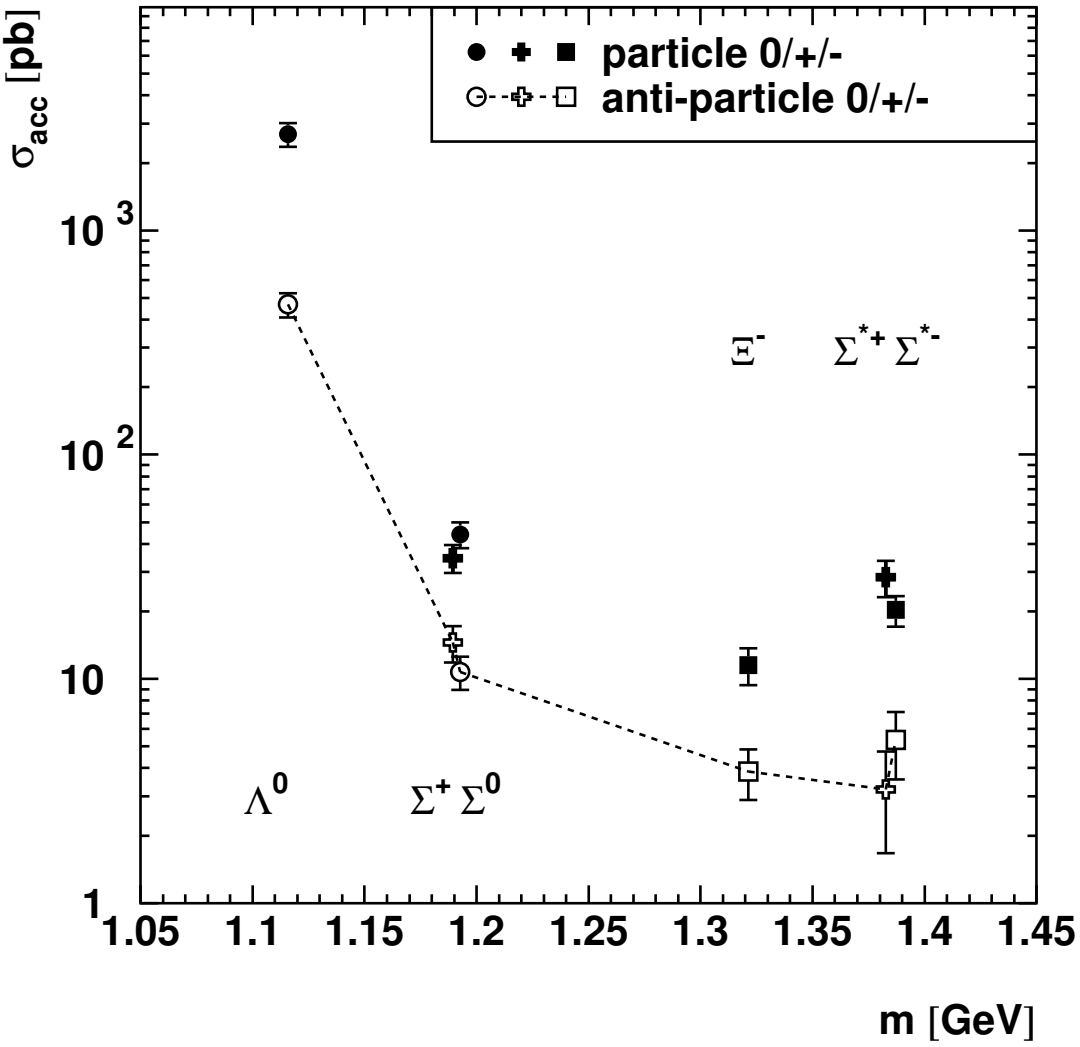

Figure 6.16: Hyperon cross sections in the HERMES acceptance for various hyperons. The cross section is plotted versus the book mass of the particle. The numbers are listed in table 6.14. All mentioned correction in the text are applied. The dashed line connects all anti-particles and its purpose is to guide the eye.

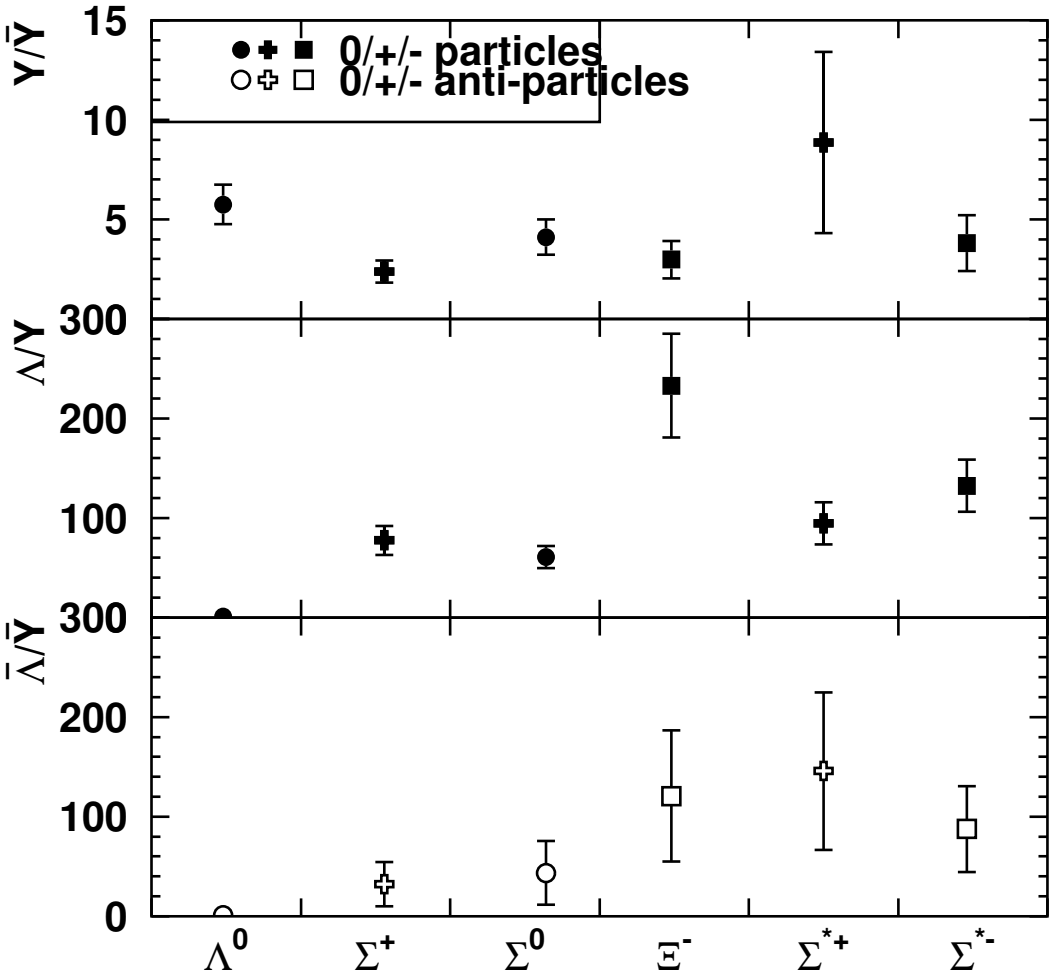

Figure 6.17: Shown are the three ratios from table 6.14. Top panel the particle to anti-particle ratio. Middle panel the Λ^0 to hyperon (Y) ratio and in the lower panel the ratio for the $\bar{\Lambda}^0$ to anti-hyperon $\bar{Y}$ ratio.

passed on to HMC which is the MC description of the HERMES detector implemented with GEANT3 [39]. Originally, PYTHIA has been tuned for higher energies like the ones available at LEP. Recently, a tuning of PYTHIA for lower energies and fixed target experiments like HERMES has come available [52].

This MC study is using the most recent tune (2004*c*) for PYTHIA. In addition two important PYTHIA parameters for the production of hyperons have different settings than the default. The first one is `PARJ_1` which has been increased from 0.1 to 0.029. This parameter controls the diquark to quark suppression in the fragmentation model. The second parameter which has been adjusted is `PARJ_3`, which regulates the so-called *extra suppression of strange diquarks*. The default of 0.4 has been changed to 1.2. With these additions it has been shown that the kinematic distributions (in W^2, Q^2, x_F and z) for Λ^0, $\bar{\Lambda}^0$ and $K^{\pm}$ electro-production are well reproduced by the MC on the cross section level [58].

The first section 6.5.1 of this part of chapter 6 discusses a MC production for a 4π acceptance. This production was not tracked through the detector. It is used to simulate the initial momentum distribution, the 4π photo-production cross sections for hyperons, and particle multiplicities. The second MC production, discussed in section 6.5.2, is tracked in the HERMES acceptance and is used to compare MC results to the data. Together these two studies are used in an attempt to extrapolate the cross section measured in the HERMES acceptance to a 4π acceptance. Additionally, the MC results are used to estimate the contribution from decaying heavier hyperons to Λ^0 production. These contributions are sometimes referred to as the subprocess fractions. Another approach for the extrapolation to 4π is discussed in subsection 6.5.3. This second approach utilizes the DCAY generator, which is a fast simulator of two-body decays. This MC generator cannot be used for a normalization to cross sections. Providing the initial momentum distributions the geometrical acceptance of a given decay can be investigated and compared to PYTHIA. More importantly, DCAY can be used to evaluate an acceptance correction needed to calculate the feeding from hyperons to the Λ^0 sample can be calculated and compared to the results of the subprocess fractions obtained from PYTHIA.

6.5.1 Monte Carlo simulations with out acceptance

This MC production does not incorporate a simulation of the HERMES detector. Consequently, it has no requirement on the decay angles of the particles. In order to reduce the amount of MC data, the presence of a Λ^0 decaying into a proton and a pion was required. As this MC data set is not tracked, and the reconstruction of decay particles is 100 % efficient.

The 4π MC was used to extract the initial momentum distributions of the various hyperons. As can been seen on the top left plot of figure 6.18 the p_t distributions are comparable in shape for all hyperons. The hyperons have a mean p_t of about 0.40 GeV with a spread of 0.23 GeV, and the antiparticles have a mean p_t of 0.44 GeV with a spread of 0.22 GeV. On the other hand, there is a difference seen in the p_z distribution

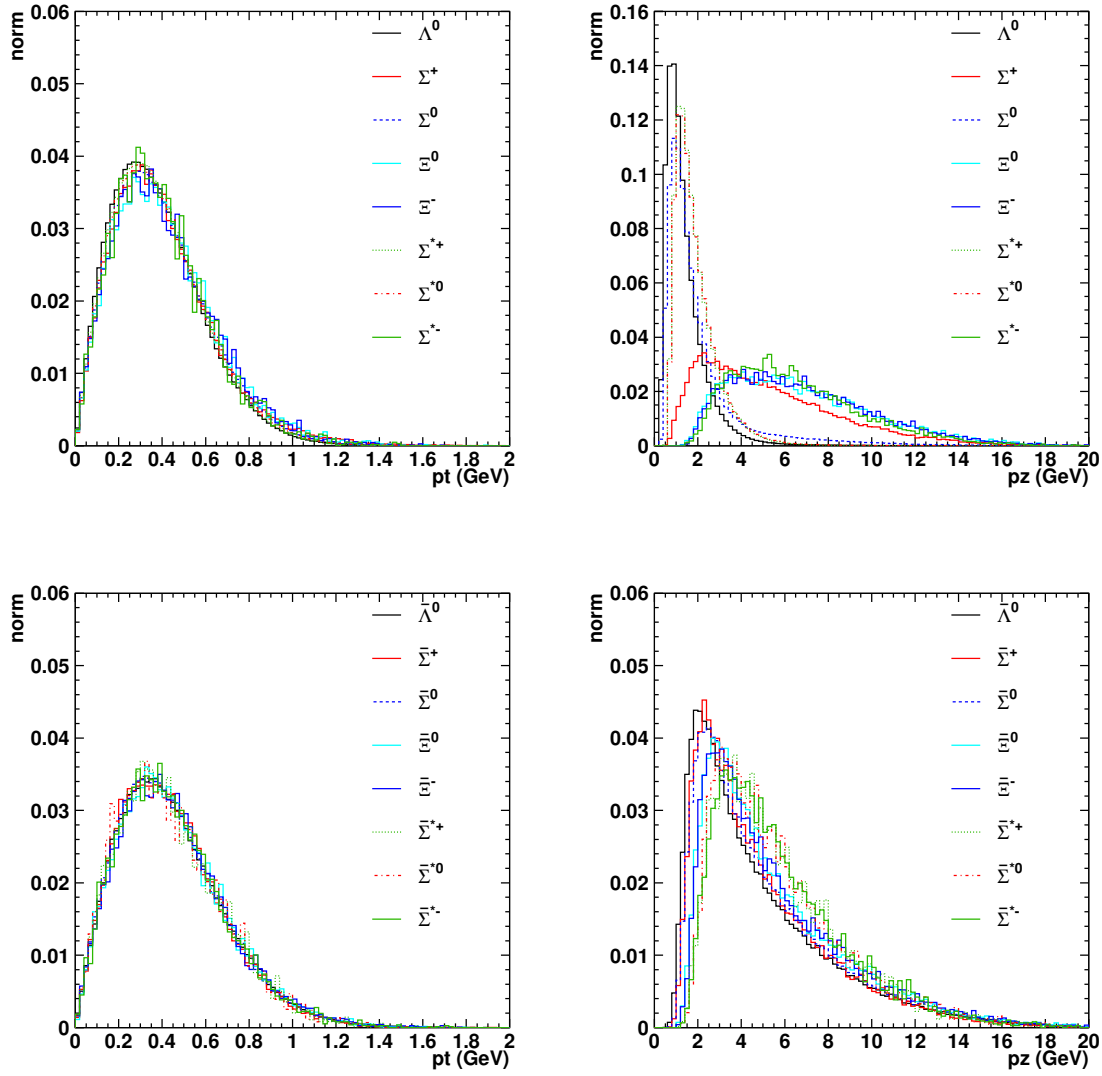

Figure 6.18: The initial momentum distributions for the hyperons under study are shown. The distributions are normalized to the number of simulated events. The p_t (left) and p_z (right) momentum distribution are compared for all hyperons. The upper figures are for the particles and the lower are for the anti=particles.

type	particle [pb]	antiparticle [pb]	ratios $Y/\bar{Y}$	Λ^0/Y	$\bar{\Lambda}^0/\bar{Y}$
Λ^0	1.8410^5	5115	36	1	1
Σ^+	982	650	1.5	188	8
Σ^0	1.6810^4	1918	8.7	11	3
Σ^-	648	734	0.88	284	7
Ξ^0	243	374	0.65	758	14
Ξ^-	235	357	0.66	782	14
Σ^{*+}	3.6510^4	156	233	5	33
Σ^{*0}	1.8210^4	162	112	10	32
Σ^{*-}	115	140	0.82	1.610^3	36
Ξ^{*0}	33	36	0.89	5.610^3	138
Ξ^{*-}	24	34	0.71	7.510^3	148
Ω^-	4	7	0.59	4.410^4	719

Table 6.15: The 4π MC quasi-real photoproduction cross sections for the various hyperons and anti-hyperons. On the right side of the table ratios of particle to anti-particles, Λ^0 respectively $\bar{\Lambda}^0$ to hyperons are shown.

of the different particles. Some have a so-called *soft* distribution with a mean of 1.9 GeV and a spread of 0.6 GeV. This class includes the Λ^0, the Σ and the Σ^{*+}. The initial momentum distribution of the Σ^{*0} is also soft but not shown in the plot. The rest of the hyperons and all anti-hyperons have a so-called *hard* p_z distribution with on average a mean of 5.9 GeV and a spread of 3.2 GeV. A small mass dependence in the hardness of the momentum distributions can also be seen. The initial momentum distribution has a big influence on the yield of particles that are reconstructed in the HERMES acceptance. This has been investigated in more detail in the following section.

Yields and cross sections The MC production without an acceptance requirement is used to determine the predicted yields and cross sections. As was mentioned before, this MC production has been done without simulating the detector response. Thus, there are no efficiencies included in the analysis. For the 10 million events the total particle yields are given in table 6.15. The direct yield, the yield of particles that come directly from the fragmentation and not from decays, is smaller. This can be seen in table 6.16. As nearly all heavier hyperons decay finally in a Λ^0 the indirect contribution depends on the yields of the heavier hyperons. Naturally, the indirect contribution to the Λ^0 hyperon yield is highest, since it is the lightest hyperon at the end of many decay chains. According to the PYTHIA calculation in 4π only about 60 % of the Λ^0 hyperons and 40 % of the $\bar{\Lambda}^0$ anti-hyperons is produced directly. Also the Σ^0 has a sizable contribution of 14 % from the $\Sigma^{*0/\pm}$. About $10-12$ % of the $\Xi^{0/-}$ come from decays of the $\Xi^{*0/-}$. The complete set of the numbers is shown in table 6.16.

The cross sections have been calculated with the MC normalization factor. For this set the normalization factor is $\mathcal{N} = 1.859(6) \cdot 10^{-8}\mu$b. The simulated 4π cross sections are also shown in figure 6.19. It can be seen that the Λ^0, Σ^0, Σ^{*+} and Σ^{*0} particles have a

type	total yield /10^3	direct yield /10^3	ratio	parents to Λ^0 /10^3	fraction	fraction to all Λ^0
Λ^0	9921	6169	0.62	—	—	—
$\bar{\Lambda}^0$	275	110	0.40	—	—	—
Σ^+	53	51	0.97	—	—	—1)
$\bar{\Sigma}^-$	35	34	0.98	—	—	—1)
Σ^0	901	775	0.86	901	0.2	0.09
$\bar{\Sigma}^0$	103	102	0.99	103	0.63	0.38
Σ^-	35	34	0.97	—	—	—1)
$\bar{\Sigma}^+$	39	39	0.98	—	—	—1)
Ξ^0	13	11	0.87	12	0.0	0.0
$\bar{\Xi}^0$	19	17	0.90	19	0.12	0.07
Ξ^-	13	11	0.88	13	0.0	0.0
$\bar{\Xi}^+$	20	18	0.90	20	0.12	0.07
Σ^{*+}	1966	1965	1.0	1839	0.49	0.19
$\bar{\Sigma}^{*-}$	8.4	8.4	1.0	7	0.05	0.03
Σ^{*0}	978	978	1.0	977	0.26	0.1
$\bar{\Sigma}^{*0}$	8.7	8.7	1.0	8	0.05	0.03
Σ^{*-}	6.2	6.2	1.0	5	0.0	0.0
$\bar{\Sigma}^{*+}$	7.6	7.6	1.0	6	0.04	0.03
Ξ^{*0}	1.3	1.3	1.0	—	—	—2)
$\bar{\Xi}^{*0}$	1.9	1.9	1.0	—	—	—2)
Ξ^{*-}	1.8	1.7	0.97	—	—	—2)
$\bar{\Xi}^{*+}$	2.0	2.0	1.0	—	—	—2)
Ω^-	0.2	0.2	1.0	147	0.0	0.0
$\bar{\Omega}^+$	0.3	0.3	1.0	255	0.0	0.0

Table 6.16: The total and direct yield of hyperons and anti-hyperons in 4π and their ratio as predicted by the PYTHIA Monte Carlo. The right side specifies the contribution to the indirect Λ^0 signal. The last column gives the ratio to all Λ^0 hyperons produced. It is noted that hyperons marked with a '1)' in the last column do not decay in a Λ^0. Similarly, it is noted that the Ξ^* marked with with a '2)' decay via a Ξ to 100 % into a Λ^0 hyperon.

comparably high cross section while the cross sections of the other particles follow an exponential decrease with mass. This can be understood considering the initial momentum distributions of these hyperons. A hyperon with a softer initial momentum distribution can be created more easily. The reason is that more of the energy available from the scattering process can be used for the creation of the particle if it does not have to contribute to its longitudinal momentum p_z.

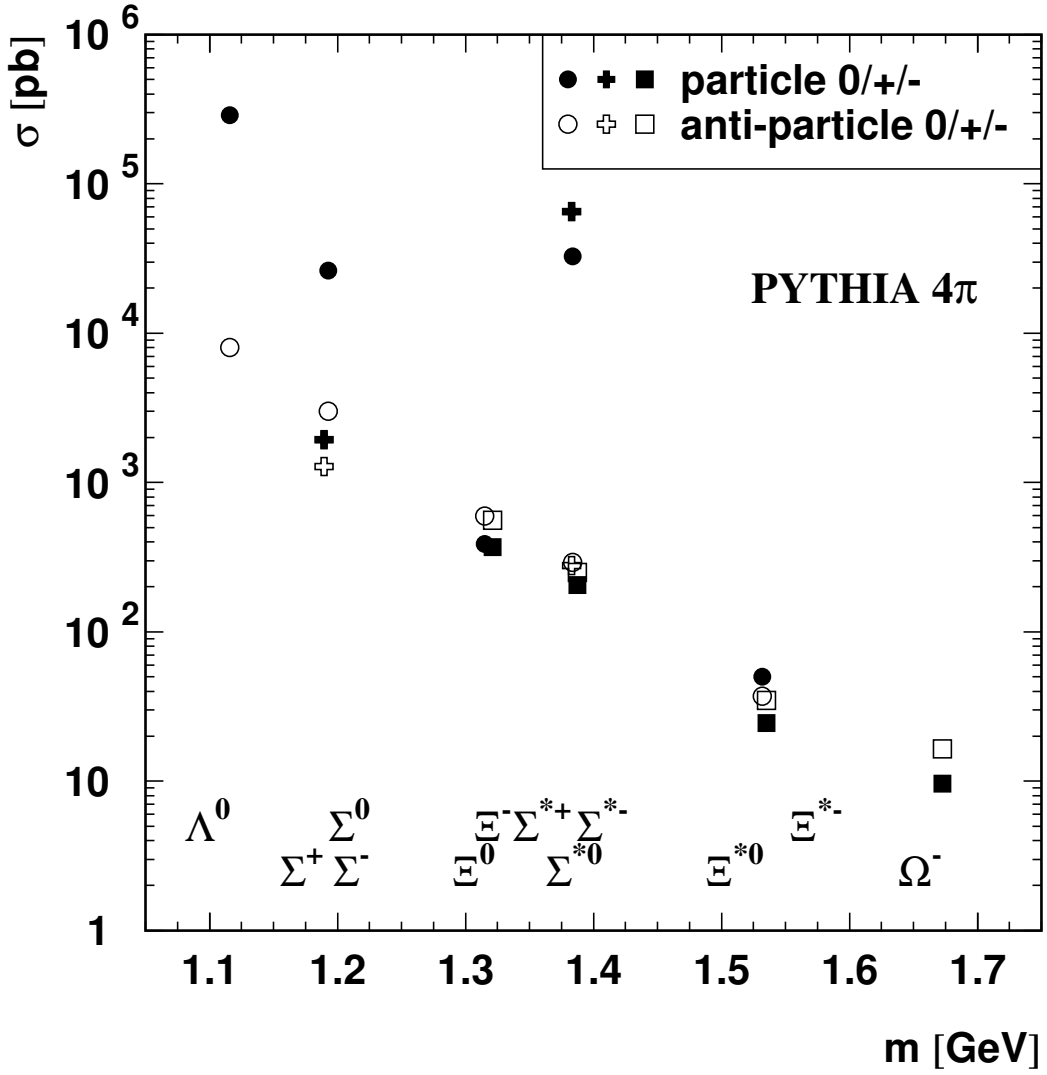

Figure 6.19: The MC quasi-real photoproduction cross section for all hyperons in 4π versus mass. The closed symbols denote particles and the open symbols anti-particles. The sign of the hyperons is encoded in the symbol type. There is no uncertainty assigned to the MC numbers and therefore no error bars are shown.

6.5.2 Monte Carlo simulation for the HERMES acceptance

The main focus of the data analysis in chapter 6.3 and 6.4 was the determination of the particle yields in the HERMES acceptance. The same analysis has also been carried out for MC events generated with PYTHIA. The goal is to be able to compare the MC hyperon production model to the existing data. In addition, the MC also helps to understand the invariant mass spectra of the data with their different backgrounds and signal shapes.

For this analysis a set of 10 million events has been generated. The production is a full MC including the simulation of the detector. For that purpose, all particles in each event have been traced through the detector and the responses of the components have been simulated. This set is used to estimate the efficiency of the cuts, to determine the invariant mass spectra and the particle yields for the hyperons in the HERMES experiment. As the simulation of the detector and the tracking of the events is very time consuming a so-called *selector* for Λ^0s has been used. This selector discards events right after the generation by PYTHIA if no Λ^0 is present. The production has an additional criterion imposed on the tracks of the decay particles of the Λ^0 hyperon. The daughters of the Λ^0, the proton and the pion, are required to have a minimum momentum of 0.5 GeV and their scattering angles are required to pass the box acceptance of the spectrometer. This acceptance cut is realized by requiring the scattering angle θ_x to be between $[0-200]$ mrad and θ_y to be between $[35-160]$ mrad.

Counting the hyperons in the MC tables, the numbers listed in table 6.17 have been found. The first column gives the type of hyperon. The second column the total and the third the direct yield inside the HERMES acceptance. The fifth column gives the number of parents of that type yielding a Λ^0. Next to it is the relative amount of hyperons of that type contributing to the indirectly produced Λ^0s. The last column represents the ratio of Λ^0soriginating from that hyperon to all Λ^0s produced. The Λ^0 again, as explained for the 4π sample, has the lowest relative yield of directly produced particles. The $\Sigma^{0/\pm}$ have contributions from the $\Sigma^{*0/\pm}$ hyperon and all $\Xi^{*0/-}$ hyperons decay into $\Xi^{0/-}$ similar to the 4π MC. With the acceptance requirement included the ratio between Λ^0 and $\bar{\Lambda}^0$ hyperons has changed. This can be understood from the higher p_z momentum of the $\bar{\Lambda}^0$ making it more likely to go forward into the acceptance.

The track reconstruction in the MC has two simplifications compared to the treatment of the data. The first one is that the separation of hadrons and leptons is not simulated. That means that there are no efficiencies for the hadron identification included in the simulation. As discussed in section 3.3.2 the efficiency to identify hadrons is 99 % with a lepton contamination of less than 1 %. Therefore, this efficiency does not play an important role and is not taken into account.

The other simplification in the MC is the particle identification of the RICH detector. As the simulation of the RICH detector is quite involved and time consuming it was decided to skip that part of the simulation during the production of the MC events. Instead, the RICH efficiencies are implemented afterward in the analysis. For every particle type an efficiency versus momentum curve is stored. Then, depending on the momentum of

type	all /10^3 hyperons	direct /10^3	ratio all/direct	parents of $\Lambda^0(\bar{\Lambda}^0)$ /10^3	ratio direct	ratio parents/all
Λ^0	9832	5188	0.53	—	—	—
$\bar{\Lambda}^0$	2173	778	0.36	—	—	—
Σ^+	416	386	0.93	—	—	—
$\bar{\Sigma}^-$	258	248	0.96	—	—	—
Σ^0	1669	1538	0.92	1659	0.36	0.17
$\bar{\Sigma}^0$	849	838	0.99	849	0.61	0.39
Σ^-	278	260	0.94	0.74	0.0	0.0
$\bar{\Sigma}^+$	293	285	0.97	0.16	0.0	0.0
Ξ^0	118	101	0.86	116	0.03	0.01
$\bar{\Xi}^0$	171	151	0.88	169	0.12	0.08
Ξ^-	120	103	0.86	116	0.03	0.01
$\bar{\Xi}^+$	166	145	0.88	161	0.12	0.07
Σ^{*+}	1847	1845	1.0	1725	0.37	0.18
$\bar{\Sigma}^{*-}$	79	79	1.0	71	0.05	0.03
Σ^{*0}	961	959	1.0	952	0.21	0.10
$\bar{\Sigma}^{*0}$	80	79	1.0	75	0.05	0.03
Σ^{*-}	61	61	1.0	56	0.01	0.01
$\bar{\Sigma}^{*+}$	69	69	1.0	63	0.05	0.03
Ξ^{*0}	14	14	1.0	—	—	—
$\bar{\Xi}^{*0}$	19	19	1.0	—	—	—
Ξ^{*-}	18	17	0.98	—	—	—
$\bar{\Xi}^{*+}$	20	20	1.0	—	—	—
Ω^-	2.3	2.3	1.0	1.5	0.0	0.0
$\bar{\Omega}^+$	3.8	3.8	1.0	2.6	0.0	0.0

Table 6.17: Total count of photo-produced hyperons in the HERMES acceptance as evaluated from the PYTHIA MC table. The hyperons have been counted in the MC table and are not reconstructed. The column 'all' denotes how many hyperons of that type have been found in the total sample and the next column how many of those have been produced directly. The fourth column lists the ratio of the numbers shown in the third to the second number. The column 'parents' gives the number of hyperons of that type that are a parent of one of the indirectly produced Λ^0s. The next column quantifies the fraction of indirectly produced Λ^0 originating from this hyperon. The last column indicates the ratio of Λ^0soriginating from that hyperon type to all Λ^0s produced.

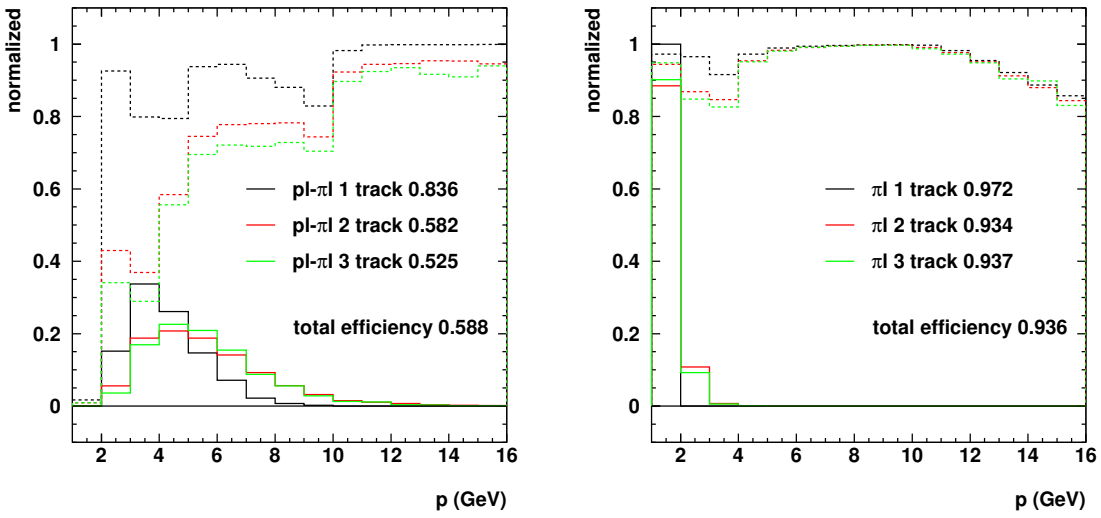

Figure 6.20: RICH particle efficiency for protons (left) and pions (right). The dashed lines are the efficiencies for one, two and more than two particles per detector half. The efficiency for each event type is indicated. The solid lines are the momentum distributions of the proton, respectively, the pion.

the particle a random efficiency is drawn for each track. If this random efficiency has a higher value than the implemented efficiencies for that momentum the track is discarded. Applying this method to the hadron tracks a better description of the particle yields is achieved. Compared to a 100 % efficient particle identification, 45 % of the Λ^0 yield is lost in this way. This loss happens mainly for low momentum Λ^0s, that also decay into a low momentum proton and pion. The efficiency for protons below 4 GeV and events with more than one track per detector half is particularly low. This can be seen in figure 6.20. There the RICH efficiencies are shown together with the normalized momentum distributions for various conditions. The listed total RICH efficiency has been applied to the MC results.

Kinematic distributions In order to assess the quality of the MC simulations, the kinematic distributions for hyperon production are compared to those of the data. Including the correction for the RICH efficiency the MC result is compared to the data. The Λ^0 particle was chosen for a comparison to the data as it is the particle with the highest yield. The distribution in momentum, scattering angle θ and ϕ of the decay products of the Λ^0 are compared. The result of the comparison is shown in figure 6.21. It is seen that data and MC distributions have a comparable shape. Only the low momentum part of the proton distributions show a sizable deviation. These protons originate from so-called *soft* Λ^0s which are the main source of discrepancy between data and MC.

Another comparison is the ratio of Λ^0s reconstructed using a long π track to those reconstructed with a short π track. The result is displayed in figure 6.22. When integrated over the whole momentum range 60 % of the Λ^0s are long tracks and 40 % short tracks. In the MC, on the other hand, the ratio is 40 % long to 60 % short. This suggests an excess

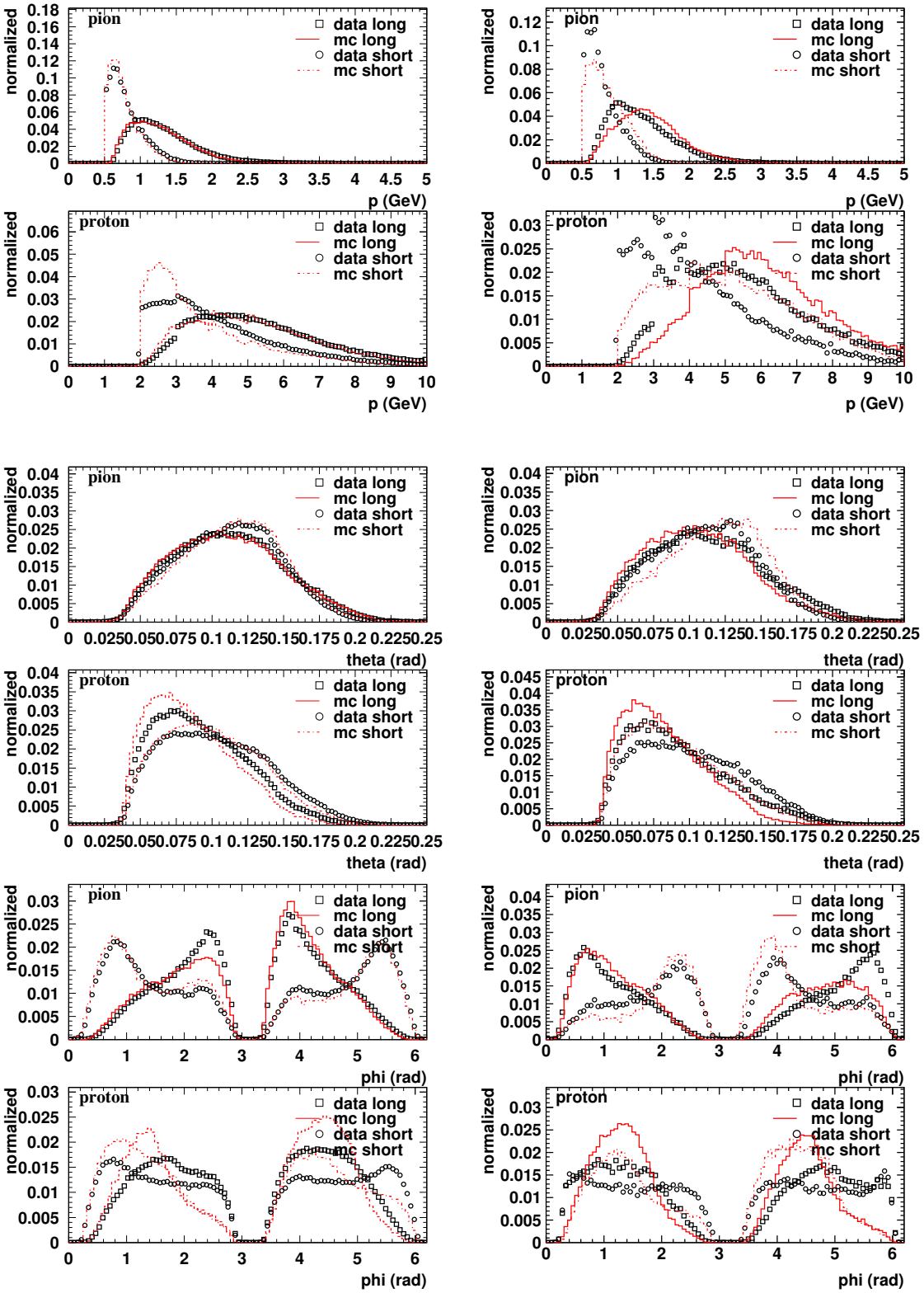

Figure 6.21: Comparison of momentum, θ- and ϕ-angle distribution of protons and pions originating from Λ^0 (left) or $\bar{\Lambda}^0$ (right) photo-produced at HERMES. The distributions are normalized to the number of events. The open symbols are for the data (squares for long tracks and circles for short tracks), while the histogram are for the MC (solid line for long tracks and dashed lines for short tracks).

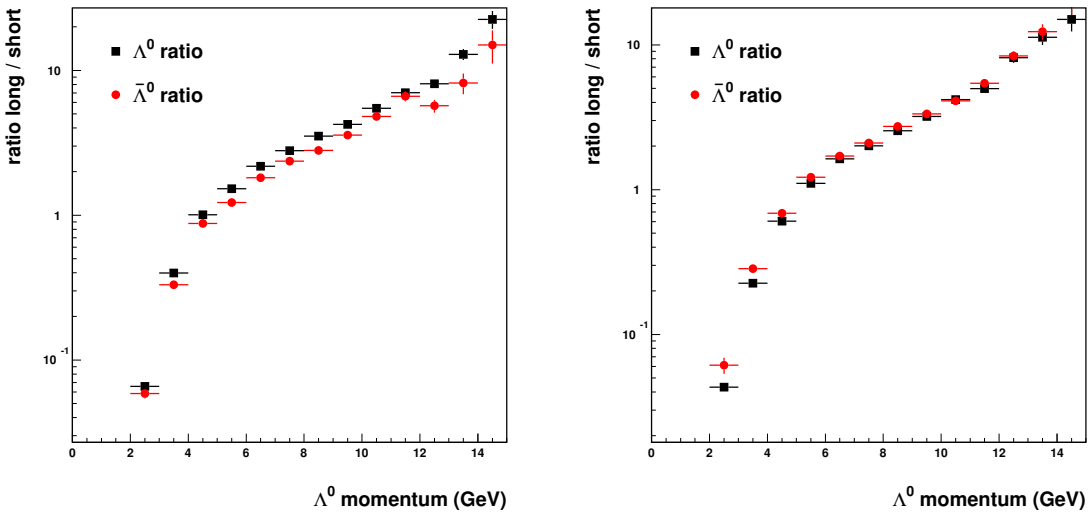

Figure 6.22: Ratio of so-called long to short Λ^0 tracks versus the momentum. On the left side this ratio is shown for the data and on the right for the MC.

of low momentum Λ^0s in the MC with pions of such a low momentum that they are only partially reconstructed. The MC events are all accepted where in the data the events have to generate a trigger. The main physics trigger T21 is unlikely to be fired with only a low momentum proton in the back part of the detector nor will the photo-production trigger fire. Maybe the trigger efficiency for those events makes the difference related to the low momentum Λ^0s comparing data and MC. The dependence of the trigger efficiencies with respect to the momentum of the Λ^0 decay products is currently under study [32].

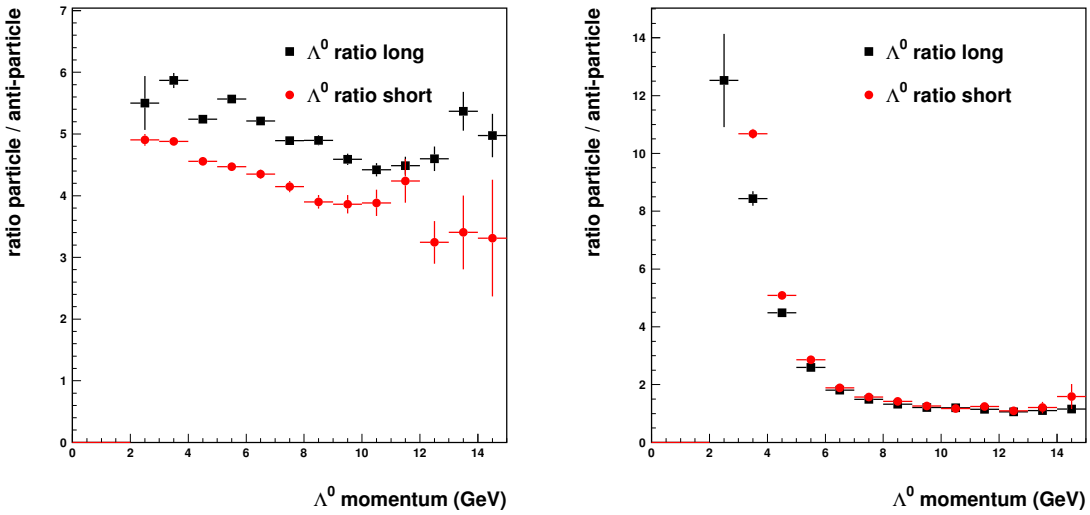

Figure 6.23: Shown is the ratio of Λ^0 to $\bar{\Lambda}^0$ versus the momentum. On the left side this ratio is show for the data and on the right side for the PYTHIA MC.

type	particle [pb]	anti [pb]	$Y/\bar{Y}$	Λ^0/Y	$\bar{\Lambda}^0/\bar{Y}$
Λ^0	163.9 ± 0.9	58.7 ± 0.4	2.79 ± 0.02	1.0 ± 0.0	1.0 ± 0.0
Σ^0	2.06 ± 0.04	1.57 ± 0.03	1.31 ± 0.04	79.4 ± 1.6	37.3 ± 0.8
Ξ^-	0.54 ± 0.02	0.66 ± 0.02	0.81 ± 0.04	305 ± 11	88.9 ± 2.9
Σ^{*+}	2.50 ± 0.06	0.44 ± 0.02	5.7 ± 0.3	75.3 ± 1.6	155 ± 6
Σ^{*-}	0.37 ± 0.02	0.40 ± 0.02	0.92 ± 0.06	514 ± 22	170 ± 7

Table 6.18: Reconstructed MC hyperon cross sections for particles (second column) and the anti-particles (third column). The ratios of particles to anti-particles is shown in the last column. The last to columns show ratios of Λ^0 respectively $\bar{\Lambda}^0$ to the heavier hyperons.

The ratio of the Λ^0 to $\bar{\Lambda}^0$ hyperon yield versus momentum has been investigated as well. The result is shown in figure 6.23. As can be seen in the left figure the data for Λ^0 to $\bar{\Lambda}^0$ are rather stable at a value of $5-6$ with a slight decrease towards higher momentum. The ratio for the short track Λ^0s is slightly lower over the whole momentum range. On the right side the MC result is shown, revealing a strong momentum dependence. For low momenta the ratio is about 12 and decreases fast to about 1.25 for high momenta. The MC shows no difference between short and long track Λ^0. This observation indicates that the MC model as encoded in PYTHIA does not give a completely adequate description of the data. Although the kinematic distribution shown in Fig. 6.21 are fairly well reproduced the results shown in Fig. 6.23 and Fig. 6.22 imply that the yield of low momentum Λ^0 is overestimated.

MC hyperon spectra and cross sections The same analysis has been applied to the hyperon MC results as was used for the data. For the MC production, though, uncorrelated backgrounds are lower due to the lower multiplicities encountered in the MC. However, the combinatorial background is comparable to the data.

The simulated invariant mass spectra for the various hyperons studied are shown in figure 6.24 and 6.25. The first one is the Λ^0 hyperon. The width of the Λ^0 peak is slightly less than found in the data, but also here the $\bar{\Lambda}^0$ width is a bit wider than that of the Λ^0. The second one is the Σ^0. The MC results confirm the high combinatorial background for the decay of a Λ^0 plus a photon. Due to the difficulty of simulating low energy photons the mean value of the peak is higher than in the data.

In figure 6.25 the spectra for the (Λ^0,π)-final states are shown. The mean values of the fits correspond nicely with the book values for the hyperon masses. The width from the Gaussian fits have to be converted to a FWHM value for the $\Sigma^{*\pm}$. The width of the Σ^{*+} is found to be 38(40) MeV and for the Σ^{*-} 42 MeV which is comparable to the values determined from the experimental data. The Ξ^- mass value is with 1322 MeV also comparable to the data while the width of 4 MeV is slightly smaller.

In a very similar way as in Sec. 6.17 the cross sections corresponding to the MC yields are calculated. The PYTHIA MC provides a normalization constant $\mathcal{N}$ which has the unit $\mu barn$ and has to be divided by the number of generated events N_g. The normalization constant provided by the MC production is $\mathcal{N}/N_g = 4.38(1)^{-10}\mu$b. This number is

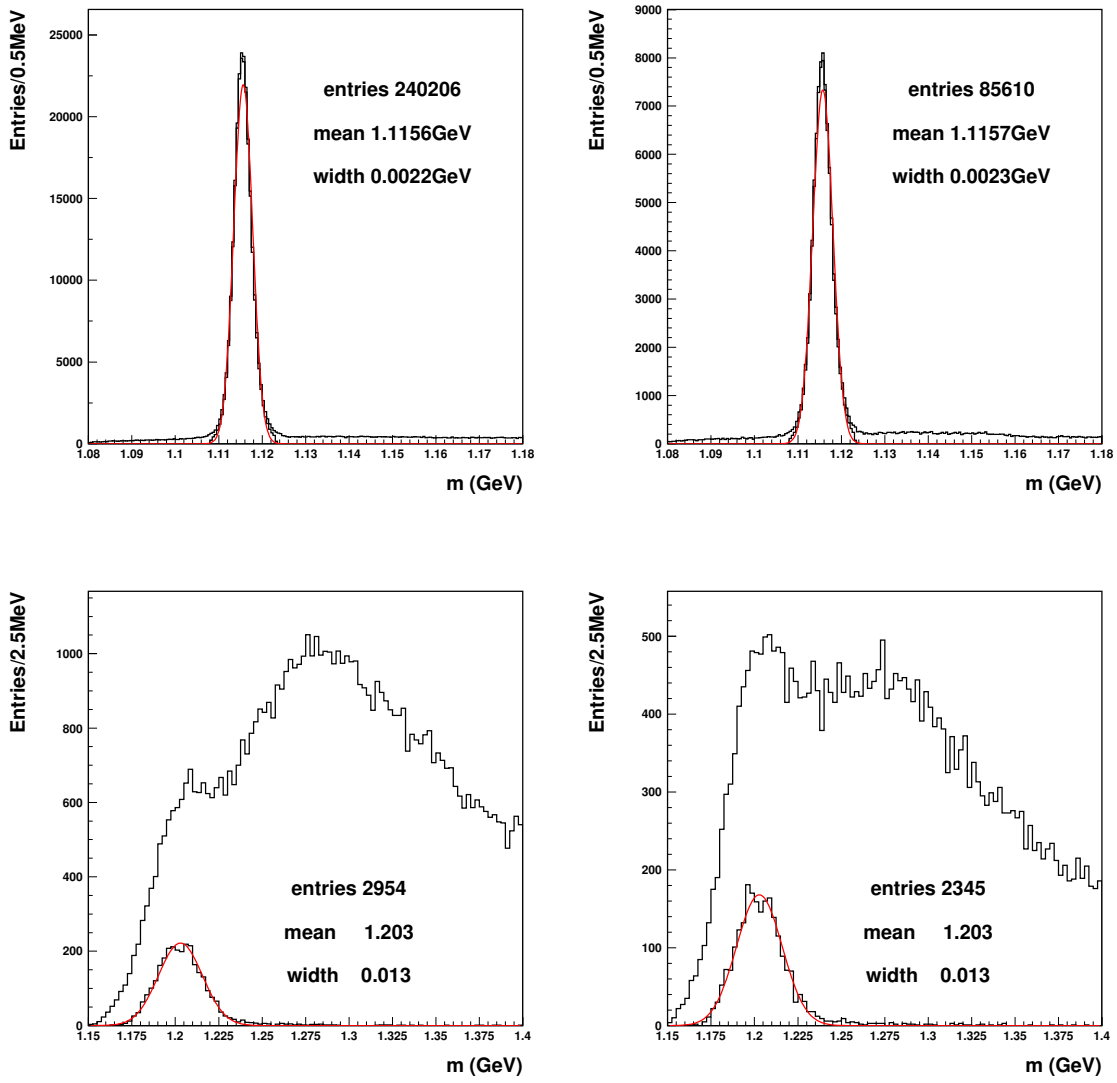

Figure 6.24: The reconstructed invariant mass spectra of Λ^0 and $\bar{\Lambda}^0$ (top panels), and Σ^0 and $\bar{\Sigma}^0$ (bottom panels) as simulated by PYTHIA for quasi-real photoproduction. The fit values of the centroid and the width of the peaks are given in each panel. Further explanations are provided in the text.

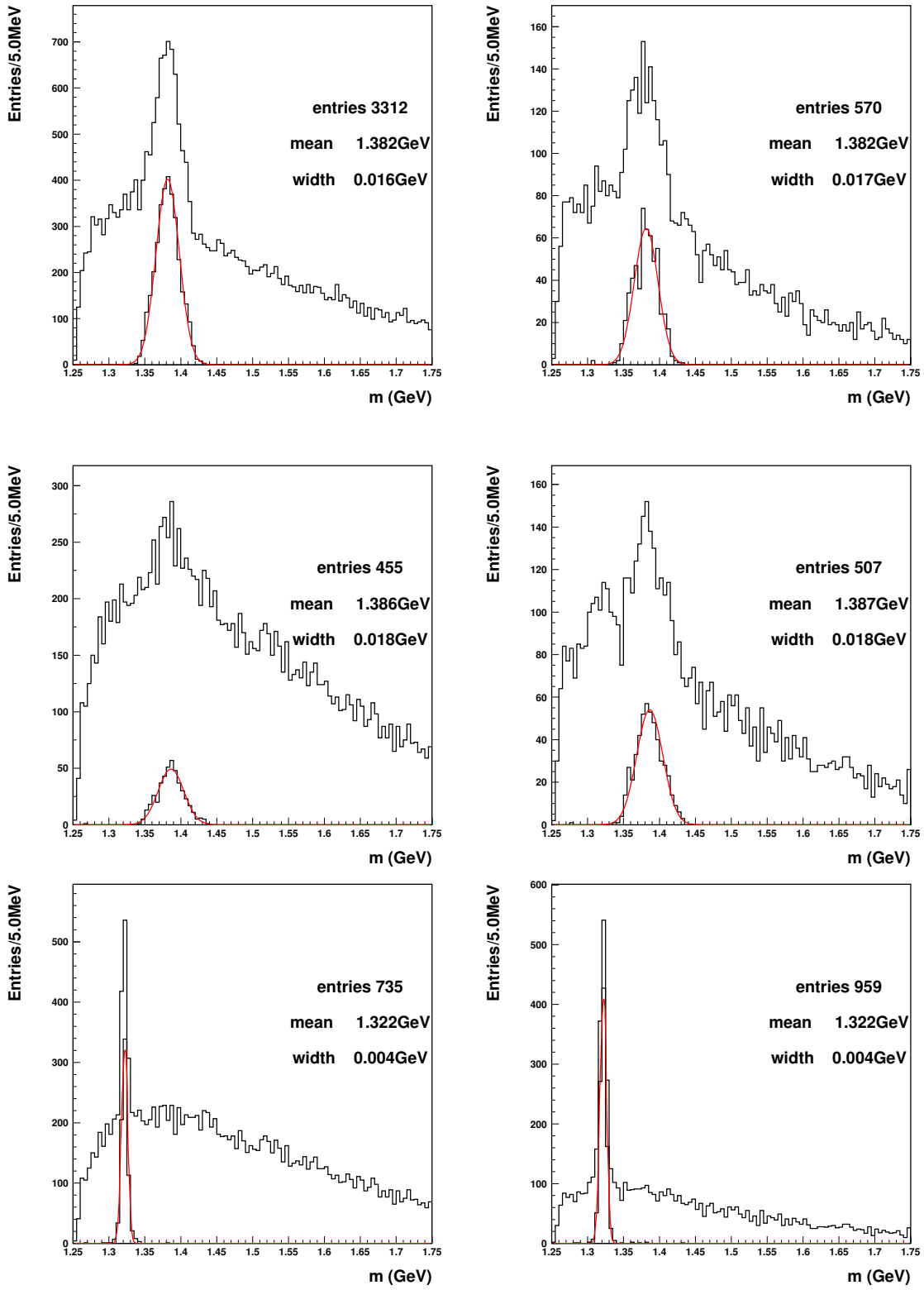

Figure 6.25: The reconstructed invariant mass spectra of the (Λ^0, π)-spectra as simulated by PYTHIA for quasi-real photoproduction. The top panels show the Σ^{*+}, the middle panels show the Σ^{*-} and the bottom panels show the Ξ^-. Shown on the left side is the particle and on the right side the antiparticle. The fit values (Gaussian) of the peaks are also shown in the figures. Further explanations are given in the text.

multiplied by the yields N_{MC} to derive the cross sections like:

$$\sigma_{MC} = \frac{N_{MC}}{B} \cdot \frac{\mathcal{N}}{N_g}, \tag{6.19}$$

with B again the branching ratio of the hyperon. The PYTHIA MC results in the HERMES acceptance can thus be used to calculate cross section predictions. The cross sections in the HERMES acceptance are given in table 6.18 and are shown in figure 6.26. A comparison to the data is made in section 7.2. Here, it is noted that further tuning of the MC parameters to arrive at an improved description of the data is beyond the scope of this analysis. This initial study is a first approach to compare all hyperon yields in data and MC. However, further MC studies should be accompanied by two improvements of the analysis as well. The first one concerns the trigger efficiency for photoproduction of hyperon events by including its momentum. The second one is an improvement of the detector response for decaying particles with respect to the hodoscopes (trigger), RICH (low momentum particle identification) and the reconstruction of neutral tracks in the calorimeter.

6.5.3 Monte Carlo DCAY simulations

The DCAY event generator is a simple toy Monte Carlo tool, its purpose is to simulate two-body decays in a fast way. The input which has to be provided is the mass and width of the decaying particle together with its transverse and longitudinal momentum. From that information random decays are calculated which can then be traced through the detector simulation. The particles are assumed to decay isotropically in ϕ. This is a fast and efficient way to generate one type of hyperon decay and study the geometrical acceptance.

Two studies have been carried out. First, the geometrical acceptance of the Λ^0 hyperon for a range of different initial momenta has been examined. Second, for all analyzed hyperons the geometrical acceptance, using the initial momentum distributions as determined by PYTHIA, has been derived. Additionally, a so-called Λ^0-yield factor for each hyperon has been determined. This factor gives the number of Λ^0 hyperons that are reconstructed in HERMES and which originate from a decay from a given heavier hyperon, divided by the number of hyperons of that type that are reconstructed in HERMES

$$C^Y_{\Lambda^0} = \frac{N^{acc}_{Y\to\Lambda^0}}{N^{acc}_Y}. \tag{6.20}$$

Utilizing this factor and the various hyperon yields from the experimental data, it can be estimated how many Λ^0 originate from decays of heavier hyperons. These factors are primarily determined by the experimental determined hyperon yields and can be compared to the subprocess fractions evaluated by PYTHIA.

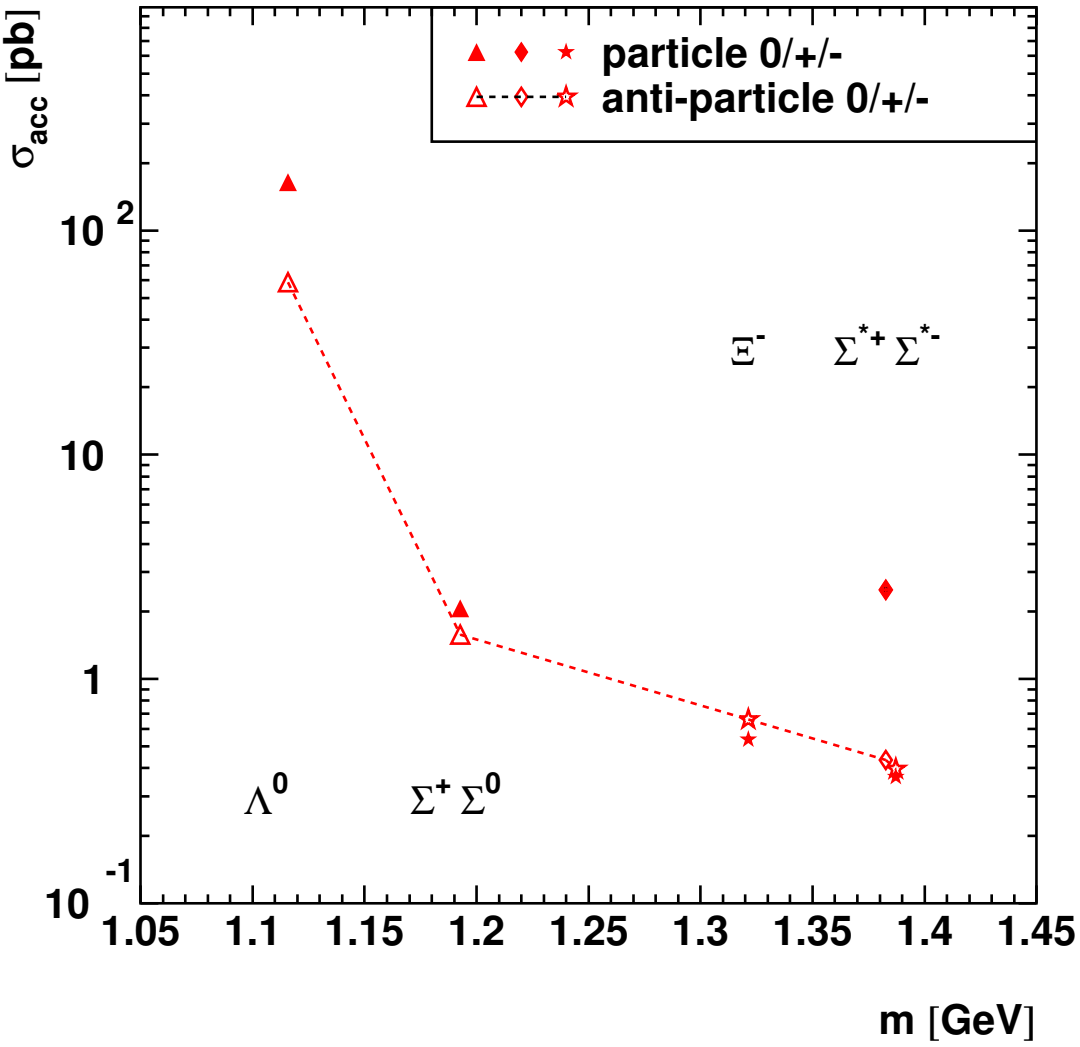

Figure 6.26: The MC cross sections for photo-produced hyperons observed in the HERMES acceptance. The errors on the cross sections are too small to be seen. The dashed line connects the cross sections for antiparticle to guide the eye.

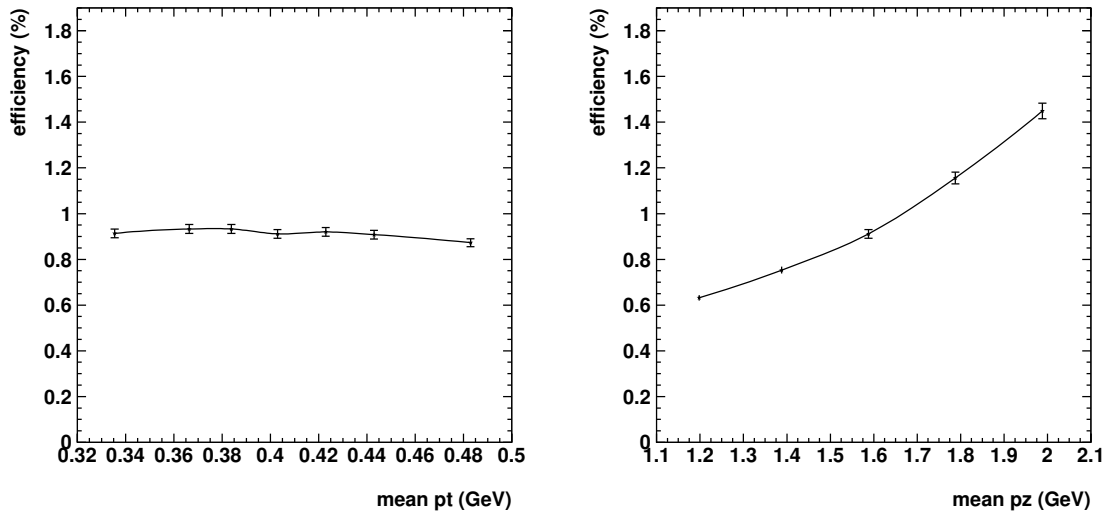

Figure 6.27: In this figure the dependence of the geometrical acceptance for Λ^0 hyperons is shown for different initial momenta used to generate the events with the DCAY generator. On the left side the dependence of the geometrical acceptance on the transverse momentum p_t is shown for $p_z = 1.6$ GeV. On the right side the same dependence is shown for the longitudinal momentum p_z is shown for $p_t = 0.4$ GeV.

Reconstruction efficiency

For the Λ^0 decay different initial momentum distributions were used to generate events. For these distributions the geometrical acceptance was calculated. As can be seen in the left plot of figure 6.27, the transverse momentum p_t of the initial distribution has only a small influence on the geometrical acceptance. For the tested range from 0.34 GeV to 0.48 GeV the efficiency changed by only a few percent. In contrast, the p_z dependence, shown in the right plot, has a large influence. Here the efficiency rises from 0.6 % to nearly 1.5 % going from 1.2 GeV to 2 GeV. The harder the initial p_z momentum distribution is, the more likely it is that the particle is reconstructed in the acceptance. This can be understood as the acceptance is forward and the decay products have to have a minimum momentum to be able to pass through the detector. When generating 'real' physics events this dependence on the initial momentum is, however, dominated by another effect. Generally, particles with a high momentum have a much lower probability to be created. This effect more than compensates the better geometrical acceptance. This effect can be seen comparing the Λ^0 and $\bar{\Lambda}^0$ efficiency and yield. The efficiency for the $\bar{\Lambda}^0$ is 13 times higher than that of the Λ^0 while the net yields have an opposite ratio.

The second analysis utilizing the DCAY generator is the estimation of the reconstruction efficiency of the hyperons which can be used to estimate the feeding. As mentioned before the initial momentum distributions of the hyperons were taken from a 4π PYTHIA MC. The DCAY generator produces just the wanted decay products and no background. The decay vertex is distributed along the z-axis modeled after the HERMES target density.

type	efficiency [%]	4π yield [nb]	Λ^0 yield factor	Λ^0 yield [pb]
Λ^0	0.317±0.002	846±103	—	—
$\bar{\Lambda}^0$	4.15 ±0.02	11.2±1.4	—	—
Σ^+	0.158±0.005	21.8±3.2	—	—
$\bar{\Sigma}^-$	0.174±0.009	8.3±1.6	—	—
Σ^0	0.018±0.001	251±34	23.3± 1.7	1027±155
$\bar{\Sigma}^0$	0.101±0.002	10.6±1.8	17.1± 0.7	184± 32
Ξ^-	0.604±0.009	1.9±0.4	3.9± 0.1	45± 9
$\bar{\Xi}^+$	0.438±0.005	0.9±0.2	4.1± 0.2	16± 4
Σ^{*+}	0.016±0.001	177±34	1.7± 0.1	48± 9
$\bar{\Sigma}^{*-}$	0.442±0.005	0.7±0.4	4.7± 0.1	15± 7
Σ^{*-}	0.533±0.006	3.8±0.6	4.5± 0.1	90±14
$\bar{\Sigma}^{*+}$	0.433±0.005	1.2±0.4	4.6± 0.1	25± 8
Ω^-	0.30 ±0.01	0.10±0.01	7.2± 0.3	1.9± 0.2

Table 6.19: On the left side the reconstruction efficiency for hyperons and the resulting 4π cross sections after extrapolating the data yields is shown. On the right side are given the Λ^0 yield factor determined with the DCAY generator and the corresponding amount of Λ^0 in the acceptance.

By including a decay length for long-lived particles the efficiency is reduced. In the case of the Λ^0 the reduction in efficiency is about 25 % and for the $\bar{\Lambda}^0$ it is about 30 %.

The efficiency is calculated as the ratio of the number of reconstructed hyperons in HERMES including all cuts divided by the number of generated events. The result of the efficiency study is shown in table 6.19 and figure 6.28. The following observation can be made on the basis of the efficiency study. While the efficiency drops by about a factor of 10 when going from two-particle to three-particle final states, about the same factor 10 is found from the difference between hyperons with a soft or hard initial momentum distribution. Moreover, clearly the efficiency to reconstruct a photon or a π^0 from two photons is lower as that of a charged π due to the low efficiency of the calorimeter for photon detection. As a result sizable fluctuations are observed in the overall efficiency.

Taking the derived efficiencies for hyperon reconstruction the data yields are extrapolated to 4π cross sections. The results are shown on the right side of figure 6.28.

Lambda-yield factor As all the hyperons in this analysis decay via a Λ^0 an additional number can be extracted from the DCAY study. This additional number is the so-called Λ^0 yield factor $C^Y_{\Lambda^0}$, as defined above. The resulting values of $C^Y_{\Lambda^0}$ for the various hyperons are listed in table 6.19. Multiplying the measured hyperon yields with this number gives an estimate of the fraction of reconstructed Λ^0s that are coming from decays of heavier hyperons independent of whether the heavier hyperon itself is reconstructed or not (see Eq. 2.3).

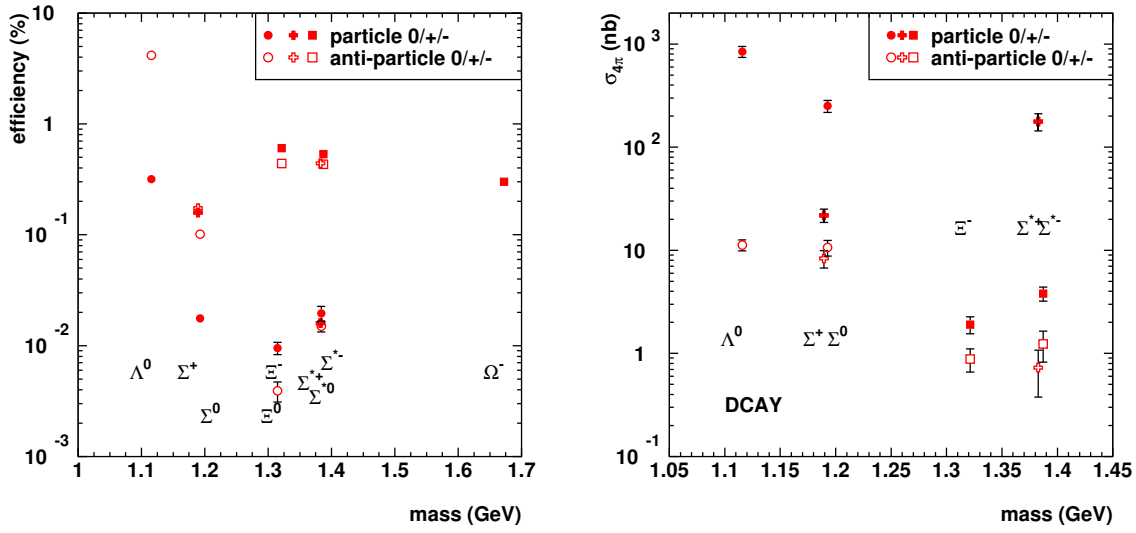

Figure 6.28: On the left the hyperon reconstruction efficiency determined with the DCAY generator is plotted versus the mass of the different hyperons. On the right the extrapolated 4π cross sections, utilizing the efficiencies, is plotted versus the mass of the hyperons.

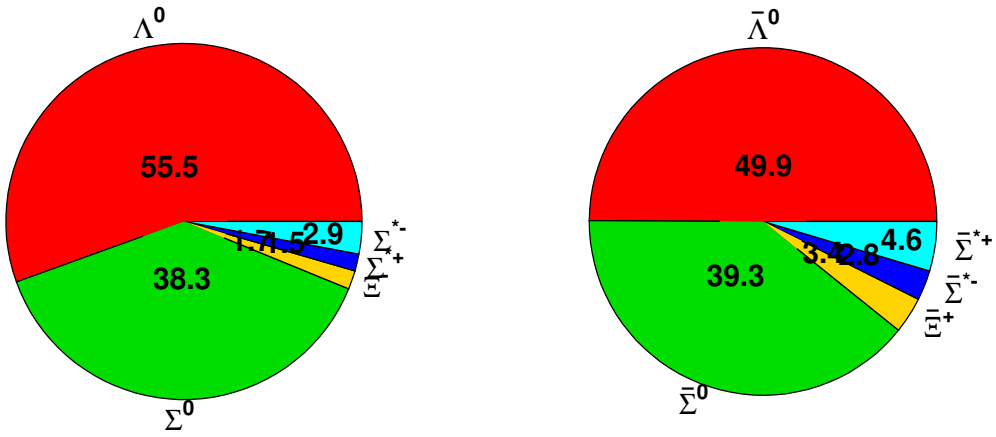

Figure 6.29: Subprocess fraction of the Λ^0 sample derived from the measured hyperon yields. On the left side the Λ^0 results are shown, while the results for the $\bar{\Lambda}^0$ are shown on the right. The values are given in percent of the total yield. The unknown contribution from the neutral heavier hyperons is not taken into account. The numbers displayed correspond to those listed in table 6.19.

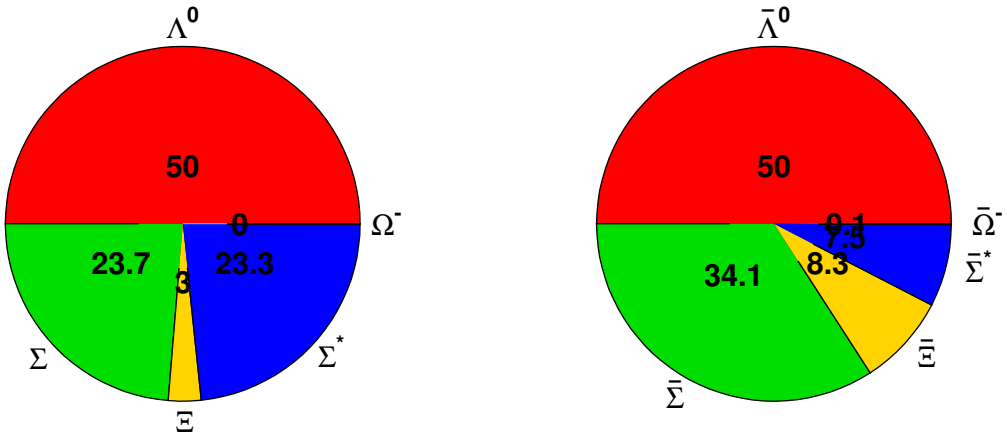

Figure 6.30: Integrated subprocess fractions for the different hyperon flavors contributing to the Λ^0 sample. The numbers are derived from PYTHIA MC simulations in the HERMES acceptance.

6.5.4 Subprocess fractions

Apart from the cross section studies, subprocess fractions for the Λ^0 and $\bar{\Lambda}^0$ hyperon have been evaluated. Knowledge of the subprocess fractions of Λ^0 production is especially relevant for polarization measurements since Λ^0s produced via the decay of heavier hyperons may dilute the signal (see sec. 2.1.1). In this section the results of two methods used to determine the subprocess fractions are presented.

The first method is based on the experimental measured hyperon yields N_Y and the lambda-yield factor C_Λ^Y as determined by DCAY (see Sec. 6.5.3). The result of this method is given in table 6.19 and visualized in the pie plots shown in figure 6.29. As can be seen the contribution of heavier hyperons adds up to about 50 % of the Λ^0 sample. There is, however, an unknown contribution of hyperons like the Σ^{*0} since these have not been reconstructed in the data. Due to similar production mechanisms it is expected that the contribution of the Ξ^0 and Σ^{*0} are similar to their charged equivalents. As these contributions are small, the result presented in figure 6.29 will not be much effected.

The second method is based on the fully simulated and tracked MC result. The fraction of Λ^0s either produced directly in the fragmentation process or those originating from heavier hyperons are evaluated in one simulation. The Λ^0 hyperons have been reconstructed in the same way as for the data as was explained in section 6.3. A scattered DIS lepton had to be present in the event to be able to calculate the kinematic variables z and x_f. The required presents of a detected lepton reduces the yield and might have some influence on the kinematical distributions. This difference is not expected to influence the overall behavior. In addition, the direct parent of the Λ^0 hyperon has been identified from

the MC output if the Λ^0 was not directly produced. This method is entirely based on PYTHIA and does not make use of any experimental inputs (apart from the HERMES acceptance).

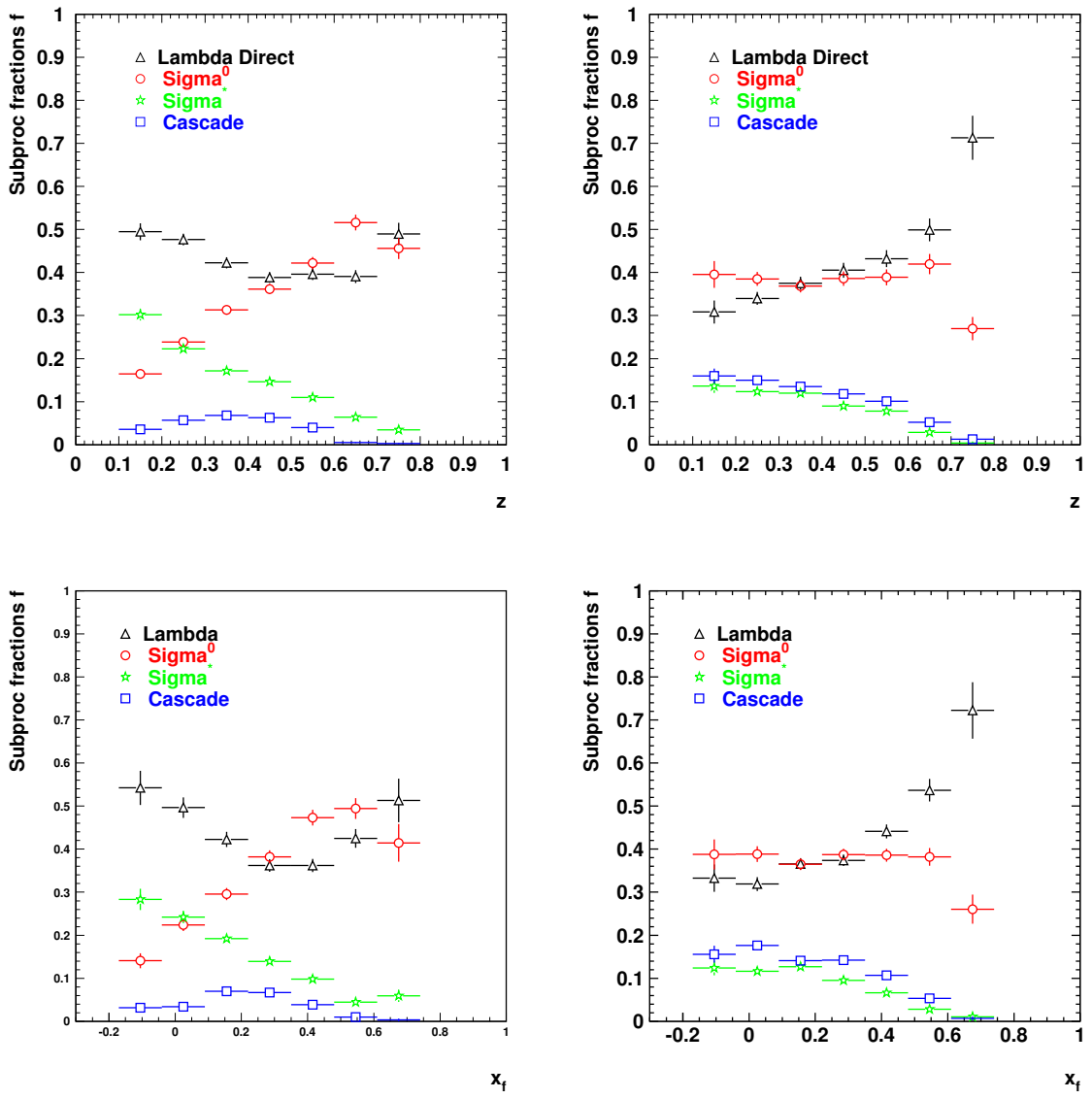

Figure 6.31: Fractional contributions of various hyperons to Λ^0 (left) hyperon production and $\bar{\Lambda}^0$ hyperon production (right) versus the hadronic variables z (top) and x_f (bottom).

The results are shown in figure 6.31 where the fractional contributions of various hyperons are plotted versus the variable z (top panels) and x_f (bottom panels). The very low ($z < 0.1$) and high ($z > 0.8$) bins have been excluded from the plot, because the MC is known to be unable to predict processes in that kinematical domain accurately and because the experimental statistics are also known to be very low in that domain. The result are also represented -in the same format as was used for method one- in fig. 6.30. In general, it can be concluded that about 50 % of the Λ^0 hyperons are directly produced in

the fragmentation process, and the largest contamination originates from the Σ^0. While the fractional contribution of the Λ^0 is rather stable versus the kinematic variable the fractional contribution of the different parents vary.

Chapter 7

Summary

The spin structure of baryons can be probed with the use of directly produced Λ^0 hyperons. In such analyses, the polarization of the Λ^0 is correlated with that of the target or the beam. However, in these analyses one has to account for the fact that the Λ^0 polarization is modified by Λ^0 particles which are produced from the decay of heavy hyperons such as Σ's and Ξ's.

In the first part of this thesis, the development of a new silicon detector for the HERMES experiment know as the Lambda Wheels, and the results obtained with this new device, are discussed. The second part describes the results of an analysis of quasi-real photoproduction of various hyperons at HERMES. This analysis is focused on a key issue in Λ^0 hyperon production, namely the contribution of Λ's originating from the decays of heavier hyperons. Since it is *a priori* not clear in which respect the Λ's produced from decays of heavier hyperons contribute to the polarization of the directly produced Λ's, it is crucial to understand the Λ production mechanism before such data can be used to study the spin structure of baryons.

7.1 Summary of the hardware project

The installation and commissioning of the Lambda Wheels in the HERMES experiment at DESY in the year 2002/2003 has led to a successful period of data taking. As shown in the chapter 4 the detector and its components meet the design specifications and are since then included as a standard component of the HERMES spectrometer. After the commissioning, the device was successfully operated; for the present data an average number of 3.1 tracks per event for the completely working detector with eleven modules was found. Additionally, it was shown that the detector can be aligned with respect to the HERMES frame with a precision ranging from 0.2 cm for the z position to 0.002 cm for the y position. Track reconstruction efficiencies of up to 92 % for a single module have been achieved. On average, the angular resolution for the complete detector is 3 mrad. Finally, a vertex resolution at $z = 0$ cm of 0.1 cm has been determined. These numbers

are in agreement with the expectations and show that the implementation of the new tracking device was successful.

Due to the fact that the Lambda Wheels are in such close proximity to the beam-pipe, a suitable device is needed to protect them from accidental beam losses near the target region. A Beam Loss Monitor (BLM) has been designed for this purpose, and was installed in 2001. After commissioning, it has been connected to the dump magnet in 2002. Since then, it was working reliably. It is the fastest beam dump currently installed at HERA. While beam dumps are occasionally triggered by the BLM, it has no detrimental effect on the operation of the accelerator.

7.2 Main conclusions of the hyperon analysis

For the first time it has been possible to reconstruct in a consistent way, in one analysis, all hyperons that can be observed in HERMES. First, the Λ^0 hyperon, which is included in most of the heavier hyperon decay channels, has been studied. Next, two Σ hyperons were investigated. The positive Σ^+ does not have a Λ^0 hyperon in its final state, but the neutral Σ^0 does. The Σ^0 hyperon might be responsible for the largest contribution of non-directly produced Λ^0 hyperons. Finally, the cascades (Ξ) and the excited sigmas Σ^* have been reconstructed. Only the charged states were accessible in this analysis. The heavier neutral hyperons decay into π^0 mesons and then further into photons causing a smearing of the signal that prevents it from exceeding the background. The excited cascades fall into a different class of events since the final state contains at least four charged tracks, and hence have a limited reconstruction efficiency. For the Ω hyperon only an upper limit has been derived.

Furthermore, the purity of Λ^0 photo-production at HERMES has been investigated. Using PYTHIA the purity was evaluated with respect to the kinematical variables z and x_f, revealing a clear dependence. By integrating these dependencies the subprocess fractions shown in figure 6.30 have been found. According to the Monte Carlo simulations, about 50 % of the Λ^0 signal is therefore predicted to be due to the decay of heavier hyperons.

For the first time the PYTHIA MC predictions for the purity of Λ^0 production have been compared to experimentally determined subprocess fractions, which are using the measured hyperon yields as an input. The results are shown in figure 6.19. Comparing the two results for the subprocess fractions several conclusions can be drawn. Both predict that about 50 % of the Λ^0s are produced directly. However, the results for the single contributions from the heavier hyperons vary between the two methods. While the method using the experimental results attributes the highest weight to the Σ^0, the method using only PYTHIA predicts a more equally shared contribution from Σ^0 and Σ^* hyperons. Both results have in common that contributions from even heavier hyperons play no important role in the Λ^0 yield. Therefore, in any analysis that deals with Λ^0 hyperon production, such as Λ polarization measurements, a correction for the dilution of Σ^0 and Σ^* hyperons needs to be taken into account. It should also be concluded that analyses in which such corrections have been included based on PYTHIA MC simulations

need to be reconsidered. The present analysis shows that -most likely- it is sufficient to evaluate a correction based on the Σ^0 hyperon alone.

Utilizing Monte Carlo event generators it was also possible to derive hyperon production cross sections in the HERMES acceptance. Moreover, an extrapolation from the HERMES acceptance to 4π has been made on the basis of estimates of the efficiency for effective acceptance of HERMES for hyperon production derived from the MC.

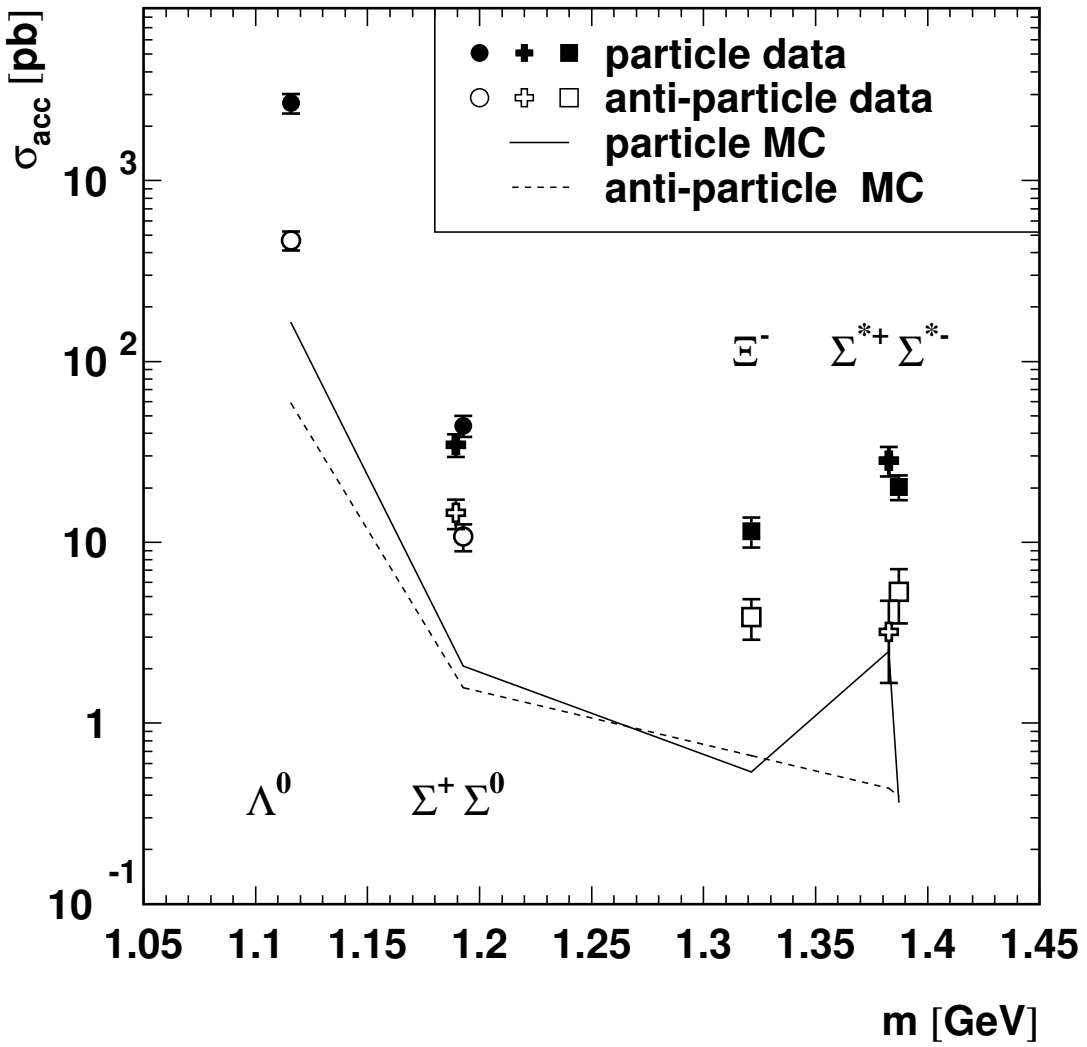

Figure 7.1: The quasi-real photoproduction cross sections in the HERMES acceptance versus the mass of the hyperons are shown for the data and the PYTHIA MC. The charge of the particles is encoded in the marker type. The circles, crosses and squares correspond to neutral, positive and negative hyperons, respectively. The closed (open) points show the (anti-)particle yields. The solid (dashed) line is for the MC (anti)-particle prediction.

The comparison between data and MC cross sections in the HERMES acceptance is shown in figure 7.1. As can be seen, for all hyperons, the MC predictions for the cross sections are on average a factor of 16 smaller than observed. The mass dependence of the cross section is quite similar. Comparing the predicted MC cross sections to the measured cross sections, two observations can be made. First, the MC cross sections are always lower than the cross sections derived from the data. This points to an underestimation of the production cross section in the MC generator. Secondly, the ratio between particles and anti-particles is substantially lower in most cases for the MC compared to the data. For the Ξ^- this ratio is opposite.

The correction to the 4π cross section including all efficiencies can only be determined from the Monte Carlo simulation of the detector. The extrapolated cross section in 4π for the HERMES kinematics can be calculated using the MC efficiency using

$$\sigma_{4\pi} = \sigma_{acc}/\epsilon_g. \tag{7.1}$$

The efficiency ϵ_g is the ratio of the MC cross section in the HERMES acceptance divided by the 4π MC cross section.

The number of counts as well as the luminosity measurement carry uncertainties which are relevant for the cross section calculation. The largest uncertainty comes from the efficiency determination with the MC. As the MC in the HERMES acceptance underestimates the data substantially, the hyperon production model contained in PYTHIA is incomplete or not sufficiently well tuned. Hence, the extrapolation to 4π is uncertain by an unknown factor as long as this discrepancy is not resolved. For the energies of the HERMES experiment there exists only one model for baryon production, namely the diquark model implemented in PYTHIA. Other models like the POPCORN [43] model are only applicable to higher energies. For future MC tuning attempts it would be necessary to include also heavier hyperon rates and other models such that a better description can be achieved of the cross section and subprocess fraction data.

The HERMES hyperon cross sections extrapolated to 4π are shown in figure 7.2. In this case the cross sections are normalized by (2J+1) in accordance with the e^+e^- production results shown in fig.2.3. It also shows the upper limit for Ω^- photo-production and the cross sections for $\Lambda(1520)$ and Ξ^{*0} production taken from Ref. [10].

The exponential decrease of the production cross section has been investigated. As can be seen from figure 7.2, there is a different slope for particles and for anti-particles. An exponential fit to the first three neutral particles has been performed. The two slopes gave an exponential decay of -31.0 ± 1.0 and -14.5 ± 0.5 for the particles anti-particles, respectively. Other experiments have also determined the slope parameter of an exponential decay. For instance, a similar fit to the OPAL data yields a slope of -9.3 ± 0.3. The present result is clearly steeper than the slopes seen in the OPAL experiment shown in figure 2.3. This results indicates that the production mechanism of hyperons is also relatively different when comparing DIS to e^+e^- experiments. In order to be able to use hyperon production for investigating baryon spin structure, an improved description of Λ^0 quasi-real photo-production is needed.

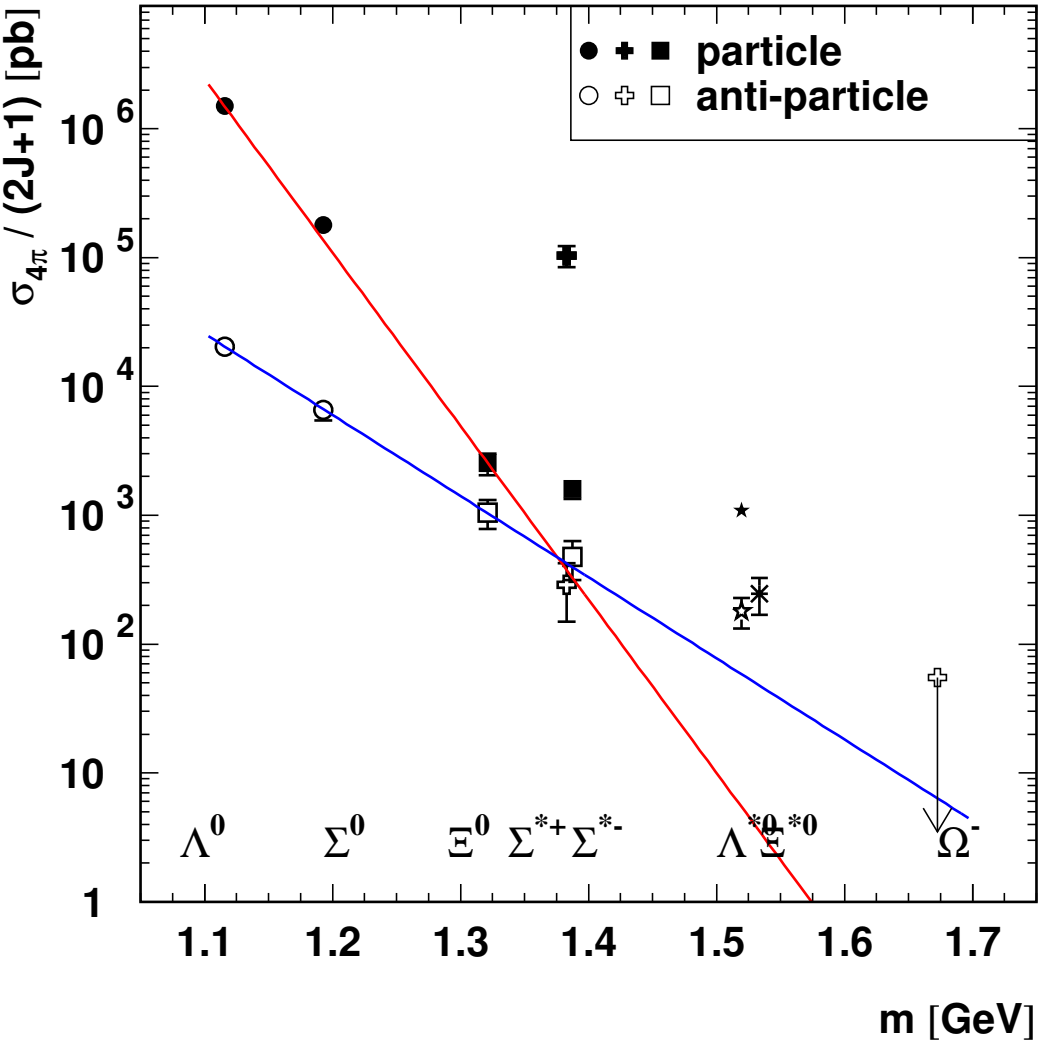

Figure 7.2: The quasi-real photoproduction cross sections for various hyperons extrapolated to 4π are shown versus their mass. The vertical axis is scaled with $(2J+1)$. For particles solid symbols are used and for the anti-particles open symbols. The charge of the particles is encoded in the marker type. The charge of the particles is encoded in the marker type. Additionally, the upper limit for the Ω^- is shown. Also the $\Lambda(1520)$ and the Ξ^{*0} from [10] are shown.

Samenvatting

Hyperonen van het type Λ^0 kunnen worden gebruikt om de spin structuur van barionen te onderzoeken. Hier wordt gebruik gemaakt van het feit dat de polarisatie van het Λ^0 barion is gecorreleerd met de polarisatie van tref-gas en/of de bundel. Echter, in dit soort analyses moet men rekening houden met het feit dat de polarisatie meting van het Λ^0 deeltje verstoord wordt door de bijdrage tot deze polarisatie meting van Λ^0 die ontstaan door het verval van zware hyperonen zoals de Σ en Ξ deeltjes.

In het eerste deel van dit proefschrift worden de ontwikkeling van een silicium detector, genaamd Lambda Wheels, en de daarmee behaalde resultaten besproken. Vervolgens worden in het tweede deel de resultaten van een analyse naar 'quasi-real photoproduction' van verschillende hyperonen met behulp van de HERMES detector beschreven. Speciale aandacht wordt besteed aan de productie van Λ^0 hyperonen door het verval van zware hyperonen. Aangezien het *a priori* niet duidelijk is hoe sterk en op welke manier de Λ^0's van hyperon verval bijdragen aan de polarisatie van alle Λ^0's, is het van essentieel belang om het Λ^0 productie mechanisme te bestuderen, voordat zulke gegevens gebruikt kunnen worden voor de spin structuur studie van barionen.

Samenvatting van het hardware projekt

De installatie en ingebruikneming van de Lambda Wheels in het HERMES experiment op DESY in het seizoen 2002/2003 heeft geleid tot een succesvolle operatie van de sub detector. Zoals beschreven in hoofdstuk 4, voldoen de Lambda Wheels aan de eisen die aan het ontwerp gesteld werden. Sindsdien zijn de Lambda Wheels een standaard onderdeel van de HERMES spectrometer geworden. Een gemiddelde van 3.1 sporen per interactie worden door de sub detector waargenomen, waarbij 11 modulen in de Lambda Wheels werden gebruikt. Bovendien is gebleken dat de Lambda Wheels uitgericht kunnen worden met betrekking tot het HERMES assen stelsel met een nauwkeurigheid variërend van 0.2 cm langs de z-as tot 0.002 cm langs de y-as. Spoor reconstructie efficiëntie tot een waarde van 92% voor een individuele module werden gevonden. Een hoek-oplossend vermogen van 3 mrad en een z-vertex resolutie van 0.1 cm voor $z = 0$ cm, laat zien dat de detector voldaan heeft aan de verwachtingen en dat de installatie en in gebruik name van dit apparaat succesvol was.

Conclusies van de hyperon analyse

Voor de eerste keer zijn in een enkele analyse alle in de HERMES detector waarneembaar hyperonen gereconstrueerd. Er is begonnen met de bestudering van het Λ^0 hyperon. Dit omdat dit deeltje een zeer kenmerkend vervals product van zware hyperonen is en omdat de bijdrage van zware hyperonen aan Λ^0 productie hetgeen is waar het uiteindelijk om gaat. Daarna zijn de twee Σ hyperonen onderzocht. Het positief geladen Σ hyperon

produceert weliswaar geen Λ in zijn verval, maar komt wel voor in het verval van het Σ^0 hyperon. Het is dit ongeladen zware hyperon dat waarschijnlijk verantwoordelijk is voor de indirecte productie van Λ^0 hyperonen. Tenslotte zijn ook de xi (Ξ) en aangeslagen sigma's (Σ^*) gevonden. In deze analyse zijn alleen de geladen toestanden geanalyseerd. De zware neutrale hyperonen vervallen in ongeladen pionen (π^0) die weer in fotonen (γ) vervallen. Dit zorgt voor een smering van het signaal, dat dan verzinkt in de achtergrond. Het xi-deeltje valt in een andere klasse van gebeurtenissen, aangezien het in tenminste 4 verdere deeltjes vervalt, en dat reduceert de reconstructie efficiëntie. Voor het omega (Ω) hyperon is alleen een boven limiet afgeleid.

Vervolgens is onderzocht hoe groot het deel van uit vervallen geproduceerde Λ^0 is in de totale hoeveelheid gevonden Λ^0's. Met behulp van PYTHIA werd de zuiverheid van deze verzameling van gebeurtenissen in termen van de kinematische variabelen z en x_{f} beschreven. Er is een duidelijke afhankelijkheid van de zuiverheid met deze twee variabelen gevonden. Door deze afhankelijkheden weg te integreren werden de subproces fracties bepaald, zie ook figuur 6.30. Volgens deze Monte Carlo berekeningen wordt ongeveer 50% van het Λ^0 signaal veroorzaakt door secundair geproduceerde Λ's.

PYTHIA Monte Carlo berekeningen voor de zuiverheid van de Λ^0 productie zijn voor het eerst vergeleken met de experimenteel bepaalde deel-proces bijdragen. Voor dit doel zijn de gemeten bijdragen aan hyperon productie gebruikt. In figuur 6.19 zijn de resultaten te zien. Uit dit vergelijk kunnen verschillende conclusies getrokken worden. Beide methoden, de Monte Carlo zowel als de experimentele, laten zien dat ongeveer 50% van alle geproduceerde Λ^0 komen van de directe productie. De twee methoden verschillen echter als het gaat om productie van Λ^0's via de vervallen van zware hyperonen. Terwijl de experimentele methode vast stelt dat de meeste secundair geproduceerde Λ^0's van het Σ deeltje komen, voorspelt de PYTHIA methode dat ongeveer evenveel secundaire Λ^0's van Σ^0 als van de Σ^* hyperon vervallen komen. Beide methoden stemmen daarin overeen dat de bijdrage tot de Λ^0 productie van nog zwaardere hyperonen niet belangrijk is. Daarom is het noodzakelijk dat elke analyse die gebruik maakt van direct geproduceerde Λ^0 hyperonen, zoals bijvoorbeeld voor Λ polarisatie metingen, een correctie doorvoert omdat deze groep gebeurtenissen verdunt is met Λ^0 uit Σ^0 en Σ^0 vervallen. Analyses die de resultaten gebruikt hebben van PYTHIA voorspellingen voor deze correctie factor zullen opnieuw ge-evalueert moeten worden. Uit de hier gepresenteerde analyse blijkt echter dat het hoogst waarschijnlijk voldoende is om een correctie door te voeren voor de bijdrage tengevolge van het Σ^0 verval.

Met behulp van Monte Carlo gebeurtenis generatoren was het ook mogelijk om verschillende hyperon werkzame doorsneden te bepalen voor de HERMES detector acceptatie. Deze resultaten konden worden geëxtrapoleerd van de HERMES acceptatie naar 4π. Dit is gebaseerd op ramingen van de efficiëntie van hyperon productie in de effectieve acceptatie van de HERMES detector met behulp van Monte Carlo berekeningen.

De vergelijking van uit de data bepaalde werkzame doorsneden met door Monte Carlo voorspelde werkzame doorsneden is te zien in figuur 7.1. Zoals is te zien, en geldt voor de werkzame doorsneden van alle hyperonen, zijn de Monte Carlo voorspellingen gemiddeld een factor 16 kleiner dan geobserveerd. Echter, de massa afhankelijkheid blijkt

een gelijkwaardige trend te volgen. Als men de door Monte Carlo voorspelde werkzame doorsneden vergelijkt met de gemeten waarden kunnen twee dingen opgemerkt worden. Ten eerste, de voorspelde MC werkzame doorsneden zijn altijd lager dan de gemeten werkzame doorsneden. Dit wordt vermoedelijk veroorzaakt door een onderschatting van de productie werkzame doorsneden in de MC generator. Ten tweede, de verhouding tussen deeltjes en anti-deeltjes is in de meeste gevallen voor de MC substantieel kleiner dan voor de metingen. Alleen in het geval van de Ξ^- is dit anders.

Om de werkzame doorsnede voor 4π te herleiden zijn detectie, reconstructie en andere rendementen noodzakelijk. Deze rendementen kunnen slechts bepaald worden met behulp van Monte Carlo simulaties van de detector. De metingen van de werkzame doorsneden voor de HERMES detector kunnen worden ge-extrapoleert naar 4π met behulp van een door Monte Carlo bepaalde rendement als volgt:

$$\sigma_{4\pi} = \sigma_{\rm acc}/\epsilon_{\rm g},$$

met $\epsilon_{\rm g}$ de verhouding tussen de MC werkzame doorsneden voor de HERMES acceptatie en die voor 4π.

Het aantal gedetecteerde deeltjes zowel als de meting van de luminositeit dragen beiden bij tot de onzekerheid op de meting van de werkzame doorsnede. De grootste bijdrage komt van de bepaling van de rendementen door Monte Carlo berekeningen. Daar de Monte Carlo berekeningen de werkzame doorsneden voor de HERMES acceptatie onderschatten, is de conclusie dat het hyperon productie model in PYTHIA incompleet is, of niet goed genoeg is afgestemd. Dat wil zeggen dat zolang deze tegenstrijdigheid niet is opgelost, de onzekerheid ten gevolge van de rendementen niet bepaald is. Voor de energieën van de deeltjes die in het HERMES experiment waargenomen worden bestaat er slechts een model voor barion productie, namelijk het di-quark model dat in PYTHIA is gemplementeerd. Andere modellen, zoals het POPCORN [43] model, kunnen alleen voor hogere energieën toegepast worden. Voor een betere beschrijving van de werkzame doorsnede en subproces verhoudingen zijn duidelijk andere modellen noodzakelijk zowel als het meerekenen van zwaardere hyperon productie graden.

De HERMES hyperon productie werkzame doorsneden, ge-extrapoleert naar 4π staan in figuur 7.2. In dit geval zijn de werkzame doorsneden genormaliseerd met $(2J+1)$, in overeenstemming met de e^+e^- productie resultaten zoals die in fig. 2.3 staan. De bovengrens voor Ω^- foto productie en de werkzame doorsneden voor $\Lambda(1520)$ en Σ^{*0} productie komen van Ref. [10].

Het exponentiële verval van de productie werkzame doorsnede is onderzocht. Zoals te zien is op figuur 7.2, de richting coefficient is verschillend voor deeltjes en anti-deeltjes. Een exponentiële functie is geadapteerd naar de curven van de eerste drie neutrale deeltjes. Voor de twee richting coefficienten werd -31.0 ± 1.0 en -14.5 ± 0.5 gevonden, voor deeltjes en anti-deeltjes respectievelijk. De richting coefficenten zijn ook door andere experimenten bepaald. Uit de OPAL gegevens, bijvoorbeeld, wordt een richting coefficient van 9.3 ± 0.3 gevonden. Het hier behaalde resultaat is duidelijk steiler dan de co-efficienten van het OPAL experiment, zoals ook blijkt uit figuur 2.3. Dit wijst er op dat het productie mechanisme voor hyperonen in DIS anders is als in e^+e^- verstrooiing. Om hyperon productie

te gebruiken voor de studie van de barion spin structuur is een betere beschrijving nodig van quasi-echte foto productie van Λ^0 deeltjes.

Figuur 7.1: Quasi echte foto-productie werkzame doorsneden in de HERMES acceptatie tegen de massa van de hyperonen voor data en de PYTHIA Monte Carlo berekenening. De lading van de deeltjes is gecodeerd, zo dat cirkels, kruisjes en blokjes corresponderen met respectievelijk, neutrale, positief en negatief geladen hyperonen. De dichte (open) punten gelden voor (anti) deeltjes. De doorgetrokken (onderbroken) lijn beschrijft de voorspelling van de Monte Carlo berekeningen.

Figuur 7.2: De quasi-echte foto productie werkzame doorsneden voor verschillende hyperonen, geëxtrapoleerd naar 4π, tegen de massa uitgezet. De verticale as is geschaald met $(2J + 1)$. Deeltjes zijn met dichte symbolen gemarkeerd, en anti-deeltjes met open symbolen. De lading van de deeltjes is gecodeerd in het symbool dat is gebruikt. De bovengrens voor de werkzame doorsnede van het Ω^- deeltje is toegevoegd. Tenslotte zijn ook de $\Lambda(1520)$ en de Ξ^{*0} [10] in de figuur weergegeven.

Appendix A

Fitting Functions

The various sections of this appendix summarize different fitting functions used in the present thesis. The fitting functions are used to describe the peaks and background distributions for the different invariant mass distributions.

A.1 Gaussian

The Gaussian function corresponds to the probability density of the normal distribution. With M the mean position of the distribution and σ the width of the distribution, the function can be written as

$$G(m, M, \sigma) = \frac{C}{\sqrt{2\pi}\sigma} \exp -\frac{1}{2}\left(\frac{m-M}{\sigma}\right)^2, \tag{A.1}$$

where C is the normalization constant. The integral of the distribution is 1 for $C = 1$. The width-parameter of the normal distribution is the variance and not the Full Width Half Maximum (FWHM). The FWHM can be calculated from the width by

$$FWHM = 2\sigma * \sqrt{2\ln 2}. \tag{A.2}$$

A.2 Breit Wigner

The general form of the Breit-Wigner (BW) distributions is called Cauchy [31] distribution and its functional form is described by:

$$f(x) = \frac{1}{\pi}\frac{1}{1+x^2} \tag{A.3}$$

The so-called non-relativistic Breit-Wigner function including the parameters width Γ, mode x_0 and intensity C is

$$F(x; x_0, \Gamma) = \frac{C}{\pi}\frac{\Gamma/2}{(x-x_0)^2 + (\Gamma/2)^2}, \tag{A.4}$$

where x_0, the first mode, is the mean and Γ is the FWHM of the distribution.

For the use of fitting mass distributions of decaying particles with a very short lifetime ($< 10^{-20}$ s) and an internal width the relativistic Breit-Wigner distribution can be used as [88]

$$BW(m; M, \Gamma) = \frac{C}{\pi} \frac{mM\Gamma}{(m^2 - M^2)^2 + (M\Gamma)^2}. \tag{A.5}$$

Taking into account that the decaying particle has an orbital angular momentum the width parameter becomes a function of m

$$BW(m; M, \Gamma(m)) = \frac{C}{\pi} \frac{mM\Gamma(m)}{(m^2 - M^2)^2 + (M\Gamma(m))^2} \tag{A.6}$$

where

$$\Gamma(m) = \Gamma \left(\frac{q}{q_0} \right)^{2l+1} \frac{2q_0^2}{q^2 + q_0^2} \tag{A.7}$$

with:

$$q = \frac{\lambda^{1/2}(m, m_1, m_2)}{2m} \tag{A.8}$$

$$q_0 = \frac{\lambda^{1/2}(M, m_1, m_2)}{2M} \tag{A.9}$$

$$\lambda^{1/2}(M, m_1, m_2) = [M^2 + m_1^2 + m_2^2 - 2Mm_1 - 2Mm_2 - 2m_1m_2]^{1/2} \tag{A.10}$$

A.3 Background functions

Naturally, there can be different functions which are able to describe the shape of the background. Commonly used are polynomial distributions of different orders, like

$$BG(x) = C_0 + C_1 \cdot x + C_2 \cdot x^2 + C_3 \cdot x^3 + ... \tag{A.11}$$

The most simple case of a background is flat which is then described by a straight line. Already the second order is difficult as the parameters are not orthogonal and in most cases the difference in the histogram limits are small compared to the actual value

$$m >> |m_2 - m_1|. \tag{A.12}$$

An improvement of this situation are orthogonal functions like the Chebychev or Legendre function for example as used for the invariant mass spectrum of the Λ^0 hyperon, together with the substitution of the mass with the lower m_1 and upper limit m_2 of the histogram. This substitution has as an effect, that y varies between $[-1; +1]$ and therefore is

$$y = \frac{x - (m_1 + m_2)/2}{0.5(m_2 - m_1)} \tag{A.13}$$

$$\begin{aligned}
0: &\quad 1 \\
1: &\quad y \\
2: &\quad 2y^2 - 1 \\
3: &\quad 4y^3 - 3y \\
4: &\quad 8y^4 - 8y^2 + 1 \\
&\ldots \\
n: &\quad C_{n+1}() = 2xC_n(y) - C_{n-1}(y)
\end{aligned} \tag{A.14}$$

Or the same with the Legendre polynomials

$$\begin{aligned}
0: &\quad 1 \\
1: &\quad y \\
2: &\quad 1/2(3y^2 - 1) \\
3: &\quad 1/2(5y^3 - 3y) \\
4: &\quad 1/8(35y^4 - 30y^2 + 3) \\
&\ldots \\
n: &\quad L_{n+1}(y) = \frac{1}{n+1}\left((2n+1)yL_n(y) - nL_{n-1}(y)\right)
\end{aligned} \tag{A.15}$$

In case of a sharp rising background starting from a threshold value m_0 a power function is used. The steep rise is overruled by an exponential at higher values

$$BG(x) = A_0 \cdot (x - m_0)^{A_1} \cdot \exp\left(-xA_2 + A_3x^2\right) \tag{A.16}$$

where

$$x = \frac{m_2 - m}{m_2 - m_1}. \tag{A.17}$$

But in this case it is not trivial to keep the parameters under control and a good starting value for the parameters has to be guessed to enable the fitting routine to converge at a minimum.

Appendix B

PYTHIA setup parameters

switch	value	switch	value	switch	value	switch	value
MSTP 1	2	MSTP 2	1	MSTP 3	2	MSTP 4	0
MSTP 5	0	MSTP 7	0	MSTP 8	0	MSTP 9	0
MSTP 11	1	MSTP 12	0	MSTP 13	2	MSTP 14	30
MSTP 15	0	MSTP 16	1	MSTP 17	6	MSTP 18	3
MSTP 19	4	MSTP 20	0	MSTP 21	1	MSTP 22	0
MSTP 23	1	MSTP 31	1	MSTP 32	8	MSTP 33	0
MSTP 34	1	MSTP 35	0	MSTP 36	2	MSTP 37	1
MSTP 38	4	MSTP 39	2	MSTP 40	0	MSTP 41	1
MSTP 42	1	MSTP 43	3	MSTP 44	7	MSTP 45	3
MSTP 46	1	MSTP 47	1	MSTP 48	0	MSTP 49	1
MSTP 50	0	MSTP 51	4046	MSTP 52	2	MSTP 53	3
MSTP 54	1	MSTP 55	5	MSTP 56	1	MSTP 57	1
MSTP 58	4	MSTP 59	1	MSTP 60	7	MSTP 61	0
MSTP 62	3	MSTP 63	2	MSTP 64	2	MSTP 65	1
MSTP 66	5	MSTP 67	2	MSTP 68	1	MSTP 69	0
MSTP 71	0	MSTP 81	0	MSTP 82	1	MSTP 83	100
MSTP 86	2	MSTP 91	1	MSTP 92	4	MSTP 93	1
MSTP 94	3	MSTP 101	1	MSTP 102	1	MSTP 111	1
MSTP 121	1	MSTP 131	0	MSTP 171	0	MSTP 172	2
MSTP 173	0						
PARP 1	0.25	PARP 2	7.	PARP 13	1	PARP 14	0.01
PARP 15	0.5	PARP 16	1	PARP 17	1	PARP 18	0.17
PARP 61	0.25	PARP 62	0.5	PARP 63	0.25	PARP 64	1
PARP 65	0.5	PARP 66	0.001	PARP 67	1.	PARP 68	0.001
PARP 71	4.	PARP 72	0.25	PARP 91	0.44	PARP 93	2.
PARP 94	1.	PARP 95	0.	PARP 96	3.	PARP 97	1.
PARP 98	0.75	PARP 99	0.44	PARP 100	2	PARP 102	0.5
PARP 103	0.5	PARP 104	0.3	PARP 111	0.	PARP 121	2.
PARP 161	2.69	PARP 162	24.6	PARP 163	18.8	PARP 164	11.5

PARP 165	0.33						
PARJ 1	0.029	PARJ 2	0.283	PARJ 3	1.2	PARJ 4	0.05
PARJ 5	0.5	PARJ 6	0.5	PARJ 7	0.5	PARJ 11	0.5
PARJ 12	0.6	PARJ 21	0.381	PARJ 23	0.01	PARJ 24	2.0
PARJ 32	1.0	PARJ 33	0.800	PARJ 41	1.94	PARJ 42	0.544
PARJ 45	1.05						
MSTJ 1	1	MSTJ 2	3	MSTJ 3	0	MSTJ 12	1
MSTJ 40	0	MSTJ 45	4				
MSTU 16	2	MSTU 21	1	MSTU 112	4	MSTU 113	4
MSTU 114	4						
CKIN 1	1.	CKIN 2	-1.	CKIN 3	0.	CKIN 4	-1.
CKIN 5	1.00	CKIN 6	1.00	CKIN 7	-10.	CKIN 8	10.
CKIN 9	-10.	CKIN 10	10.	CKIN 11	-10.	CKIN 12	10.
CKIN 13	-10.	CKIN 14	10.	CKIN 15	-10.	CKIN 16	10.
CKIN 17	-1.	CKIN 18	1.	CKIN 19	-1.	CKIN 20	1.
CKIN 21	0.	CKIN 22	1.	CKIN 23	0.	CKIN 24	1.
CKIN 25	-1.	CKIN 26	1.	CKIN 27	-1.	CKIN 28	1.
CKIN 31	2.	CKIN 32	-1.	CKIN 35	0.	CKIN 36	-1
CKIN 37	0.	CKIN 38	-1.	CKIN 39	4.	CKIN 40	-1.
CKIN 65	1e-09	CKIN 66	60.0	CKIN 77	2.0	CKIN 78	-1.

Table B.1: In this table the settings for the PYHTIA Monte Carlo simulations are shown.

Appendix C

Data Quality

BIT	Quality	value	explanation	SET
0	g1DAQ iTargetBit	4||8	nuclear states	0
1	g1Beam rPolFit	$30 - 80$	beam polarization	0
2	g1DAQ rDeadCorr		dead time	1
3	g1DAQ rLength	$> 0\& \leq 11$	burst length	1
4	g1Beam rMdmCurr	$\geq 5\& \leq 50$	beam current	1
5	g1Beam rLumiFitBstGai	$\leq 5\& \leq 80$	luminosity	0
6	g1Quality iuDSTbad		first burst in a run	1
7	g1Quality iuDSTbad		bad uDST records	1
8	g1Quality iuDSTbad2		no PID	1
9	g1Quality iExpment	1	Logbook: analyzable	1
10	g1Quality iExpMode	2	select two state	1
11	g1Quality iExpMode	0 16	unpolarized	1
12	g1Quality iExpMode	<0	not analyzable	1
13	g1Quality iExpMode	3	3 state	1
14	g1Quality iExpMode	4	4 state	1
15	g1Unpol iGasType	> 0	unpolarized data	1
16	g1Target rPol		target bad	0
17	g1Quality bCaloDead		dead block in calorimeter	1
18	bH2LumiDead		dead block in H2	1
19	iTrdDQ		TRD bad	1
20	g1HVtrip iDetId		HV trips	1
21	g1Daq iRun		exclude certain runs	1
22	g1HVTrip		HV trips	1
23	g1ABS		ABS data quality	0
24	g1ABS		ABS data quality	0
25	g1Quality bCereDQ		RICH bad	1
26	g1DAQ iTargetBit		tensor polarized	0
27	g1ABS CalCarryOver			0
28	g1Beam iPolFitGap			0

29	g1Target rPol		not used	0
30	rDeadCorr artificial		not used check bit 2	1
31	bClaoDead		dead blocks in calorimeter	1
			resulting bit pattern $\rightarrow 0xc27effdc$	

Table C.1: Data Quality bit pattern for polarized burst lists

C.1 Requirements and Constants

CUT variable	min	max	unit	explanation
Lepton:				
rPID3+5	1.0	+99.0	-	PID cut
rEnergy	3.5	-	GeV	cut on momentum
rVertZ	-18.0	18.0	cm	z-vertex cut
rVertD	0.0	0.75	cm	radial distance from beam-line
DIS:				
x	0.0	1.0	-	x Bjorken cut
y	0.1	0.85	-	y cut
Q^2	1.0	99.0	GeV^2	q2
W^2	4.0		GeV^2	w2
Lambda:				
rPID3+5	-99.0	0.0	-	PID cut
AP	0.0	-	-	relative proton pion energy cut
DCA	0.0	1.5	cm	secondary vertex track distance
collinearity	-1.0	1.0	-	collinearity of lambda momentum and direction
ΔZ	0.0	200	cm	decay length of the Λ
mass	1.07	1.17	GeV	mass range for the Λ
Hyperon:				
ΔZ	-15.0	200	cm	
DCA		2.5	cm	
vertex		1.6	cm	
Fiducial Volume:				
vertical	33.0	105.0	cm	
horizontal		125.0	cm	
values of some used constants:				
E_b	from UDST		GeV	Beam energy (g1Beam.rHeraElEnergy)
M_l	0.510998902E-03		GeV	mass of the lepton
M_p	0.938271998		GeV	mass of the proton
$M_{\pi^\pm}$	0.13957018		GeV	mass of the charged pion
CALOZ	747.5		cm	Calorimeter position
CALOCON	0.97		-	Calorimeter energy calibration

Table C.2: All Requirements and constants used in this analysis are displayed.

Abbreviations used in this thesis:

ADC	Analogue to Digital Converter
BLM	Beam Loss Monitor
BNC	Bayonet Nut Connector
CAEN	Costruzioni Apparecchiature Elettroniche Nucleari
CAN	Controller Area Network
DESY	Deutsches Elektronen Synchrotron
DIS	Deep Inelastic Scattering
DRT	Direct Ray Tracing
DVC	Drift Vertex Chamber
ET	Electronic(s) Trailer
GEANT	Detector Description and Simulation Tool
GMC	General Monte Carlo
HERMES	HERA Measurement of Spin
HERA	Hadron Elektron Ring Anlage
HERA-B	HERA B physics program
HLCU	Hermes Logic Control Unit
HMC	Hermes Monte Carlo
HRC	Hermes Reconstruction Code
HV	High Voltage
IRT	Indirect Ray Tracing
JETSET	Lund string fragmentation program
LEP	Large Electron Positron collider
LINUX	computer operating system
LW	Lambda Wheels
NIKHEF	Nationaal Instituut voor Kernfysica en Hoge Energiefysica
PCI	Peripheral Component Interface
PDF	Parton Distribution Function
PYTHIA	Monte Carlo event generator
PRC	Physics Review Commitee
QCD	Quantum Chromo Dynamic
QED	Quantum Electro Dynamics
RICH	Ring Imaging Čerenkov
UDST	micro Data Summary Table
XTC	eXternal Tracking Code

List of Tables

List of Figures

Bibliography

[1] K. Abe et al. Measurements of the proton and deuteron spin structure functions g1 and g2. *Phys. Rev.*, D58:112003, 1998.

[2] K. Ackerstaff et al. The HERMES spectrometer. *Nucl. Instrum. Meth.*, A417:230–265, 1998.

[3] K. Ackerstaff et al. Flavor decomposition of the polarized quark distributions in the nucleon from inclusive and semi-inclusive deep- inelastic scattering. *Phys. Lett.*, B464:123–134, 1999.

[4] D. Adams et al. Spin structure of the proton from polarized inclusive deep- inelastic muon proton scattering. *Phys. Rev.*, D56:5330–5358, 1997.

[5] M. R. Adams et al. Λ and $\overline{\Lambda}$ polarization from deep inelastic muon scattering. *Eur. Phys. J.*, C17:263–267, 2000.

[6] A. Airapetian. Longitudinal spin transfer to the lambda hyperon in semi- inclusive deep-inelastic scattering. *Physics Review D*, D74:072004, 2006.

[7] A. Airapetian et al. Flavor decomposition of the polarized quark distributions in the nucleon from inclusive and semi-inclusive deep- inelastic scattering. *Phys. Rev. Lett.*, 92:012005, 2004.

[8] A. Airapetian et al. The HERMES polarized hydrogen and deuterium gas target in the HERA electron storage ring. *Nucl. Instrum. Meth.*, A540:68, 2005.

[9] A. Airapetian et al. Quark helicity distributions in the nucleon for up-, down-, and strange-quarks from semi-inclusive deep-inelastic scattering. *Phys. Rev.*, D71:012003, 2005.

[10] A. Airapetian et al. Search for an exotic S=-2, Q=-2 baryon resonance at a mass near 1862 MeV in quasi-real photoproduction. *Phys. Rev.*, D71:32004, 2005.

[11] A. Airapetian et al. The time-of-flight technique for the HERMES experiment. *Nucl. Instrum. Meth.*, A540:305–310, 2005.

[12] N. Akopov et al. The HERMES dual-radiator ring imaging Čerenkov detector. *Nucl. Instrum. Meth.*, A479:511–530, 2002.

[13] G. Alexander et al. Strange baryon production in hadronic Z0 decays. *Z. Phys.*, C73:569–586, 1997.

[14] AMS. *http://www.austriamicrosystems.com/*. AMS Austria Micro Systems, 2005.

[15] B. Andersson et al. Parton fragmentation and string dynamics. *Z. Phys.*, C20:317, 1983.

[16] A. Andreev et al. Multiwire proportional chambers in the HERMES experiment. *Nucl. Instrum. Meth.*, A465:482–497, 2001.

[17] J. Ashman et al. A measurement of the spin asymmetry and determination of the structure function g(1) in deep inelastic muon proton scattering. *Phys. Lett.*, B206:364–370, 1988.

[18] P. Astier et al. Measurement of the lambda polarization in ν/μ charged current interactions in the nomad experiment. *Nucl. Phys.*, B588:3–36, 2000.

[19] B. Aubert et al. Search for strange pentaquark production in e+ e- annihilations at $\sqrt{s} = 10.58$ GeV and in upsilon(4s) decays. *Phys.Rev.Lett. 95 (2005) 042002*, 2004.

[20] H. Avakian et al. Performance of the electromagnetic calorimeter of the HERMES experiment. *Nucl. Instrum. Meth.*, A417:69–78, 1998.

[21] E. Avetisyan. Calorimeter calibration constant. private communication, 2005.

[22] D.P. Barber et al. The HERA polarimeter and the first observation of electron spin polarization at HERA. *Nucl. Instrum. Meth.*, A329:79–111, 1993.

[23] D.P. Barber et al. High spin polarization at the HERA electron storage ring. *Nucl. Instrum. Meth.*, A338:166–184, 1994.

[24] C. Baumgarten et al. An atomic beam polarimeter to measure the nuclear polarization in the HERMES gaseous polarized hydrogen and deuterium target. *Nucl. Instrum. Meth.*, A482:606, 2002.

[25] C. Baumgarten et al. A gas analyzer for the internal polarized target of the HERMES experiment. *Nucl. Instrum. Meth.*, A508:268, 2003.

[26] C. Baumgarten et al. The storage cell of the polarized H/D internal gas target of the HERMES experiment at HERA. *Nucl. Instrum. Meth.*, A496:277, 2003.

[27] M. Beckmann et al. The longitudinal polarimeter at HERA. *Nucl. Instrum. Meth.*, A479:334, 2002.

[28] T. Benisch. *Polarisierte Bhabha-Streuung und Luminositätsmessung im* H*ERMES-Experiment.* PhD thesis, Naturwissenschaftlichen Fakultäten der Universität Erlangen-Nürnberg, Erlangen-Nürnberg, 1998.

[29] T. Benisch. The luminosity monitor of the HERMES experiment at desy. *Nucl. Instrum. Meth.*, A471:314, 2001.

[30] S. Bernreuther et al. The HERMES back drift chambers. *Nucl. Instrum. Meth.*, A416:45–58, 1998.

[31] R.K. Block. The data analysis brief-book. http://rkb.home.cern.ch/rkb/.

[32] C. Bonomo. Trigger efficiency dependence on proton momentum. private communication, 2005.

[33] O. Bouhali et al. The HERMES beam loss monitor. Internal HERMES report 01-013, DESY, 2001.

[34] O. Bouhali et al. Test of the HERMES beam loss monitor with x-rays. Internal HERMES report 01-054, DESY, 2001.

[35] J. T. Brack et al. The HERMES forward tracking chambers. *Nucl. Instrum. Meth.*, A469:47–54, 2000.

[36] CAEN. Caen web page. http://www.caen.it/.

[37] CERN. *EPIO Experimental Physics Input Output Package*, 1994. CERN Program Library Long Writeup I101.

[38] CERN. *ADAMO web page*, 1999.

[39] CERN. *GEANT - Detector Description and Simulation Tool*, 2003. CERN Program Library Long Writeup W5013.

[40] H1 Collaboration. The H1 detector at HERA. *Nucl. Instrum. Meth.*, A386:310–347 and 348–396, 1997.

[41] HERA-B Collaboration. An experiment to study CP violation in the b system using an internal target at the HERA proton ring. *DESY-PRC-95-01*, page 491, 1995.

[42] M. Demey. *The polarization of Λ^0 hyperons in quasi-real photoproduction.* PhD thesis, Universiteit van Amsterdam, The Netherlands, March 2007. to be written.

[43] P. Eden and G. Gustafson. Baryon production in the string fragmentation picture. *Zeitschrift für Physik C*, 75:41–49, 1997.

[44] U. Elschenbroich. Analysis of luminosity monitor data for different years. Internal HERMES report 02-013, DESY, 2002.

[45] U. Elschenbroich. Bhabha-streuung und luminositätsmessung im HERMES-experiment. Master's thesis, Heinrich Heine Universität, Düsseldorf, Aug 2001.

[46] T. Ferber. *Experimental techniques in high energy nuclear and particle physics.* Addison-Wesley Publishing Company, Inc., Menlo Park California, 1987.

[47] Martin Feuerstack-Raible. *Helix128 Documentation.* Kirchhoff Institut für Physik, 1999.

[48] Data Quality group. Data quality web page. http://www-hermes.desy.de/groups/daqlgrp/.

[49] D. Heesbeen. *Quasi-real photo-production of hyperons on polarized 1,2H targets.* PhD thesis, Rijksuniversiteit Groningen, The Netherlands, Juni 2003.

[50] K. Heller. Spin and high energy hyperon production, results and prospects. *Proceedings of the 12th International Symposium on High-Energy Spin Physics (SPIN 96)*, page 23, 1997.

[51] The HERMES Collaboration. Technical design report. *DESY-PRC*, 93/06, 1993.

[52] A. Hillenbrand. *Measurement and Simulation of the Fragmentation Process at HERMES.* PhD thesis, Friedrich-Alexander-Universität, Erlangen-Nürnberg, 2005.

[53] D. Kharzeev J. Ellis and A. Kotzinian. The proton spin puzzle and Λ polarization in deep-inelastic scattering. *Z. Phys*, C 69:467–, 1996.

[54] R.L. Jaffe. Polarized lambdas in the current fragmentation region. *Phys. Ref.*, D54:R6581–R6585, 1996.

[55] R. Kaiser. Likelihood analysis for the RICH IRT method. Internal HERMES report 00-026, DESY, 2004.

[56] R. Kaiser et al. Particle identification at HERMES. Internal HERMES report 97-025, DESY, 1997.

[57] M. Kopytin. TOF measurements for particle identification. Internal HERMES report 01-053, DESY, 2004.

[58] P. Kravchenko. Monte carlo lambda studies. Private communication, 2005.

[59] W.R. Leo. *Techniques for nuclear and particle physics experiments.* Springer-Verlag, Berlin, 1994.

[60] B. Levchenko. Kinematic selection criteria in a new resonance searches: Application to pentaquark states. -, -, 2004. hep-ph/0401122.

[61] P. Liebig. *Can the Gluon Polarization in the Nucleon be Extracted from HERMES Data on Single High-pT Hadrons?* PhD thesis, Universität Hamburg, Hamburg, 2004.

[62] W. Lorenzon. Beam polarimetry at HERA. Internal HERMES report 97-068, DESY, 1997.

[63] V. Mexner. *Determination of the gluon polarization in the nucleon.* PhD thesis, University of Amsterdam, Amsterdam, 2005.

[64] Reinhard Mey. Gute Nacht Freunde. Über den Wolken - Lieder aus 4 Jahrzehnten, 2003.

[65] C.A. Miller. Proposal for a HERMES drift vertex chamber. Internal HERMES report 95-072, DESY, 1995.

[66] A. Nass et al. The HERMES polarized atomic beam source. *Nucl. Instrum. Meth.*, A505:633, 2003.

[67] PDG. Pdg web page. http://pdg.web.cern.ch/pdg/.

[68] J. Podolanski and R. Armenteros. Analysis of V-Events. *Philosophical Magazine*, 45:13, 1954.

[69] A. Reischl, M. Demey, D. Heesbeen, and J. Steijger. Lambda wheel alignment (part I/II/III). Technical report, NIKHEF, 2003.

[70] D. De Schepper et al. The HERMES cerenkov detector. Internal HERMES report 00-021, DESY, 2000.

[71] T. Sjöstrand, P. Eden, C. Friberg, L. Lonnblad, G. Miu, S. Mrenna, and E. Norrbin. High-energy-physics event generation with PYTHIA 6.1. *Computer Physics Commun*, 135:238, 2001.

[72] T. Sjöstrand et al. *PYTHIA 6.3 and JETSET webpage*, 2005.

[73] T. Sjöstrand, L. Lonnblad, and S. Mrenna. *PYTHIA 6.2 Physics and manual*, 2002.

[74] A.A. Sokolov and I.M. Ternov. On polarization and spin effects in the theory of synchrotron radiation. *Sov. Phys. Doklady*, 8:1203, 1964.

[75] J. Steel. Zermatt observatory panorama. http://www.flickr.com/photos/jimsteel/9744566/, 2005.

[76] J. J. M. Steijger. The HERMES silicon project. *Nucl. Instrum. Meth.*, A447:55–60, 2000.

[77] J. J. M. Steijger. The Lambda Wheels, a silicon vertex detector for HERMES. *Nucl. Instrum. Meth.*, A453:98–102, 2000.

[78] J. J. M. Steijger. -. private communication, 2005.

[79] M. G. van Beuzekom, O. Bouhali, V. Mexner, A. Reischl, and J. J. M. Steijger. The HERMES silicon project - the radiation protection system. *Nucl. Instrum. Meth.*, A512:44–51, 2003.

[80] M. G. van Beuzekom, E. Garutti, D. Heesbeen, J. J. M. Steijger, and J. Visser. First experience with the HERMES silicon detector. *Nucl. Instrum. Meth.*, A461:247–250, 2001.

[81] M.G. van Beuzekom et al. Technical design report of the new silicon-detector system. Internal HERMES report 98-014, DESY, 1998.

[82] G. van der Steenhoven et al. New silicon-detector systems for the HERMES front region. Internal HERMES report 97-032, DESY, 1997.

[83] Vector Informatic GmbH. *CAN web page*, 2005.

[84] J. Visser. *Deep inelastic scattering off hydrogen and deuterium.* PhD thesis, Rijksuniversiteit Groningen, The Netherlands, September 2002.

[85] J. Visser et al. Design and performance of a silicon test counter for HERMES. *Nucl. Instrum. Meth.*, A521:430–440, 2004.

[86] J. Wendland. Particle identification for HERMES Run I. Internal HERMES report 01-067, DESY, 2004.

[87] G. Wolf et al. The ZEUS detector: Technical proposal. *DESY*, 1986. DESY-HERA-ZEUS-1.

[88] M. Zavertyaev. The invariant mass spectra fit. HERA-B 02-079, 2002.

Acknowledgment

The first person I met closely related to my thesis was you Gerard. From the first moment your enthusiasm fascinated me and carried me along my work and finally helped to finish this work. Thank you Gerard for all your support and the positive spirit.

Next is Jos whom I want to thank. Everybody knows that you are an expert in science, in general. We had many discussions not only on work but also about fun stuff over lunch. But what I admire most of you is that even though we had our arguments you never took it personal. Your advises were always so sincere and from the heart like a father would give them to his son.

My colleagues from Hamburg ('Mahlzeit') I want to thank for the wonderful time I had during my stay there. Alphabetical ordered: Achim, Alexander, Arne, Avetik, Bino, Caroline, Dominik, Jim, Eduard, Frank, Iouri, Marc, Markus, Riccardo, Sabine, Stan, Wouter, Vitaly, Yves, York. A special thank you goes to Elke, Delia, Beni, Larry and Maurice.

Johan, you definitely have earned and deserve my special thanks here. I should basically name you as my co-author :) for all the discussions we had and the prove reading you did for me. Also a thank you to the colleagues of Johan at the MPI who survived my many visits: Bernhard, Michaela, Misha and Mizzi.

Gabriel, thanks for being such a nice friend and supporting me during my second phase in Amsterdam. I very much enjoyed our time together. And thanks to you David for being a true friend in Amsterdam. I think we are similar characters in the way we mess up our stuff.

I also want to thank the rest of my group: Armen, Chiara, Henk, Keith, Jan, Louk, Paul, Vanessa, Willem and specially Michiel. Also to the many other NIKHEF people I had a nice time with just to name a few: Arnold, Hella, Martin, Max, Rob, Jo, Yke. It was fun living in the Netherlands and especially in Amsterdam.

To my friends in Germany: Heinz, Kumar, Marco and Stefan who have supported me not only with their friendship, I want to say: Dankeschön.

Usually, my family goes first only here the most important come last, I owe you everything. First my parents Adelheid and Anton who started everything and brought me on track. Now with my daughter Antonia I only start to understand what it means to have children. Danke füer alles Mutter. My brother Alexander, I also want to thank you for your big support.

And the last and biggest thank you goes to Mechthild to whom I dedicate this work. Without you nothing would be like it is. Thank you for your love and support ♡

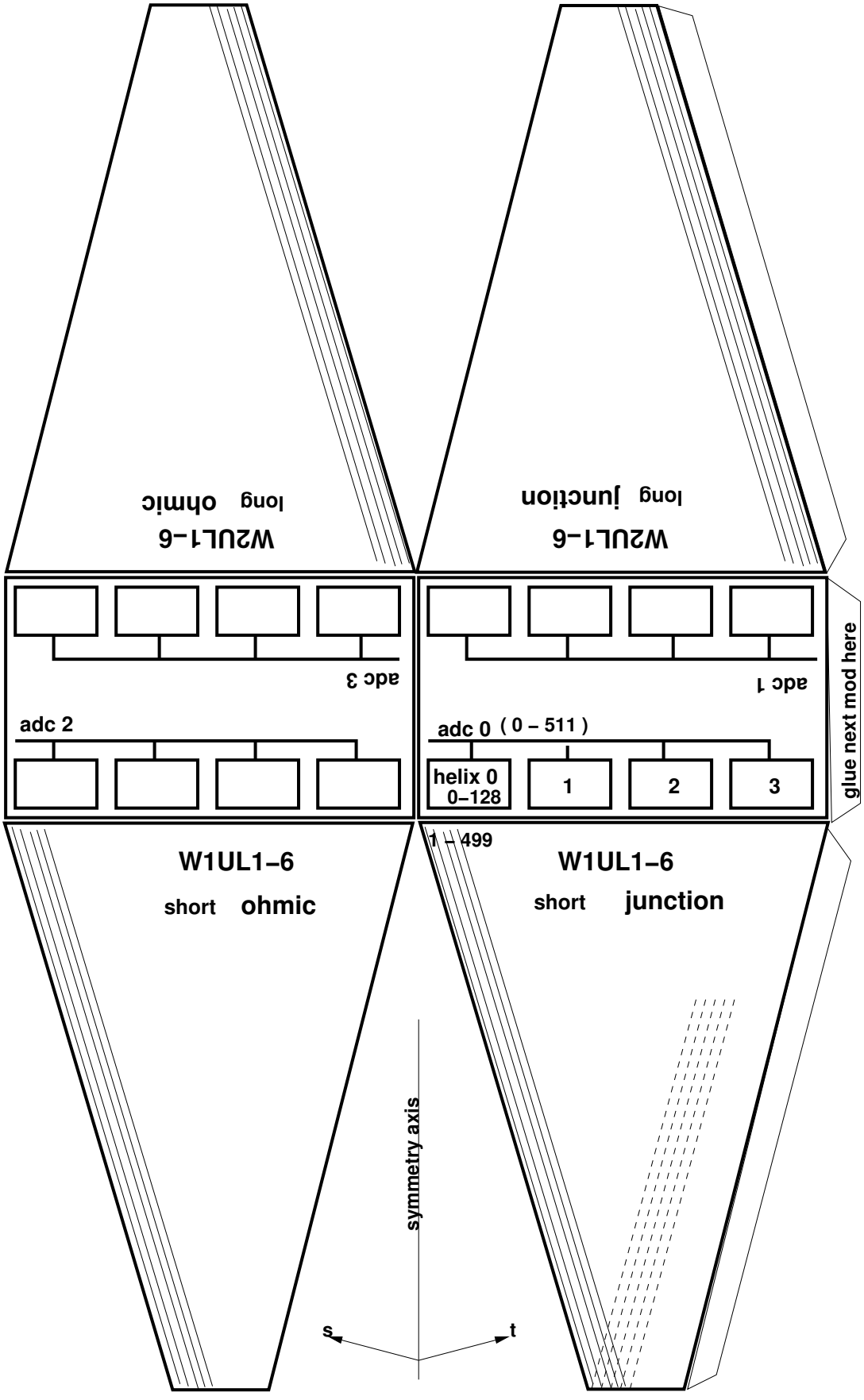

Figure C.1: To construct a paper version of the LW one has to print out this figure 12 times, cut it out along the surrounding line, fold it and glue the next one at the indicated place.

Gute Nacht, Freunde, es wird Zeit für mich zu geh'n.
Was ich noch zu sagen hätte, dauert eine Zigarette
und ein letztes Glas im Steh'n.[64]